The Geometric Correction and Registration of Airborne Line-Scanned Imagery for Temporal Thermal Studies

Simon Gregory

Doctor of Philosophy

Aston University

January 2001

Aston University

The Geometric Correction and Registration of Airborne Line-Scanned Imagery for Temporal Thermal Studies

Simon Gregory
Doctor of Philosophy

Summary

This thesis begins by providing a review of techniques for interpreting the thermal response at the earth's surface acquired using remote sensing technology. Historic limitations in the precision with which imagery acquired from airborne platforms can be geometrically corrected and co-registered has meant that relatively little work has been carried out examining the diurnal variation of surface temperature over wide regions. Although emerging remote sensing systems provide the potential to register temporal image data within satisfactory levels of accuracy, this technology is still not widely available and does not address the issue of historic data sets which cannot be rectified using conventional parametric approaches.

In overcoming these problems, the second part of this thesis describes the development of an alternative approach for rectifying airborne line-scanned imagery. The underlying assumption that scan lines within the imagery are straight greatly reduces the number of ground control points required to describe the image geometry. Furthermore, the use of pattern matching procedures to identify geometric disparities between raw line-scanned imagery and corresponding aerial photography enables the correction procedure to be almost fully automated. By reconstructing the raw image data on a truly line-by-line basis, it is possible to register the airborne line-scanned imagery to the aerial photography with an average accuracy of better than one pixel. Providing corresponding aerial photography is available, this approach can be applied in the absence of platform attitude information allowing multi-temporal data sets to be corrected and registered.

KEYWORDS: Geometric Correction, Line-Scanned Imagery, Pattern Matching, Thermal Remote Sensing, Airborne.

Acknowledgements

I would like to thank the National Remote Sensing Centre and Aston University for providing the funding enabling this research project to go ahead, and the Natural Environment Research Council for providing the remotely sensed imagery on which this project was based. I would also like to thank the James Watt Memorial Foundation for their financial support, granting the opportunity to study with Professor Toby Carlson of Pennsylvania State University, USA. Many thanks also to Professor Carlson for his invaluable help and experience whilst abroad.

I would like to offer my sincere gratitude to my colleagues at Aston University who have provided both moral and technical support throughout the course of this research project, namely Dr. Peter Hedges and Dr. John Elgy. Also deserving of thanks are Dave Hall, Trevor Hewings, Rob Poole and Andy Crowcombe who have assisted in many capacities throughout my research.

I would also like to thank my friends and colleagues who have all helped make my research project an extremely enjoyable experience, particularly Dr. Danny Anstice, Alistair Buchanan, Dr. Phil Purnell and Colin Thompson.

I would like to say a final thank you to my parents, John and Norma Gregory, and my girlfriend, Alison Bisson, for their unwavering love and support.

List of Contents

List of Figures

List of Tables

1. Introduction

1.1 Origins of Project

Airborne remote sensing offers significant advantages over satellite-based systems. Improved spatial resolution available at lower altitudes combined with higher temporal capabilities lends airborne remote sensing to a vast array of applications. Many airborne line-scanning instruments also possess the ability to record radiation in the thermal wave band, a feature which is offered on only a limited number of satellite imaging systems. By combining daytime and dawn thermal image pairs acquired from airborne platforms, differential thermal activity can be assessed at the local scale (typically, at pixel resolutions of 1-2m) providing an additional dimension to thermal remote sensing.

However, one of the major problems associated with airborne remote sensing systems is the severe geometric distortions caused by atmospheric turbulence during image acquisition. Traditional methods of rectifying these errors are unable to meet the demands of applications requiring precise registration of multiple scenes, and this has been a significant factor limiting the development of studies into multi-temporal thermal imaging.

In 1997, Ellis carried out a study to investigate the use of airborne remote sensing to monitor landfill gas and leachate within urban environments (Ellis, 1997), and highlighted a number of problems associated with the airborne thermal imagery. Ellis found that although it was possible to identify local venting of warm gas in the imagery using the thermal band, it was difficult to carry out any quantitative work due to problems in removing the geometric errors. Furthermore, the influence of the thermal inertia of the ground cover could not be assessed because the daytime and dawn thermal image pairs could not be registered accurately enough to allow precise multi-image analysis. As a consequence, Ellis was unable to detect any widespread response to heat generation within the landfill sites using the airborne thermal imagery.

In order to address the problems of geometric correction of airborne line-scanner imagery, the Natural Environment Research Council (NERC) introduced in 1994 a new correction facility to their existing airborne imaging system. The new facility consisted of an Ashtech 3-DF global positioning system (GPS) mounted on the aircraft fuselage, which simultaneously monitored and recorded the aircraft attitude with the image data throughout a flight line. It was hoped that this new system would enable the resulting

imagery to be corrected, using a parametric approach, to a far higher degree of accuracy than was previously possible, therefore enabling quantitative multi-temporal studies to be carried out.

1.2 Initial Project Aim and Objectives

In the wake of experiences gained from the work carried out previously by Ellis, it was hoped to use the new NERC airborne remote sensing system to investigate multi-temporal thermal imagery. The original research project, titled *The Influence of Land-Based Human Activity on Airborne Thermal Imagery*, was therefore proposed, with the primary aim being to;

> *evaluate the geometric accuracy of the NERC GPS-corrected line-scanned imagery, and utilise the image data to acquire a detailed understanding of the information carried within the thermal band.*

It was proposed to achieve this aim by satisfying five broad objectives;

1. determine the accuracy of the GPS-corrected imagery by comparison with maps and geo-correlation techniques;
2. explore the local influence of vegetation on high resolution thermal imagery;
3. study the effects of varying soil characteristics on the imagery, with respect to both local discontinuities, and more gradual spatial changes;
4. use the experience gained from objectives 2 and 3 to develop a methodology for differentiating between human-induced heating and the effects of solar warming;
5. identify potential applications for combined geo-corrected dawn and daytime thermal imagery, and where possible evaluate their viability.

1.3 Data Acquisition Problems

The current research project commenced on the 1st October, 1996, and was scheduled for completion at the end of September, 1999. A successful application was submitted for inclusion in the NERC Airborne Remote Sensing Programme for 1996/1997, and flights were carried out on a number of dates in October and November, 1996. From past experience of obtaining imagery through similar NERC flying programs, it was initially envisaged that the pre-processing stage for the image data sets would require approximately 6 months for completion. However, a number of significant problems were encountered during these pre-

processing stages and, as a consequence, NERC suffered very large delays in delivering the image data. The first digital imagery was not made available until March 1999, and the full set of imagery was eventually delivered in September 1999. The delay in receiving the image data resulted in severe knock-on time implications, and a decision was made towards the end of 1997 to redirect the main thrust of the research project.

1.4 Revised Project Aims and Objectives

In light of the problems experienced by NERC, the direction of the research project was changed to investigate alternative methodologies for rectifying airborne line-scanned imagery. The new project aim was therefore modified to;

> *investigate alternative approaches for rectifying airborne line-scanner imagery, which can be applied without the need for synchronous platform attitude information.*

In achieving the modified project aim, it was proposed to use remotely sensed image data acquired previously within the department, and the methodology extended to the NERC image data set when it eventually arrived. This revised project aim would then enable the original project aims (described in Section 1.2) to be investigated using the NERC imagery corrected using the alternative technique.

It was planned to achieve the new project aim through the following objectives:

1. examine existing image correction techniques to identify sources of error, and investigate potential methods of overcoming these problems;
2. utilise previously acquired image data to develop a methodology for rectifying airborne line-scanned imagery;
3. assess the accuracy of alternative methods of image correction through use of maps and geo-correlation methods;
4. assuming the NERC image data arrives within the project duration, apply the NERC GPS correction and compare the results with those obtained using the alternative approaches developed through objective 2;

5. utilise the corrected imagery to fulfil the original project objectives (objectives 2,3 and 4 described in Section 1.2) and identify potential applications for combined geo-corrected dawn and daytime thermal imagery.

However, as no reliable indication was available as to the likely time-scales involved in obtaining the NERC image data, objectives 4 and 5 were subject to the time constraints, imposed by delays in receiving the imagery.

1.5 Structure of Thesis

Because the main thrust of the research was redirected almost half way through the project, this thesis effectively comprises two parts. The first part provides a detailed review of current approaches of interpreting thermal image data, whilst the second describes the work carried out in investigating alternative methods of rectifying airborne line-scanner imagery. Both of these topics were included in the thesis as it was felt that they were essential for providing a thorough understanding of the problems encountered in firstly registering airborne imagery, and secondly, utilising the information derived from daytime-dawn thermal image pairs.

Chapter 2 begins by examining the primary factors which influence the instantaneous and cyclic temperature at the earth's surface. After introducing some relevant terminology, early empirical approaches for the interpretation of thermal remotely sensed imagery are examined. With the development of computer technology during the late 1970's, more comprehensive methods of modelling thermal behaviour began to emerge, and these are described with respect to their ease of application and the accuracy with which meaningful information can be determined. Finally, the main points are considered and the primary advantages of combining daytime-dawn thermal image pairs are summarised.

Chapter 3 describes the collection of both ground truth and remotely sensed image data used in this project. The location of the study area is illustrated and the nature of the region is discussed in terms of solid geology and soil series. However, due to problems experienced by NERC during pre-processing of the image data, the imagery acquired over the intended study area was not available until September 1999. The majority of work for this project was therefore carried out on additional image data acquired during previous research projects, and the essential characteristics of this data are described.

Chapter 4 begins by providing an overview of airborne imaging systems and examines the main sources of geometric error. Current methods of compensating for these geometric distortions are then described, with particular emphasis on the reliability of each method and the ease of application. A review of the methods of assessing the geometric accuracy of airborne remotely sensed imagery is also given. Finally, Chapter 4 is summarised and potential methods for improving the accuracy and reliability of geometric correction are suggested.

Chapter 5 establishes the main hypotheses investigated in this study. The fundamental requirements of the project are discussed, and an overview is given of the approaches employed in achieving the project's aim.

Chapter 6 describes the practical investigations carried out for this research project. Firstly, the approach used in removing the geometric distortions from the daytime image data set is described, and preliminary results are discussed. The methodology is then refined in order to overcome a number of problems which were encountered after applying the first approach, and the reasoning behind these refinements is discussed in detail. Chapter 6 continues with a description of the final, definitive method, along with the results obtained for the test imagery.

Chapter 7 describes the application of the alternative methods of geometric correction to a number of test scenes, and results are illustrated and described in qualitative terms. Chapter 8 builds on the recommendations described in Chapter 4 for improving the methods of quantitatively assessing the geometric accuracy of remotely sensed imagery, and a number of approaches are developed. Using these alternative methods, the accuracy of the corrected test imagery is quantitatively assessed allowing a number of conclusions to be made.

Due to the different spectral characteristics between the daytime and dawn thermal imagery, the methods for removing the geometric distortions developed in Chapter 6 do not lend themselves directly to the dawn image data set. Chapter 9 therefore describes a series of additional steps required to apply the technique to the dawn image data.

Chapter 10 provides a discussion of the main issues which have evolved through the course of this research project, and these are consolidated in Chapter 11 where a series of conclusions are drawn.

2. Principles of Thermal Remote Sensing

Remote sensing can be defined as 'the use of electromagnetic radiation sensors to record images of the environment which can be interpreted to yield useful information' (Curran, 1985). Whilst there are a vast range of remote sensing systems operated around the world, work carried out previously within the department have concentrated largely on airborne remote sensing for environmental studies. Ellis (1997) evaluated the potential of remote sensing for the detection of landfill gas and leachate in urban environments. Ellis examined a number of different airborne remote sensing systems, and one of the main conclusions drawn from the study was that thermal remote sensing offered considerable potential for identifying landfill sites. However, difficulties in interpreting the thermal response over varying surface conditions meant that the full potential of thermal remote sensing was not realised. The following chapter provides a detailed review of the techniques used for deriving useful information from remote measurements of the thermal response at the earth's surface.

2.1 Electromagnetic Energy

Any object whose temperature is greater than absolute zero (-273°C) continuously emits electromagnetic radiation. The kinetic energy of particles of matter moving in random motion cause collisions which result in changes in the energy state and an emission of electromagnetic radiation from the surface of the material. The concentration of electromagnetic energy radiated from a source is called the radiant exitance, and the Stefan-Boltzman law describes its relationship with temperature,

$$M = \sigma T^4 \qquad (2.1)$$

where M is the total radiant exitance from the material, σ is the Stefan-Boltzman constant, and T is the kinetic temperature of the material. This law was developed for a black body, which is a theoretical object assumed to absorb all incident radiation, and then re-emit all of this energy in a wavelength distribution pattern that is dependent only on kinetic temperature. Just as the total energy emitted by an object varies with temperature, the spectral distribution of emitted radiation also varies. The wavelength of the peak radiant exitance (λ_{max}) is given by Wien's displacement law,

$$\lambda_{max} = \frac{A}{T} \qquad (2.2)$$

where A is Wien's constant and T is the temperature. Whilst very hot objects such as the sun (6000K) emit high energy radiation with a peak radiant exitance at about 0.5μm, cooler objects such as the earth's surface (300K) have a peak exitance at around 9.7μm. Terrestrial emissions are of a much lower intensity and are therefore more difficult to sense remotely.

2.2 Thermal Observations of the Earth

Although remote sensors observe and record the thermal response at the surface of the earth, interactions between many levels of the earth's substrate and atmosphere influence the instantaneous and cyclic temperature range. Carlson *et al.* (1981) state that the greatest amplitude of the diurnal temperature wave occurs immediately at the ground-air interface and decreases rapidly with height both upward and downward from the interface. Diurnal variations in solar heating account for temperature differences up to 1m below the earth's surface, whilst seasonal heating accounts for temperature differences up to depths of 10-20m below the surface (Elachi, 1987). Advection and large-scale atmospheric mixing processes can significantly influence the surface temperature by moulding the vertical profiles of heat and moisture. Between these two extremes lie a vast range of surface materials, each displaying their own characteristic thermal properties and forming a complex surface environment. Figure 2.1 shows a schematic representation of the earth's surface illustrating the primary factors influencing the surface temperature. Schmugge *et al.* (1978) categorises these into internal and external factors. Internal factors include the thermal conductivity (K), density (ρ) and the heat capacity (C), which together describe the thermal inertia (P) of the surface layer, where

$$P = (K\rho C)^{1/2} \qquad (2.3)$$

External factors are primarily meteorological and include solar radiation, air temperature, relative humidity, cloudiness, wind speed etc. These external effects combine to provide the driving force for the diurnal temperature variation, whilst the thermal inertia is an indication of the surface resistance to this force. The following sections will describe the main aspects of Figure 2.1.

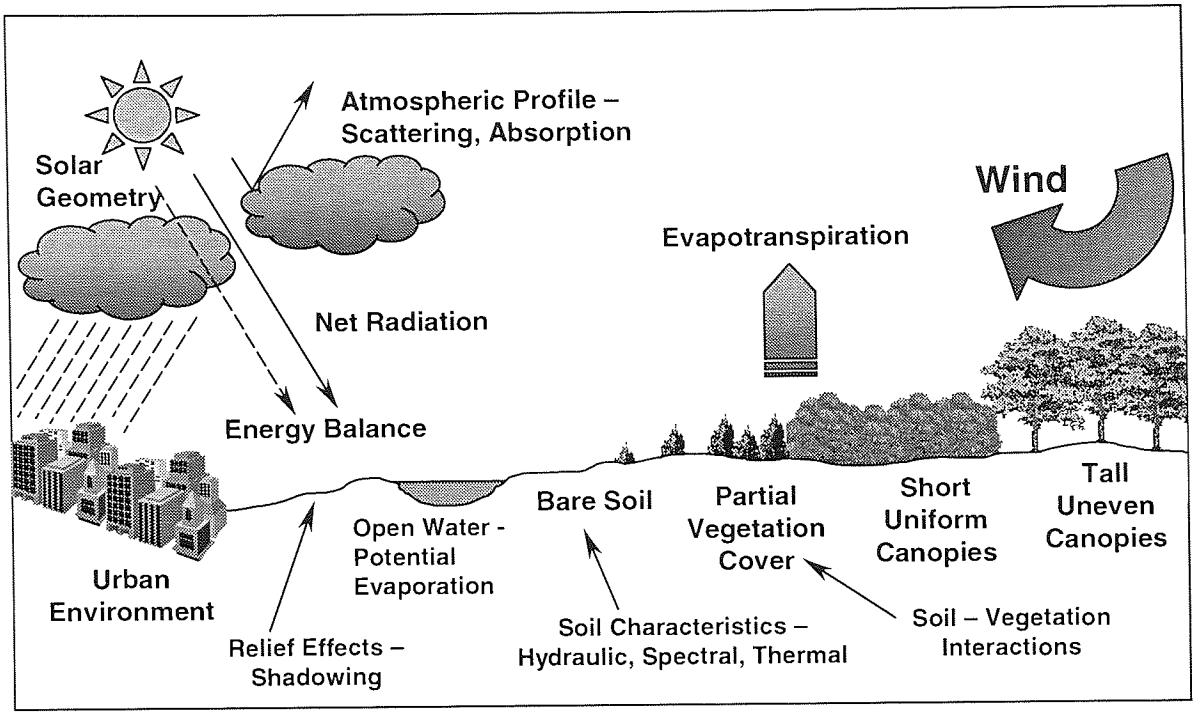

Figure 2.1 Schematic representation of the Earth's surface.

2.2.1 Solar Radiation and the Energy Balance

Solar radiation reaches the outer atmosphere at an average flux of approximately 1400 Wm^{-2}, and is the primary driving force influencing the surface temperature. Virtually all of this radiation is in the wavelength range of 0.3-3 μm and although the earth also emits radiation, terrestrial emissions are of a much lower intensity with a greater wavelength range of 3-50 μm. Between these two radiation spectra there is very little overlap, and it is customary to refer to the former as 'short-wave' and the latter as 'long-wave' radiation (Sellers, 1965).

Although electromagnetic radiation travels through empty space without modification, a series of interactions occur as solar and terrestrial radiation travels through the earth's atmosphere. Radiated energy interacts with the atmosphere in the following ways (Avery and Berlin, 1992);

1. it may be reflected and scattered without change to either its velocity or wavelength;
2. it may be absorbed and re-radiated at longer wavelengths, which causes the air temperature to rise;
3. it may be transmitted in a straight-line path directly through the atmosphere.

Atmospheric scattering is the unpredictable diffusion of radiation by particles in the atmosphere. Absorption is the effective loss of energy to atmospheric constituents such as water vapour, carbon dioxide and ozone. For a review of scattering and absorption see Lillisand and Kiefer (1994). Due to the processes of scattering and absorption, only a varying fraction of the solar radiation actually reaches the earth's surface. On a cloudless day, light scattered within the earth's atmosphere can account for up to 25% of radiation received at the earth's surface, whilst the remaining fraction is contained in the direct solar beam (Monteith, 1973).

The radiation balance describes the net flow of radiant energy at the surface of the earth. Net radiation, R_n, is composed of a number of elements, and is described by Equation 2.4;

$$R_n = S_d + S_u + L_d + L_u \qquad (2.4)$$

where S_d and S_u are the incoming and reflected fluxes of shortwave radiation (direct and diffuse), L_d is the longwave radiation from the sky, and L_u is the reflected and emitted longwave radiation from the earth's surface. Monteith (1973) provides a detailed discussion of the radiation balance.

Net radiation forms a single component in a wider expression known as the energy balance, which describes the balance between incoming and outgoing energy fluxes at the earth's surface, and is defined as

$$R_n = G + H + LE \qquad (2.5)$$

where H and LE are the upward fluxes of sensible and latent heat into the atmosphere, and G is the flux of sensible heat into the ground (Carlson, 1986). The surface composition plays an important role in partitioning the net radiation between each component of the energy balance, which in turn effects the amplitude of the diurnal temperature wave. During hours of daylight, the ground receives a net gain of energy during a period of heating, whilst at night there is a net loss of energy in a period of cooling. Furthermore, if a complete 24-hour cycle is considered it may be assumed that no net heating or cooling of the earth occurs and the soil heat flux term can be neglected, giving

$$\langle R_n \rangle = \langle H \rangle + \langle LE \rangle \qquad (2.6)$$

where the brackets <> represent a 24-hour average (Price, 1980; Carlson, 1986).

2.2.2 Emissivity

The Stephan-Boltzman law described in Section 2.1 was developed for a black body, but since no actual material behaves as a true black body, a property called emissivity (ε) has been defined as;

$$\varepsilon = \frac{M_r}{M_b} \qquad (2.7)$$

where M_r and M_b are radiant exitances for a real and black body respectively. Emissivity is a measure of a material's ability to both absorb and radiate energy. Equation 2.7 can be developed to provide a relationship between the radiant (T_{rad}) and kinetic (T_{kin}) temperature;

$$T_{rad} = \varepsilon^{1/4} T_{kin} \qquad (2.8)$$

Equation 2.8 allows the kinetic temperature of a body to be determined from the radiant temperature, provided the emissivity is known. However, natural bodies display a wide range of emissivities, and Table 2.1 illustrates how the kinetic temperature calculated using Equation 2.8 varies with emissivity for a constant radiant temperature. It can be seen that the calculated kinetic temperature may contain significant errors if the emissivity is not accurately known.

Becker and Li (1993) review a number of methods for deriving emissivity, whilst Schmugge (1995) demonstrates a multi-channel approach to deriving surface emissivity using a thermal infrared multispectral scanner (TIMS). Studies show that emissivity varies more widely over soil and artificial surfaces than over vegetation, and Carlson *et al.* (1993) suggests that errors associated with emissivity are usually less than 1-2°C.

Material	Emissivity [1]	Kinetic Temperature [2] (= $T_{rad} / \varepsilon^{1/4}$ °C)
Granite	0.815	31.57
Sand, quartz, large grain	0.914	30.68
Asphalt pavement	0.959	30.32
Concrete walkway	0.966	30.26
Pure water	0.993	30.05

[1] Source: Sabins (1986)
[2] Kinetic temperature calculated based on a radiant temperature of 30°C.

Table 2.1 Emissivity of materials measured in the 8-12μm waveband.

2.2.3 The Substrate Layer

Whilst a single instantaneous observation of surface temperature is useful for qualitative observations, quantitative analyses usually require a pair of thermal images acquired at times of maximum and minimum temperatures so that thermal inertia images can be obtained. Thermal inertia is a measure of the response of a material to changes in temperature, and is defined by Equation 2.3. The most important component described in Equation 2.3 is density since this generally has a linear relationship with thermal inertia. Figure 2.2 illustrates the effects of thermal inertia on the diurnal variation of surface temperature for a number of different materials. Objects with a low thermal inertia experience a wide temperature range, whilst objects with a high thermal inertia have a greater resistance to changes in temperature, and display a narrower temperature variation.

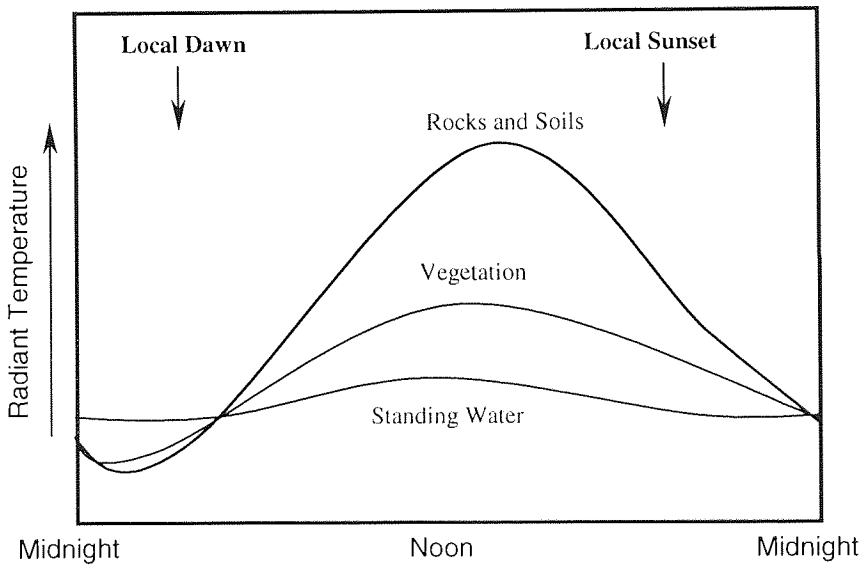

Figure 2.2 Effect of differences in thermal inertia on surface temperature (after Curran, 1985).

Pratt and Ellyett (1978) identified a number of authors who have examined thermal inertia images acquired from airborne surveys and report how much of the early work was directed towards the understanding of the many problems associated with airborne imagery. The main difficulties are due to the severe geometric distortions inherent in virtually all airborne imagery caused by the way in which the sensor platform is buffeted by atmospheric currents during image acquisition. Despite these problems, results from studies by Khale *et al.* (1975, 1976), who appear to have produced the first thermal inertia images from aircraft imagery, suggest good interpretable discrimination of geological units for both hard rock and unconsolidated sediments. Singhroy and Barnett (1984) and Sabins (1984) carried out similar studies and identified a number of factors which influence the surface temperature:

1. Darker coloured materials may display higher emissivities, resulting in higher radiant temperatures;
2. smooth surfaces may be more efficient radiators of heat;
3. distinct tonal contrasts in the thermal imagery exist between sunlit and shadowed regions, although these effects (and those of differential heating) are largely undetectable in the night-time imagery;
4. unconsolidated surface materials have lower thermal inertia than consolidated materials, and hence experience wider temperature variations;
5. soil moisture influences the daytime surface temperature considerably - moist regions display cooler temperatures than dry regions;
6. surface winds produce characteristic patterns of smears and streaks downwind from obstructions, owing to differential evaporative cooling.

Vincent (1984) combined the use of multispectral and thermal data for hydro-thermal alteration mapping and concluded that the presence of vegetation on the surface greatly reduced the reliability of observations. Studies by Fukuhara *et al.* (1978) also identify the problems of geologic and soil mapping in vegetated areas and suggest that image acquisition during times of minimal vegetation growth (i.e. in early spring) may limit the influence of vegetation on the surface response. However, problems caused in regions consisting of perennial vegetation or winter agricultural crops led Fukuhara to try and maximise the soil information by using ratios of the visible-red and near-infrared response to discriminate between soil and vegetation.

2.2.4 Soil and Soil Moisture

In order to understand the influence of the substrate layer in the overall soil-plant-atmosphere system a better understanding of the physical processes of soil is required. The following section is aimed at familiarising the reader with some common principles and terminology. For a detailed discussion of the physical processes of soil see Hillel (1971), Hilton (1986).

Soils are produced from rocks by a combination of three processes - weathering, erosion and transportation. During weathering, rocks are broken up into smaller fragments and in most cases, this loose, unconsolidated regolith overlies bedrock. Soil is defined as the upper layers of regolith that supports plant life (Thompson and Turk, 1991).

Soil texture is an expression of the predominant size, or size range, of the soil particles. Soil texture refers to the relative proportions of textural fractions (namely sand, silt and clay) according to one of a number of international scales (Figure 2.3). It is also common for soils to be referred to merely by class names (Figure 2.4).

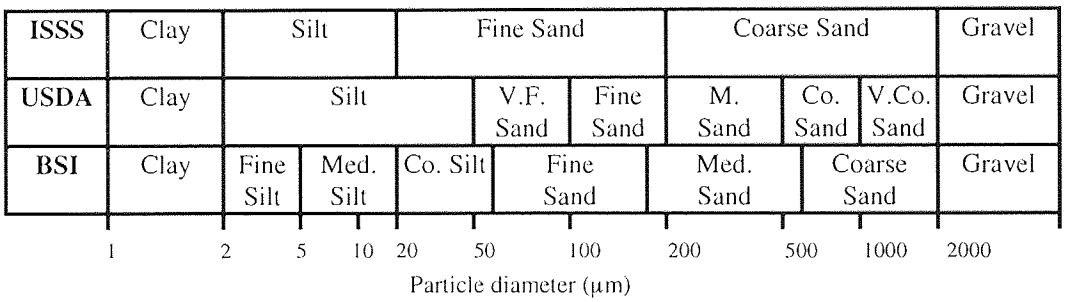

Figure 2.3 Standards of particle size classes; ISSS: International Society of Soil Science, USDA: US Department of Agriculture and BSI: British Standards Institution (after Shaw; 1993).

Figure 2.4 Classification of soils based on US soil triangle (Shaw ;1993).

The quality of plant life which a soil mass can sustain depends on the relative proportions of each particle size. The most fertile soils contain a mixture of sand, silt and clay along with a substantial amount of organic matter, or humus. Soil rich in humus is soft and spongy, and will readily absorb moisture. Organic matter also insulates soil from excessive heat and cold and reduces water loss through evaporation.

Soil texture influences the amount of moisture which can be held in the soil structure, since water storage depends on the packing of the clay and sand particles, and the space between the solids. Figure 2.5 illustrates the mechanisms by which water is held in soil. Water infiltrating the surface moves by gravity and surface tension through the pore spaces on a path smoothed by a film of hygroscopic water on each soil particle. The aeration zone contains a complex mixture of soil particles, liquid and air where the voids are partially filled with moisture. The aeration zone gives way to a layer of saturated soil where capillary forces hold moisture above the water table at less than atmospheric pressure. This pressure is commonly referred to as the capillary potential, or its negative, the matric suction. Beneath the water table, the soil is fully saturated and hydrostatic pressure increases with depth.

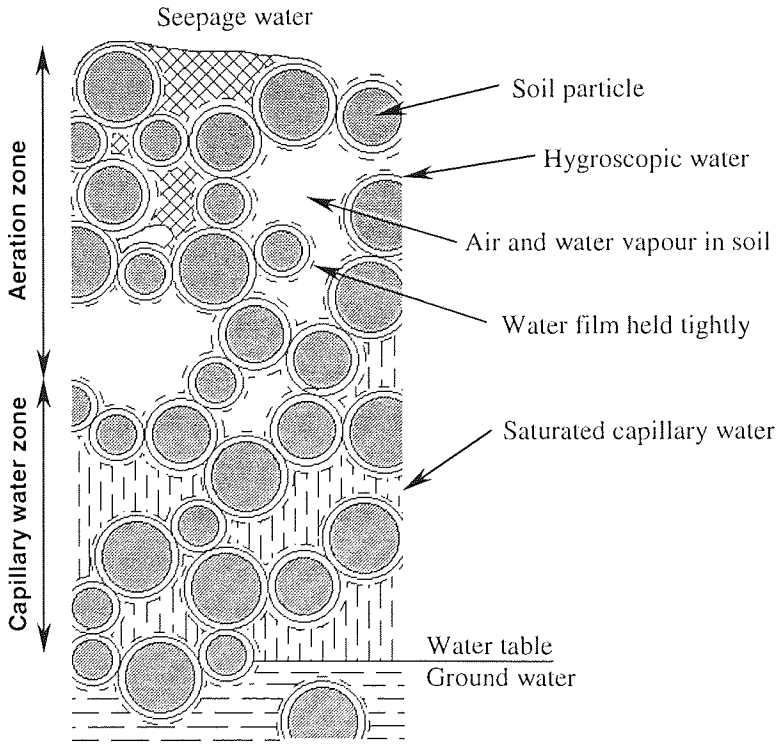

Figure 2.5 Water in soil (after Wiesner, 1970).

Matric suction is important in the assessment of soil moisture. Matric suction is strongly affected by soil texture - sandy soils generally contain larger pores which can be emptied (through drying) without developing high capillary suctions, whilst clayey soils exhibit a more uniform pore distribution and contain much smaller pores giving rise to higher matric suctions. Hydraulic conductivity is also an important property of soils. Saturated soil has a high hydraulic conductivity since all of the pores are filled with water and readily conduct moisture. However, as the soil begins to dry some of the pores fill with air and the conductivity correspondingly decreases. Furthermore, as the matric suction develops, the first pores to empty are the largest ones (which are the most conductive) so the hydraulic conductivity is initially very sensitive to moisture content.

Clapp and Hornberger (1978) examined more than 1800 soil samples in an attempt to model the moisture characteristic describing the variation of soil suction with volumetric moisture content. It was found that a power curve could be fitted reasonably well to the soil wetness, and that the exponent of the power relationship was correlated extremely closely to the clay fraction of the soil. Cosby *et al.* (1984) developed the work of Clapp and Hornberger to investigate whether there was any significant variation of the soil moisture parameters with physical properties of the soil other than texture. The study also extended the work of McCuen *et al.* (1981) to investigate any possible inter-relationships between different soil parameters. Cosby *et al.* showed that in virtually all cases the texture was sufficient to describe hydraulic parameter variability.

One of the major problems associated with modelling systems at the earth's surface stems from the assumption of homogeneity in both the horizontal and vertical planes. Variations in soil physical properties have obvious implications on the thermal behaviour of the substrate layer and Bell *et al.* (1980) illustrated the natural variation of soil moisture within large field sites. Statistical analyses were carried out on moisture data taken from five discrete soil layers extending from the surface to 15cm in depth from 58 different field sites in Kansas and Arizona, USA. A typical moisture profile using data obtained from a 36-point square grid contained a range of moisture contents from 4% to 14% (average 7.1%, standard deviation 2.5%). Although factors such as topography and relief are relatively minor contributors to variability, Bell *et al.* argued that moisture variations are a form of inherent variation which can be neither controlled or reduced.

Relationships between moisture content and the diurnal temperature variation were established as early as 1971. Abdel-Hady (1971) tried to establish a relationship between maximum temperature and depth to water table for clay and sand soils, and although little prior work had been carried out in this field it

appeared that thermal remote sensing had the most potential for future development. In field tests Schmer and Werner (1974) established a positive correlation between soil moisture and surface radiant temperatures.

Schmugge *et al.* (1980) report that because water is so close to the extremes in its thermal behaviour, the corresponding properties of soil are highly dependent on the moisture content. This hypothesis has been explored by a number of authors (Schmugge *et al.*, 1978; Idso *et al.*, 1975a; Vlcek and King, 1983; Pratt and Ellyett, 1979) who attempted to associate the diurnal temperature wave with moisture content in the upper layers of the surface. Although Idso *et al.* (1975a) found that soil moisture was a linear (or near-linear) function of the diurnal temperature wave, when the relationship was tested with different soils it was found to be sensitive to soil type. However, when the pressure potential was plotted against the diurnal temperature variation a well-defined relationship was produced irrespective of soil class, allowing the soil water status to be inferred without prior knowledge of the soil type.

Pratt and Ellyett (1979) examined the relationship between pressure potential and thermal inertia for three very distinct soil types. Thermal inertia was determined from simulations over a wide range of pressure potentials, which showed a strong non-ambiguous dependence on soil moisture and only a small dependence on soil type. When the thermal inertia was plotted against pressure potential a marked separation was found between soil types. Their results appear to contradict the findings of Idso *et al.* (1975a) who argue that pressure potential derived from the diurnal temperature wave is not sensitive to soil type. Whilst Pratt and Ellyett account for these differences through albedo effects, they also express concern regarding the uncontrolled variables in their simulations which influence soil moisture estimation. Furthermore, the results of Idso *et al.* were drawn from samples 'artificially' placed in the field, and temperature measurements taken from these sites failed to correspond to those taken from the natural field site. This apparent lack of correspondence between the artificial and natural field sites illustrates how such temperature studies are largely site-specific, and care should be exercised when interpreting temperature and moisture data from different sources.

2.2.5 Evaporation Over Bare Soil

It has been reported previously how dry soils experience a wider diurnal temperature range than moist soils because of the extreme thermal properties of water (Section 2.2.4). This phenomenon is further enhanced by the processes of evaporation and transpiration due to the latent heat requirements of changing water from a liquid to a vapour phase. Idso *et al.* (1975b) discussed the importance of assessing evaporation in agriculture where the scheduling of many operations in both irrigated and dryland farming rely on accurate predictions of the water status. The significance of evapotranspiration has also been identified in hydrology where evaporative losses account for a considerable proportion of the water balance (Hillel, 1971).

Hillel (1971) identifies three conditions which are necessary for evaporation from bare soil to occur, and like Schmugge *et al.* (1978) categorise these into internal and external factors. The first two conditions are influenced by meteorological factors; there must be a continual supply of energy to meet the latent heat requirement, and there must be a vapour pressure gradient between the evaporating body and the atmosphere allowing vapour to be transported away by processes of diffusion and convection. The third condition is that there be a continual supply of moisture through the structure of the soil to the site of evaporation and this is influenced by the hydraulic characteristics of the soil.

Idso *et al.* (1974) describe the processes of drying of a field soil where three distinct phases of evaporation are identified. The first stage is characterised by a relatively high evaporation rate controlled by atmospheric conditions - constant external conditions will result in a constant evaporation rate. The second stage begins when the soil water cannot be transmitted to the site of evaporation quickly enough to meet the evaporative demand, and the rate of evaporation experiences a rapid decline with the mode of moisture transfer shifting from primarily liquid to vapour movement. The final stage is characterised by a low, relatively constant rate of evaporation where absorptive forces acting over molecular distances at the solid-liquid interface are the controlling factor.

Two basic procedures of determining evaporation are discussed by Idso *et al.* (1975c); the first is through use of lysimeters (Harrold and Dreibelbis, 1958; Pruitt and Angus, 1960; Van Bavel and Reginato, 1965), whilst the second method is based on calculations using a variety of meteorological and soil parameters (Penman, 1948; Monteith, 1963, 1965; Tanner and Fuchs, 1968). Idso *et al.* (1975c) report that whilst calculative approaches are relatively successful at predicting evaporation during the first stage of drying these methods are often inadequate for falling rate (third stage) drying, where soil factors are much more dominant. Idso *et al.* described an empirical approach to mapping evaporation based on the thermal

inertia theory already discussed in Section 2.2.3. A simple correlation procedure is developed by plotting the ratio of daily totals of actual to potential evaporation against the amplitude of the diurnal temperature wave. Results illustrate the three distinct phases of drying although Idso *et al.* argued that the second stage is actually a transition between the two basic regimes of potential and falling rate evaporation.

2.2.6 Transpiration Over Vegetated Surfaces

Transpiration can be defined as the gaseous diffusion of water from vegetation, driven by the net radiation absorbed by plant foliage (after Gates, 1966). The majority of transpiration takes place through the stomatal openings in leaves, and over any considerable period of time the energy utilised is balanced by the absorption of radiant energy. The rate of water vapour loss by transpiration is highly variable and is influenced by a number of factors. These can be divided into two groups (Greulach, 1973); environmental (external) factors which provide the driving force for transpiration, and internal factors influencing the movement of water through the plant. The main environmental factors include temperature, atmospheric humidity, availability of soil water, and light. Internal factors include the water potential gradients and the resistances of various plant tissues to transpiration, which combine to give the diffusive capacity of a plant. Internal factors affecting transpiration will not be considered further, but for a review of plant physiology see Meyer *et al.* (1973) and Levitt (1974).

A number of factors influencing the behaviour of leaf stomata have been documented. Monteith (1981) describes how, in response to light, leaf stomata open, thus reducing the resistance to transpiration. During darkness, stomata close causing the resistance to increase. The degree of stomatal opening is also reduced when the supply of water from the soil is limited. The reduced hydration of the plant may result in wilting accompanied by an increase in the temperature of the plant canopy. This rise in temperature is caused by the reduced transpiration of water vapour from the plant foliage. The humidity of the air surrounding the plant foliage is also important in determining the rate of transpiration. A vapour pressure gradient must exist between the leaf surface and the atmosphere to enable moisture to be diffused. This vapour pressure is influenced by the concentration of water vapour and the temperature of the foliage and surrounding air.

Jackson *et al.* (1977) explored the concept of using the temperature of vegetation canopies to indicate the water status of plant communities. In a review of previous work, Jackson *et al.* reported how similar work was carried out as early as 1966 with publications from various authors who attempted to correlate crop water stress with canopy temperature (Wiegand and Namken, 1966; Ehrler and Van Bavel, 1967). Hiler and Clarke (1971) introduced a quantitative measure of plant stress by describing the 'stress day index' which was used to characterise the effects of water stress and schedule irrigation. Jackson *et al.*

introduced their own stress index called the 'stress degree day' (SDD) which was calculated by summing the temperature differential between the air and the canopy over the period of a growing season (see also Seguin and Courault, 1993). Results from a study over a wheat canopy show that the regularly irrigated plots remained relatively stress-free, whilst plots which were starved of water displayed large cumulative differences between the air and canopy temperature. Idso *et al.* (1977) examined the relevance of the SDD and showed that within an arid environment crop yields may be reduced if the SDD becomes positive. More recently, the thermal response number (TRN) has been used to assess canopy structure and biomass where large differences in TRN were found among different forest types (Luvall and Holbo, 1989; Luvall, 1997).

Jackson *et al.* (1977) also developed a simple empirical model to estimate 24-hour totals of evapotranspiration from a crop canopy based on the temperature difference between the canopy and the air. The benefit of using a simple empirical approach is that detailed ground-based meteorological data are not required, and results can be obtained from single temperature measurements. The basic form of their model is given by

$$\langle LE \rangle - \langle R_n \rangle = A + B\,(T_c - T_a) \qquad (2.9)$$

where A and B are constants determined statistically from lysimeter data, and T_c and T_a are the crop and air temperatures respectively. Jackson *et al.* arrived at values for A and B of 0 and 0.064 respectively, whilst Seguin *et al.* (1982) found A = 0.1 and B = 0.025. Seguin and Itier (1983) developed a modified version of Equation 2.9 of the form

$$\langle R_n \rangle - \langle LE \rangle = B\,(T_0 - T_a)^n \qquad (2.10)$$

where n and B are determined empirically. Seguin and Itier found that the value of n depends upon atmospheric stability whilst that of B depends upon the roughness length, z_0, and windspeed. However, problems associated with selecting an appropriate roughness length for an entire region illustrates the limitations of using relatively simple models to represent complex processes at the earth's surface.

2.3 Mathematical Modelling for the Interpretation of Thermal Data

The energy balance described in Section 2.2.1 forms the underlying theory behind virtually all the quantitative methods of interpreting thermal imagery, and Carlson (1986) categorises these into four different types; empirical, analytic, predictive and diagnostic. Empirical approaches formed much of the early work in thermal remote sensing, and have been discussed in Section 2.2. Analytical models attempt to relate the amplitude of the diurnal temperature wave to different surface parameters by means of analytical expressions which satisfy the surface boundary conditions. Predictive models are more physically-based allowing changes in the substrate and atmospheric conditions to be estimated over time. Diagnostic models are similar to predictive models but require more comprehensive measurements of surface conditions for their solution. For a review of diagnostic models the reader is referred to Carlson (1986).

2.3.1 Analytical Approaches

Analytical estimates of thermal inertia have been used for a number of applications ranging from rock type discrimination (Watson *et al.*, 1971; Watson, 1973, 1975; Khale *et al.*, 1975, 1976; Miller and Watson, 1977; Price, 1977), soil type discrimination (Pratt and Ellyett, 1979), and soil moisture determination (Pratt and Ellyett, 1978, 1979; Price, 1980). Reliable quantitative estimates of thermal inertia depend largely upon the accuracy of the calibration models used in converting values of the ground surface diurnal temperature wave to thermal inertia. Pratt *et al.* (1980) described three predominant forms of numerical simulation that have emerged since the 1950's which include Fourier series, Laplace transforms and finite difference algorithms. Jaeger (1953) used the Laplace transform method in developing a one-dimensional periodic heating model to simulate the temperature variations on the surface of the moon. Carslaw and Jaeger (1959) later proposed the use of a linear Fourier series for solution of the heat conduction equation, which was subsequently developed by Watson (1975) for use in geological applications. Finite difference methods have the ability to manage a wider range of boundary conditions and sub-surface thermal properties, and have been used to assess the thermal behaviour of bare and sparsely vegetated soils. Pratt *et al.* (1980) identify the advantages of the Fourier series approach in providing analytical solutions which are computed rapidly compared to the Laplace and finite difference methods. Carlson (1986) compounds this view but comments on the severe limitations of this approach due to the simplified manner in which atmospheric processes are dealt with.

Watson *et al.* (1971) extended the work of Carslaw (1953) to incorporate a comprehensive parameterisation of the earth's surface in an attempt to better quantify the role of different parameters in governing the diurnal temperature variation of surface geologic materials. Watson *et al.* derived an expression relating the surface temperature to the ground heat flux (G) giving;

$$G = (1 - \alpha)\, S_d + L_d - L_u \qquad (2.11a)$$

$$= f\, S\, (1 - \alpha)\, V \cos(Z) + \sigma T_{AD}^{4} - \varepsilon_g \sigma T_s^{4} \qquad \text{daytime} \qquad (2.11b)$$

$$= \sigma T_{AN}^{4} - \varepsilon_g \sigma T_0^{4} \qquad \text{night-time} \qquad (2.11c)$$

where α is the albedo of the ground

f is a cloud cover factor

S is the solar constant

V is the atmospheric transmission

Z is the zenith angle

σ is the Stephan-Boltzman constant

T_{AD} is the 'effective' daytime air temperature

T_{AN} is the 'effective' night-time air temperature

ε_g is the emissivity of the ground

T_s is the daytime surface temperature

T_0 is the night-time surface temperature

S_d, L_u, and L_d are defined previously.

Watson *et al.* treated the atmospheric heat transfer as 'effective' heat exchange, where the atmosphere is considered to behave as an emitting black body with an 'effective' sky temperature. The model is further simplified by ignoring lateral heat transfer (one-dimensional heat flow) and assumes the ground to be horizontal, uniform and homogeneous in depth. Sensible and latent heat fluxes are also ignored, which Watson argued that for dry, arid conditions does not result in appreciable error. Results showed a strong dependence of the diurnal temperature wave on thermal inertia and albedo, whilst solar geometry was important in governing the overall magnitude of the surface temperature.

Although Watson ignored the turbulent energy exchanges in his analysis of the boundary layer, a study by Price (1980) illustrates the importance of turbulent heat transfer in modelling variations of the surface

temperature. Price derived a simple analytic solution to the heat flow equation describing the approximate diurnal variation in surface temperature. Price found the model greatly over-predicted the day-night temperature variation and concluded that energy exchanges within the boundary layer must be considered.

Whilst the analytical models of Watson *et al.* (1971) have been used to examine certain aspects of the variability of surface conditions such as ground slope (Miller and Watson, 1977) and surface coverings (Watson, 1973), the effects of these variations have not been expressed in terms of their influence on thermal inertia. Pratt (1980) investigates the problems associated with assuming both the meteorological conditions and surface physical characteristics are constant across the survey area, and in addressing this problem extends his theory to incorporate the turbulent transfer of heat from the ground to the atmosphere. Pratt defines the energy balance as

$$G = (1 - \alpha)\, S_d + L_d - L_u - H \qquad (2.12)$$

where H_0 is the turbulent transfer of sensible heat to the atmosphere (temperature T_{air}) given by;

$$H = c_p\, f_h(u)\, (T_{air} - T_s) \qquad (2.13)$$

where c_p is the heat capacity of air and $f_h(u)$ is an atmospheric transfer coefficient for heat. S_d is derived as a function of season and latitude which control the solar declination and atmospheric absorption. Pratt also represents the incident longwave flux by means of a fixed sky radiation temperature to reduce the number of variables, and argues that this does not significantly affect the results. In order to test the effects of two-dimensional variability Pratt established a table of 'standard' parameters and varied only one or two at any time in order to investigate their influence on thermal inertia. A number of significant conclusions were drawn from the results. Firstly, albedo effects can largely be eliminated if flying is restricted to the pre-dawn period. Over-estimation of thermal inertia was caused by reduced heating of south-facing slopes (Southern Hemisphere). Considerable errors in estimating thermal inertia arose for simulations investigating strong winds with increasing roughness heights. These results are especially important because of the uncertainties involved in obtaining values for surface roughness. In most instances representative values must be estimated from knowledge of the study area, and these can vary considerably within a given region.

Whilst the evaporative heat transfer term can be ignored in dry and arid climates Pratt (1980) argues that this assumption is not valid in temperate climates. Price (1980) examined the evaporative heat flux term

in his analysis of the energy balance in an attempt to quantify the soil moisture content in the near-surface layer. Time averaging of surface fluxes over a 24 hour period allows the ground heat flux to be ignored (assuming no net heating of the ground) giving the energy balance expressed in Equation 2.6. Price describes the different components of the energy balance based on the analysis of Sellers (1965) to give;

$$\langle R_n \rangle = \langle H \rangle + \langle LE \rangle = S_d - S_u + L_d - L_u \qquad (2.14a)$$

where

$$S_d - S_u = S\,V\,(1 - \alpha)\,\mathrm{Cos}\,Z \qquad (2.14b)$$

$$L_d = \varepsilon_g \sigma T_{air}^4\,(a + b\sqrt{q_{air}}) \qquad (2.14c)$$

$$L_u = \varepsilon_g \sigma T_s^4 \qquad (2.14d)$$

$$\langle H \rangle = c_p\, f_{h(u)}\,(T_s - T_{air}) \qquad (2.14e)$$

$$\langle LE \rangle = L_e\, f_{e(u)}\,(q_s - q_{air}) \qquad (2.14f)$$

T_{air}, u and q_{air} are the air temperature, windspeed and specific humidity at a height z_1 above a surface of characteristic roughness length; z_0, and q_s is the specific humidity at the surface. The atmospheric transfer coefficients for heat and water vapour are given by;

$$f_{h(u)} = f_{e(u)} = [\rho\, k^2 u] \,/\, [\ln(z_1/z_0)]^2 \qquad (2.15)$$

where ρ is the density of the radiating material and k is the Von Karmen constant (≈ 0.4). Price defines an expression for the absorbed longwave radiation, L_d, based on the work of Brunt (1932) where the term $(a + b\sqrt{q})$ is used to convert the actual air temperature to an 'effective' air temperature (Equation 2.14c). Using Equation 2.14, Price is able to write an explicit expression for evaporation by averaging the various terms over a 24-hour period, and by imposing a number of simplifications concerning the averaging procedure.

Evaporative heat flux was thus defined as

$$\begin{aligned} \langle LE \rangle = {} & SV(1 - \alpha)\, C_0 + \varepsilon_g \sigma \langle T_{air}^4 \rangle (a + b\sqrt{\langle q_{air} \rangle}) \\ & - \varepsilon_g \sigma \{ \langle T_s \rangle^4 + 0.75 \langle T_s \rangle^2 (T_{max} - T_{min})^2 \} \\ & - \rho k^2 c_p / [\ln(z_1/z_0)]^2 \{ \langle u \rangle \langle T_s \rangle - \langle u\, T_{air} \rangle \} \end{aligned} \qquad (2.16)$$

where C_0 is a constant term obtained from the Fourier expansion of the angle of solar incidence (Price, 1980). It is clear from Equation 2.16 how remote measurements of the maximum and minimum surface temperature can be used in conjunction with a range of meteorological parameters to predict the evaporation, and hence water balance over large regions. The quantities u, q_{air}, T_{air} and V may be obtained from meteorological and weather station data, and the quantities α, ε_g and z_0 must be estimated from a knowledge of the study area. The remaining temperature terms, T_{max}, T_{min} and T_s, are obtained from remote sensing methods.

2.3.2 Predictive Models

The underlying constraint in virtually all models which predict the surface temperature and associated parameters is the energy balance, and pioneering work by Penman (1948) provided the means of assessing evaporation from natural surfaces using minimal ground truth in conjunction with standard meteorological data. Penman considered two approaches in his investigations, the first was based on aerodynamic transfer of vapour by a process of eddy diffusion, and the other was based on the energy balance. Penman defines the energy balance expressed in Equation 2.5, and calculates the net radiation based on the available short-wave radiation;

$$R_n = R_c (1 - \alpha) - \sigma T_a^4 (0.56 - 0.092\sqrt{e_d})(1 - 0.09m) \qquad (2.17)$$

where R_c is the incident short-wave radiation and m/10 is the fraction of sky covered by cloud. The processes of heat and vapour transport by eddy diffusion are essentially controlled by the same mechanisms - the former governed by $(T_s - T_a)$ and the latter governed by $(e_s - e_d)$. The terms e_s and e_d refer to the saturation vapour pressure at the surface and dew point temperatures respectively. Penman writes;

$$H / LE = \beta = \gamma (T_s - T_a) / (e_s - e_d) \qquad (2.18)$$

where β is the Bowen ratio (after Bowen, 1926) and γ is a standard constant. By combining Equation 2.18 with the aerodynamic approach Penman arrives at a more general expression describing evaporation based on the energy balance and turbulent transport of water vapour. The general form of the Penman equation is thus written

$$LE = \frac{\Delta}{(\Delta+\gamma)} (R_n - G) + \frac{\gamma}{(\Delta+\gamma)} E_a \qquad (2.19)$$

where Δ is the slope of the saturation vapour pressure-temperature curve at mean temperature, and E_a is an aerodynamic vapour transport term of the form $E_a = f_{(u)}(e_a-e_d)$.

The Penman equation has a number of limitations - the primary objective in its formulation was to estimate evaporation from saturated surfaces only, and, without the need for measurements of surface temperature. However, the Penman equation is an important step in the study of evaporation because it explicitly deals with both the energy aspects of evaporation as well as the aerodynamic transfer between the surface and the atmosphere. Following Penman's approach, the only effective parameters discriminating between different types of surface are α and γ - the albedo and psycometric constant respectively. The sensitivity of this method to surface characteristics was subsequently recognised and numerical approaches were expanded to incorporate a wide range of surface parameters.

Carlson *et al.* (1981) note the surface heat flux and surface temperature are intimately related, and thus the partitioning of energy into sensible and latent heat is directly reflected by the amplitude and nature of the surface temperature wave. Studies by Saltzman and Pollack (1977) and Carlson and Boland (1978) explore the sensitivity of the surface temperature wave to terrain characteristics and found that the three most important surface parameters governing the temperature response are the moisture availability, thermal inertia and albedo. Out of these three parameters moisture availability is widely considered to be the single most important variable since this effects the near-surface humidity and strongly influences the partitioning of net radiation between sensible and latent heat fluxes.

One component which proves troublesome in a large proportion of boundary layer models is the soil heat flux, and Deardorff (1978) reviews a number of ways in which it is dealt with. Manabe *et al.* (1974) and Gates (1975) both ignored the soil heat term completely in their analyses, whilst Kashara and Washington

(1971) assumed it is equal to one third of the sensible heat flux. Idso *et al.* (1975d), in applying a more logical approach, assumed the soil heat flux is proportional to the net radiation and derived a series of empirical relationships. However, since the soil heat flux can be equated to the sum of all the other terms in the energy balance (Equation 2.5), any assumption that it is proportional to one particular component seems dangerously non-general.

Carlson (1986) argued that the strong sensitivity of surface temperature to surface and substrate parameters suggests that remote sensing can be used in conjunction with an atmospheric-substrate model to infer values for surface fluxes and these surface and substrate parameters. Carlson describes the advantages of using predictive models to infer surface parameters and argues that the surface boundary layer is treated in greater detail permitting fuller use of the governing equations. Furthermore, by allowing solutions to proceed from a single set of initial conditions the results do not depend upon continuous meteorological measurements. The following section examines the fundamental components of such time-dependent prediction models.

2.3.2.1 Soil Moisture

McCumber and Pielke (1981) developed a multi-stage soil model for incorporation into a prediction model to assess the importance of properly simulating the temperature and moisture budgets at the ground surface. McCumber and Pielke determine the surface temperature by solving the energy balance and present a review based on the work of Mahrer and Pielke (1977). The model is extended to account for the eleven different characteristic soil types described by the USDA soil textural classification (Figure 2.4).

Numerical simulations carried out by McCumber and Pielke identified the moisture content in the surface layers to be the most important soil variable influencing the surface heat fluxes. Relative humidity at the soil surface, which is a function of soil moisture, determines the partitioning of surface energy between latent and sensible heat. The degree of wetness has an additional effect on the radiation balance at the surface by altering the surface albedo. Soil heat flux is also influenced by soil moisture since the thermal conductivity is directly related to the moisture content. McCumber and Pielke discuss the importance of correctly modelling the initial soil moisture profile since surface heat fluxes are almost an order of magnitude more sensitive to the initial moisture profile than to the temperature profile.

It is recognised that soil moisture is the singlemost important factor controlling the diurnal temperature variation in the surface layer of the earth (Carlson, 1986). It is also apparent, however, that the *surface*

soil moisture exhibits a very large inhomogeneity which deserves spatial and temporal specification (Carlson *et al.*, 1995), and in order to estimate the water budget from remotely sensed data it is necessary to know accurately the hydraulic characteristics of the soil studied (Prevot *et al.*, 1984).

Bell *et al.* (1980) identify a natural variability of soil moisture within large bare field sites, and Burrough (1983) showed that soil texture, the primary controlling factor, is also highly variable. Clapp and Hornberger (1978) developed a series of empirical relationships to express the hydraulic parameters (namely matric suction and hydraulic conductivity) as a function of the moisture content (Section 2.2.4). Their results are widely accepted in many hydrological and surface process models (Mahrt and Pan, 1984; Sellers *et al.*, 1986; Noilhan and Planton, 1989; Dickinson, 1993). However, whilst their work provides a useful reference for hydraulic characteristics within broad textural classes, knowledge of the subtle spatial variations in soil parameters is vital to properly describe the highly variable nature of surface drying.

A study by Ek and Cuenca (1994) examined the effect on simulated results of varying the soil hydraulic characteristics by one standard deviation about the mean. Capehart and Carlson (1997) discuss the importance of the soil hydraulic parameters and develop the work of Ek and Cuenca to examine the effect on drying rates within given textural classes. Both investigations found that the movement of moisture within the surface soil layer along with the associated energy fluxes showed a considerable dependence on the hydraulic characteristics of soil.

Capehart and Carlson (1997) show how variations in the soil hydraulic characteristics can contribute to rapid and uneven drying. Furthermore, drying led to the surface moisture profile becoming 'decoupled' from the root zone. Initially, when the soil is sufficiently wet, drying proceeds at about the same rate for the surface layer as for the root zone. However, at some threshold water content the hydraulic conductivity is reduced to such a state where the evaporation rate at the surface becomes greater than the rate at which the surface can be recharged with moisture from the lower layers. When this divergence between drying rates occurs the water profile in the surface layer is said to become 'decoupled' from that below, and the drying rates at the surface and root zone cease to be linearly correlated. When this phenomenon occurs the surface temperature can increase severely and may provide no reliable indication of the soil water status beneath the dry surface layer.

2.3.2.2 Evaporation From Bare Soil

Monteith (1981) describes the process of progressive drying of a bare soil where it is recognised that saturated soil surfaces behave similarly to open water in so far as the relative humidity of the air in contact with the surface is 100%. In this instance, the evaporation rate can be calculated using an equation with

the same general form as the Penman equation (Equation 2.19). However, as drying progresses the rate of evaporation is limited by the upward diffusion of water towards the surface and the relative humidity drops from that of unity to a fixed value at the onset of second stage drying (Section 2.2.5). At this point the amplitude of the diurnal temperature wave increases abruptly and Monteith discusses the potential of remote sensing to estimate the water content in the upper layers of the earth's surface. Monteith showed that whilst a definite increase in the diurnal temperature wave can be observed in hot and dry climates the corresponding temperature change for temperate climates is less obvious, and Monteith questions the ability to detect this temperature change radiometrically.

Rosema and Bijleveld (1978) described an algorithm to permit the evaluation of thermal inertia and relative humidity over bare and scarcely vegetated soils from the diurnal temperature variation. The simulations were based upon the energy balance with solution of the heat flow equation, and although results showed a sizeable error when estimating evaporation due to simplifications inherent in the model, reasonable results were reported for soil moisture estimation.

Tanner and Fuchs (1968) examined a development of the Penman combination formula (Equation 2.19) to include a surface resistance to vapour transport (Monteith, 1963; 1965). By accounting for internal resistances to heat and vapour transport the evaporation from a *drying* surface could be calculated. Soares *et al.* (1988) described a number of methods for determining the evaporation over bare soil, and found that the rate of evaporation depends on the atmospheric demand (well represented by potential evaporation) as well as the hydraulic state of the soil surface layer. Mahfouf and Noilhan (1991) presented a detailed study of different formulations of evaporation from a drying soil, and categorise the various approaches into bulk aerodynamic methods and 'moisture availability' methods. Whilst aerodynamic methods provide an explicit relationship between evaporation and water content based on a parameterisation of surface specific humidity (Deardorff, 1978; Noilhan and Planton, 1989; Kondo *et al.*, 1990), moisture availability methods (also termed threshold methods) are based upon the concept of water supply and demand (Mahrt and Pan, 1984; Dickinson, 1984; Wetzel and Chang, 1987).

Mahfouf and Noilhan followed the conceptual scheme illustrated by Figure 2.6 in their analysis of the surface layer, where it is assumed that free water in an unsaturated soil is mainly retained in the smaller pores of the soil matrix, and diffusion occurs through the larger pores. Aerodynamic formulations either treat evaporation as a function of $(q_g - q_a)$ or $(q_s - q_a)$ - the so-called α and β methods, where q_s, q_g and q_a are the specific humidity at the soil water surface, ground surface and atmosphere respectively. R_{air} and R_{soil} are resistance terms relating to evaporation over the distances illustrated. The threshold method

consists of estimating the water flux from lower layers and therefore requires considerable information concerning hydraulic properties of the soil layer. Mahfouf and Noilhan tested a number of different evaporation formulations against detailed measurements of water and energy exchanges over bare ground. It was found that the bulk aerodynamic formulations provided comparable results during the daytime although there was a difference in cumulative evaporation of approximately 20% between the α and β methods. The threshold formulations were found to be very sensitive to the depth over which the near-surface water content was predicted, and strongly underestimated evaporation.

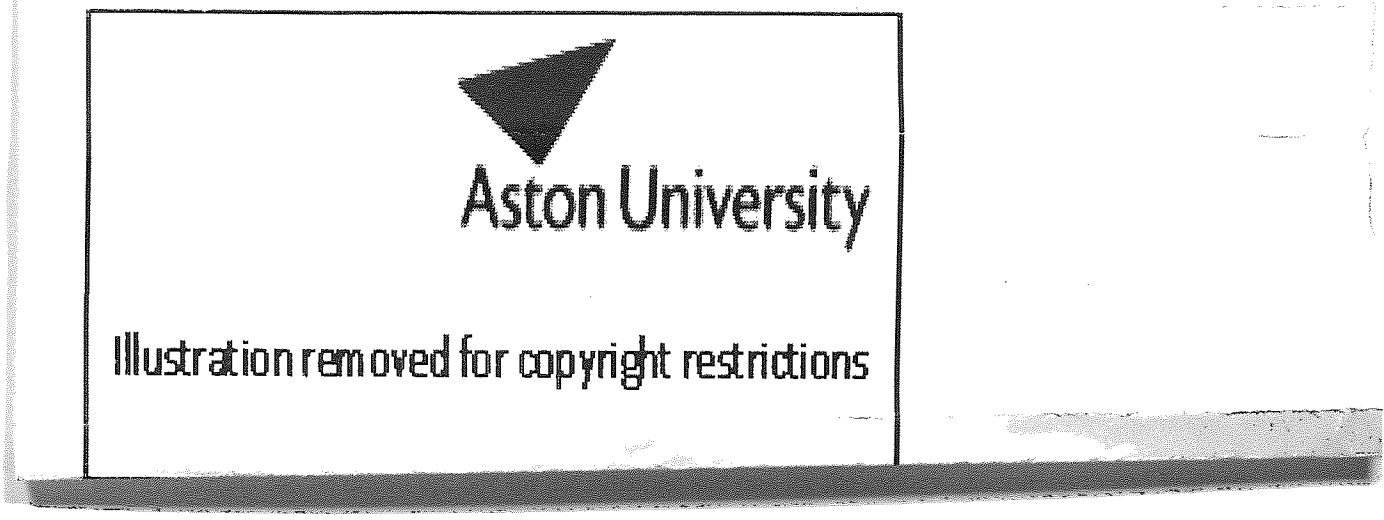

Figure 2.6 Conceptual scheme followed by Mahfouf and Noilhan (1991) in assessing bare soil evaporation.

2.3.2.3 Evapotranspiration Over Fully and Partially Vegetated Surfaces

The problem of trying to calculate the surface energy budget over vegetated regions is a complex one, since transpiration depends upon the structure and distribution of the vegetation canopy, the depth of the root zone and its moisture content. The problem becomes one of trying to distinguish between bare soil and vegetation since the spatial variation of surface radiant temperature is highly dependent on the fraction of bare soil observed and the moisture content in the surface layer. Shuttleworth and Wallace (1985) noted how previous physically based models of the vegetation-atmosphere interaction explicitly treat the vegetation as a closed, stable canopy of uniform structure. Deardorff (1978) dealt with the vegetation canopy as a bulk layer and introduced a vegetation shielding factor to partition the solar flux between that reaching the ground and that intercepted by the canopy. Deardorff found that even by using this simple parameterisation of the vegetation layer the surface temperature could be predicted surprisingly well, and noted the strong need to incorporate a vegetation layer to improve the accuracy of ground surface models. Similar results were obtained in a study by Ritchie (1972) who used the leaf area index (LAI) to account for the influence of the ground surface over a sparsely vegetated region.

Shuttleworth and Wallace (1985) approached the problem of sparse crops using the assumption that the two asymptotic limits, full cover and bare soil, can be represented by a one-dimensional model and that the three-dimensional structure of a real canopy can be ignored in practical terms. The model considered a two-component structure (similar to Deardorff, 1978) where the energy partition is treated as occurring either at the crop or at the soil. By considering the canopy and soil as separate entities two different energy budgets can be drawn up, one for the substrate and one for the canopy. Shuttleworth and Wallace identified a number of problems associated with this assumption, primarily because no distinction is made between the soil beneath the vegetation and that between crop rows, and also because no account is made of the shadowing effects from low solar orientation.

Parameters such as soil moisture and surface temperature are not well defined in the presence of vegetation as the surface temperature depends on the radiance from both the vegetated surface and the soil surface. Through investigations of the thermal response over partially vegetated surfaces, it has been reported how scatterplots of vegetation cover against surface temperature yield a triangular (or trapezoidal) distribution (Figure 2.7). Price (1990) described the characteristic triangle shape in developing a methodology to infer evapotranspiration from satellite data, and it has since been well documented by a number of authors (Carlson and Gillies, 1993; Carlson *et al.*, 1995; Gillies and Carlson, 1995; Moran *et al.*, 1994). Experiments have shown that the triangle shape emerges in both high and low resolution imagery, provided a sufficient number of pixels are sampled (Diak *et al.*, 1995).

By imposing a number of physical constraints on the triangular distribution, values for surface parameters over partially vegetated regions may be inferred. This approach capitalises on the fact that values of many surface properties are easier to simulate for either full vegetation cover or bare soil, than for partially vegetated surfaces. Figure 2.7a shows a schematic representation of the scatterplot which is used to demonstrate the physical constraints imposed at each vertex. Since the vegetation cover is not directly measurable from remote sensing observations, the normalised difference vegetation index (NDVI) is used as a surrogate, which ranges in practical terms from zero for bare soil to approximately 0.6 for complete vegetation cover (Gillies and Carlson, 1995).

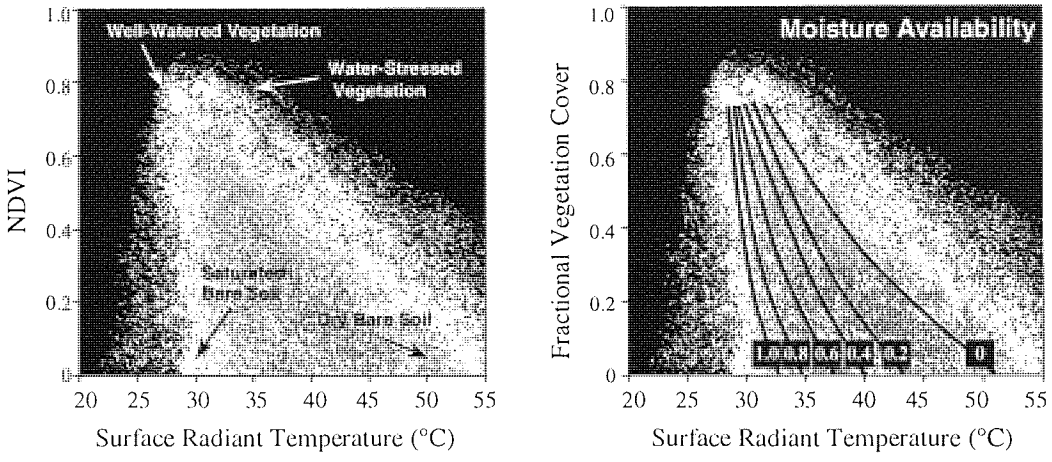

(a) **Physical constraints on scatterplot** (b) **Isopleths of moisture availability**

Figure 2.7 Triangular distribution obtained from scatterplot of vegetation cover against temperature (after Carlson *et al.*, 1995).

Examination of Figure 2.7a reveals that the base of the triangle corresponds to bare soil, and contains a wide range of temperatures reflecting moisture contents from field capacity (cool) to minimum extractable water (hot). At maximum vegetation cover the surface temperature varies far less due to the regulating effects of transpiration. However, what little variation there is can be associated to crop water stress such that well-watered vegetation displays cooler temperatures than water-stressed vegetation (Section 2.2.6).

Before the scatterplot can be used to infer surface parameters quantitatively, observations of radiant temperature must be coupled with a model of the surface layer to align them with simulated surface conditions (see Carlson, 1999 for a comprehensive review of such a scheme). Within the scatterplot, the locus of highest temperatures for differing amounts of bare soil and vegetation delineate a boundary called the 'warm edge'. This boundary is generally well defined and describes the relationship between NDVI and surface temperature for the lower limiting surface soil moisture content.

However, NDVI is simply an index and has no unique correlation with vegetation cover (Price, 1990). The fractional vegetation amount (Fr) is therefore assumed to vary monotonically along the warm edge between bare soil and full vegetation cover (Gillies *et al.*, 1990). Surface radiant temperature is simulated as a function of Fr, and NDVI is equated to Fr by matching the simulated and measured temperatures along the warm edge for the complete range of vegetation cover. Using this derived relationship between NDVI and Fr a family of isopleths of moisture availability can then be generated and superimposed onto the scatterplot (Figure 2.7b).

This inversion approach enables the moisture conditions in the surface layer to be directly inferred from the scatterplot for the complete range of vegetation cover. However, isopleths of moisture availability converge in the truncated vertex of the triangle, and this is the area where errors in the estimated soil water content are largest. Further sources of error include those associated with simulating surface parameters to obtain the relationship between NDVI and Fr.

2.4 Summary

This chapter has examined a wide range of techniques for interpreting the thermal response at the earth's surface. Initial approaches were largely empirical, and the strong relationship between radiant temperature and moisture content in the upper layers of the earth's surface was established in the early 1970's. These techniques were subsequently developed to investigate the relationships between evapotranspiration and surface temperature, but simple empirical studies were found to be site specific and difficult to reproduce. Analytical approaches also began developing in the 1970's, in an attempt to model the diurnal variation of surface temperature using numerical models to describe processes at the earth's surface. A number of standard mathematical techniques were used which were significantly more reliable than simple empirical methods because actual physical processes were considered. However, the overall accuracy achievable using analytical approaches is limited due to the simplified manner in which the atmospheric processes are dealt with. Predictive models are more physically-based and enable a far greater parameterisation of the earth's surface. As such, they have the potential to predict surface

temperature and associated energy fluxes with a far greater precision. However, the greater versatility and accuracy available using these approaches is balanced by the multitude of parameters which are required for simulations, and therefore may not always lend themselves well to small, site-specific studies.

The most important factor influencing surface temperature is the moisture content in the upper layers of the earth's surface. Water displays unusually high values of specific heat capacity, and the presence of water in the pore structure of soil therefore plays a significant role in determining the overall thermal characteristics of the substrate layer. Soil moisture also directly affects the near-surface humidity and strongly influences the partitioning of net radiation between sensible and latent heat fluxes. However, despite the strong relationship between moisture content and surface temperature, the determination of a representative water content in the upper layers using remote measurements of surface temperature presents no trivial task. The moisture content in a drying soil is strongly influenced by the textural characteristics of that particular soil, and for a given textural class these characteristics may vary spatially. This can often lead to uneven and patchy drying whereby a region of soil may appear to have a significantly different moisture content than a neighbouring region. Furthermore, if drying progresses to the point where the surface moisture content becomes decoupled from lower layers, considerable temperature differences may develop between the two adjacent regions.

The presence of vegetation further reduces the reliability with which measurements of surface temperature may be interpreted. For closed, uniform canopies the surface temperature offers a useful measure of crop water stress, but where the canopy is incomplete the thermal response of the underlying ground surface can often contaminate the canopy temperature readings. The conventional approach of dealing with partial vegetation cover has been to estimate the relative amounts of vegetation and bare soil in a given scene using a vegetation index such as the NDVI or LAI. Once the relative fraction of vegetation is known a separate energy balance can be drawn for both the bare soil and vegetation components, which are then integrated according to the relative fractions of each. Treating a partial vegetation canopy in this manner enables surface parameters to be predicted more accurately than methods which do not consider partial vegetation cover. However, the benefits of this approach must again be balanced by the introduction of large numbers of parameters.

Studies of thermal inertia were carried out predominantly during the 1970's as a tool for geological mapping. However, difficulties in removing the many geometric distortions associated with airborne imagery has meant that relatively little success was achieved in this field. Until recently, the methods for removing geometric errors from airborne image data have been unable to provide precisely registered imagery, and since satellite imagery does not currently offer a sufficient temporal resolution, thermal

inertia studies have remained largely undeveloped. The recent introduction of a number of new airborne remote sensing facilities has provided the means to remove these geometric errors to a far higher degree of accuracy, and this has opened up new potential for thermal inertia studies. By subtracting dawn thermal imagery from the daytime imagery, differential heating can be monitored over an entire region providing an additional dimension to thermal remote sensing.

3. Data Collection

The original aim of the research project was to investigate the thermal response at the earth's surface, in order to help differentiate between natural and human-induced thermal anomalies. In achieving this aim it was planned to take advantage of the new Natural Environment Research Council (NERC) image correction facility, which was designed to enable image data to be corrected to a precision far greater than that attainable using conventional rectification procedures (Chapter 4). A successful application was made to NERC for inclusion into the Airborne Remote Sensing Programme for 1996. Section 3.1 describes the location of the study area, and details the nature of the region in terms of solid geology and soil series. Section 3.2 outlines the programme of image acquisition for this project, and describes the essential image characteristics. Section 3.3 describes the main features of the ground truth data collected at the time of image acquisition.

During the pre-processing stages, NERC encountered a number of problems which resulted in considerable delays in the delivery of the image data. Section 3.4 describes the nature of these problems, and discusses the effects they had on the overall project. In light of the problems outlined in Section 3.4, the final section in this chapter describes the additional imagery which was used in this study. This image data was acquired through a similar NERC flying programme, and was used in the study by Ellis (1997). Again, the location of the study area is described, along with the essential image characteristics.

3.1 The Study Area

The Black Brook Catchment (Figure 3.1) lies approximately 30 miles north of the West Midlands conurbation, and was chosen for the study because of the wealth of different land cover and human activity within the area. The region, centring on a small village called Shenstone, is surrounded by predominantly agricultural land, and is relatively flat and open. Within the Black Brook Catchment there are three sewage treatment works, and these rely on the Black Brook and its tributaries to carry treated effluent from the area.

A successful application was submitted to the Natural Environment Research Council (NERC) for two flight patterns over the study area (Figure 3.1). The first pattern comprises a flight path along the Black Brook river corridor and includes coverage over three sewage treatment works. The second flight pattern provides detailed coverage over Shenstone and the surrounding catchment. This region contains a wide

range of land use including relatively concentrated residential buildings in the heart of Shenstone, a small industrial estate on the western outskirts and significant agricultural activity in the surrounding areas.

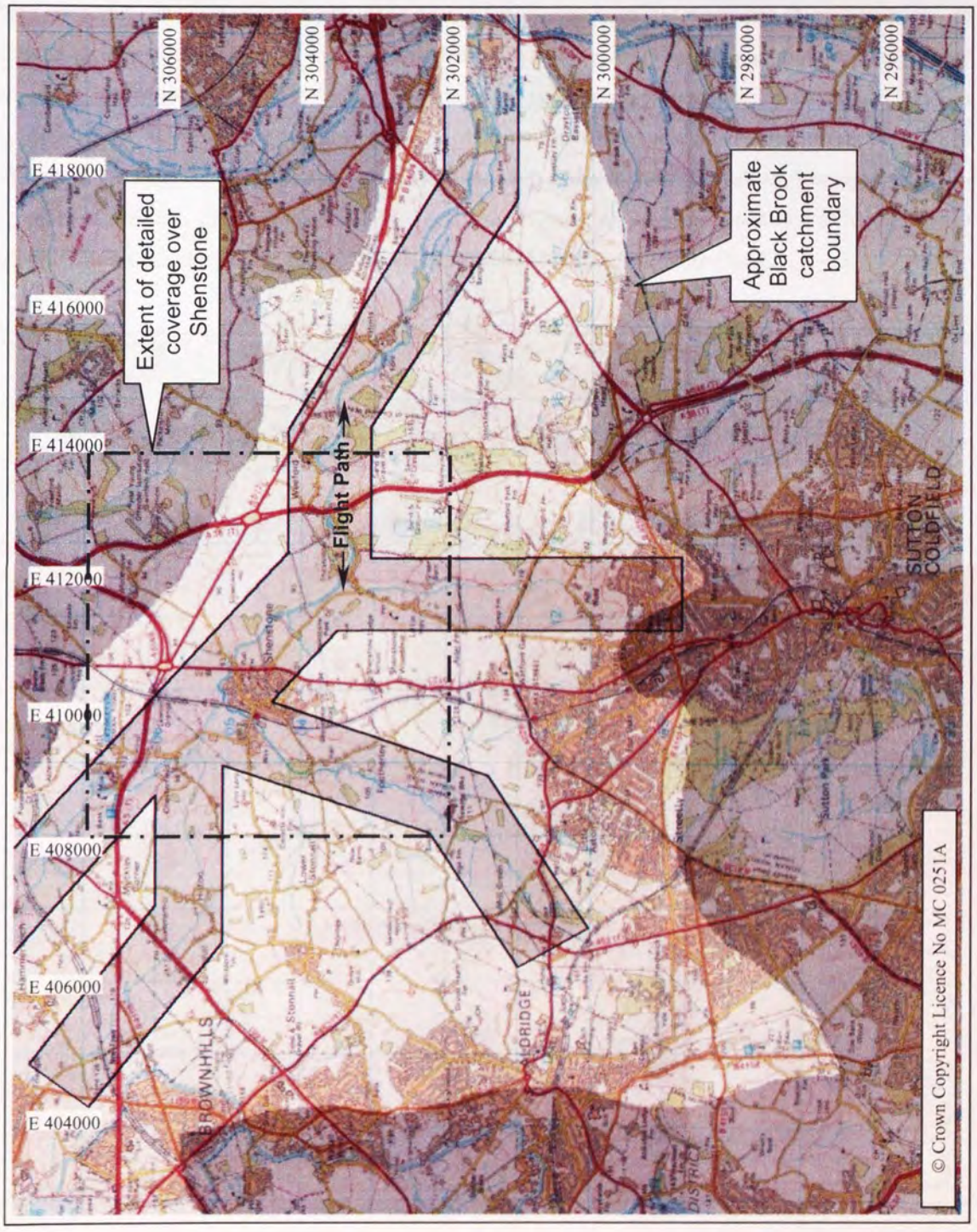

Figure 3.1 The Black Brook catchment and flight coverage along river corridor

3.1.1 Detailed Study Sites

Figure 3.2 illustrates the location of the detailed study sites used in this project. Both Saxton's and Abel's Farm sites were chosen because of the significant spatial variation of soil properties at each location. In order to investigate the effects of these spatial changes it was decided to sample ground truth data along two transects, positioned to bisect the maximum possible number of soil textural classes (Figure 3.3). At the time of the over-flights, both field sites had recently been tilled and sown with winter barley. In addition to the transects, a 125×100m grid was set out with nodes at 25m intervals to investigate the two-dimensional variation of soil properties. The grid site (Figure 3.4) was positioned in a field adjacent to the Abel Farm site, which at the time of the study consisted of ploughed, fallow land.

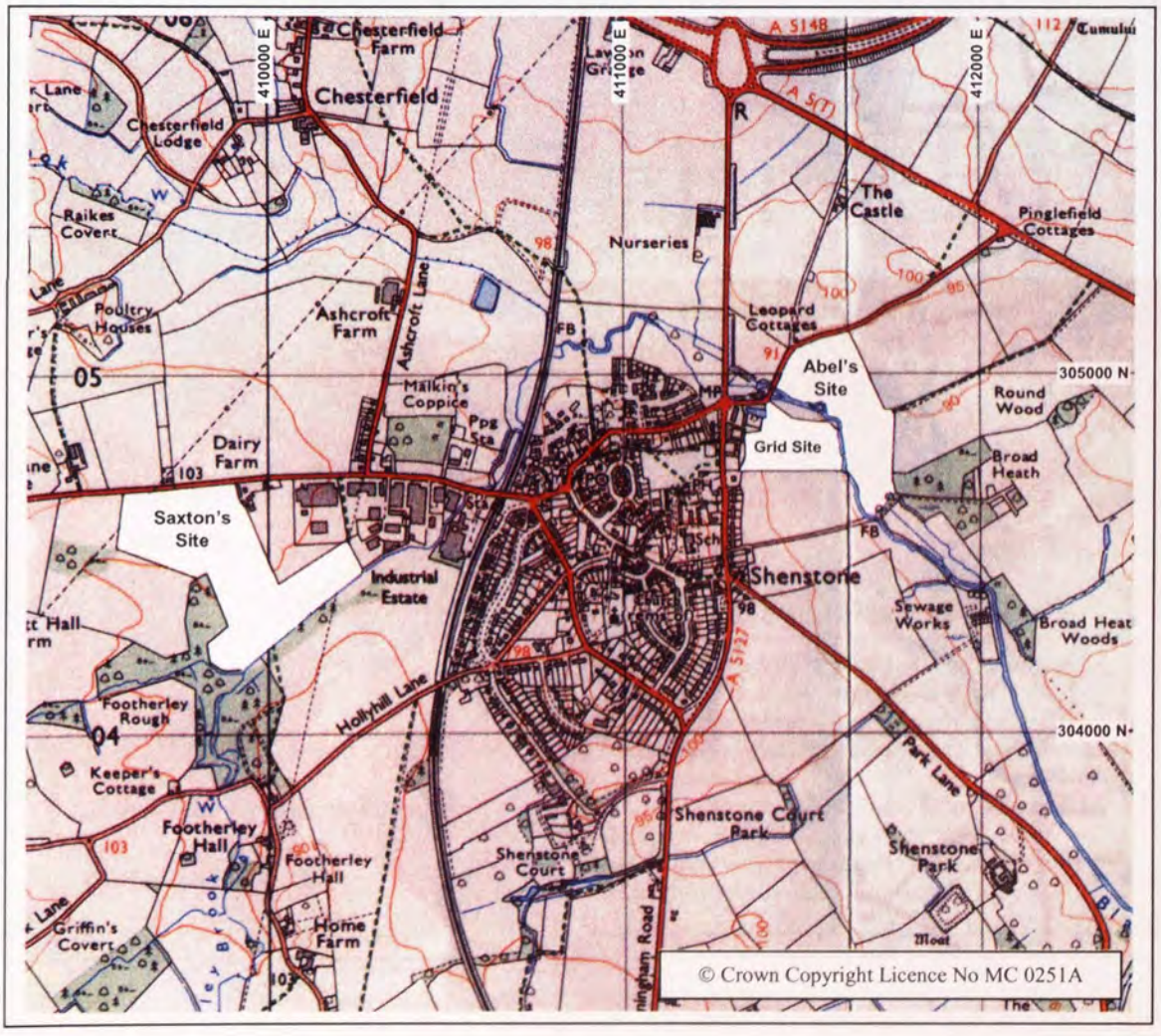

Figure 3.2 Detailed study sites.

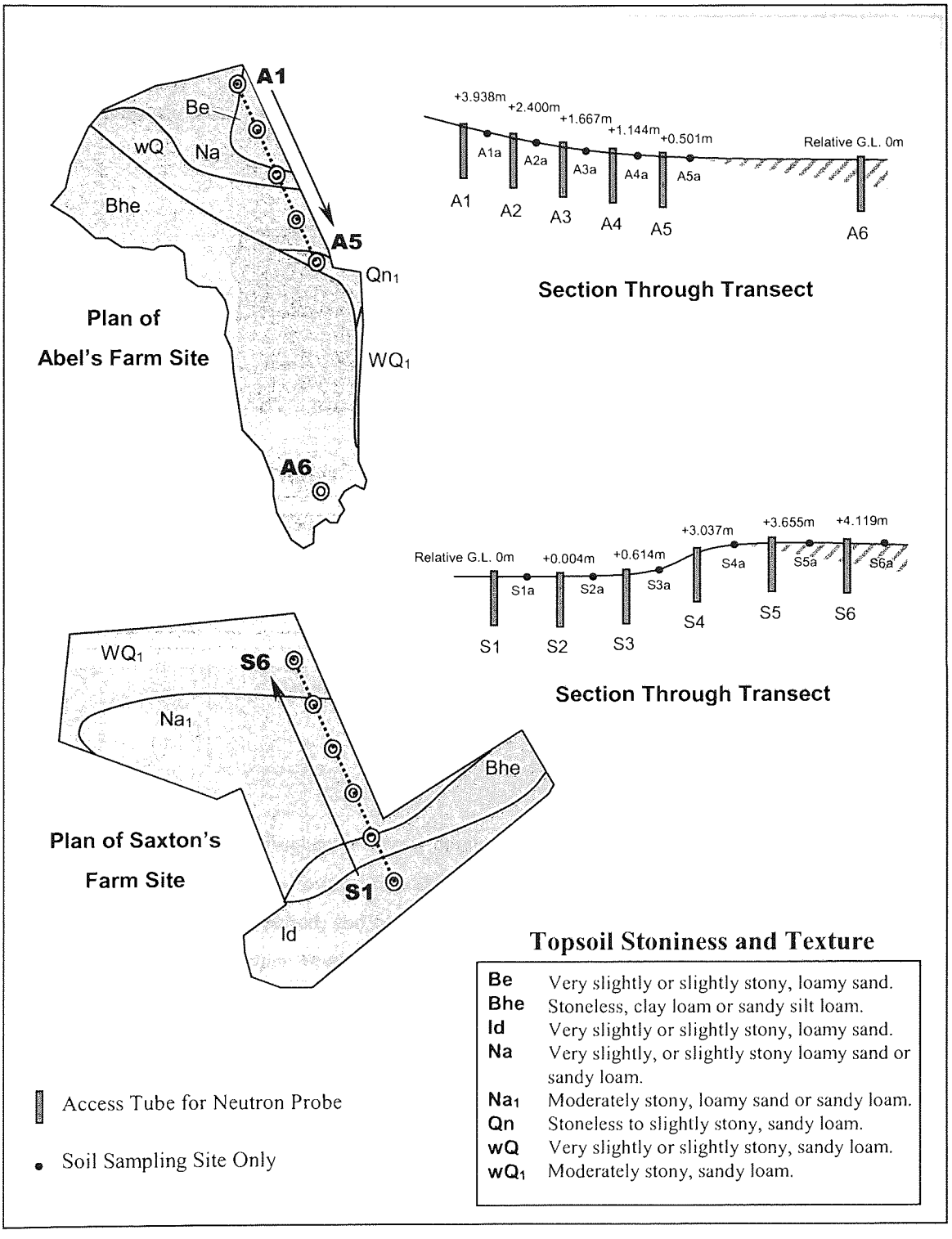

Figure 3.3 Sketch of detailed study sites.

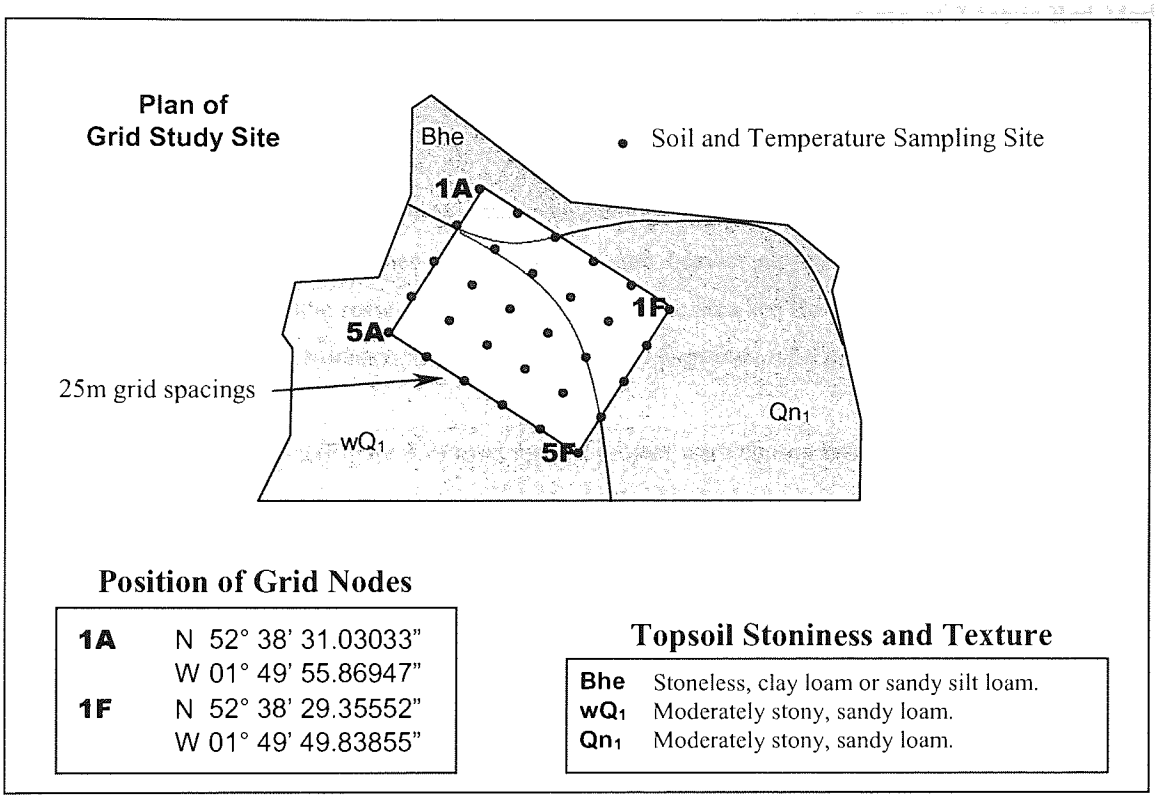

Figure 3.4 Sketch of grid study site.

3.1.2 Geology

The solid geology of Central England is largely dominated by the 'New Red Sandstone', which describes a series of Permo-Triassic rocks forming the relatively low-lying Midland plain. Bunter sandstones were formed in the early Triassic period, and consist of *Lower Mottled Sandstone*, giving way to the *Bunter Pebble Beds*, overlain by *Upper Mottled Sandstone*. Above the Bunter sandstone lies the Keuper series, consisting of *Keuper Sandstone* and the *Keuper Marl*. The geology of the study area is illustrated on Sheet Number 154 of the British Geological Survey's *One-Inch Series*. For a detailed description of the regional geology of Central England see Hains and Horton (1986).

Figure 3.5 shows the geology of the study area. The village of Shenstone sits on a bed of Keuper Sandstone, and these beds stretch northward beyond Lichfield and extend beyond Whittington in the east, and Hammerwich in the west. First Terrace and Alluvium deposits lie in a thin band running north-west to south-east, following the line of the Black Brook. In the north-west these deposits run into Bunter Sandstones and pebble beds. However, in the west and south of Shenstone, the geology becomes far more fragmented with a mixture of Bunter Sandstone, outcrops of the Hamstead Group of Red Marl and

Sandstone, and Hopwas Breccia. Towards the far south-east lies a large outcrop of Triassic Red Marl with sandy beds.

3.1.3 Soil Series

Much of the soils in the Shenstone area reflect the geological parent material and are characterised by relatively sandy loams on the higher ground running into heavier clayey and peaty soils in low-lying regions. For a comprehensive review of soils in the Shenstone area see Hollis (1985). A soil map for the region is illustrated on the Ordnance Survey *Soil Survey for England and Wales* (sheet number SK 00/10).

The two detailed study sites (Figure 3.2) used for this project were chosen based on the gradually varying soil characteristics along each transect (Figure 3.3). At the Abel's Farm site the soil varies from a slightly stony, loamy sand through to stoneless clay loam. Similarly, at Saxton's Farm site, the soil texture ranges from a moderately stony, sandy loam to clay loam and loamy peat. It was hoped that this positioning of the transects would enable the effects of gradual spatial changes in soil characteristics to be investigated.

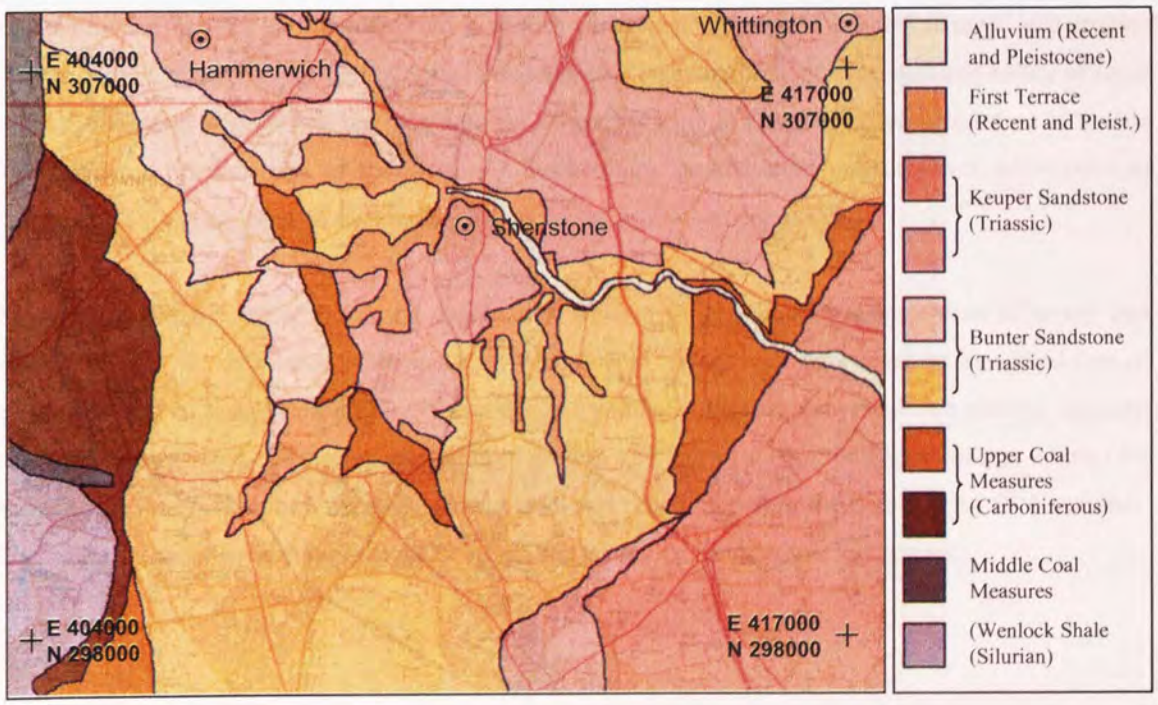

Figure 3.5 Solid geology of the Shenstone area.

3.2 The Acquisition of Image Data

Remotely sensed image data for this project was acquired through the NERC Airborne Remote Sensing Programme for 1996. The digital imagery was acquired using the Daedalus 1268 airborne thematic mapper (ATM), which operates in eleven spectral wave bands ranging from visible to thermal infrared. For a description of the operating capabilities of the ATM see Wilson (1994, 1999). In order to assess differential heating within the study area it was necessary to acquire thermal imagery at times of maximum and minimum surface temperature, namely at midday and dawn. The planned flights took place on the afternoon of the 23rd October and the dawn period of the 24th October, 1996. However, it was not realised until the image data was eventually delivered that the region was re-flown on 8th November, 1996 in order to infill missed data between adjacent flight lines. Imagery was acquired at an approximate altitude of 1000m, which resulted in a nominal pixel resolution of 2m. In addition to the ATM imagery, aerial stereo colour photography was acquired during the afternoon flight, providing an additional source of image data for the study.

3.3 The Acquisition of Ground Truth Data

Ground truth data plays an important role in studies where remotely sensed imagery is used, as it enables remote observations to be verified by actual measurements taken in the field. The dynamic nature of some surface conditions necessitates the measurement of ground truth at times of image acquisition to enable more accurate interpretation of the imagery. Furthermore, ground truth measurements taken prior to image acquisition may provide useful information on the antecedent conditions.

In order to facilitate the accurate and timely measurement of ground truth data, a plan of action was devised prior to the acquisition of the imagery. Sampling of ground truth data began at the agreed time of commencement of image acquisition on both the 23rd and 24th October, and progressed until all required data had been gathered. The whole operation of ground truth retrieval required approximately 3 hours for each flight. It should be noted that no ground truth was recorded during the flight on the 8th November. The following sections describes the nature of ground truth data recorded for this project.

3.3.1 Temperature Measurements

Temperature measurements were recorded during the times of over-flight, at both Abel's and Saxton's farm sites and the grid site, using a *Hanna Instruments* temperature probe. The temperature probe has a measurement range of -50 to 150°C, and a stated accuracy of ± 0.3°C. Three sets of temperature measurements were recorded at each sampling site. Firstly, the air temperature was recorded at a height of approximately 1m above the ground surface by holding the temperature probe in the free atmosphere. Secondly, the surface temperature was measured by positioning the probe flat on the ground surface, ensuring the probe itself was embedded in the surface layer. Finally, the sub-surface temperature was recorded by fully inserting the probe (approximate length of 100mm) vertically into the ground.

It was envisaged that measurements of the surface temperature would enable the thermal remotely sensed data to be calibrated to actual surface temperatures. The air temperature is an important parameter in many models of the earth's surface layer (Chapter 2), whilst the subsurface temperature provides information on the relative temperatures between the surface and substrate layers. Appendix 1 provides a summary of the temperature measurements for both the midday and dawn flights.

3.3.2 Soil Moisture Determination Using the Neutron Probe

Due to the strong influence of moisture content on surface temperature, the soil moisture profile was determined both prior to, and during the time of the over-flights. This was carried out using a neutron moisture probe, which provides a direct measurement (after calibration) of volumetric moisture content (for a description of the operating characteristics see Shaw, 1994).

Soil moisture measurements using the neutron probe were limited to the two transects at Abel's and Saxton's Farms. Access tubes were sunk to varying depths (depending on ground conditions) on the 15th October 1996. The moisture profile was monitored prior to image acquisition on the 20th and 22nd October, and again during the time of over-flights on the 23rd and 24th October 1996. The tubes were finally retrieved on the 5th November 1996, when the last set of moisture probe readings were taken. Appendix 1 summarises the moisture readings for each of the days when measurements were recorded.

3.3.3 Gravimetric Soil Samples

Gravimetric soil samples were retrieved at all three study sites to enable the soil particle distribution to be determined. Furthermore, since the neutron probe is unable to provide reliable estimates of soil moisture close to the ground surface, the gravimetric samples also enabled a precise measure of surface moisture content to be determined. Samples were taken from two depths (0-50mm and 50-100mm) during both the midday and dawn over-flights. Once the soil samples were retrieved, they were stored in sealed plastic bags to prevent any moisture loss.

Soil Moisture Determination

Soil moisture was calculated gravimetrically in accordance with BS1377:1975. Field samples were initially weighed and subsequently placed in an oven at 105°C until dry, whereupon the dry weight was determined. The moisture content is expressed as the mass of water divided by the original mass of the sample, and Appendix 1 summarises the results for each study site.

Particle Size Distribution

The determination of the particle size distribution was carried out in two stages in accordance with BS1377:1975. The first stage determined the range of particle sizes down to 63μm by wet sieving, whilst the second stage determined the distribution by sedimentation using the pipette method. Appendix 1 summarises the particle size distribution for all three study sites.

3.3.4 Wind Speed and Rainfall Measurements

The final set of ground truth data were the rainfall and wind speed measurements. Rainfall was assessed both prior to and during the time of image acquisition using a rain gauge positioned adjacent to the Abel's Farm study site. The rain gauge was installed on the 15th October 1996, and measurements were recorded on the same days on which the soil moisture was measured using the neutron probe. An additional measurement was also made on the 2nd November 1996, and all these readings are summarised in Appendix 1.

The wind speed was estimated using a handheld anemometer at an approximate height of 2m above the ground surface. Wind speed measurements were recorded at Abel's Farm site during both over-flights, where the mean and gusting wind speeds were estimated at 15 minute intervals. Again, Appendix 1 summarises these measurements.

3.4 Problems of Image Pre-Processing and Redirection of Study

Raw remotely sensed image data must undergo a pre-processing stage to remove the geometric errors inherent to the methods of image acquisition (see Chapter 4). From previous experience of obtaining imagery through NERC flying programmes, it was originally envisaged that the pre-processing stage for the Shenstone data set would require approximately 6 months for completion.

However, a number of significant problems were encountered during the pre-processing stages of the remotely sensed imagery. The problems were due to what are termed 'jumps' in the synchronous navigation data, and these most commonly occur when the aircraft GPS system fails to lock on at the start of a flight line, or when there are an insufficient number of GPS satellites in the sky during a flight line. The software which was developed to use the navigation data to remove geometric distortions was unable to cope with these jumps, and as a consequence, NERC suffered very large delays in delivering image data products. Whilst the stereo aerial photography arrived on the 20th January 1997, the first digital imagery was not made available until March 1999, some 28 months after the date on which the flights were carried out. The full set of imagery was eventually delivered in September1999.

This delay in receiving the digital image data led to obvious knock-on time implications, and as a direct result of the problems experienced by NERC, a decision was made towards the end of 1997 to redirect the main thrust of the research project. Since the primary objective of the original project was to use the NERC GPS correction facility to co-register the daytime and dawn thermal imagery, it was decided, in the absence of the NERC data, to investigate alternative methods of co-registering line-scanned imagery. The overall aim of the project remained basically unchanged: to register the daytime and dawn thermal imagery to investigate widespread differential heating within the study area. The investigations were carried out using imagery acquired previously within the department (the Black Country data set), with the intention of extending the methodology to the Shenstone data set, once it eventually arrived.

3.5 The Black Country Data Set

In addition to the imagery which was acquired specifically for this project, a number of alternative flight lines were available which were acquired through previous remote sensing programmes. Ellis (1996) describes the acquisition of airborne image data for the detection of landfill gas and leachates in urban environments. This imagery was provided by NERC as part of the Airborne Remote Sensing Programme of 1992, and extended across an area of the Black Country between Birmingham and Wolverhampton (Figure 3.6). The region is largely built up and consists of light industrial buildings and densely packed residential properties. The imagery was acquired at 9.30am on the 25th June 1992, using the ATM flown at a nominal altitude of 1000m. This was also supplemented with stereo aerial photography with an approximate scale of 1:5000. A second source of image data was acquired at a later date as part of the same study, during the dawn period of 8th April 1994. The area of coverage was similar to the June 1992 data set, although the study region was extended to cover a number of additional sites.

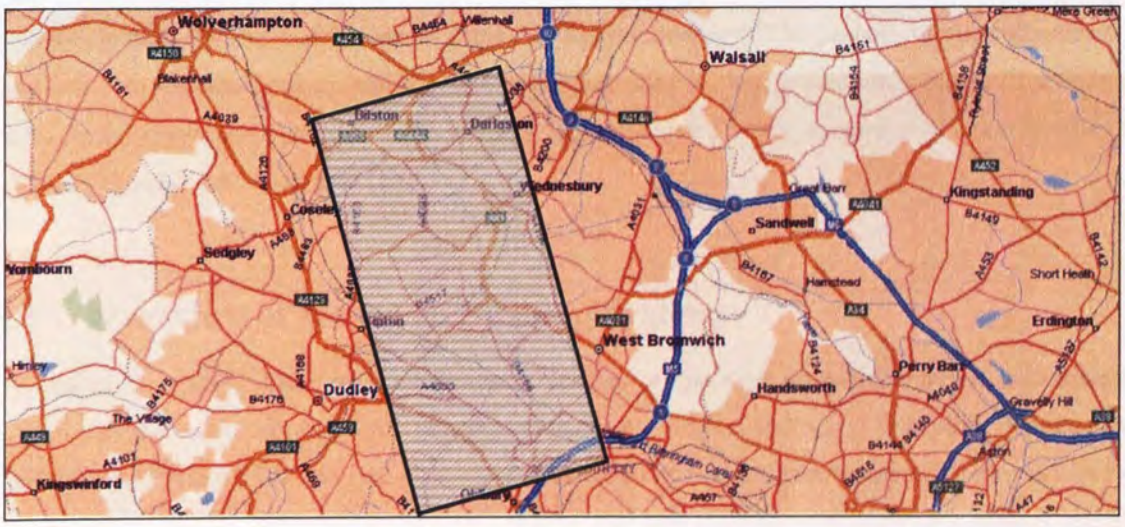

Figure 3.6 Approximate coverage of the Black Country data set.

4. Geometric Correction and Registration of Airborne Imagery

With the development of remote sensing technologies around the world, ever-increasing volumes of image data obtained with different spectral and spatial characteristics are available. Many applications require imagery to be integrated with other sources of geographic information, and in such cases the issue of image geometry becomes one of great importance. Geometry refers to the projection, scale and orientation of the imagery, and in order that multiple sources of geographic information may be reliably integrated and analysed each data source must exhibit identical geometry. Since most sources of geographical information are referenced to a pertinent grid co-ordinate system, it is common to use this for the reference on which to register additional image data sets.

Before a remotely sensed image can be integrated with other sources of geographical data, it must first undergo a transformation to remove the many distortions caused by errors inherent to the methods of image acquisition which effect its geometry. The following section reviews the principles of operation of airborne imaging systems and introduces some relevant terminology. The primary sources of geometric error are then examined, along with current techniques used in their correction. Finally, methods of assessing the geometric accuracy of the imagery are investigated where a number of improvements to existing techniques are suggested.

4.1 Overview of Airborne Imaging Systems

Electro-optical sensors differ from photographic sensors in that they do not capture an instantaneous snapshot of the earth, but rather the image is built up by viewing individual scan lines contiguously. Electro-optical sensors fall into two main categories; whiskbroom and pushbroom type sensors - Figure 4.1 illustrates the fundamental differences between the two systems. Whiskbroom sensors predate pushbroom sensors, and use a mechanically driven mirror to scan the ground in the across-track direction. Pushbroom sensors use a linear array of charged coupled devices (CCDs) to scan the surface enabling a complete scan line to be recorded instantaneously. Both sensors rely on the forward motion of the sensor platform to provide one direction of scan (the so-called along-track direction), allowing successive scan lines to be recorded.

Wadsworth *et al.* (1992) describe the advantages and disadvantages of each type of sensor and criticise pushbroom scanners because of their complex calibration requirements. However, pushbroom sensors offer a number of advantages over whiskbroom sensors. Improved spatial resolutions are available because of the increased dwell time on each ground resolution element. Furthermore, enhanced geometric accuracy is possible in the across-track direction because of the fixed geometry of the detector array. Whiskbroom sensors offer no geometric integrity within or between scan lines, and the resulting imagery therefore suffers more complex geometric distortions. Whiskbroom sensors also offer the ability to sense in the thermal infrared waveband, a feature which pushbroom scanners are yet to acquire. For a review of the operating characteristics of airborne imaging systems see Avery and Berlin (1992) and Lillesand and Kiefer (1994).

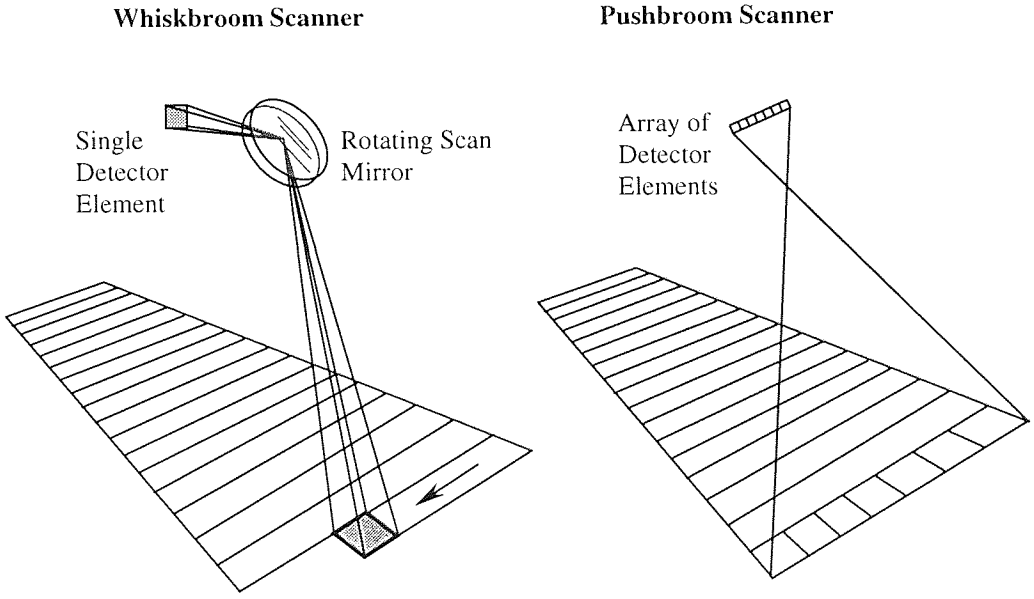

Figure 4.1 Whiskbroom and pushbroom electro-optical sensors.

4.2 Sources of Geometric Error

Geometric errors can be categorised into system dependent and system independent distortions. System dependent errors can generally be successfully compensated for by constructing mathematical models which reflect the nature and magnitude of image distortions. However, system independent errors cause potentially the most severe problems due to the unpredictable pattern with which they distort image geometry.

4.2.1 System Dependent Errors

System dependent errors can be classified in the following way;

1. image skew caused by the rotation of the earth during image acquisition (satellite platforms only),
2. image skew caused by the finite scan rate of whiskbroom sensors,
3. panoramic distortions due to the wide field of view of some sensors,
4. errors due to imperfections of the scanning mirror, and
5. band to band offset errors.

System dependent errors (with the exception of number 1 above) affect both satellite and aircraft imagery to some degree. However, these errors are deterministic and can be successfully compensated for by constructing mathematical models which reflect their nature and magnitude. Since their effects on the quality of remotely sensed imagery are negligible they will not be considered further. For a review of the procedures of correcting deterministic errors see Richards (1986), Mather (1999), Ehlers (1997).

4.2.2 System Independent Errors

System independent errors include those relating to terrain effects and the relative motion of the sensor platform and underlying surface. Platform errors are most significant in imagery obtained from airborne line scanning sensors since distortions continually vary from one line to the next as the sensor platform is buffeted by atmospheric currents during image acquisition. Variations in the aircraft velocity may cause distortions in the along-track direction due to under or over-sampling.

Terrain Effects

Terrain effects can distort image geometry considerably, and are a function of sensor altitude, terrain relief height, and distance of the terrain from the nadir. Figure 4.2 illustrates the effects of relief distortion on image geometry, where terrain features appear to be displaced away from the nadir. Since aerial

photographs capture imagery in two dimensions, surface relief creates distortions which radiate away from the nadir. However, line scanning sensors only record a single scan line at a time, so radial distortions resulting from terrain effects only occur in the across-track direction. Relief distortion can be calculated by similar triangles, and using the terms defined in Figure 4.2, is given by;

$$relief\ distortion = \frac{h.x}{H-h} \qquad (4.1)$$

Devereux *et al.* (1990) note that displacements due to surface relief can be substantial – approaching 0.9 × terrain height at the extremes of the scan line. In the absence of terrain elevation information, relief effects cannot be reliably removed from the imagery. However, the effects of surface relief can be minimised by ensuring that the platform altitude is high with respect to terrain elevation, and by minimising the sensor's field of view. If an accurate terrain model exists for the region under investigation, it is possible to compensate for surface relief effects and Section 4.4 describes the use of digital elevation models in ortho-rectifying aerial photography.

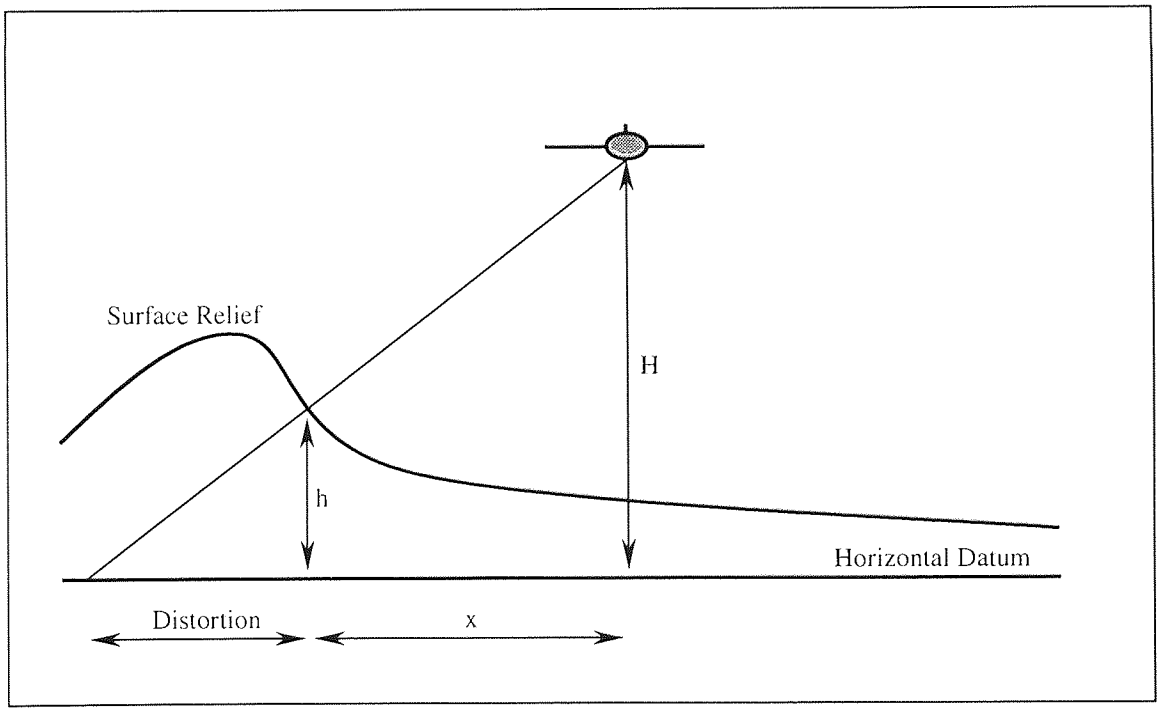

Figure 4.2 Effects of surface relief on scan line geometry.

Platform Attitude, Altitude and Velocity

Perturbations in the trajectory of the airborne sensor due to fluctuating wind currents can potentially cause the most significant errors in remotely sensed line scanner imagery due to the unpredictable pattern with which they distort image geometry. In the absence of platform ephemeris data it is impossible to determine exactly how the aircraft moves with respect to the underlying ground scene, and the resulting errors are effectively random in nature.

Platform attitude movements can be resolved around three axes termed roll, pitch and yaw. Figure 4.3 illustrates the effects of these errors, along with distortions associated with variations in altitude and velocity, in an image built up of a contiguous series of scan lines. Aircraft roll causes displacements purely in the across-track direction, whilst variations in pitch cause errors predominantly in the along-track direction. Aircraft yaw causes distortions in both directions, and the combined effects of all three sensor movements on a line-scanned image are also illustrated in Figure 4.3.

Roy *et al.* (1997) carried out sensitivity analyses to determine the effects of variations in aircraft attitude on the resulting imagery, and derived the equations grouped together as Equation 4.2. These expressions show that the magnitude of attitude-induced displacements, Δx and Δy (across and along-track respectively), are directly proportional to the attitude perturbation ($\Delta_{pitch,\ roll,\ yaw}$), the sensor altitude ($h$) and the scan angle ($\theta$).

The essence of a successful geometric correction model is the ability to recognise and compensate for these platform attitude errors. Section 4.3.2 discusses how measurements of platform attitude can be used to correct image geometry. However, in the absence of such devices aircraft attitude distortions may be reduced by mounting the sensor on a gyro-stabilised platform (Crabtree and Brown, 1989). Whilst platform stabilisation systems can remove a large proportion of errors resulting from variations in platform attitude, Roy *et al.* (1997) identify that even these systems cannot guarantee compensation of very rapid attitude perturbations, or account for changes in the sensor position.

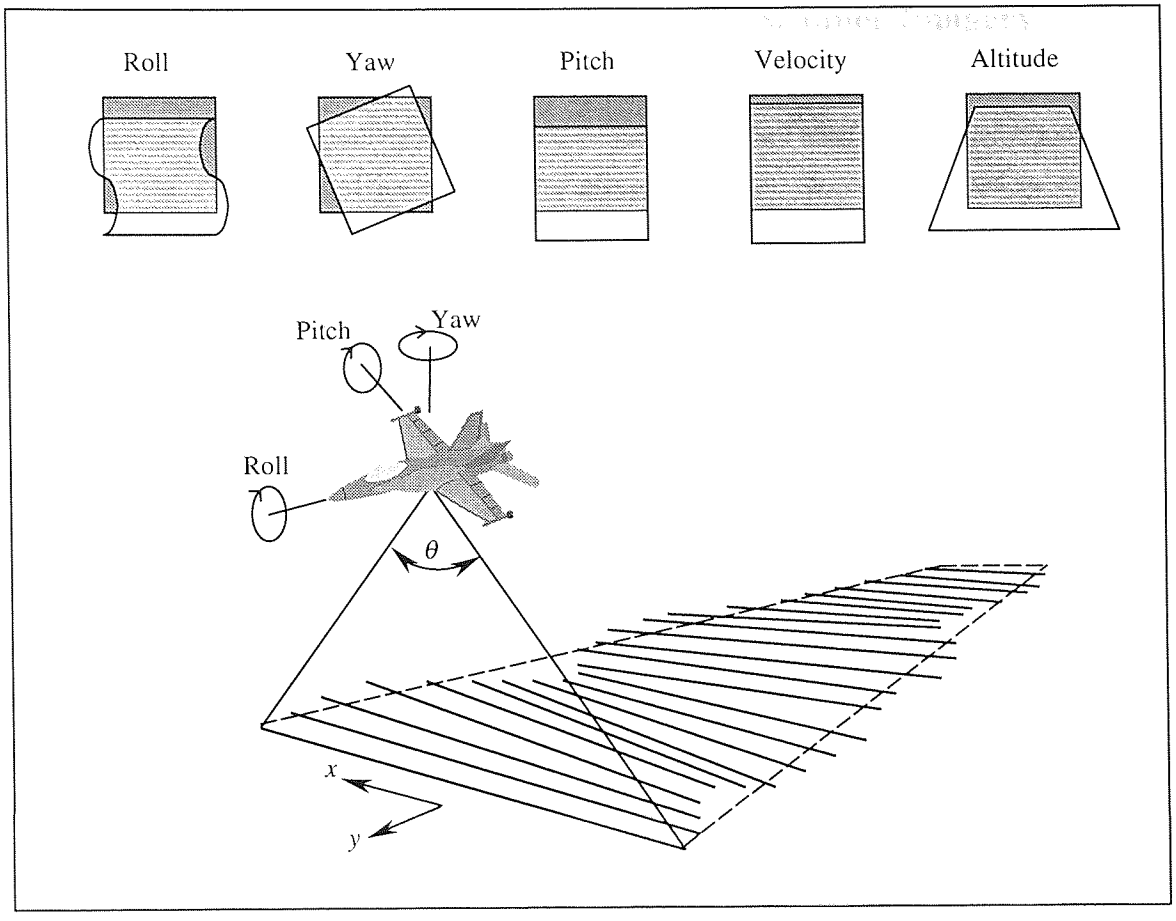

Figure 4.3 Effects of aircraft platform movements on the geometry of line-scanned imagery.

$$
\left.
\begin{aligned}
\Delta x_{\Delta pitch} &= \frac{h}{\tan(\theta)}\left(1 - \frac{1}{\cos(\Delta pitch)}\right) \\
\Delta y_{\Delta pitch} &= -h\tan(\Delta pitch) \\
\Delta x_{\Delta roll} &= \frac{h}{\tan(\theta)} - \frac{h}{\tan(\theta + \Delta roll)} \\
\Delta y_{\Delta roll} &= 0 \\
\Delta x_{\Delta yaw} &= \frac{h}{\tan(\theta)}\left(1 - \cos(\Delta yaw)\right) \\
\Delta y_{\Delta yaw} &= \frac{-h\sin(\Delta yaw)}{\tan(\theta)}
\end{aligned}
\right\} \qquad (4.2)
$$

4.3 Geometric Correction of Airborne Line-Scanner Imagery

Geometric correction of remotely sensed imagery is the process of eliminating, to a satisfactory degree, errors of a geometric nature resulting from sensor imperfections, surface relief and the relative motions of the sensor platform and underlying scene. This procedure is also commonly referred to as image rectification, geo-rectification, and geometric enhancement, although they all essentially describe the same process. Many applications of remote sensing require two or more scenes of the same geographical region to be analysed and processed together. Image registration is the transformation of a raw image so that its pixels conform to a specified geometry, provided typically by a map co-ordinate system or an additional image data set. The advantage of registering imagery to a map co-ordinate system is that pixels can be referenced in terms of co-ordinates rather than row or column addresses. Furthermore, registration to a map provides the imagery with a measurable scale, enabling areas and distances to be calculated quickly and accurately.

The processes of geometric correction and registration are generally carried out in parallel, and can be classified into parametric and non-parametric techniques. Non-parametric approaches attempt to remove geometric errors by developing general expressions to describe image distortions, irrespective of the nature of error. Parametric methods attempt to model the nature of image distortions by utilising platform ephemeris data, whereby each scan line can be theoretically projected on to its true ground position in the corrected image. The following sections review both parametric and non-parametric methods of rectifying airborne line scanner imagery, emphasising on the accuracy achievable using each technique.

4.3.1 Non-Parametric Methods

4.3.1.1 Polynomial Correction

One of the most common methods of correcting remotely sensed imagery relies on the use of ground control points (GCPs) located in the image and corresponding map to determine empirically a mathematical transformation to correct the image geometry. This process, called polynomial correction, offers a rapid and computationally efficient solution to the problem of image correction, and is carried out in three main stages.

The Polynomial Mapping Function

The first stage of the procedure is to define a mathematical relationship between the raw image data and a map co-ordinate system pertinent to the region. The mapping function is generally chosen to be a bivariate polynomial, which was first employed by Markarian *et al.* (1973). Defining the map co-ordinates as (x,y) and the image co-ordinates as (u,v), the mapping functions are given by;

$$u = f_1(x, y) = \sum_{j=0}^{q} \sum_{k=0}^{q-j} a_{jk} x^j y^k \qquad (4.3)$$

$$v = f_2(x, y) = \sum_{j=0}^{q} \sum_{k=0}^{q-j} b_{jk} x^j y^k$$

where q is the order of the polynomial and $\{a_{jk}\}$ and $\{b_{jk}\}$ are unknown transformation coefficients. Ford and Zanelli (1985) base their choice of q on the degree of non-linearity within the imagery. First order polynomial functions can remove affine type distortions such as translation, scale, rotation and skew, whilst more complex non-linear distortions require higher order polynomials to correct the geometry. Ford and Zanelli found that low order polynomials provided sufficient accuracy for geometric correction of satellite imagery. Satellite sensing systems offer relatively stable platforms and the resulting imagery is largely free from platform attitude effects. As demonstrated in the previous section, aircraft imagery contains considerable platform attitude errors, and only a polynomial with an extremely high order could possibly match the variation of distortion. However, McGwire (1996) warns of the dangers of using high order mapping functions, where there is a trade off between the mathematical stability of lower order polynomials versus the ability of higher order polynomials to fit more complex patterns of geometric distortion. For this reason, the degree of polynomial used for rectification is generally limited to two or three, and the accuracy with which aircraft imagery can be corrected using this technique is consequently limited.

Selection of Ground Control Points and Determination of the Mapping Function

The coefficients for the mapping polynomials are calculated from GCPs selected in the imagery. GCPs are well-defined and spatially small features which can be located both within the image and on a corresponding map of the region. Typical GCPs might include road intersections, corners of buildings, or airport runways.

By comparing the measured map co-ordinates with the pixel addresses for each GCP, the coefficients of the mapping functions described by Equation 4.3 can be determined using a least-squares regression

approach. The order of the mapping function directly influences the number of GCPs required for solution. First order polynomials require at least three GCPs, second order transformations require at least six GCPs, and third order functions need at least ten. However, this requirement is purely to ensure that the procedure is mathematically feasible – statistical requirements are concerned with the reliability and interpretability of the image correction, and suggest that far more GCPs are necessary. Mather (1999) suggests that for a small region of satellite data, a reasonable geometric accuracy is achievable using 10-15 GCPs. Furthermore, it is suggested that GCPs should be evenly distributed to limit the extrapolation errors at the extremes of the imagery when employing high order polynomials.

Once the GCPs have been selected, the accuracy of the resulting transformation can be estimated by calculating the root-mean-square-error (RMSE) of the residuals between the actual and predicted position for each GCP in the set. The RMSE is a statistical measure of how accurately the polynomial transformation can fit GCPs to their true map co-ordinates, and is generally expressed in terms of metres or number of pixels. If the positional residuals at GCPs are small then the RMSE will consequently be small, indicating a relatively accurate transformation. If the geometry of the raw imagery is severely distorted, positional residuals at GCPs are likely to be higher indicating a less accurate transformation. Since satellite imagery is inherently more accurate than airborne imagery, geometric corrections can commonly yield RMSEs of better than one pixel. However, airborne imagery often contains significant distortions due to variations in platform attitude, and RMSEs of this order are almost impossible to achieve using simple affine transformations. Section 4.5 describes the use of RMSE for estimating the geometric accuracy of remotely sensed imagery, and highlights some of the shortcomings of this approach.

Resampling to the Corrected Image Grid

Once the coefficients for the mapping polynomials have been determined, the final stage of the correction procedure is to estimate the digital numbers (DNs) associated with each location in the corrected image space. The assignment of DNs to the pixel co-ordinates in the output image is known as resampling, and is carried out through two approaches; direct (or forward) and indirect (or reverse) interpolation. With direct interpolation, the DNs to be registered in the input image are transferred on a pixel-by-pixel basis to the output data set, so that the new position of every input pixel is calculated. However, using this technique it is possible that a number of output pixel locations will not be addressed at all, leaving gaps which later need to be filled through interpolation.

The indirect resampling method generates the output image on a pixel-by-pixel basis by determining which input pixel maps the closest to the output pixel. This method is the preferred method of resampling,

since every pixel in the output image is referenced ensuring gaps do not occur. However, since pixel centres in the raw imagery will rarely project to exact pixel centres in the corrected image, interpolation is required to estimate a representative DN for placement in the new grid. Interpolation is carried out using one of three main techniques; nearest neighbour resampling, bilinear interpolation, and cubic convolution (also commonly referred to as cubic splining).

Nearest neighbour resampling is the simplest and quickest method for estimating DNs, since the pixel centres in the corrected grid take the actual value of the nearest projected pixel from the raw image. This is the most commonly used method of resampling since the final corrected image consists of the original DNs, simply rearranged into the correct image geometry. However, nearest neighbour resampling is criticised for the blocky appearance of the output image. Bilinear interpolation and cubic convolution draw DNs from the surrounding four or sixteen pixels respectively. Interpolation type functions yield imagery which is smoother in appearance due to the averaging process, but requires far greater computational effort than the nearest neighbour technique. Interpolation type functions are generally not recommended if the imagery is to be subsequently classified, since the new brightness values may not represent actual radiance values detected by the sensor (Richards, 1986). Since the processes of resampling are well documented in a number of texts, they will not be discussed further. For a review see Mather (1999).

4.3.1.2 Error Analysis and Critique

A number of measures can be taken to minimise errors and improve the overall accuracy when using polynomial mapping functions to correct image geometry. The first decision to be made is the order of the polynomial, and although this is generally limited to two or three, care must still be taken in choosing the most appropriate transformation. Figure 4.4 demonstrates the differences between first, second and third order curves which have been fitted to a number of points using least-squares regression. It can be seen that whilst the second and third order polynomials fit a more representative curve within the range of points, outside this range the curves vary wildly. Figure 4.4 also illustrates the importance of GCP distribution. Within the imagery, the transformation outside the range of GCPs becomes one of extrapolation rather than interpolation, and with increasing order of polynomial extrapolation errors can escalate severely. Extrapolation errors can therefore be limited by ensuring GCPs are distributed evenly, reaching into the extreme edges of the imagery.

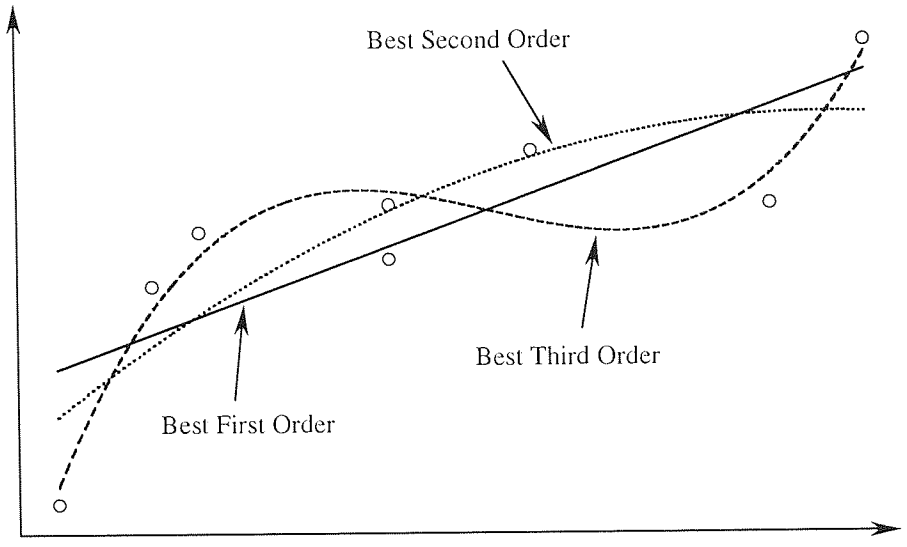

Figure 4.4 First, second and third order curves fitted to data points.

Once the desired transformation polynomial has been selected, the coefficients must be estimated from the GCPs. The accuracy with which GCPs are selected directly influences the accuracy with which the imagery can be corrected, and precautions must be taken to minimise unnecessary errors. Co-ordinates for GCPs should be measured from a map with a suitable scale. Tobler (1988) suggested a relationship between the map scale and the precision with which an individual map feature may be extracted;

$$map\ precision\ (m) = \pm \frac{Smallest\ mark\ (mm) \times map\ scale}{1000} \qquad (4.4)$$

Assuming that the smallest mark which can be confidently measured on a 1:10,000 scale map is 0.25mm (Serpell, 1979), the precision with which a feature may be extracted from such a map is given by Equation 4.4 as ±2.5m. This represents a considerable error when compared to the scale of a typical airborne image, which at an altitude of 1000m would yield a pixel resolution in the order of 2m.

Once the GCPs have been selected, the coefficients for the mapping polynomials can then be calculated using least-squares regression. As more control points are added to the analysis, the number of degrees of freedom increases and the residual errors at each control point may become more significant. This is

another severe limitation of the polynomial transformation method in correcting airborne line scanner imagery. In trying to minimise the positional errors of GCPs, the regression procedure averages out local regions of distortion over the entire image, such that considerable residual errors can develop at the very points used to correct the imagery.

Despite the problems outlined above, the overriding criticism of the polynomial correction method is the basic inability of the transformation polynomial to accurately model the true nature and magnitude of image distortion. It was concluded in Section 2 that thermal inertia studies using daytime and dawn thermal image pairs require imagery which can be registered uniformly accurate to one pixel to allow cross-image analysis. However, experience has shown that whilst accuracies of this order are achievable for satellite-based imaging systems, aircraft imagery contains complex distortions which can not be accurately corrected by low order polynomials. Alternative methods of rectification are therefore required, and these are discussed in the following section.

4.3.1.3 Hybrid Methods of Non-Parametric Correction

The polynomial correction method has undergone a number of modifications to address some of the limitations described previously, and the following section describes the underlying principles behind these modifications.

Selection of GCPs

In order to improve the reliability and accuracy of GCP selection, a number of alternative methods have been proposed. Ton and Jain (1989) suggest desirable properties of region-based GCPs and describe potential points based on stability, extractability and frequency. Stability refers to the structure of the control points, which should remain consistent between the imagery. Extractability describes the ease with which a feature can be extracted using standard image processing techniques, whilst frequency refers to the number and distribution of control points throughout the imagery. In their study, Ton and Jain (1989) used water regions, oil and gas platforms and road intersections for automatic control point location in registering satellite imagery. Once GCPs were located, a simple affine transformation was applied giving a RMSE of approximately 0.5 pixels.

Medioni and Nevatia (1984) highlight the adverse effects of different imaging conditions (sun angle, environmental conditions, and seasonal effects) on the above method. However, Goshtaby *et al.* (1986) overcame these problems by employing a region-based technique using the centroids of closed boundaries for automatic location of GCPs. The benefits of this approach are that closed-boundary centroids remain

relatively stable in the presence of noise and different imaging conditions, thus enabling accurate location of GCPs. In their analyses, Goshtaby *et al.* (1986) achieved a RMSE of 0.98 pixels by using a bivariate, second order polynomial to correct satellite imagery.

Benny (1981) implemented a pattern matching routine to position GCPs between two similarly orientated satellite images. To describe GCPs, Benny used windows of 19×19 pixels containing well-defined spatial features, and stored these along with their true map co-ordinates in a reference database. For each additional image which required geometric correction, the reference GCPs were located in the imagery using digital correlation techniques. The approximate location of each GCP was initially predicted, and a search area defined as the number of pixels in each direction which the search window could 'roam'. At each search location the correlation coefficient was calculated and the most likely match was given by the point which had the highest correlation. The correlation function is defined as

$$CC = \frac{\left(\sum_{i=1}^{n}(x_i-\bar{x})(y_i-\bar{y})\right)}{\left(\sum_{i=1}^{n}(x_i-\bar{x})^2\sum_{i=1}^{n}(y_i-\bar{y})^2\right)^{1/2}} \qquad (4.5)$$

where x_i and y_i are the digital numbers (DNs) of the i'th pixel in the reference and search windows respectively, $\bar{x}$ and $\bar{y}$ are the average DNs contained in the reference and search windows respectively, and n is the number of pixels in each window. The numerical value of the correlation coefficient (CC) ranges from +1.0 indicating a perfect correlation, to −1.0 indicating one pattern is the negative of the other. The problems of varying atmospheric conditions are largely removed by the inclusion of the average DN terms, as the correlation function calculates similarity based on the relative brightness about the mean. Benny (1981) demonstrated that well over 90% of all GCPs were correctly recognised, reducing human input from 80 man-hours to 20 minutes.

Piecewise Polynomial Approaches

Whilst globally defined transformations may fail to account for the complex, local distortions found within airborne imagery, simple linear transformations may suffice provided the imagery is first partitioned into sub-regions on a scale finer than the distortions. Piecewise polynomial approaches use information about local geometric distortion to register local areas of the image, and not to register all image areas identically. These techniques treat image correction as a surface fitting problem, and as such characterise local geometric distortion between the imagery.

The first stage of the correction process is to identify GCPs in a fashion similar to the conventional polynomial mapping procedure. Once a sufficiently dense network of GCPs have been selected, the image is partitioned using a Delaunay tessellation. The Delaunay tessellation is significant since it ensures that the same triangular tessellation will be found for a given data set regardless of the ordering of GCPs (see McCullagh and Ross, 1980). Furthermore, it has the desirable property of creating triangles which tend to be equilateral, which is advantageous for subsequent resampling. A separate linear transformation is then applied within each triangle, such that the mapping along common boundaries agree. Using this method, GCPs act as absolute ties ensuring registration is exact at the vertices. Misregistration in the interiors of the triangles decreases as more GCPs are used making the triangles smaller.

White *et al.* (1990) used this technique to register airborne imagery, using 31 GCPs for a 512×512 pixel scene. They obtained a RMSE of approximately 1 pixel, which was significantly better than the RMSE of 2.8 obtained using the conventional polynomial correction. It is important to note that since GCPs are exact ties they can not be used to calculate RMSE, and consequently independent checkpoints must be located. Devereux *et al.* (1990) used an identical approach to White *et al.*, and recorded a RMSE in the region of 2.4 pixels, compared to 4.4 pixels for the conventional polynomial correction. Goshtaby (1988) describes a similar approach which was applied to satellite imagery, where a RMSE of 0.43 pixels was achieved.

Craig and Green (1987) stress the need for a dense network of GCPs in regions containing considerable distortions, and describe a technique to semi-automatically select control points. Chen and Rau (1993) also developed a technique to automatically locate GCPs using an ortho-photo of the region as a reference on which to base image registration. Using 80 registration control points located in the imagery they achieved image-to-image registration accuracies of around 0.67 pixels, which is considerably better than that achievable using conventional polynomial methods. However, the accuracy of these piecewise polynomial approaches is directly proportional to the number of GCPs used in the correction, and as such, imagery where GCPs are far less abundant can not be corrected with such a high level of accuracy.

Multiquadric Rectification Technique

The multiquadric function was first proposed by Hardy (1971) for interpolation of irregular surfaces, and was later developed for image correction of remotely sensed data (Gopfert, 1982). The first stage of the procedure is to perform the standard polynomial correction described in Section 4.3.1. The residual errors occurring in the corrected image are then 'attached' to the GCPs in the raw image, so that every GCP yields an exact fit. The multiquadric method interpolates transformation vectors for every pixel based on the GCP improvements in the pre-rectified image. These vectors are distance weighted ensuring local regions of distortion do not influence the transformation in other parts of the imagery. This technique describes a continuous interpolation function whereby all GCPs contribute to the transformation. Again GCPs yield an exact fit, so accuracy must be assessed through the use of checkpoints.

Ehlers (1994) applied the multiquadric technique to correct airborne line scanner imagery and achieved a RMSE of 2.9 pixels using 83 GCPs. This is a vast improvement on the level of accuracy provided using conventional polynomial mapping approaches, which gave RMSEs of 30.4, 14.7 and 9.4 pixels for first, second and third order polynomials respectively. McGwire (1998) also used the multiquadric technique to mosaic imagery acquired from five different flight lines and obtained an overall RMSE of approximately 6 pixels, which compared to almost 12 pixels for the conventional polynomial correction.

The advantages of the multiquadric technique over the piecewise polynomial approach are that a single mathematical relationship exists to correct the image geometry, rather than a number of relationships which work independently in different parts of the imagery. Furthermore, because the piecewise polynomial approach splits the image into a series of segments, difficulties arise in the transition from one segment to another as both sub-images are treated independently. Although the overall geometric accuracy using both of these methods is significantly higher than the conventional polynomial approach, both methods rely on the collection of a considerable number of GCPs. Whilst automatic location of GCPs using feature-based pattern matching may improve the speed and reliability of selection, the number of GCPs required to provide acceptable levels of accuracy may not always be available.

4.3.2 Parametric Approaches

The methods of parametric correction of line-scanner imagery developed from photogrammetry and use the principles of projective geometry and the collinearity equations which arise from them (Ghosh, 1988). Central to photogrammetry are the concepts of interior and exterior orientation. Interior orientation refers to the internal characteristics of the lens system, whilst exterior orientation refers to the position and attitude of the sensor platform. Six parameters are used to define the exterior orientation of the sensing platform at any given moment in time. The attitude parameters were discussed in Section 4.2.2 and include roll, pitch and yaw. The remaining parameters define the three-dimensional co-ordinates of the sensor platform in space, which allow the image geometry to be tied into a set of real ground co-ordinates.

For a two-dimensional aerial photograph, the exterior orientation of the sensing platform can be used to correct the image geometry (see Hallert 1960, for a review of photogrammetric techniques). However, due to the temporal nature of line-scanning instruments, the exterior orientation of the sensing platform continually varies throughout the imagery. For pushbroom sensors the exterior orientation fluctuates for each individual scan line, whilst whiskbroom scanners suffer variations in orientation, albeit by a small amount, for every pixel in the imagery.

4.3.2.1 Space Resection to Determine Exterior Orientation

Space resection techniques, as applied to aerial photography, can be used to determine the orientation of the camera platform by locating three GCPs within the imagery. The three dimensional positions of each GCP are used to calculate the exterior orientation parameters for the sensor platform. Parametric correction techniques for line-scanned imagery have been developed using space-resection approaches by assuming exterior orientation parameters vary smoothly with respect to time. GCPs selected within the imagery are used to calculate the exterior orientation of the sensor platform at regular intervals. A smooth curve can then fitted to the platform attitude data allowing the exterior orientation to be estimated throughout the whole flight line. With the modelled exterior orientation parameters as input, the earth-based co-ordinates for each pixel in the imagery can finally be calculated using projective geometry.

Baker *et al.* (1975) and Konecny (1976) both used polynomial equations to model the exterior orientation, whilst Gee (1988) fitted a cubic spline to the data. However, the major drawback with this approach is that aircraft attitude may be subject to rapid variations caused by atmospheric turbulence, and therefore, the exterior orientation data inferred using space-resection techniques can not always model the true orientation accurately.

4.3.2.2 Inertial Navigation Systems

Rather than using space resection techniques to calculate exterior orientation parameters they can be measured directly by instruments onboard the aircraft. This approach is more attractive than other methods due to the reduced reliance on GCPs and the potential for full automation.

Inertial navigation systems (INS) have been used to record the exterior attitude and body accelerations of an aircraft as it moves through space (Gibson *et al.*, 1987). Roy *et al.* (1997) describe such a system to parametrically correct airborne line scanner imagery, and developed a technique to correct the imagery using the navigation data alone. Although inertial systems do not measure the absolute position of the aircraft, this information was estimated from the acceleration and velocity data. Whilst the high frequency distortions relating to platform attitude were successfully removed, the imagery was distorted in a curvilinear manner in the along track direction, causing errors in the order of hundreds of metres. This distortion was attributed to propagating errors in the sensor position computation, and to overcome these problems a secondary polynomial correction was applied which reduced errors to no greater than 10 pixels.

Zhang *et al.* (1994) describe a technique where platform attitude data was recorded along with aircraft latitude and longitude measurements for the correction of airborne line scanned imagery. They removed the high-frequency distortions resulting from variations in platform attitude and projected each scan line onto a temporary grid system. The image was finally tied into a map co-ordinate system using polynomial mapping procedures. After integrating a digital terrain model (DTM) of the region into their model they obtained an overall RMSE of approximately 2-3 pixels. Zhang *et al.* conclude that an accuracy better than two pixels is difficult to achieve due to the limitations in the resolution of flight parameters. Errors in the DTM and the polynomial correction were also identified as minor causes of error, but despite these it was suggested that an accuracy of better than 3 pixels was quite achievable.

4.3.2.3 GPS Navigation Systems

The concept of using differential GPS navigation data to rectify airborne line scanner imagery is relatively new, and relies on the synchronous measurement of platform attitude parameters throughout a flight line. Wilson (1994) describes the implementation of a GPS system onboard the aircraft operated by the Natural Environment Research Council (NERC). The system consists of four separate antennae, which form a rigid cruciform shape on the aircraft roof. This arrangement provides measurements of both absolute position and aircraft attitude throughout a flightline enabling the imagery to be corrected using projective geometry. Wilson (1994) claims that the platform attitude can be resolved to an accuracy better than

1mrad, which at an altitude of 1000m would result in a ground accuracy of approximately 1.5m at the nadir.

However, since the NERC system was made available to the academic community, a number of problems have arisen which have severely limited the ability to produce geometrically corrected imagery. The main problems relate to the occurrence of what are termed 'jumps' in the GPS navigation data. Jumps occur when the aircraft GPS system fails to lock on at the start of a flight line, or when there are an insufficient number of GPS satellites in the sky during a flight. Although measures are currently ongoing to address these problems and deliver imagery with GPS correction capabilities, there is currently no published information describing the actual geometric accuracy achievable using this technique.

4.3.2.4 Combined GPS and INS

Despite the problems encountered with the NERC GPS facility, differential GPS has the potential to offer precise platform positional information, irrespective of its failure to provide fully synchronous attitude data. Roy *et al.* (1997) highlight the potential advantages of integrating both GPS and INS, enabling platform attitude data from inertial systems to be supplemented with positional data provided by the GPS facility. Indeed, Wilson (1999) recognised the potential benefits of integrating GPS positional information with INS data and developed a new system to address some of the problems previously encountered when using GPS data alone. Wilson describes the synergistic use of GPS and INS data, which combine the best characteristics of each (absolute measurements of GPS and high data rates of INS), whilst eliminating their current weaknesses (slow measurement rates of GPS and drift of time integrated values of INS data). By using this combination of methods the sensor position and attitude can be accurately fixed enabling each scan line to be projected onto its exact ground position.

Some of the first results to emerge since the implementation of these GPS/INS correction facilities have been published by Wewel *et al.* (1999), who describe a multiple-line pushbroom scanner providing high resolution stereo digital imagery. The system offers nine CCD arrays - five of which are panchromatic arranged at specific viewing angles providing multiple stereo capabilities, whilst the remaining four enable the acquisition of multispectral images. Wewel *et al.* claim that exterior orientation parameters can be determined with an accuracy of ± 2.2cm for position, ± 0.0004° for roll and pitch, and ± 0.008° for heading (yaw). Test flights were carried out at an altitude of 3000m giving a ground resolution of 15cm for the nadir channel and 30cm for the remaining channels. The mean absolute accuracy determined from 120 checkpoints was ± 23cm, corresponding to vertical and horizontal accuracies of ±18cm and ±13cm respectively.

4.3.2.5 Critique

Parametric methods offer potentially far more accurate means of correcting image geometry than non-parametric methods as they enable the true nature of image distortions to be modelled. The combined use of GPS and INS positional information appears to offer the most attractive solution to geometric correction due to the high precision available and the potential for full automation. However, GPS/INS technology is still relatively new and vast archives of historical data exist which remains uncorrected. Current methods of correction are still unable to accurately correct and register historical image data, rendering these data sets inadequate for quantitative temporal studies.

4.4 Ortho-Rectification of Aerial Photography

Aerial photography is the oldest and most frequently used remote sensing instrument, and has been used for a wide range of landuse and mapping applications. An orthophotograph is defined as a vertical photograph showing images of objects in their true orthographic position, and as such, is geometrically equivalent to conventional linear planimetric maps (Colwell, 1983). The vast majority of aerial photography is recorded using photographic film, and hence the output is generally analogue in nature. However, the primary drawback of analogue aerial photography is the limited spectral coverage, which gives rise to a trade-off between the high geometric fidelity of aerial photography and the broad spectral capabilities of digital line-scanned imagery. However, with the development of CCD technology, new photographic devices are emerging which use large arrays of CCDs to measure and record the spectral response in wider spectral bands. These provide a source of digital data with far greater fidelity than line-scanning instruments. However, despite the advantages offered by digital photographic systems the academic community has currently not adopted the widespread use of digital photography - the NERC airborne remote sensing system operates a number of line-scanning instruments accompanied by analogue stereo colour photography.

Although aerial photographs represent an instantaneous 'snap-shot' of the earth, platform attitude effects can still significantly affect the geometry of the imagery. Furthermore, the effects of surface relief were demonstrated in Section 4.2.2, where radial distortions at the extremes of the imagery can be as great as *0.9×terrain height*. Photogrammetric techniques such as resection and projective geometry enable the camera view-angle effects to be largely removed. Furthermore, if the aerial photography is acquired in stereo, or a digital elevation model (DEM) of the corresponding region exists, surface relief effects can also be removed from the imagery. Many image processing packages offer the ability to ortho-rectify

aerial photography, and although it is not the intention to discuss the principles behind the rectification process here, it is useful to consider the capabilities of such techniques. For a description of ortho-rectification of aerial photography see Hallert (1960) or the American Society of Photogrammetry (1960).

The accuracy with which aerial photography can be ortho-rectified depends on a number of factors. The accuracy with which the exterior orientation parameters can be determined will directly influence the accuracy of rectification. Furthermore, the quality and resolution of the DEM is also important when rectifying aerial photography. Since terrain effects can result in errors up to $0.9 \times feature\ height$ in the extremes of the image, errors in the DEM will also result in distortions of $\pm 0.9 \times DEM\ error$.

4.5 Accuracy Assessment

Very little current literature is directed towards the assessment of geometric accuracy in remotely sensed imagery. The standard method of describing geometric accuracy is by calculating the RMSE of positional differences between the actual and predicted location of control points located in the imagery. RMSE is calculated as;

$$RMSE = \sqrt{\left(\frac{1}{n}\sum_{i=1}^{n}\sigma_i^2\right)} \qquad (4.6)$$

where n is the number of GCPs and σ_i is the Pythagorean distance between the estimated and actual position of each control point. The RMSE is a standard statistical measure of the ability of the mapping polynomial to transform image pixel addresses to map co-ordinates, and as such is often cited as a measure of geometric accuracy for the entire image. If the RMSE is small, the positional difference between the actual and predicted GCP locations is small, and hence the image is considered relatively accurate. An increase in RMSE indicates greater positional differences at GCPs, which reflects a decrease in geometric accuracy.

McGwire (1996) warns of the dangers of using GCPs for accuracy assessment. Since GCPs are not independent from the transformation coefficients, the RMSE will under-predict the actual error found elsewhere in the image when the number of GCPs is small. McGwire (1996) found that the RMSE calculated from 20 GCPs based on second order transformation residuals under-predicted the actual error by 40%. McGwire (1996) describes the idealised relationship between actual and predicted error for increasing numbers of GCPs, which is illustrated in Figure 4.5.

When considering a first order polynomial transformation, there are six unknown coefficients each requiring three GCPs for mathematical solution. If only three GCPs are used in the correction, the polynomials will yield a perfect fit and the RMSE will be zero. As more GCPs are added to the analysis, the number of degrees of freedom increases and local regions of distortion influence the calculation of coefficients for the entire imagery. The RMSE will consequently experience an increase as the residual errors at GCPs increase, indicating a deterioration in geometric accuracy. However, since more GCPs have been used to calculate the coefficients the mapping polynomials are theoretically more representative of the actual image distortions, and as such, the resulting correction should be more accurate.

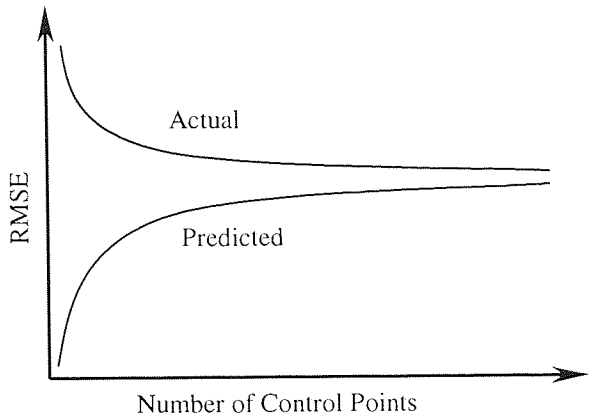

Figure 4.5 Idealised curves of estimated and actual RMSE.

This increase in RMSE with the addition of GCPs has led some authors to remove problematic GCPs in an attempt to improve the accuracy of the geometric correction (Sunar and Kaya, 1996). Whilst the removal of GCPs may make the procedure appear more accurate, the actual consequence is one of reducing the overall reliability of the correction since the mapping polynomials are less representative of the true pattern of distortions.

An alternative method of assessing the accuracy involves the use of checkpoints, since these are independent from the transformation coefficients. However, very frequently the most suitable GCPs have been used to perform the correction and additional reliable checkpoints are difficult to locate in the imagery. McGwire (1996) describes the so-called cross-validation technique to measure geometric accuracy. Rather than simply taking the residuals of a single transformation, the cross-validated RMSE is calculated by removing the first GCP from the pool and calculating the geometric transformation using the remaining GCPs. This transformation is then applied to the first GCP and the positional residual determined. The first GCP is then replaced in the pool, and the process is applied iteratively to each GCP in the entire set. The residuals calculated for each transformation are then used for the overall RMSE calculation, providing the cross-validated RMSE.

McGwire (1996) found that whilst the standard RMSE calculated using transformation residuals greatly under-predicted the actual error for small numbers of GCPs, the cross-validation method greatly over-predicted the error. It was found however, that with increasing numbers of GCPs the cross-validation

approach converged towards the actual error, whilst the standard RMSE still underestimated the error by 15 - 25%. The actual error was given by calculating the RMSE for the residuals of random checkpoints selected throughout the imagery.

Estimating the geometric error for an entire image from a small set of GCPs is clearly not a simple, reliable task. The RMSE calculated using transformation residuals significantly underestimates actual error within the imagery, whilst the cross-validation method greatly over-predicts the error when the number of GCPs is small. Both methods converge towards a limiting value for increasing numbers of GCPs, although standard RMSE estimates still under-predict the actual error by up to 40%. Whilst residuals calculated from random checkpoints within the imagery provide a relatively stable measure of accuracy, the difficulties in identifying reliable checkpoints independent from GCPs are often considerable.

White *et al.* (1990) identify the potential advantages of constructing map overlays or multi-temporal composite images to identify any mis-registration resulting from geometric errors. Although this approach provides a good qualitative description of the magnitude and location of image disparities, it does not provide an attractive quantitative measure of accuracy.

4.6 Summary

In recent years, considerable advancements in the processes of geometric correction have provided airborne imagery with far higher fidelity than has previously been available. Whilst polynomial approaches using GCPs are both time-consuming and inadequate for modelling the true nature of image distortions, parametric techniques offer the potential to fully automate a precise geometric correction. Recent literature suggests that image rectification using combined GPS and INS can provide geometric accuracies approaching 1 pixel (rms), which is a considerable improvement on conventional polynomial approaches.

However, these techniques fail to address the issue of historic data, which in the absence of navigation data can only be corrected using non-parametric techniques. These techniques generally rely on the collection of large numbers of GCPs, which can be time-consuming and difficult to locate. Digital correlation techniques offer the potential to semi-automate GCP collection, and using a variety of techniques enable imagery to be corrected with an accuracy approaching, in isolated cases, one pixel.

However, these approaches fail to provide geometric accuracies of this order when GCPs are less abundant, and RMSEs in the region of 2-3 pixels are more common.

Increasing numbers of applications require remotely sensed data to be overlaid with other geographical data sets. When comparing temporal image data, the issues of overlay accuracy and reliability are extremely important. Despite this fact, very little effort has been directed towards developing a suitable means of quantitatively assessing the accuracy with which multiple scenes may be overlaid. The current standard measure of accuracy, the RMSE, has been shown to under-estimate actual error by up to 40%. Furthermore, the RMSE neither tells the observer anything about where the errors actually occur, nor provides any information relating one image to another. The potential advantages of using map overlays to identify the magnitude and location of image disparities have been examined, but these approaches have so far only been able to offer qualitative indications of geometric error.

5. Development of Alternative Geometric Correction Procedure

The modified project aim defined in Chapter 1 identifies the requirement for developing an alternative method of geometrically correcting and registering airborne line-scanner imagery. Due to the lengthy delays in obtaining the NERC image data set, this aim forms the main component of the current study, and is the primary focus of discussion in the remaining chapters of this thesis. It is important to note that the ultimate project aim of examining widespread differential heating by comparing daytime and dawn thermal imagery has remained unchanged. Simply, the study has been orientated towards the geometric correction of image data due to the lack of reliable, correctable imagery from the NERC airborne remote sensing system. The present chapter describes the development of the hypothesis used to explore alternative approaches for rectifying airborne line-scanned imagery, and draws on a number of important issues raised in the previous chapters.

5.1 Theoretical Considerations

Chapter 2 investigated the main approaches commonly used to interpret thermal remotely sensed imagery over the earth's surface. In line with the original aim of the project, it was found that relatively few investigations have been carried out examining the temporal aspects of airborne thermal remote sensing. Airborne imaging systems offer significant spatial and temporal resolution advantages compared with satellite-based systems, and therefore provide a valuable tool for monitoring thermal activity at the regional scale. However, the considerable geometric distortions associated with airborne platforms, and the current lack of reliable methods for compensating for these errors, has meant that the potential of temporal thermal imagery has remained largely undeveloped.

Chapter 4 examined a number of techniques for rectifying airborne remotely sensed imagery. The fundamental problems associated with the geometric correction of line-scanned imagery stem from the ephemeral nature of the platform attitude throughout a flight line. When the platform is subject to attitude perturbations, the sensor's view angle changes with respect to the underlying scene, creating distortions in the resulting imagery. The nature of these distortions are characterised by the type of platform movement (roll, pitch and yaw), and these are illustrated in Chapter 4.

Standard non-parametric techniques for correcting line-scanned imagery are unable to reconstruct the image geometry to a satisfactory degree of accuracy (Section 4.3.1). This is due to the least-squares regression analysis used to minimise positional differences at ground control points (GCPs) when determining the transformation coefficients. In minimising these positional errors, the regression procedure averages out local regions of distortion over the entire image, such that significant residual errors can develop at the very points used to correct the imagery. Whilst the geometry of the resulting imagery may broadly reflect the region under study, the image data may often still possess the high frequency distortions associated with variations in platform attitude.

It is acknowledged in Chapter 4 that the essence of a successful method of geometric correction is the ability to recognise and compensate for platform attitude effects. Current parametric approaches for correcting airborne line-scanned imagery require the sensor's exterior orientation parameters to be recorded simultaneously with the image data, such that the geometry can be corrected *post priori* using the principles of projective geometry. With advances in remote sensing technology, parametric approaches for image rectification are sure to become a reliable, automated procedure in the future. However, this approach does not address the issue of historic data, which have no associated navigation information.

In order to complement the emerging parametric approaches of image correction, it would be valuable to develop an alternative technique for rectifying and registering airborne line-scanned imagery, which can be applied to historic data sets without the need for platform attitude data. This would open vast archives of image data, such that historic imagery could be registered and directly compared with recent imagery, providing an extra dimension to airborne remote sensing. Furthermore, such a technique would demonstrate value in circumstances such as those experienced during this project, whereby emerging technology has failed to provide a suitable solution to the problems of image rectification. Without an alternative technique for correcting the image geometry, the data acquired for the current project would be rendered unusable for quantitative temporal studies.

Accompanying line-scanned digital imagery, many airborne remote sensing surveys acquire stereo colour photography to provide contextual information about the underlying scene, and the ability to map the terrain elevation. Section 4.4 describes the process of ortho-rectification of aerial photography, and these well-established photogrammetric techniques enable the effects of terrain and platform orientation to be largely removed from the imagery. Since aerial photography represents a 'snapshot' in time, platform attitude errors are not ephemeral in nature, and the resulting imagery does not suffer the localised distortions which cause such severe problems in the line-scanned digital imagery. This creates a

dichotomy between the relative geometric fidelity of aerial photography and the greater spectral capabilities offered by digital line-scanned systems.

5.2 Development of Approach

The key stage in developing a methodology for rectifying airborne line-scanner imagery is the identification of image distortions – in particular, those associated with variations in platform attitude. Consider an aerial photograph whose geometry has been corrected using a standard polynomial correction, and compare this with an airborne line-scanned image which has been similarly rectified using identical ground control points. Although the line-scanned image may broadly reflect the same geographical region as the corresponding aerial photograph, the polynomial correction is inherently unable to remove the high frequency distortions caused by perturbations in platform attitude. The differences in geometry between the two images therefore represent the effects of platform attitude on the line-scanned image (Figure 5.1). If these differences could be quantitatively identified, a methodology would exist whereby the effects of variations in platform attitude can be determined, and hence compensated for, without the need for platform attitude data. Since the sensor used to record the imagery for this project was a whiskbroom scanner, the geometry theoretically varies for every pixel comprising the imagery. The term *quantitative identification* refers to this unique, two-dimensional positional transformation associating each pixel in the line-scanned imagery with its counterpart in the aerial photography.

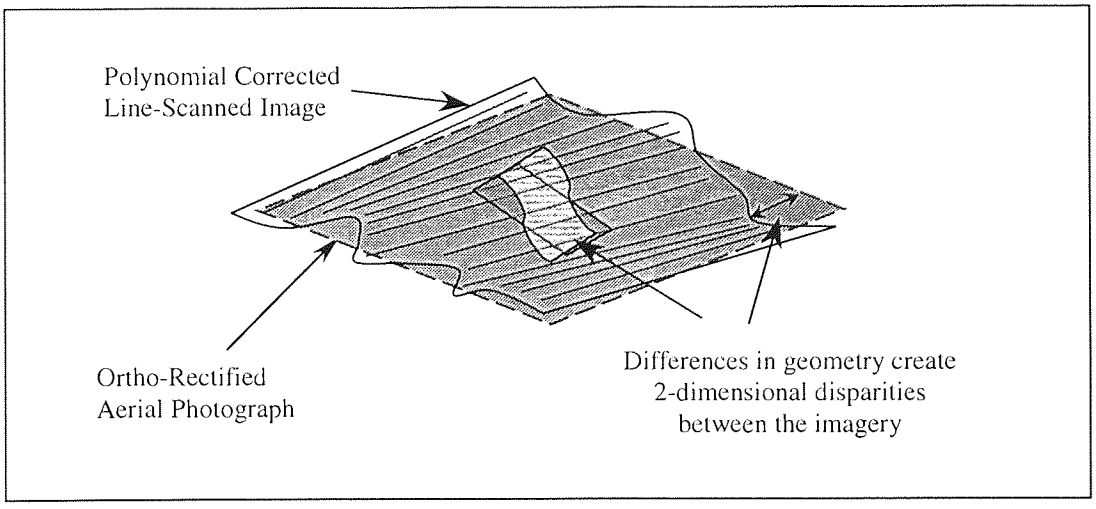

Figure 5.1 Sketch of differences in geometry between corrected aerial photography and ATM imagery.

The main reason for subjecting the imagery to an initial polynomial correction is to remove the effects of deterministic errors, such that the only geometric differences between the imagery are those resulting from variations in platform attitude. This is a useful assumption since for a given pixel, the number of degrees of freedom which define its geometry have effectively been reduced to two, i.e. the two-dimensional transformation mapping each pixel in the line-scanned image onto its counterpart in the corrected aerial photograph.

5.3 Scan Line Geometry

Very often, platform attitude errors can be identified qualitatively simply by examining the image geometry, where it is common to find linear features distorted in a curvilinear fashion. Figure 5.2 illustrates a practical example of this, which displays a section of raw ATM imagery extracted from the Black Country data set. The important aspects to note from Figure 5.2 are the grossly distorted features in the centre of the imagery, and the localised nature of these errors. The pixel resolution here is approximately 1.5m, so the illustrated distortions represent actual ground errors approaching 10m.

Whilst these errors are often easily identifiable within the imagery, defining them quantitatively without platform attitude data presents no trivial problem. The aircraft attitude is subject to six degrees of freedom; three parameters describing the attitude at any point in time, and the three-dimensional co-ordinates of the aircraft position. These, together with the effects of surface relief, combine to form extremely complex distortions within the imagery.

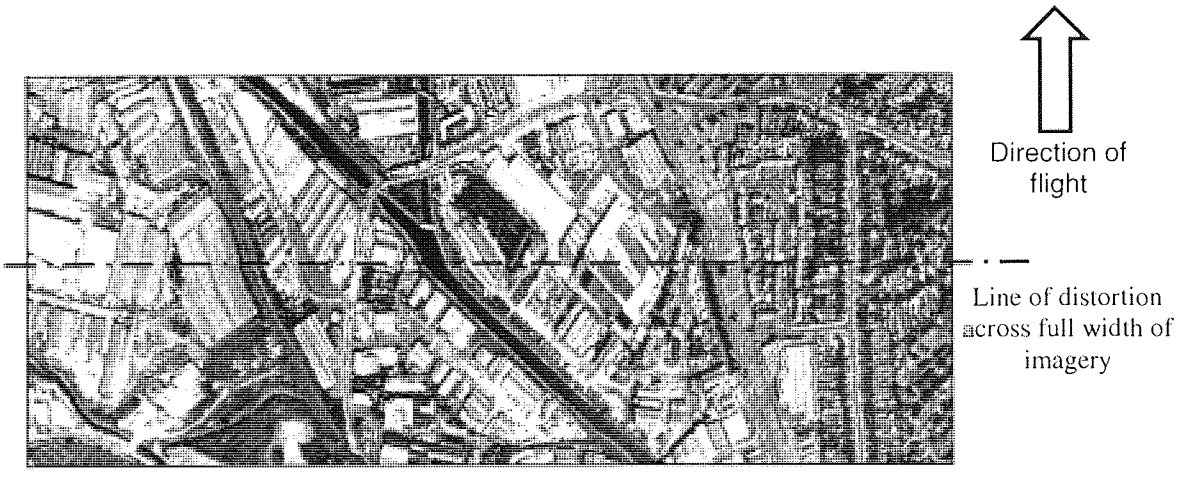

Figure 5.2 Platform attitude errors found within raw ATM imagery.

However, closer inspection of Figure 5.2 reveals a number of interesting points. It can be seen how the image distortions extend across the full width of the image, that is, normal to the direction of flight. Since the sensor used to record this imagery was a whiskbroom sensor, the geometry theoretically varies for every pixel in the imagery. It can also be seen from Figure 5.2 that the variation in geometry along a given scan line is not significant, as suggested by the consistency of distortions across the width of the image. This linear nature is an artefact of the high scan frequency of the ATM sensor, and allows each scan line drawn from the imagery to be regarded as straight, and without significant variation in geometry along its length. Accordingly, the raw ATM image data can then be considered as a series of straight, independent, contiguous scan lines, similar in geometry to that acquired using a pushbroom sensor. Pushbroom sensors consist of a linear array of sensor elements giving rise to entirely straight scan lines.

The assumption that scan lines acquired using whiskbroom sensors can be regarded as straight has important implications when attempting to identify platform attitude errors in the imagery. Rather than requiring a unique transformation for every single pixel in the imagery, scan lines can be regarded as rigid entities, and therefore only require knowledge of disparities at two positions to define the transformation for each pixel belonging to that scan line. The transformation for each pixel within a scan line can then be interpolated (or extrapolated) from these positions. For a typical line-scanned image consisting of 1,000 rows x 1,000 columns, the number of transformations that need to be calculated is therefore reduced from 1,000,000 (number of pixels in the image) to 2,000 (2 calculations per scan line).

Further assumptions can be made about the acquisition of line-scanned image data in order to reduce the amount of effort required to define geometric disparities. Because the scan rate of whiskbroom sensors is high relative to the rate at which the position of the aircraft platform varies, it is logical to assume that once the position of one scan line has been determined, the position of the next scan line is, by definition, very close to the first. This assumption leads to further significant reductions in the amount of effort required to quantitatively identify the geometric disparities between the aerial photography and the line-scanned imagery.

5.4 Sensor Geometry and Terrain Effects

Since the polynomial transformation used to align the two sets of imagery does not take into account the effects of terrain elevation, surface relief gives rise to an additional source of geometric error within the imagery. If the sensor characteristics were common to both remote sensing instruments, terrain distortions would be identical in each set of imagery. However, aerial photography and line-scanning sensors have significantly different characteristics, and the effects of surface relief create geometric disparities between the two sets of imagery. These are in addition to the disparities resulting from

variations in platform attitude, and therefore present problems when attempting to identify the effects of platform attitude by directly comparing the geometry of aerial photography and line-scanned imagery.

The fundamental differences between an aerial camera and a line-scanning instrument is that the camera captures a two-dimensional snapshot of the underlying scene, whilst the line-scanner builds up the image with a series of effectively one-dimensional scan lines. Aerial photography therefore suffers geometric distortions in two dimensions (across-track and along-track directions), whilst the line-scanned imagery contains distortions in the across-track direction alone. Figure 5.3 illustrates the effects of different sensor characteristics on the image geometry for a simulated terrain.

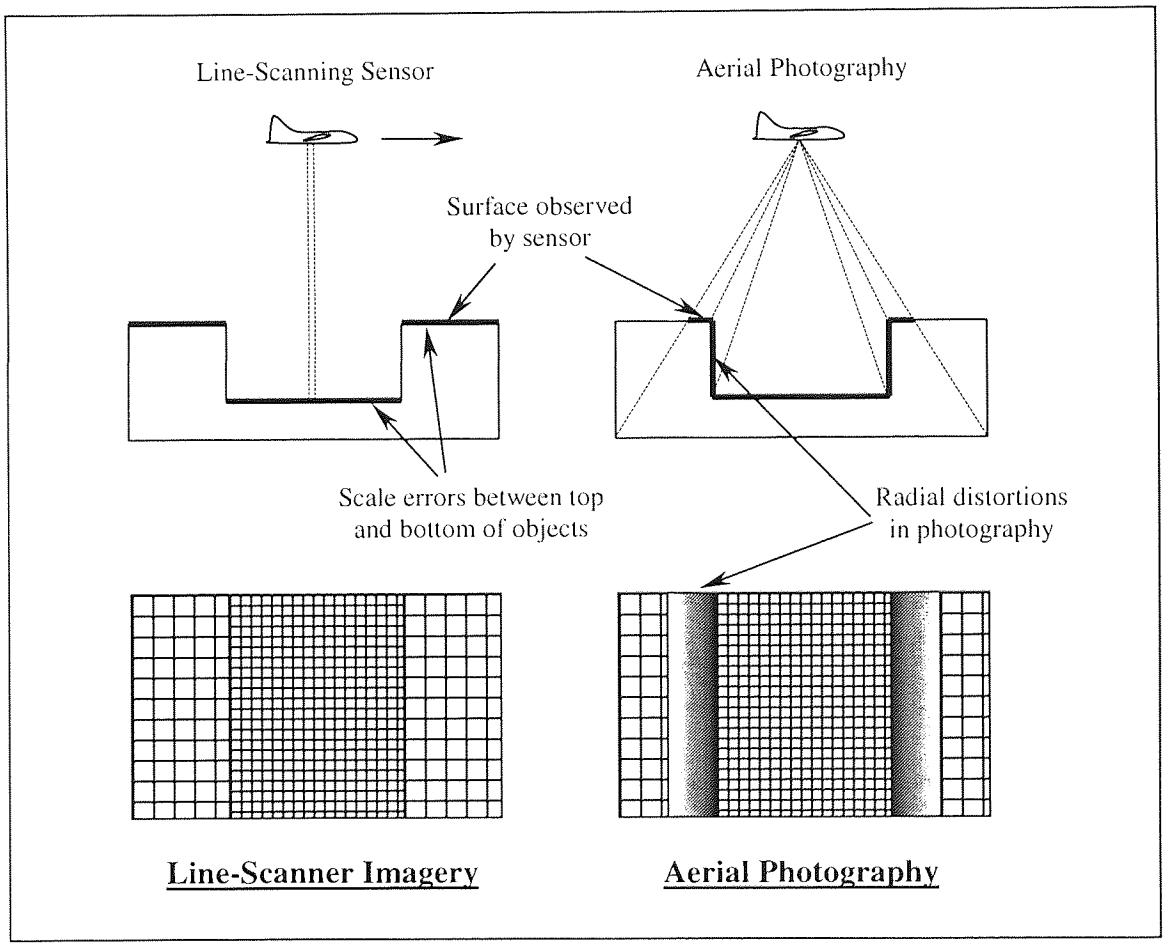

Figure 5.3 Effects of surface relief on imagery geometry for different sensors.

It can be seen from Figure 5.3 that changes in surface relief produce not only variations in scale, but radial distortions as well. Radial distortions are caused by differences in the relative height between the top and bottom of objects, and these become more pronounced with distance away from the nadir. However, it can be seen from Figure 5.3 that image distortions in the photography and line-scanned imagery are largely coincident in the across-track direction. The most significant differences occur in the along-track direction, where the aerial photography displays both scale and radial errors at the extremes of the imagery.

It is important to note that the diagram shown in Figure 5.3 demonstrates a grossly exaggerated scenario. In practice, the surface relief would rarely change as dramatically as shown, nor would the terrain height represent such a large proportion of the aircraft altitude. In order to limit these effects, good remote sensing practice suggests maintaining high altitude with respect to terrain elevation. Furthermore, since the effects of surface relief in the across-track direction are largely coincident between the aerial photography and ATM imagery, geometric disparities in the across-track direction can be attributed to variations in platform attitude. It is therefore suggested that surface relief does not unduly influence the reliability and accuracy with which platform attitude errors can be detected by comparing polynomial corrected aerial photography and line-scanned imagery.

5.5 Overview of Approach

The current chapter has so far described the principles by which the effects of variations in platform attitude can be identified within the line scanned imagery. However, it is necessary to discuss the overall methodology in using this information to rectify airborne image data. Figure 5.4 illustrates the main stages in this procedure.

In order to bring the scale and orientation of the image data into alignment, both sets of imagery must initially undergo a polynomial correction (Step 2 in Figure 5.4). Once the initial correction is carried out, any geometric disparities between the two images can be regarded as those occurring from variations in platform attitude during the acquisition of the line-scanned imagery.

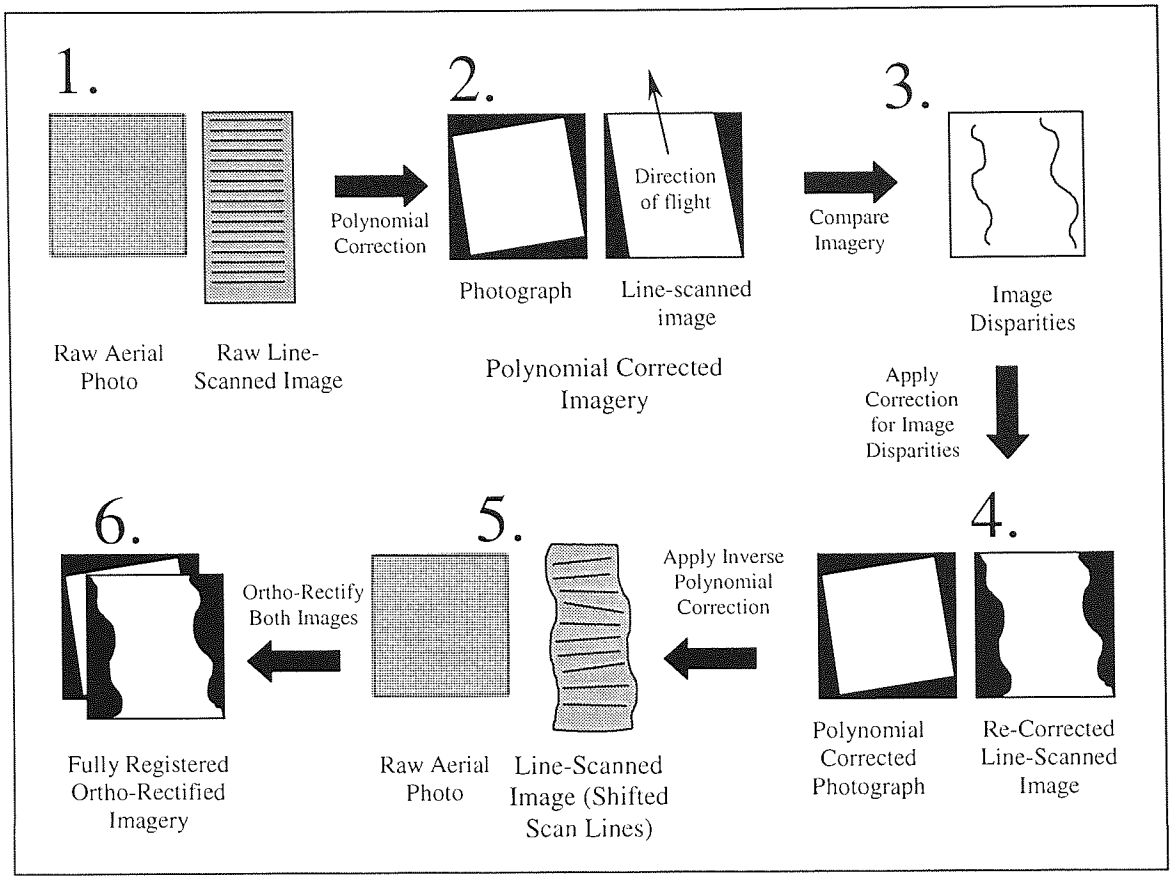

Figure 5.4 The main stages for rectifying airborne line-scanned imagery.

By exploiting the linear nature of scan lines, it is possible to identify how the geometry of polynomial corrected airborne line-scanned imagery differs to that of aerial photography simply by determining the two-dimensional positional disparities for two points along each scan line (Step 3). This disparity information is then used to reconstruct the line-scanned imagery using standard resampling techniques (Step 4), such that its geometry conforms to that of the aerial photography.

Once the two sets of imagery have been registered in this manner, the geometry of the line-scanned imagery corresponds to that of the aerial photography and any transformation which can be applied to the photography can now be reliably applied to the line-scanned imagery. The final processing stage is therefore to subject the line-scanned imagery and aerial photography to an ortho-rectification using standard image processing techniques (Steps 5 and 6).

6. Geometric Correction of Airborne Line-Scanner Imagery

Chapter 5 described the main theoretical considerations in developing a methodology for rectifying airborne line-scanner imagery. The approach exploits the geometric differences between airborne line-scanner imagery and simultaneously acquired aerial photography to identify errors resulting from variations in platform attitude. This information is then used to reconstruct the geometry of the line-scanned imagery such that it conforms to that of the aerial photography, therefore removing the influence of platform attitude errors. Section 6.1 describes the computer hardware and software used in applying the approach detailed in Chapter 5. Section 6.2 describes the main stages of this approach, and illustrates the application of the method on a test image acquired from the Black Country data set. The accuracy with which the line-scanned imagery can be corrected is also examined, and compared with current alternative geometric correction procedures.

Throughout the development of the approach, refinements to the methodology were continually made in order to improve the accuracy and reliability with which geometric disparities could be identified and corrected. The evolution of the methodology is described in Sections 6.3 and 6.4, where particular attention is paid to the accuracy and reliability of each approach.

Due to the lack of available imagery from the Black Brook data set, all of the work carried out in developing the techniques for rectifying the line-scanner imagery was carried out on image data from the Black Country data set. For the remaining chapters in this thesis, the terms airborne line-scanner, airborne thematic mapper, and ATM are used interchangeably to describe the sensor employed to acquire the test imagery over the Black Country data set.

6.1 Computer Hardware/Software

All of the data management and image processing for this research project was carried out on two computer systems – Unix SUN Sparc Workstations and a standard personal computer (PC). Data management was carried out using a package called the Geographic Resource Analysis Support System (GRASS) operating on the SUN Sparc workstations. GRASS is a fully integrated GIS/image processing application which facilitates a wide range of data manipulation techniques (Shapiro, 1993). GRASS offers considerable flexibility due to the freely available source code of image processing procedures, and the ability to build into the base software additional applications and tools. Furthermore, the raw image data is supplied by NERC in a format accessible by the Unix systems, so the use of GRASS as a data management tool was a natural choice.

However, advances in both hardware and software for PC-based systems means that PCs now offer processing capabilities comparable to those of Unix-based systems. A standard 200 MHz PC was therefore chosen to develop and implement the methodology for rectifying the line-scanner imagery. The computer language used was Turbo Pascal, which is a relatively straightforward high-level programming language operating under Windows 95. In addition to the GRASS GIS/image processing application, a PC-based image processor was also used in this study. IDRISI for Windows is a commercial application offering a wide range of GIS and image processing techniques (Eastman, 1995). However, IDRISI does not offer the same level of flexibility as GRASS, but the graphical user interface (GUI) is more intuitive and provided greater ease of use. In addition to IDRISI, a wide range of Windows-based shareware applications were used to manipulate and view image data.

Since the Unix and PC-based systems are not directly compatible, data transfer between the two systems was carried out using binary File Transfer Protocol (FTP). The combined use of both computer systems led to a highly flexible development environment, which aided the overall research project through exploitation of the respective strengths of each computer system.

6.2 End Correlation Method

The first stage of the procedure required the aerial photography and ATM imagery to undergo a polynomial correction in order to bring the scale and orientation into alignment. Once achieved, a program was developed in Turbo Pascal to determine the geometric disparities between the imagery based on a series of ground control points (GCPs) located at the ends of each scan line (hence the name End Correlation Method). After interpretation of the disparity data, the process for compensating for these distortions is described, and the results are illustrated and discussed. Finally, the End Correlation Method is reviewed and a number of refinements are suggested.

6.2.1 Polynomial Correction of Imagery

Figures 6.1 and 6.2 illustrate the raw imagery used in developing the rectification procedure. Whilst Chapter 3 describes the nature of the study area, it can be seen from the figures that the imagery consists of medium sized industrial buildings and densely packed residential properties. Since the aerial photography was originally acquired and stored on photographic film, it was necessary to digitally scan the photography for use with computer processing packages. This was carried out using an Epson GT-4000 colour scanner to a resolution of 200dpi.

Figure 6.1 Aerial photography over study area (reference data set).

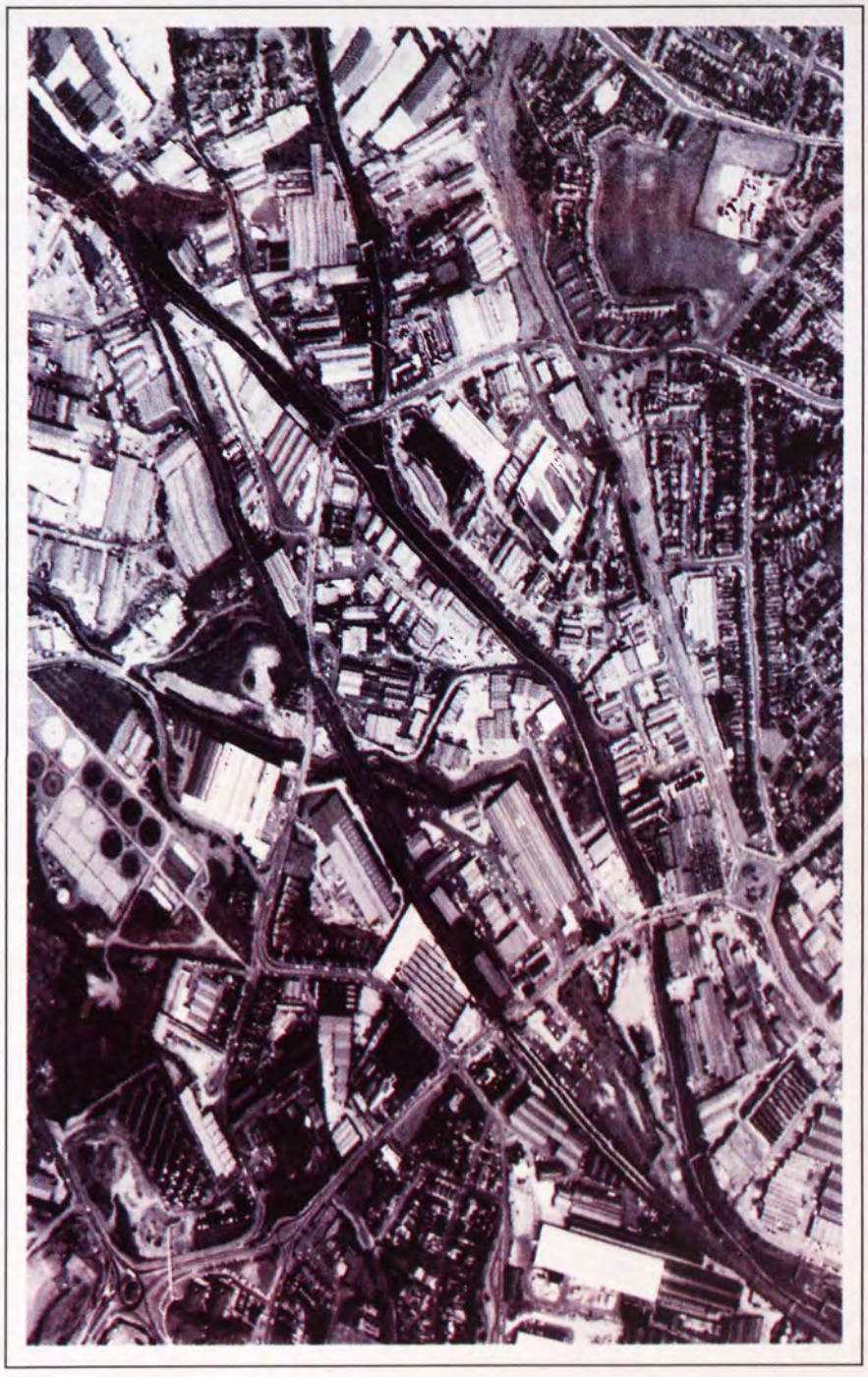

Figure 6.2 Raw ATM imagery over study area.

The polynomial correction was carried using GRASS, and due to the abundance of well-defined buildings and features within the imagery, identification of GCPs was a relatively straightforward process. In all, 13 GCPs were identified and these were distributed evenly throughout the imagery. It was decided to use a first order polynomial transformation to correct the imagery – since the correction technique relies on the linear nature of platform attitude errors (along the scan lines), it was felt that a high order polynomial might introduce non-linearities which would reduce the reliability with which platform attitude errors could be determined. Furthermore, high order transformation polynomials introduce extrapolation errors at the extremes of the corrected imagery, also reducing the overall reliability with which platform attitude errors can be determined.

Despite the desirable spread of GCPs used in the polynomial correction process, the RMSE error for the transformation polynomials were 14.3m for the aerial photography, and 12.1m for the ATM imagery. It was felt that these poor RMSE values were attributable to the low order polynomial used in the correction, and clearly demonstrate the basic inability of the polynomial approach to remove even deterministic errors. However, as described in the previous chapter, the End Correlation Method simply requires the scale and orientation of the imagery to be brought into alignment, and for this purpose, the accuracy achieved was sufficient. Figures 6.3 and 6.4 illustrate the corrected aerial photography and ATM imagery respectively.

It can be seen by comparing Figures 6.3 and 6.4 that considerable geometric disparities exist between the imagery. Of particular note is the line of distortion that runs across the ATM imagery in Figure 6.4, which distorts buildings and other features in a curvilinear manner. In verifying the overall success of the End Correlation Method, particular attention was paid to this feature.

Figure 6.3 Polynomial corrected aerial photography.

Figure 6.4 Polynomial corrected ATM imagery.

6.2.2 Quantitative Identification of Image Disparities

An approach was described in Chapter 5 to identify the nature and magnitude of image distortions simply by determining the disparities for two points on each scan line comprising the ATM imagery. The approach relies on the assumption that distortions along a given scan line are negligible, and this greatly reduces the number of calculations required to describe the geometry. However, even with these timesaving measures, the amount of time to manually determine the geometric disparities between the two sets of imagery would be unreasonably high. Therefore, it was proposed to automate the procedure by using digital pattern matching techniques.

6.2.2.1 Automatic Pattern Matching Techniques

Chapter 4 described a number of techniques which have been used to automatically identify GCPs between two similarly aligned sets of imagery. Of particular note was the approach employed by Benny (1981), who calculated the correlation coefficient between a reference window containing the pixel values for each GCP, and a search window drawn from the target image requiring rectification (see Section 4.3.1.3).

In developing an automated procedure for determining the disparities between two corresponding points in the aerial photography and ATM imagery, a similar approach to that of Benny was used. However, rather than storing a list of reference GCPs in a database, GCPs are dynamically drawn from the ATM imagery and matched to their corresponding location in the aerial photography. By performing this routine iteratively down each side of the imagery, an overall pattern of image distortions can be established.

The pattern matching function used to determine the correlation coefficient (defined in Equation 4.5) calculates similarity based on the relative brightness about the mean for each data window. This effectively standardises the range of pixel values and removes the problems associated with varying atmospheric conditions. In applying the automatic pattern matching algorithm to the remotely sensed image data, a routine was written in Turbo Pascal. The correlation function defined in Equation 4.5 can be re-written in the form:

$$CC = \frac{\left(N\sum_{i=1}^{n} x_i y_i - \sum_{i=1}^{n} x_i \sum_{i=1}^{n} y_i \right)}{\sqrt{\left(\left(N\sum_{i=1}^{n} x_i^2 - \left(\sum_{i=1}^{n} x_i \right)^2 \right) \left(N\sum_{i=1}^{n} y_i^2 - \left(\sum_{i=1}^{n} y_i \right)^2 \right) \right)}} \qquad (6.1)$$

where x_i and y_i are the pixel values in the reference and search windows respectively, and n is the number of pixels in each data window. Equation 6.1 offers a number of advantages over Equation 4.5 when calculating the correlation coefficient in an iterative procedure. Firstly, there is no need to pre-determine the average pixel values for a given data window since the $\overline{x}$ and $\overline{y}$ terms have disappeared. Secondly, all summations in Equation 6.1 contain only integer values which can be processed more rapidly than real numbers. Furthermore, since the term $\Sigma(x^2) - (\Sigma x)^2$ only contains values relating to the reference window, this term only needs to be calculated once for each reference window. Although these timesaving measures may appear trivial, they become very significant when iterated many thousands of times.

6.2.2.2 Application of Pattern Matching Technique to Image Data

Once the correlation routine was successfully coded, a further routine called *ENDCORR.PAS* was developed in order to apply the correlation function to the polynomial corrected imagery (Appendix 2 contains the complete source code for *ENDCORR.PAS*). However, a number of parameters which influence the performance of the correlation procedure had to be initialised before the program could be executed. These parameters govern the size of the reference window (in pixels), and the extent of the search area in which the correlation coefficient is calculated.

The size of the reference window is an important parameter and its choice is influenced by a number of factors. Since the correlation coefficient describes the similarity between two data windows, the windows need to be large enough in order to define a unique pattern, otherwise the correlation surface may suffer false peaks giving rise to miscorrelation and inaccurate disparity data. However, if the data windows are too large, the pattern may become too complex resulting in low correlation coefficients, again introducing the possibility of miscorrelation. The ideal choice for the size of window depends on the size of the features held within the imagery. If the features are generally small, then the size of the data window should be reduced, and conversely, if the features are large, the data window generally needs to be bigger. Furthermore, the overall size of the window should not be so large that the effects of platform attitude

errors significantly distort the features held within the window. This would again have the effect of reducing the correlation coefficient resulting in possible miscorrelation.

The extent of the search area is also an important parameter, and should be chosen to reflect the maximum disparities which are likely to be found within the imagery. If this parameter is set too low, it is impossible for the correlation routine to identify a 'correct' match. However, the computational burden of calculating the correlation coefficient increases exponentially with both size of data window and size of search area, so these parameters must be kept as small as possible without reducing the reliability of the method. By experimenting with a range of window and search area sizes for the test imagery, the optimum size for the data window was found to be 19×19 pixels, moving in a search area of ± 30 pixels.

The correlation routine was applied along two transects representing the ends of the scan lines down the sides of the polynomial corrected imagery. Whilst the transects can theoretically be positioned anywhere in the imagery, it is advantageous to place them towards the edges in order to reduce the extrapolation errors when calculating pixel disparities at the extremes of each scan line. However, it can be seen from Figures 6.3 and 6.4 that the polynomial correction has re-orientated the image data with respect to the grid co-ordinate system, so the transects were chosen to reflect the approximate direction of flight. These had to remain within the bounds of the image data for both the aerial photography and the line-scanned imagery and Figure 6.5 illustrates the location of the transects used for the correction procedure.

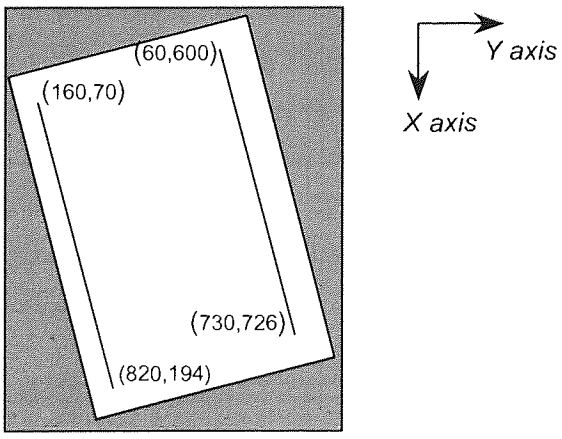

Figure 6.5 Location of the transects used in the End Correlation Method.

In applying the correlation routine to the test imagery, the reference kernel was positioned on each consecutive row along a transect, and the search kernel centred on the corresponding location in the photograph. The address of the maximum correlation found in the search area defined the 'correct' position of the reference kernel, and a record was written to an output file. The output file consisted of the pixel addresses of the centres of the reference kernel and optimum search kernel, along with the value of the correlation coefficient to indicate the reliability of the correlation. The correlation routine was then iterated for each scan line in the transect, enabling a picture to be built up of how the disparities varied from one scan line to the next.

6.2.2.3 Results for the End Correlation Method

Figure 6.6 illustrates the disparities found between the imagery. Disparities are defined as the difference between the row and column addresses in the ATM image and the corresponding location in the aerial photograph. It can be seen that despite a certain amount of noise in all of the graphs, a general trend can be observed throughout the disparity data. These results are pleasing, as they are indicative of the types of error associated with a smooth and undulating flight path during image acquisition.

However, in order to verify the disparity data was a true reflection of the actual image distortions it was necessary to carry out a manual check of the image distortions. A number of GCPs were selected from each transect and the precise pixel addresses were measured and compared with those determined using the correlation routine. Figure 6.6 illustrates these manually identified disparities (shown as red dots) superimposed on top of the disparity data obtained using the correlation routine. It can be seen that in the large majority of cases there is considerable correspondence between the two sets of data. Where the manually measured disparities fail to correspond with those determined using the pattern matching technique, it is clear that the routine suffered miscorrelations. These are an inevitable occurrence whose influence on the overall pattern of image disparities can be limited by selecting appropriate correlation parameters as discussed in Section 6.2.2.2.

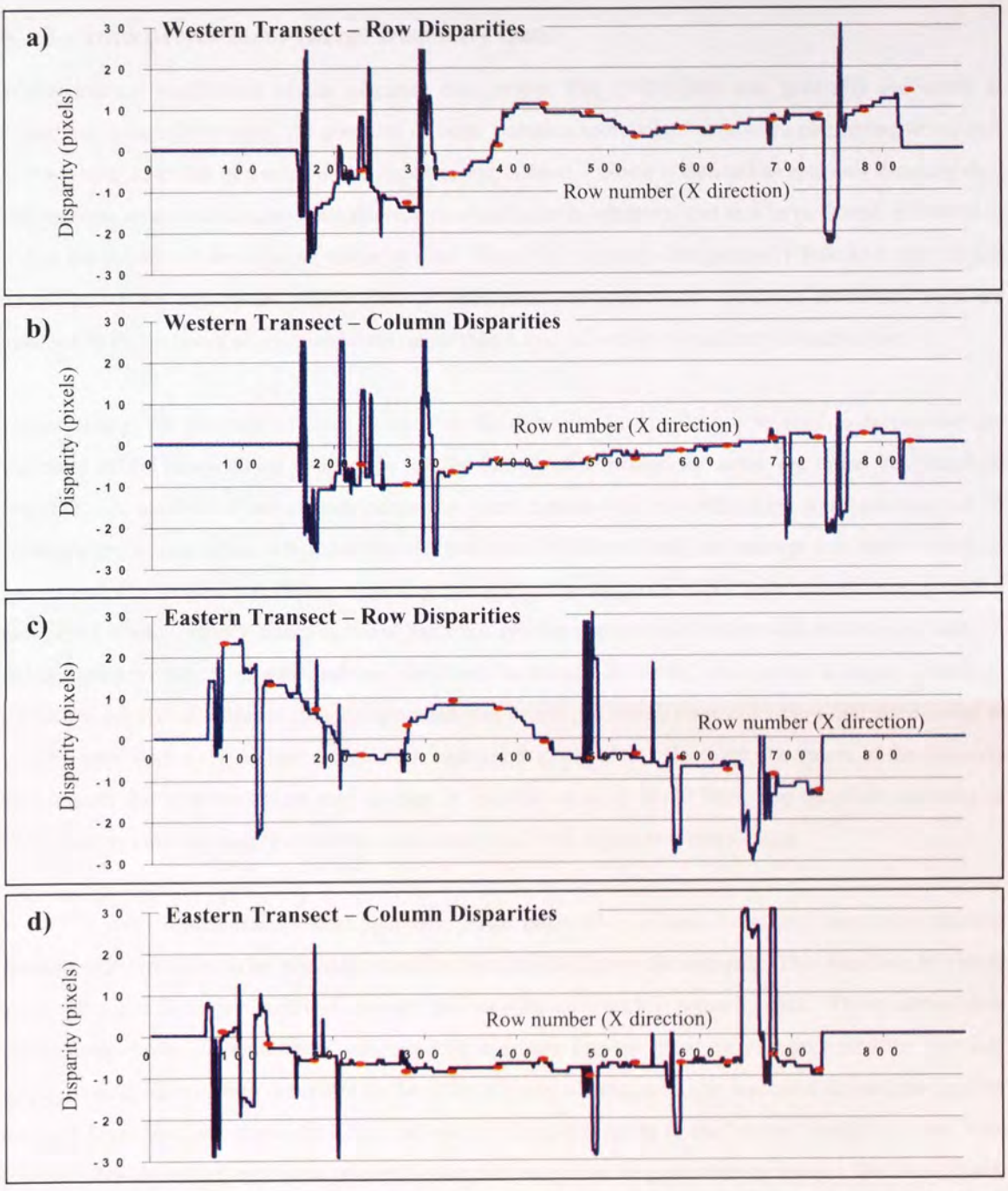

Figure 6.6 Disparities between the polynomial corrected aerial photography and ATM imagery. Blue line represents raw disparity data. Red points illustrate disparities verified manually.

6.2.3 Interpretation of Image Disparity Data

Whilst manual verification of the disparity data proves that *ENDCORR* was generally successful at identifying image distortions, the presence of noise becomes more significant when attempting to use this data to reconstruct the geometry of the line-scanned imagery. Noise is defined as spurious disparity data arising from miscorrelation between the reference and search windows, and to a large extent, is identified within the context of the adjacent disparity data. Since the disparity data generally follows a smooth and undulating trend, any values which show a rapid and 'uncharacteristic' deviance from this trend are assumed to be the result of miscorrelation rather than a true reflection of platform attitude errors.

Unfortunately, the presence of noise meant that the disparity data could not be used to reconstruct the geometry of the line-scanned imagery in its raw form, and a method for removing noise was therefore required. A number of automated techniques were considered, but difficulties were encountered in removing erroneous values whilst leaving the true data in place. Firstly, an attempt was made to reduce the influence of noise by applying a moving average to the disparity data. After experimenting with a number of window sizes it was concluded that although this approach did reduce the influence of noise, it did not preserve the 'true' data and was therefore discarded. Secondly, since noise is largely identified within the context of adjacent data, an approach was developed which removed values that were found to vary by more than a certain percentage from adjacent disparity data. However, the nature of the disparity data is such that miscorrelations tend to exist in 'blocks' of up to 30-40 lines, and therefore instances of noise were not always readily identified when compared with adjacent disparity data.

Finally, it was decided that the best approach would be to adopt a semi-automated procedure enabling areas of miscorrelation to be manually identified and removed from the analysis. This was done by fitting a smooth curve through a series of 'correct' points selected from the disparity data. These correct data points were chosen as regularly as was required to ensure that the fitted curve represented the 'correct' disparity data. Gee (1988) describes the benefits of using a cubic spline to represent aircraft movements during a flight line, and it was therefore decided to fit a cubic spline to the 'correct' disparity data. This approach has the advantage that a relatively complex curve can be generated by using a few data points, and Figure 6.7 illustrates the smoothed data superimposed on top of the original data. Since the correlation routine was not run for every row comprising the imagery (see Figure 6.5), it was necessary to extrapolate the smoothed data outside the bounds of the transects. It can be seen from Figure 6.7 that the smooth and undulating nature of the disparity data has been maintained whilst removing the influence of noise.

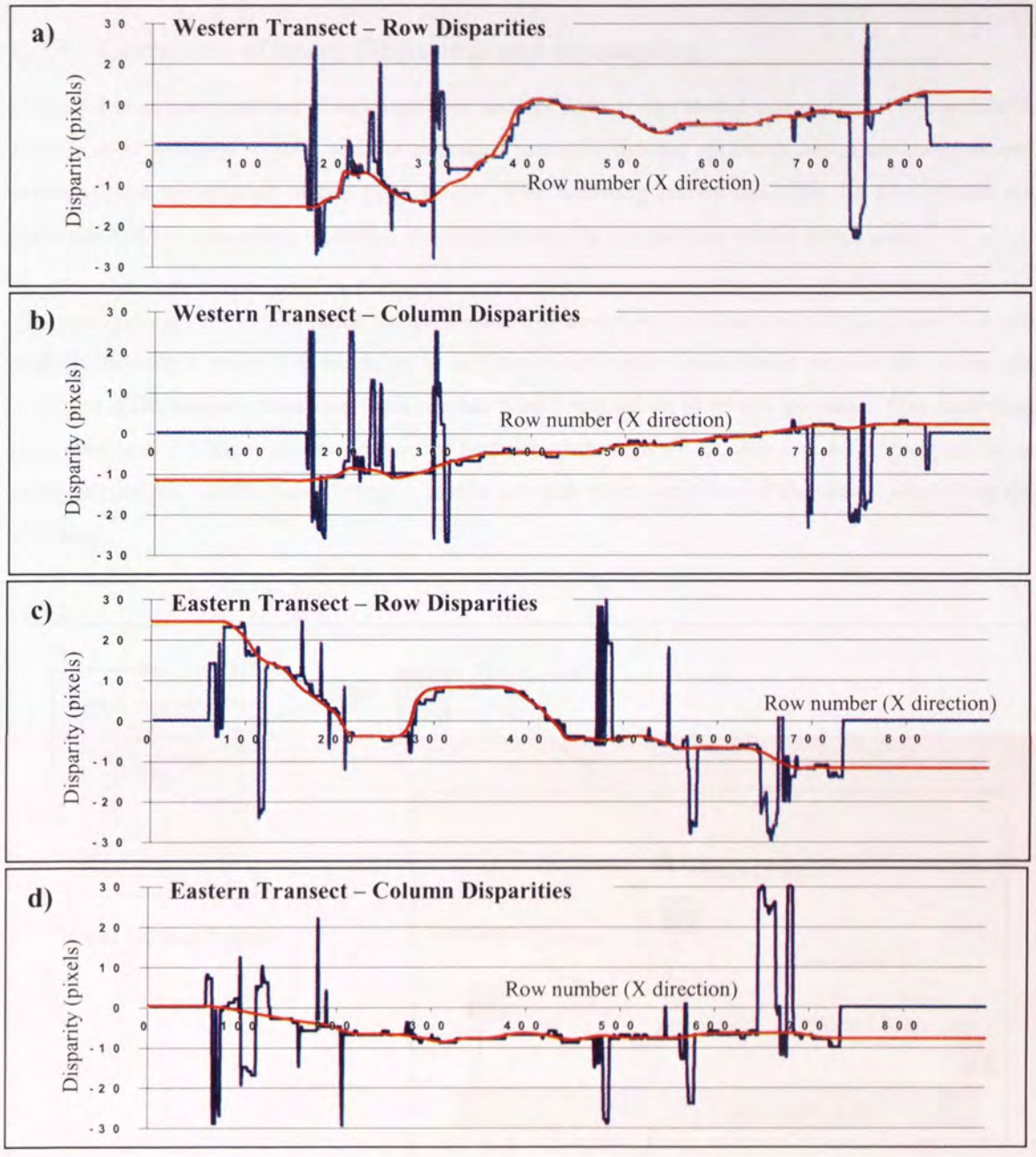

Figure 6.7 Disparities between the polynomial corrected aerial photography and ATM imagery after removal of noise.

6.2.4 Correction of Image Disparities and Resampling

Chapter 4 described a number of techniques for resampling remotely sensed imagery and it was concluded that the most preferred method was the backward nearest neighbour approach due to the computational efficiency and preservation of raw pixel values. The following section describes the development and application of this resampling technique in reconstructing the geometry of the test image data.

The main theoretical considerations for the resampling procedure are illustrated in Figure 6.8. For each pixel in the output image it is necessary to find the co-ordinates of the closest pixel in the polynomial corrected ATM imagery, after each scan line has been projected on to its true position. This resampling procedure can be broken into two stages; the first stage is to identify the *scan line* which projects closest to the target pixel, and the second stage is to then calculate the co-ordinates of the nearest *pixel* along that scan line.

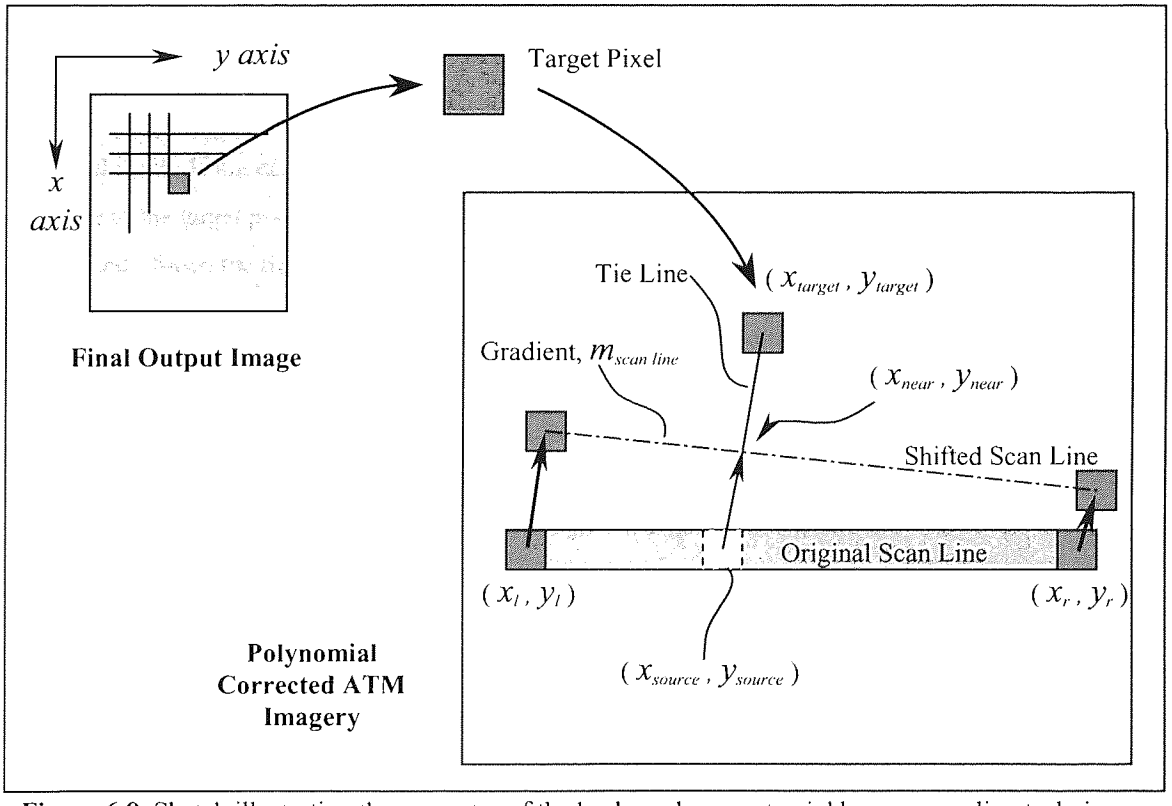

Figure 6.8 Sketch illustrating the geometry of the backward, nearest neighbour resampling technique.

In calculating the closest projected scan line, the orientation of each scan line after applying its associated disparities must be expressed as an equation of a straight line, of the form given in Equation 6.2;

$$x = c - y \,.\, m \qquad (6.2)$$

where m and c are the gradient and intercept on the x axis respectively. This expression refers to the image co-ordinate system illustrated in Figure 6.8 where the x axis describes the North-South direction and the y axis describes the East-West direction. Furthermore, all co-ordinates illustrated in Figure 6.8 refer to the pixel centres within the image co-ordinate system.

For any given scan line, the gradient and intercept can be calculated using the following relationships (note that the expressions refer to the *image* co-ordinate system);

$$grad,\ m_{scan\ line} = (x_l - x_r) / (y_r - y_l) \qquad (6.3a)$$

$$intercept,\ c_{scan\ line} = x_l + y_l \,.\, m_{scan\ line} \qquad (6.3b)$$

where all symbols are defined in Figure 6.8. In identifying the co-ordinates of the closest point along the scan line to the target pixel, the linear equation describing the tie-line illustrated in Figure 6.8 must also be determined. Since the tie-line bisects the target pixel and runs perpendicular to the scan line, the gradient and intercept can be expressed using the following equations;

$$grad,\ m_{tie\ line} = -1 / m_{scan\ line} \qquad (6.4a)$$

$$intercept,\ c_{tie\ line} = x_{target} + y_{target} \,.\, m_{tie\ line} \qquad (6.4b)$$

where all symbols are defined in Figure 6.8. By substituting into Equation 6.2 the expressions for the gradient and intercept for both the scan line and the tie-line, and equating the two relationships, the intercept which describes the co-ordinates of the point closest to the target pixel along that scan line (x_{near} , y_{near}) can be determined. The co-ordinates of this point are thus defined as;

$$y_{near} = (c_{scan\ line} - c_{tie\ line}) / (m_{scan\ line} - m_{tie\text{-}line}) \quad (6.5a)$$

$$x_{near} = c_{scan\ line} - y_{near} \cdot m_{scan\ line} \quad (6.5b)$$

The second stage of the resampling procedure is to identify the pixel belonging to the closest projected scan line which is nearest to the target pixel. Figure 6.9 illustrates how this source pixel can be interpolated using the image disparity data.

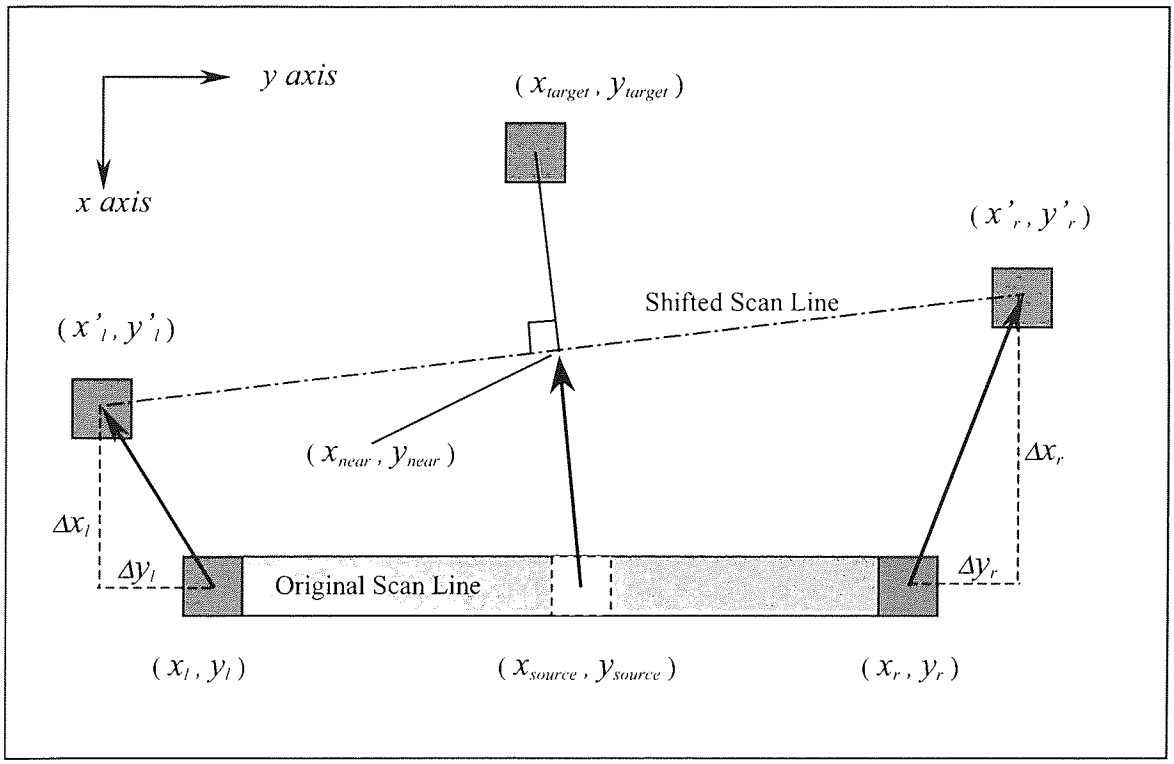

Figure 6.9 Interpolation of source pixel for backward, nearest neighbour resampling procedure.

Using the symbols illustrated in Figure 6.9, a relationship can be derived which enables the source pixel corresponding to the point (x_{near} , y_{near}) to be determined by interpolation, where;

$$\left(\frac{y_{near} - y_l^{'}}{y_r^{'} - y_l^{'}}\right) = \left(\frac{y_{source} - y_l}{y_r - y_l}\right) \tag{6.6}$$

This expression can be rearranged to give;

$$y_{source} = \frac{\left(y_{near} - y_l^{'}\right)\left(y_r - y_l\right)}{\left(y_r^{'} - y_l^{'}\right)} + y_l \tag{6.7}$$

However, the co-ordinates describing the ends of the shifted scan line can be determined from the co-ordinates of the original scan line and the associated disparity data;

$$y_l^{'} = y_l - \Delta y_l \tag{6.8a}$$

$$y_r^{'} = y_r - \Delta y_r \tag{6.8b}$$

Finally, these expressions can be substituted into Equation 6.7 to give;

$$y_{source} = \frac{\left(y_{near} - y_l + \Delta y_l\right)\left(y_r - y_l\right)}{\left(y_r - y_l\right) - \left(\Delta y_r - \Delta y_l\right)} + y_l \tag{6.9}$$

Since the source scan line has already been determined during the first stage of the resampling procedure (giving x_{source}), Equation 6.9 is sufficient to enable the co-ordinates of the source pixel to be calculated using the image disparity data and the previously determined co-ordinates (x_{near} , y_{near}).

6.2.4.1 Summary of Resampling Procedure

The following section summarises the main steps in compensating for image disparities and resampling to the output image grid system. Appendix 2 contains the complete source code (*RESAMPLE.PAS*) for the resampling procedure.

The first step was to convert the disparity data for each scan line into equations of a straight line using the expressions derived in Equations 6.2, 6.3 and 6.4. However, due to the re-orientation of the image data during the initial polynomial correction, the association between scan lines and pixel rows was lost. For this reason, rather than calculate the equations of a straight line for each scan line, the disparity data was used to define the transformation for individual pixel rows. Although this procedure does not strictly follow the theoretical reasoning developed in Chapter 5, it was felt that the approximation was reasonable given the relatively close correspondence between scan lines and pixel rows.

The second step of the resampling procedure was to determine the closest projected scan line (pixel row) to each target pixel in the output image. This was done by calculating the equation of the tie-line, which intersects the target pixel and bisects the shifted scan line at 90°. The co-ordinates (x_{near} , y_{near}) were then determined by equating the two equations to find the intersection. However, in determining the scan line which projects closest to the target pixel, it was not necessary to scan all scan lines comprising the ATM imagery. The total number of scan lines which have the potential to project closest to the target pixel is limited by the numeric value of the search area when determining image disparities in Section 6.2.2. A search area of ± 30 pixels was used in this study, so it therefore follows that only scan lines within a 30 pixel range of the target pixel need to be considered.

Once the closest scan line has been determined, the co-ordinates of the pixel which projects closest to the target pixel were calculated. Since the source scan line has already been determined in step 2, it was only necessary to determine the y co-ordinate using the expression derived in Equation 6.9. Once determined, the brightness value of the target pixel was replaced by that of the source pixel, and the process repeated until all pixels in the target image were filled.

6.2.5 Results of End Correlation Method

Figure 6.10 illustrates the ATM imagery after compensating for the image disparities and resampling to the output grid. As with all the output images shown throughout this thesis, the resampled image data is illustrated within a black frame, the size of which corresponds to the full extent of the reference image. This helps maintain a common scale for all images illustrated throughout this thesis, and allows the output image data to be observed in the context of the reference image. It can be seen from Figure 6.10 that the imagery generally displays good internal geometry – that is, geometric features have retained their structure and have not been adversely distorted by the additional correction stage. However, the building and canal junction pictured in the frame illustrate that whilst the additional correction stage has gone some way towards rectifying the imagery, regions still exist which contain obvious geometric distortions. The

features shown in Figure 6.10 were identified in Section 6.2.1 as being caused by variations in platform attitude, and the End Correlation Method has clearly had difficulties rectifying distortions of this magnitude. However, elsewhere in the corrected imagery, the internal geometry appears consistent with that of the polynomial corrected aerial photography.

A further criticism of the results obtained using the End Correlation Method is the 'blocky' appearance of the output imagery. Nearest neighbour resampling often produces imagery with blocky features due to the approximations in converting one grid system to another (Mather, 1986). Application of the End Correlation Method leads to the ATM imagery being resampled twice, and this double resampling has therefore given rise to cumulative resampling errors.

In order to visualise the geometric differences between the photography and output imagery, a colour composite image was created by assigning the polynomial corrected aerial photograph to the red colour VDU gun, whilst the resampled ATM image (corrected using the End Correlation Method) was assigned to the green and blue guns. This technique of overlaying image data was possible since both images shared the same characteristics and referenced the same grid co-ordinate system. Figure 6.11 illustrates the resulting composite image where the structures of both sets of image data can be identified. Differences in geometry appear as 'shadows' of colour, and whilst it can be seen that there is significant correspondence between large areas of the imagery (predominantly at the edges), large areas of disparity also exist in the centre of the imagery. The depth of these 'shadows' provides a measure of the extent of the registration error, and these were identified as ranging from 0 up to 7 pixels.

It is not the intention to provide a quantitative review of the accuracy of the End Correlation Method here – the reader is referred to Chapter 8 for a comprehensive review of the accuracy for all of the methods of correction developed in this thesis. However, the colour composite images can be used to qualitatively compare the accuracy of the End Correlation Method with that of the polynomial correction method. Figure 6.12 illustrates the aerial photography displayed using the red VDU gun, and the polynomial corrected ATM imagery using the green and blue guns. It can be seen that considerable disparities exist between the two sets of imagery – towards the North-Eastern corner of the composite image the observed disparities approach 30 pixels. This observation corresponds to the magnitude of errors identified when the aerial photography and polynomial corrected ATM imagery were compared using the correlation procedure.

By comparing Figures 6.11 and 6.12 it can be seen that in some places the End Correlation Method has actually increased the disparities between the imagery. This is a significant observation as the End

Correlation Method is clearly not able to precisely compensate for platform attitude errors. Section 6.2.6 reviews the End Correlation Method with respect to the source and magnitude of potential errors, and a number of refinements are suggested in order to improve the reliability and accuracy of the approach.

Figure 6.10 ATM imagery after compensation for image disparities using the End Correlation Method.

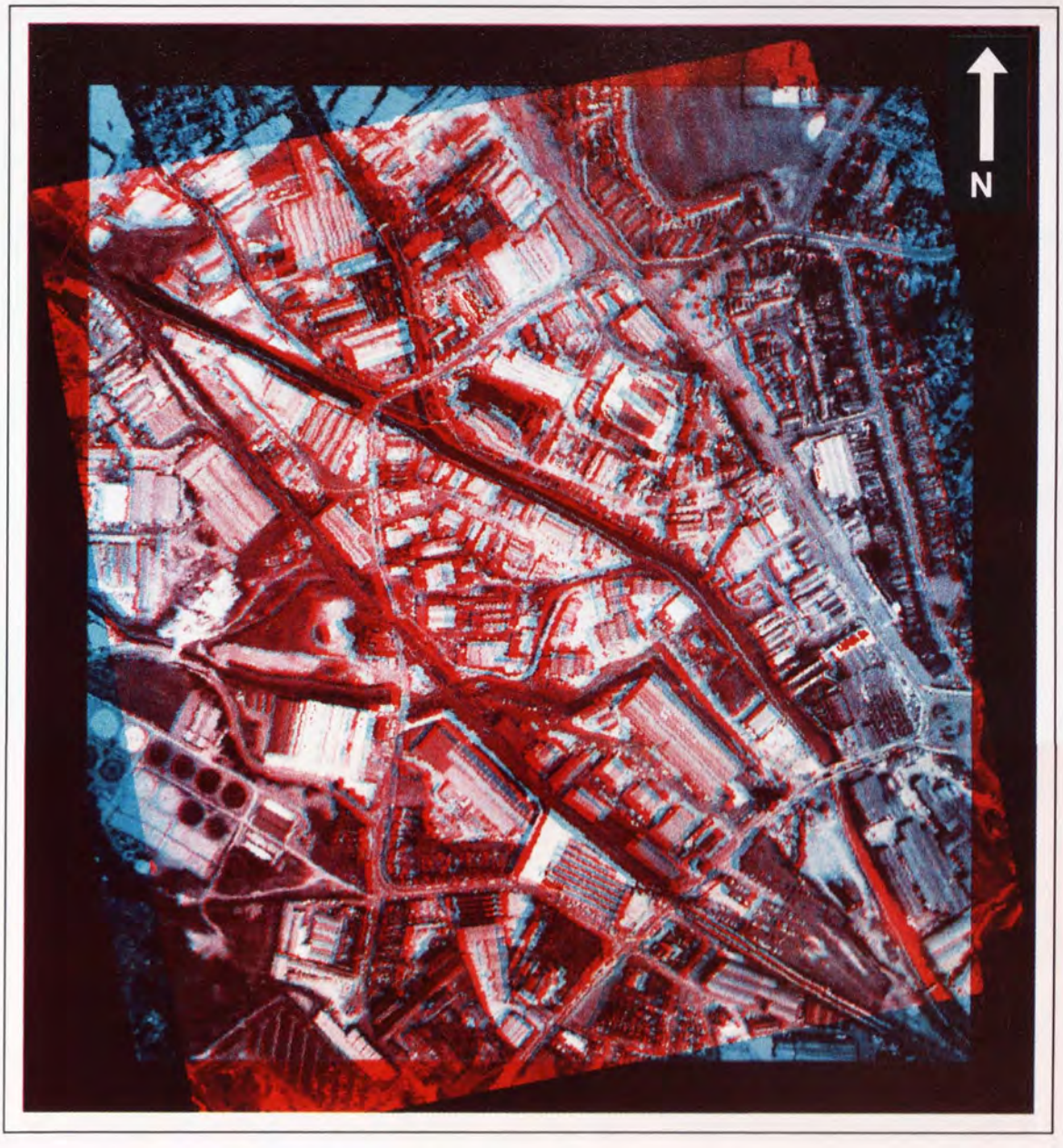

Figure 6.11 Colour composite image of polynomial corrected aerial photography (red) and ATM imagery (green and blue) corrected using the End Correlation Method.

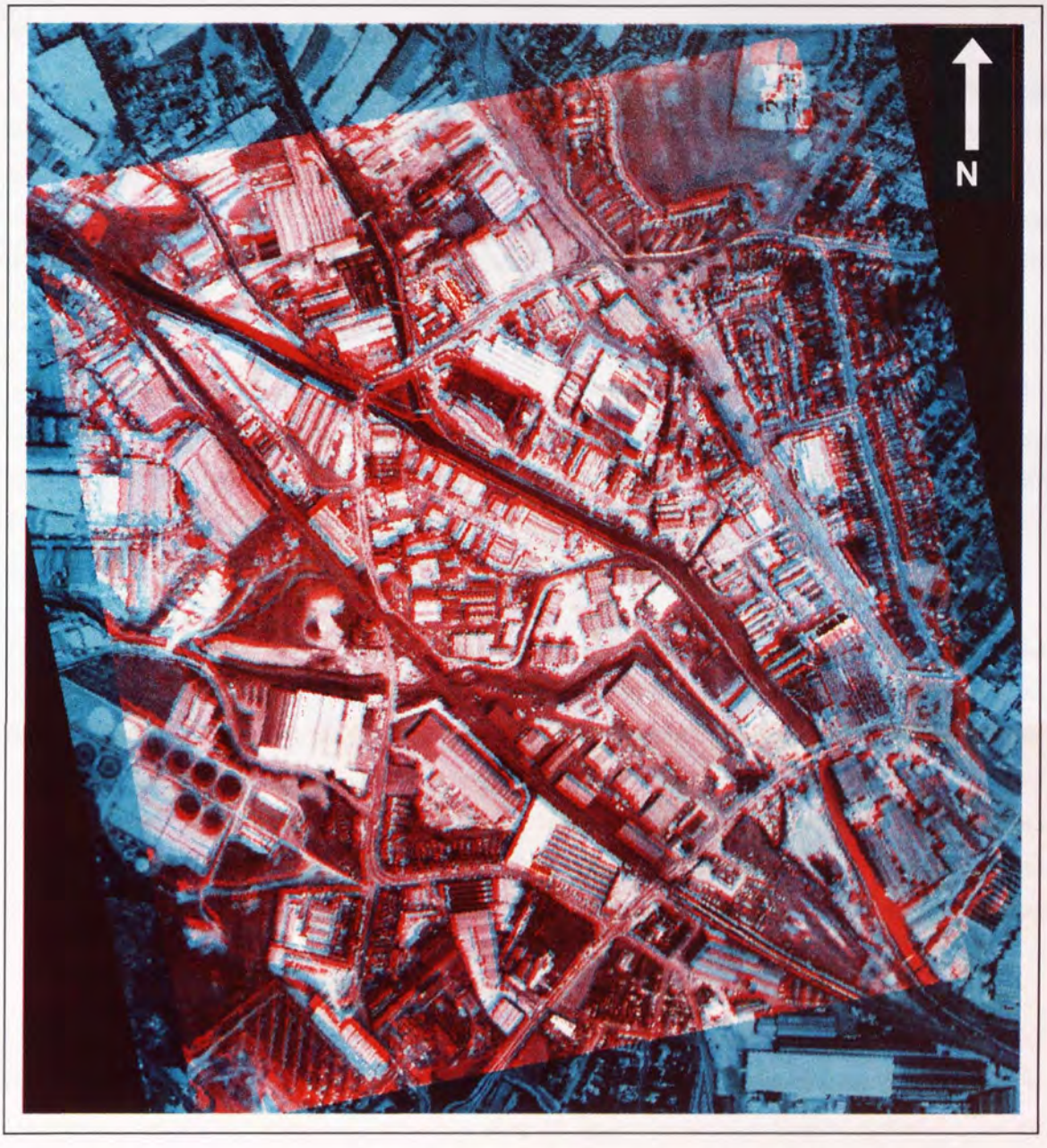

Figure 6.12 Colour composite image of polynomial corrected aerial photography (red) and polynomial corrected ATM imagery (green and blue).

6.2.6 Review of End Correlation Method

The first step in the rectification procedure was to align the two sets of imagery using a linear polynomial correction. Whilst every effort was made to limit the introduction of errors, the basic inability of the transformation procedure to account for complex distortions led to considerable disparities between the corrected aerial photography and line-scanned imagery. However, the application of the End Correlation Method was specifically designed to remove these disparities, and therefore does not significantly influence the overall accuracy of the correction procedure.

The application of the correlation routine was found to be successful at identifying the disparities between the imagery. Manual verification proved that, with the exception of a few isolated cases, disparities identified by hand corresponded closely to those identified using a fully automated pattern matching procedure. However, the presence of noise meant that the disparity data required an additional processing stage before it could be used to reconstruct the geometry of the line-scanned imagery.

Noise removal was by no means an automated process, and the necessity for human interpretation of the disparity data reduces the overall appeal of the technique. To a large degree noise is identified within the context of adjacent data, and the potential obviously exists for mistaking the presence of true platform errors for noise (and vice versa). However, the curve fitting procedure was relatively flexible and allowed the selection of 'correct' points to be concentrated in areas where disparities were most complex. Figure 6.7 illustrates the raw and smoothed disparity data where for the vast majority there is a close correspondence between the data. In isolated regions deviations of up to 2 pixels are observed, and these have a direct influence on the overall accuracy of the output image.

The final stage of the correction process was to reconstruct the line-scanned image geometry with respect to the disparity data and resample to the output grid. In arriving at the final output image the raw ATM imagery underwent two instances of resampling using the backward nearest neighbour approach. This led to the geometry becoming very blocky which reduced the overall appeal of the technique. Furthermore, it was felt that the distribution of errors in Figure 6.11 was the result of the approximations used during the resampling procedure. In resampling the imagery, the disparity data was used to defined transformations for pixel rows rather than individual scan lines. However, differences in orientation between pixel rows and scan lines meant that the disparities at opposite ends of a pixel row correspond to entirely different scan lines.

Despite the difficulties encountered during the removal of noise and resampling procedures, it was felt that the approach was generally successful at identifying image disparities. In utilising this information in a more effective manner, a number of refinements were made to the correction process, and these are the subject of discussion in Sections 6.3 and 6.4.

6.3 Development of Line Correlation Method

In order to overcome some of the problems discussed in the previous section, a number of refinements to the End Correlation Method were made. The most significant modification was to the way in which the image disparities were identified - rather than positioning each scan line using 2 separate data windows, the correlation coefficient was calculated along an entire scan line (hence Line Correlation Method). Section 6.3.1 describes the development and application of this approach to the test imagery, and the results are illustrated in Section 6.3.2. The overall method is reviewed in Section 6.3.3, where further improvements are discussed.

6.3.1 Overview of Approach

The basic concept of the Line Correlation Method is to identify image disparities by positioning an entire scan line drawn from the raw ATM imagery in the rectified aerial photography. Figure 6.13 illustrates the main stages of this approach. Since each individual scan line is effectively a one-dimensional element, the Line Correlation Method overcomes the need to align the scale and orientation of the two sets of imagery. By allowing the position of each end of the scan line to vary in two dimensions, the correlation coefficient can be calculated for the pixel values in the raw scan line and its projected position on the corrected aerial photograph. This procedure embodies all the transformations achievable using existing correction methods (i.e. scale, rotation and translation), but applies them in a per scan line fashion. Since the ATM imagery does not have to undergo an initial polynomial correction, the problems of double resampling are eliminated. Furthermore, correspondence is maintained between the orientation of scan lines and pixel rows in the raw image data, which overcomes the problems encountered during the resampling stages in the End Correlation Method.

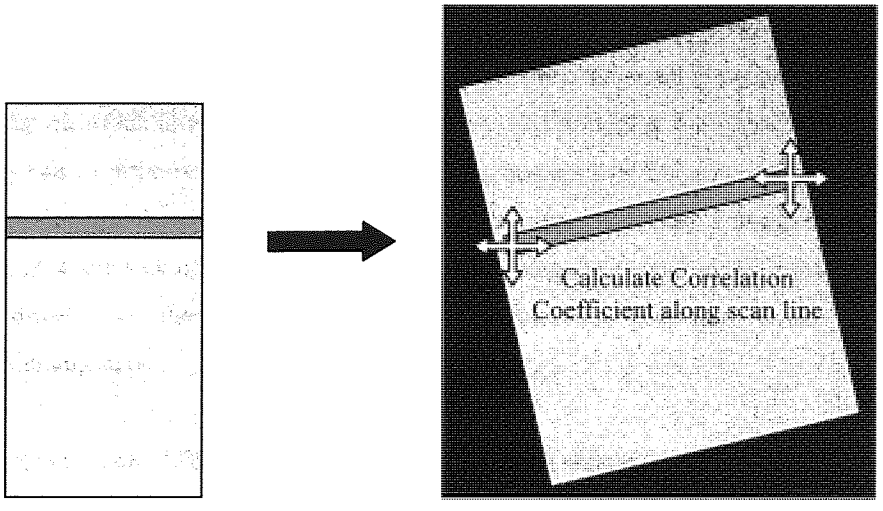

Raw ATM Imagery

Polynomial Corrected Aerial Photography

Line Correlation Method

1. Draw scan line from raw ATM imagery.
2. Find approximate position of first scan line on polynomial corrected aerial photography.
3. Vary end positions within bounds of search area, and calculate correlation coefficient.
4. Peak of correlation surface defines true position of scan line.
5. Starting position of next scan line calculated by incrementing row number of previous scan line position.
6. Repeat steps 3 to 5 for remaining scan lines in the raw ATM imagery.

Figure 6.13 Basic theory behind the Line Correlation Method.

The first stage of the Line Correlation Method was to rectify the aerial photography. Since there was no requirement to maintain similar geometry between the photography and line-scanned imagery (as was the case with the End Correlation Method), it was therefore acceptable to subject the aerial photography to a full ortho-rectification. In fact, this is positively beneficial since the aerial photography then represents a true digital map on which to reference the ATM imagery, and providing full registration is achieved, the ATM imagery can be ortho-rectified in a single step. An attempt was therefore made to ortho-rectify the aerial photograph using the GRASS image processing package. However, a number of problems were encountered due to the lack of available information describing the aircraft exterior orientation. Without reasonable estimates for the required parameters, the correction procedure failed to complete the necessary processing steps.

However, in light of these difficulties it was decided to apply a simple polynomial correction to the aerial photography. For the purpose of this study, which is concerned primarily with the subsequent process of image registration, it was felt that a polynomial correction was sufficient to demonstrate the validity of the approach. The previously rectified aerial photography was therefore used, and the reader is referred back to Section 6.2.1 for a description of the rectification procedure.

The second stage of the Line Correlation Method was to extract a single scan line from the ATM imagery, and find its location in the rectified aerial photography. A routine (called *LINECORR.PAS*) was written in Turbo Pascal to handle the iterative processing, and the complete source code for the Line Correlation Method can be found in Appendix 2. The position of the first scan line was identified manually by visually locating the approximate co-ordinates of the ends of the scan lines in the aerial photography. The co-ordinates were then passed to the computer routine which calculated the correlation coefficient using the expression in Equation 6.1. However, rather than carrying out summations for all pixels belonging to a data window, the correlation coefficient was calculated for the pixel values in the ATM scan line and its projected position in the photography. By varying the end positions of the raw scan line, the optimum location was found.

Once the position of the first scan line had been determined, the position of the next scan line was, by definition, very close to the previous. The starting position of each subsequent scan line was therefore initially assumed adjacent to the previous, thus overcoming the need for manual identification and greatly increasing the efficiency of the approach. The position of the ends of the scan line were then varied within the bounds of the search area, and the correlation routine implemented to determine the optimum location of the scan line.

Once all of the scan lines in the raw ATM image had been positioned in this manner, the final stage of the correction procedure was to resample the output image using the backward nearest neighbour approach, as described in Section 6.2.4. However, since the raw ATM imagery was not subjected to a polynomial correction (as was the case in the End Correlation Method), pixel row / scan line correspondence was maintained and image disparities refer to actual scan lines. Source pixels were therefore drawn directly from the raw ATM imagery, overcoming the problems of double resampling.

6.3.2 Results From Line Correlation Method

Because the scan line transformations identified using the Line Correlation Method are subject to four degrees of freedom (two-dimensional transformation for each end of the scan line), it is more difficult to illustrate the magnitude and nature of geometric disparities. An alternative method of illustrating image disparities was therefore required to demonstrate the relationship between consecutive scan lines.

A routine was developed to illustrate the nature of image disparities simply by plotting the position of each shifted scan line (calculated using the Line Correlation Method) on a blank image sharing the same co-ordinate system as the corrected aerial photography. By constructing an image in this manner, the positional variation from one scan line to the next can easily be seen. Figure 6.14 illustrates the distribution of scan lines obtained after applying the Line Correlation Method to the test imagery. The background of the image is shown in black, whilst the position of each scan line is plotted in white. Where solid regions of white occur, this indicates that consecutive scan lines have been positioned adjacent to each other, having a positive influence on the quality of the final resampled imagery. Where gaps between adjacent scan lines occur (seen as darker shades), this indicates regions where the correlation routine has had difficulties positioning scan lines consistently, and the quality of the output imagery was adversely affected.

Figure 6.14 Distribution of scan lines achieved by applying the Line Correlation Method to the test image data.

A number of significant conclusions can be drawn from Figure 6.14. Although the first scan line (top of image) was initially positioned manually, subsequent scan lines have been positioned purely through application of the pattern matching routine. The search area defining the distance that the ends of each scan line can 'roam' was set to ± 1 pixel (after incrementing the row number), so the position of each subsequent scan line is free to 'wander' in pursuit of the greatest correlation coefficient. It can be seen by comparing Figure 6.14 with Figure 6.3 that the orientation of the scan line distribution corresponds to that of the aerial photography. This is extremely promising as the Line Correlation Method has clearly compensated for scale and rotational differences between the aerial photography and raw ATM imagery.

Another indication of the reliability of the Line Correlation Method in identifying the position of scan lines is the relative 'stability' of the scan line distribution. Although the position from one scan line to the next will vary as a reflection of the movement of the sensor platform during image acquisition, the high scan rate of the ATM means that the positional differences between adjacent scan lines should be small. The presence of bunches of scan lines, or gaps between adjacent scan lines (over and above expected levels), provides an indication of the amount of mis-correlation encountered during the correlation procedure. It can be seen from Figure 6.14 that both gaps and bunches occur in the scan line distribution, and the presence of these directly influences the quality of the final resampled image.

A further indication of the reliability of the Line Correlation Method in identifying the true position of scan lines is the roughness of the edges of the scan line distribution. In describing a smooth and undulating flight path, one would expect to find a smooth and undulating scan line distribution. However, it can be seen from Figure 6.14 that this distribution is somewhat broken.

The information derived from Figure 6.14 can be used to predict the accuracy with which the Line Correlation Method has identified the true position of scan lines. From the presence of gaps and bunches, along with the broken edges of the scan line distribution, it can be deduced that the final output image is likely to contain a significant amount of noise. However, the orientation of the scan line distribution would suggest that the overall geometry of the output image reflects that of the corrected aerial photography relatively closely. Figure 6.15 illustrates the resampled ATM imagery.

Figure 6.15 Resampled ATM imagery after application of the Line Correlation Method.

It can be seen from Figure 6.15 that the final output image does indeed suffer the types of error predicted from the scan line distribution. However, the overall geometry corresponds relatively closely to that of the polynomial corrected photography. Of significant importance is the accuracy with which the Line Correlation Method has identified and compensated for the platform attitude errors at the canal junction.

However, despite the relative success of the correction for the canal junction, the geometry of the building (labelled in Figure 6.15), which belongs to the same group of scan lines, has not been rectified with the same level of accuracy. Similarly, the features at the opposite end of the same scan lines also suffer a considerable amount of noise. This distribution of geometric error is produced due to the averaging out of transformational errors with distance from the ends of the scan line. Since pixel transformations are interpolated from the end positions, the effects of noise will always be smaller than those experienced at the ends.

In interpreting the results obtained using the Line Correlation Method it is again useful to observe a colour composite image showing the superimposition of the corrected aerial photography and the resampled ATM imagery. However, in order to better understand the influence of the scan line distribution on the quality of the output image, Figure 6.16 is constructed such that the red VDU gun corresponds to the aerial photograph, the green to the resampled ATM image and the blue corresponds to the scan line distribution. It can be seen from Figure 6.16 that the scan line distribution (visible on the composite image as magenta) closely follows the orientation of the aerial photography. The extent of the resampled ATM imagery is also visible in the imagery, and areas which have been resampled outside the scan line distribution show up clearly in yellow.

Figure 6.16 emphasises the need to eliminate the presence of noise from the transformation data. Noise occurs due to difficulties in determining the precise position of the scan line ends on the aerial photograph. It can be seen that areas of poor image quality correspond to regions displaying high levels of noise, and as explained earlier, these effects diminish towards the centre of the resampled imagery.

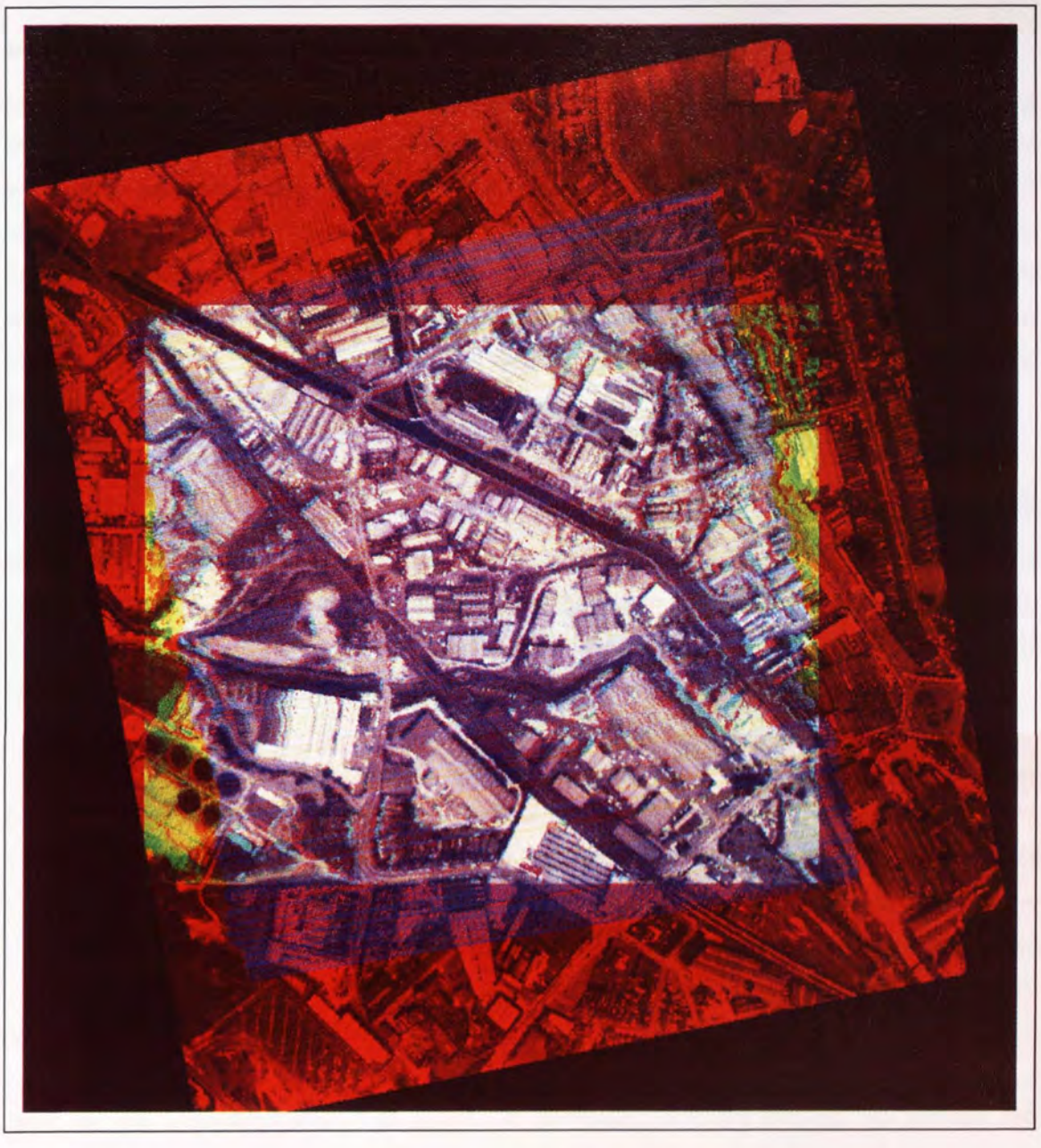

Figure 6.16 Colour composite image consisting of polynomial corrected aerial photography (red), resampled ATM imagery (green) and scan line distribution (blue).

6.3.3 Techniques for Improvement of Image Quality

In defining the position of raw ATM scan lines in the corrected aerial photograph, the Line Correlation Method identifies the disparities associated with two points along each line. If this positional information is subject to noise, the quality of the final output image will also suffer the effects of noise, and this is clearly observed in Figure 6.15. In order to improve the quality of the final output imagery it is therefore necessary to remove the noise associated with the scan line transformations. The following section describes a number of techniques which were used in an attempt to improve the quality of the final output image. Whilst each of the methods for removing noise are described independently, it is possible to apply one or more of these techniques collectively.

6.3.3.1 Brightness Correction

Ellis (1997) used the Black Country Data Set in his study of landfill sites within the West Midlands conurbation, and found that the ATM image data suffered significant variations in brightness intensity across the imagery. These variations are attributable to the angular reflectance properties of earth surface materials and the anisotropic scattering of radiation within the atmosphere. The effects are wavelength specific and are particularly significant in ATM imagery due to the wide sensor field of view.

In his study, Ellis described a technique to remove these scan angle effects by normalising the average brightness value in each of the 716 columns comprising the imagery (for a description see Ellis, 1997). This technique was used to calculate the average brightness for each column comprising the line-scanned test data, where it was found that the imagery had already been corrected by Ellis during his study (Figure 6.17 illustrates the variation in brightness value for the test image data). However, the same technique had not been applied to the aerial photography, and so the brightness variation between the two sets of image data was different (see Figure 6.17).

Since the End Correlation Method calculated the correlation coefficient between two separate data windows positioned at the edges of the imagery, these radiometric disparities did not influence the reliability of the correlation routine. This was because the correlation function effectively standardises the brightness values about the mean, and within a small data window the variation in brightness across the window was negligible. However, in calculating the correlation coefficient for an entire scan line, the variations in brightness become more significant. The technique described by Ellis (1997) was therefore applied to the aerial photography in order to reduce radiometric differences between the test image data, and improve the reliability if the correlation routine.

However, despite applying these radiometric corrections to the test image data, the geometric disparities identified using the Line Correlation Method still suffered considerable amounts of noise. The radiometric correction did influence the correlation function since there were differences between the scan line distributions obtained using the radiometrically corrected and uncorrected image data. However, the radiometric correction did not appreciably improve the stability of the scan line distribution, and the resulting impact on the quality of the output imagery was low.

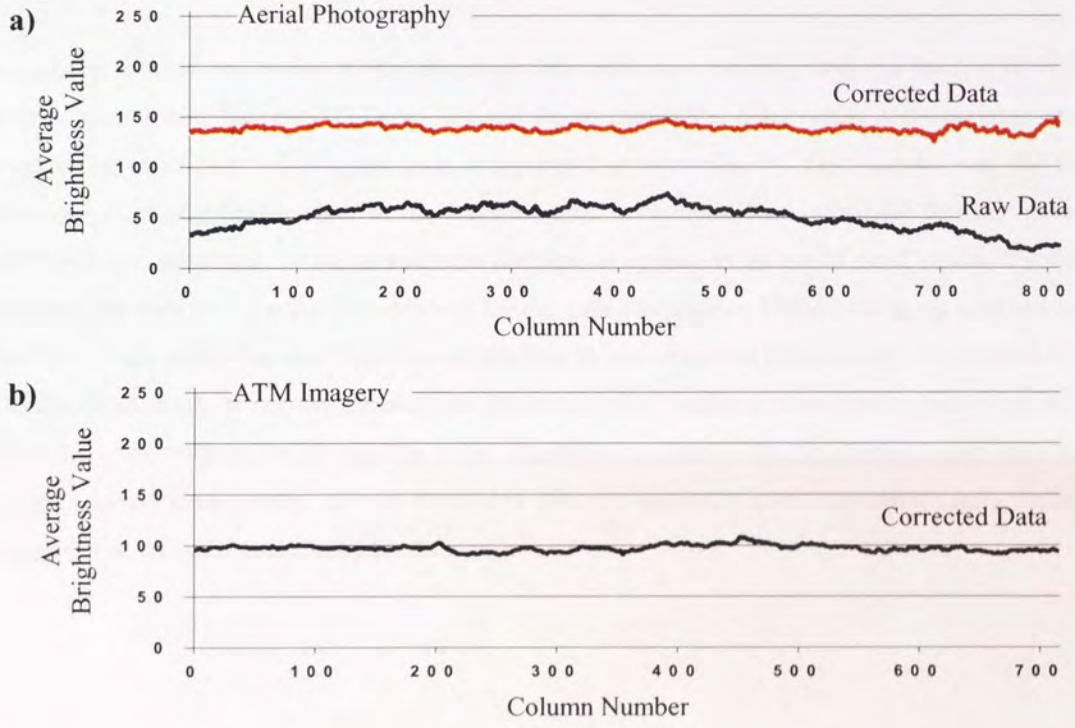

Figure 6.17 Average brightness of pixels for (a) aerial photography and (b) ATM imagery.

6.3.3.2 Rank Correlation

In order to improve the reliability with which individual scan lines were positioned on the corrected aerial photograph, an alternative correlation function was employed. The standard correlation function illustrated in Equation 6.1 determines similarity based on the relative brightness of pixels about the mean. However, rank correlation calculates similarity based on the relative brightness of pixels with respect to adjacent pixels which, it was hoped, would reduce the influence of radiometric differences between the imagery by using this approach.

In applying the rank correlation to the test image data, a routine was integrated into the *LINECORR.PAS* program to rank both the raw ATM scan line and the corresponding pixel values in the aerial photograph in ascending order (the full program code is presented in Appendix 2). Once carried out, the method proceeded in an identical manner to the standard Line Correlation Method except that the correlation coefficient was calculated for the ranked scan line data as oppose to the actual pixel values. Figure 6.18 illustrates the scan line distribution obtained for the Line Correlation Method using the rank correlation function. It can clearly be seen from the distribution of scan lines that the presence of noise has to some extent been reduced. However, the scan line distribution still suffers a considerable amount of noise, so whilst the rank correlation provides a valid alternative technique for positioning scan lines on the corrected aerial photography, it was concluded that the approach does not significantly reduce the presence of noise in the transformation data.

Figure 6.18 Scan line distribution calculated using rank correlation on test image data.

6.3.3.3 Data Smoothing

Brightness correction and the use of the rank correlation were both techniques aimed at improving the quality of the final output image by limiting the development of noise in the transformation data. However, it was demonstrated that no appreciable benefits were realised by carrying out these additional processing stages. In light of these difficulties a method was developed which, given the inevitable presence of noise in the transformation data, attempted to reduce its influence on the quality of the final output image.

In order to remove the occurrence of gaps and bunches in the scan line distribution it was decided to smooth the transformation data by apply a moving average. Although difficulties had been experienced when this approach was applied during the End Correlation Method (Section 6.2.3), observations indicated that, due to the search constraints imposed during the pattern matching routine, the noise obtained for the Line Correlation Method was more uniform and of a higher frequency. After experimentation with a range of window sizes, a moving average consisting of 41 rows was applied to the transformation data, and Figure 6.19 illustrates the resulting scan line distribution. It can be seen from Figure 6.19 that the scan line distribution is considerably more uniform than that acquired using the unsmoothed transformation data. Figure 6.20 illustrates the final output imagery resampled using the smoothed transformation data, where the quality of the resulting imagery is predictably far superior to that achieved using the raw transformation data. The influence of noise has been almost completely removed from the image data, and many features which suffered severely from the presence of noise in Figure 6.15 now display crisp, well-defined boundaries which correspond to the corrected aerial photography. However, it can be seen that Figures 6.19 and 6.20 still suffer relatively low frequency geometric distortions. These errors are due to difficulties in positioning the ends of consecutive scan lines – a basic criticism of the Line Correlation Method.

Figure 6.19 Scan line distribution obtained after smoothing the scan line transformation data.

Figure 6.20 Resampled ATM image for smoothed transformation data.

6.3.4 Review of Line Correlation Method

The Line Correlation Method represents a considerable improvement on the End Correlation Method in both accuracy and reliability in identifying and removing platform attitude errors from airborne line scanned imagery. The most significant improvements come through the removal of a number of processing stages, which were both time consuming and susceptible to the introduction of errors.

Since scan lines in the raw ATM imagery are effectively one-dimensional elements, there was no need to align the orientation and scale of the image data to that of the corrected aerial photography. The need to apply an initial polynomial correction to the line scanned imagery prior to applying the Line Correlation Method was therefore removed which reduced the problems experienced with double resampling of the final output image data.

Due to the limitations imposed on the search area during the pattern matching routine, the presence of noise is generally far more uniform and of a higher frequency than that experienced during the End Correlation Method. A number of approaches for removing noise were developed and applied to the image data with varying levels of success. Whilst each of the methods described in Section 6.3.3 were applied to the test imagery independently of each other, they can also be applied simultaneously However, this combined approach was applied to the test imagery and no appreciable improvement in accuracy was gained over the application of the moving average alone.

Initial results from the application of the Line Correlation Method on the test image data demonstrate that this approach is able to successfully identify and remove platform attitude errors and register the line scanned imagery with the corrected aerial photography. However, despite the application of a number of techniques to reduce the presence of noise from the disparity data, the effects of noise have not been completely removed from the final output imagery. The level of accuracy therefore still fails to satisfy the desired level of better than 1 pixel throughout the imagery.

6.4 Dumbbell Correlation Method

In an attempt to further improve the accuracy of the correction technique, it was decided to combine the strengths of the previous two methods. Since the Line Correlation Method was relatively sensitive to positional errors at the ends of each scan line (resulting in high frequency noise), it was decided that an additional weighting was required during the correlation routine to anchor the end positions more reliably in the aerial photography. The correlation coefficient was therefore calculated for a scan line drawn from the raw ATM image with two data windows positioned at the ends of each line. This in effect created a dumbbell shape, which provided an additional weighting to the correlation function at the ends of each scan line, whilst the line itself limited the noise experienced in the End Correlation Method resulting from miscorrelation of data windows. The following section describes the development and application of this approach in rectifying the line scanned imagery.

6.4.1 Overview of Approach

By adding two data windows to the ends of each scan line during the correlation routine, the scan line basically loses its one-dimensional properties, along with the processing benefits associated with this. In order to calculate the correlation coefficient for the 'dumbbell' shape, the scale and orientation of the aerial photography and ATM imagery need to be approximately aligned. During the End Correlation Method this was achieved by applying a linear polynomial correction to the two sets of imagery, which introduced considerable errors into the correction procedure.

In light of the experiences gained with the End Correlation Method an alternative approach for aligning the scale and orientation of the test imagery was therefore developed. In order to maintain scan line – pixel row correspondence the raw ATM imagery was kept in its original form, and the raw aerial photography was transformed to match the approximate scale and orientation of the raw ATM imagery. Since the orientation of the raw aerial photography already corresponded to that of the ATM imagery (they were both acquired from the same aircraft platform), the scale of the aerial photography was adjusted simply by stretching the image data to fit to the ATM imagery. The amount of stretch (or compression) required to align the two sets of imagery was determined by measuring the distance between two well-defined features in both the along-track and across-track directions, and using the equations defined below;

$$\text{Vertical Scale} = \text{Vdist}_{ATM} / \text{Vdist}_{photo} \quad (6.10a)$$

$$\text{Horizontal scale} = \text{Hdist}_{ATM} / \text{Hdist}_{photo} \quad (6.10b)$$

where Vdist and Hdist refer to the vertical and horizontal distances respectively, for the ATM image and raw aerial photography. Once the scale factors were determined, the aerial photograph was resampled to match the raw ATM image using the Turbo Pascal routine *RESCALE1.PAS* (see Appendix 2 for the complete source code).

The processing procedure for the Dumbbell Correlation Method was virtually identical to that of the Line Correlation Method (see Section 6.3), except that two data windows at the ends of each scan line were included in the correlation coefficient calculations. The final output image was then resampled using the positions of each dumbbell (representing a scan line) in an identical manner to that described for the End Correlation Method (see Section 6.2.4). Appendix 2 lists the complete source code (*DUMBBELL.PAS*) for the Dumbbell Correlation Method.

6.4.2 Results of Dumbbell Correlation Method

The raw ATM imagery was corrected using the Dumbbell Correlation Method with a window size of 15×15 pixels, and Figure 6.21 illustrates the resulting scan line distribution. In order to better observe the relationship between the position of adjacent scan lines, consecutive scan lines have been plotted in white and grey. The position of individual scan lines can therefore be observed, providing a clearer indication of errors. It should be noted that the apparent line running vertically down the centre of the scan line distribution is an artefact of the raster representation of the scan lines, rather than a feature of the scan line plot.

It can be seen that the distribution of scan lines is far more stable than that obtained using the Line Correlation Method – there are significantly less occurrences of gaps and bunches of scan lines, and the edges of the distribution are far smoother than that obtained previously. Figure 6.22 illustrates the final output imagery resampled using the scan line transformations determined using the Dumbbell Correlation Method, and it can be seen that this approach has had a dramatic influence on the overall image quality. The effects of noise have been significantly reduced and distortions experienced in the raw ATM imagery have been removed to a considerable degree. It should be noted that the disparity data used to produce Figures 6.21 and 6.22 has not been smoothed, and using the approaches described in Section 6.3.3 it is anticipated that further significant improvements in image quality could be achieved.

Figure 6.23 is a colour composite image showing the re-scaled aerial photography (red) superimposed on top of the line-scanned imagery corrected using the Dumbbell Correlation Method. It can be seen that the geometric disparities between the imagery (which show up as 'shadows' of red and blue) have been drastically reduced when compared with Figure 6.11 (End Correlation Method) and Figure 6.16 (Line Correlation Method). These findings suggest the Dumbbell Correlation Method is the most reliable and accurate approach for registering the ATM image data with aerial photography.

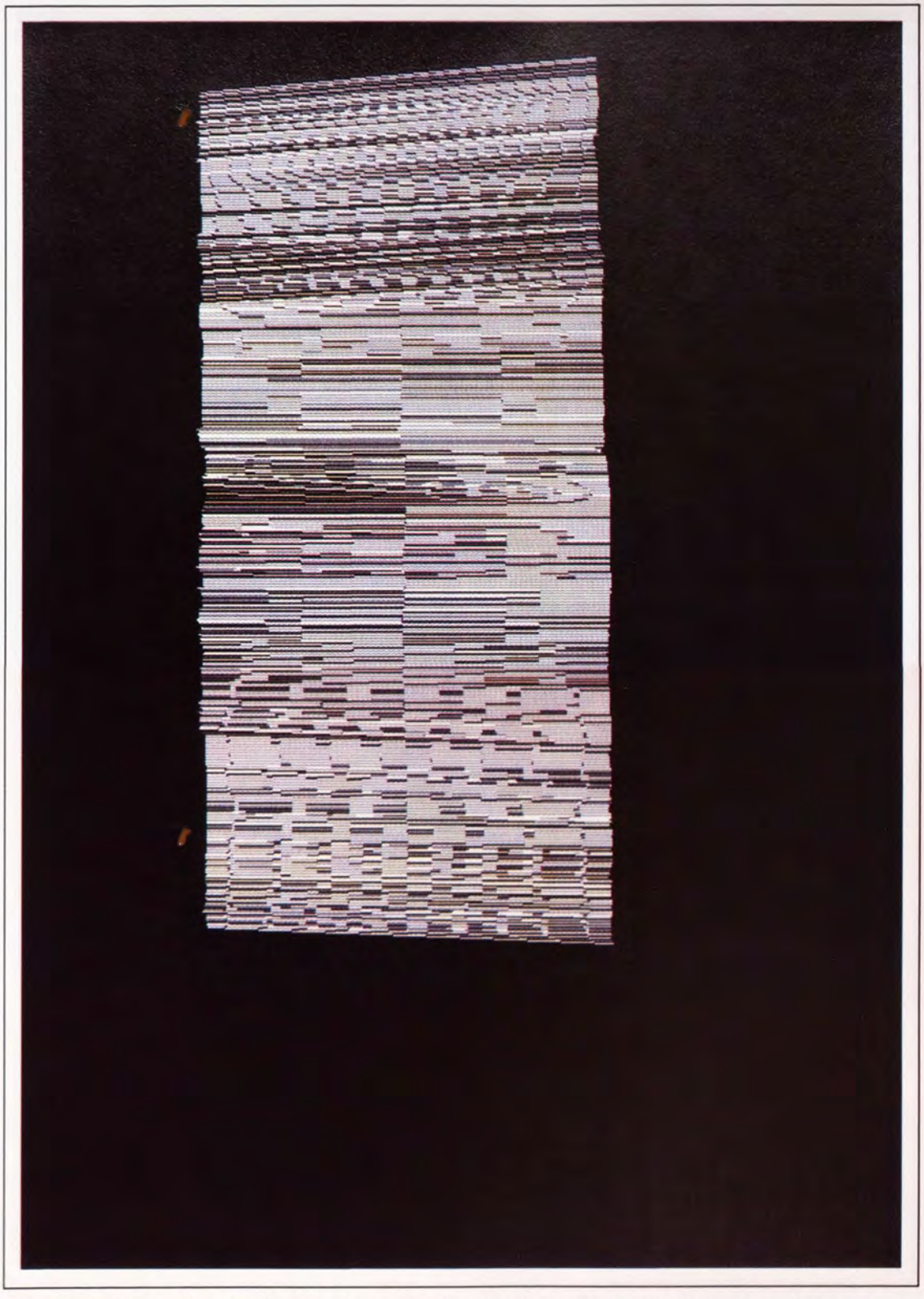

Figure 6.21 Scan line distribution obtained for Dumbbell Correlation Method using a data window size of 15×15 pixels.

Figure 6.22 Resampled ATM imagery obtained using the Dumbbell Correlation Approach.

Figure 6.23 Colour composite image showing re-scaled aerial photograph (red) and final output image (green and blue).

6.4.3 Review of Dumbbell Correlation Method

The Dumbbell Correlation Method is virtually identical to the Line Correlation Method except that individual scan lines are represented by a dumbbell shape rather than a single line of pixels. Due to the two-dimensional nature of the dumbbell shape it was necessary to align the scale and orientation of the raw imagery to enable the correlation coefficient to be calculated. In order to preserve the scan line – pixel row orientation of the raw ATM imagery, the aerial photography was re-scaled to match the ATM image data. The resulting scan line distribution was significantly more stable and this had a direct influence on the quality of the output image.

6.5 Summary of Alternative Methods of Geometric Correction

Chapter 6 has described the development and application of three separate techniques for removing from the line-scanned imagery the geometric distortions associated with variations in platform attitude. All three methods have used digitally scanned aerial photography as the reference on which to map the ATM imagery.

Through the qualitative accuracy assessment carried out by construction of colour composite images, it is clearly shown that the most reliable and accurate method of image correction was the Dumbbell Correlation Method. This approach is virtually completely automated and does not require any human interpretation of the disparity data.

The only significant criticism of the Dumbbell Correlation Method (and the Line Correlation Method) is that the stability of the scan line distribution is often sensitive to the position of the transects down which the correlation routine is applied. If the ends of the scan line fall within regions devoid of detail, the subsequent correlation coefficients are low resulting in potential mis-correrlation. Since all subsequent scan lines are located purely on the basis of the correlation coefficient, the routine has a tendency to become 'lost' from the true pattern of scan lines, which results in meaningless disparity data. However, it is possible to overcome this problem by selecting alternative transects down which to run the correlation routine. Furthermore, the overall accuracy of the approach can be improved by selecting transects which coincide with high levels of detail, which increases the reliability of the pattern matching routine.

The assessment of registration accuracy during the current chapter has been limited purely to qualitative investigations. The use of colour composite images enable the location and magnitude of image disparities to be observed at a glance. However, Chapter 8 describes the development and application of

an alternative technique for determining a quantitative measure of registration accuracy, which is applied to test imagery extracted from the Black Country and Black Brook data sets.

7. Geometric Correction and Registration of Black Brook Imagery

The following chapter describes the application of the Dumbbell Correlation Method to a number of scenes extracted from the Black Brook data set. Section 7.1 illustrates the test image data and describes the main characteristics of the imagery. Section 7.2 describes the application of the Dumbbell Correlation Method, and discusses the accuracy with which the image correction and registration has been applied. Although Section 7.2 only describes the accuracy of the output imagery in qualitative terms, a full quantitative assessment of the geometric accuracy is carried out in Chapter 8. The eventual delivery from NERC of the Black Brook data set in a format enabling parametric correction allowed a number of flight lines to be corrected using the NERC correction process. Section 7.3 describes the application of this technique, and discusses a number of issues relating to the overall correction procedure. Finally, Section 7.4 summarises the main issues encountered during the application of the approaches described above.

7.1 Test Image Data

Towards the end of the research project a limited quantity of line-scanned image data from the 1996/1997 flying programme was delivered, and this provided an additional data set on which to test the alternative methods of geometric correction. A number of individual scenes were extracted and the corresponding aerial photographs located and digitally scanned in the manner described in Chapter 6.

Since the aerial photography was acquired during the scheduled daytime flights on the 23rd October 1996, the projection and orientation of the aerial photography and ATM imagery (acquired on 8th November) were markedly different. Furthermore, since the two sets of imagery were acquired during different flights, each data set was therefore subject to entirely different platform attitude errors. However, the underlying principles of the Dumbbell Correlation Method are not affected by the time difference between the acquisition of the image data, and the method is therefore equally applicable to imagery acquired during different flights. The results illustrated in the following sections therefore demonstrate the application of the correction routine to truly multi-temporal image data.

7.1.1 Test Scene 1

Figure 7.1 is a section of raw ATM imagery extracted from the Black Brook data set, centred on a sewage treatment works lying approximately 3 km South-West of Shenstone at grid co-ordinates E409300 N301900 (see Figure 3.1). The region surrounding the sewage treatment works primarily consists of large open fields with a number of small outcrops of woodland. Within the raw ATM imagery, it is not possible to identify any significant distortions caused typically by variations in platform attitude. However, elongated scale in the direction of flight shows that the imagery has been over-sampled in the along track direction.

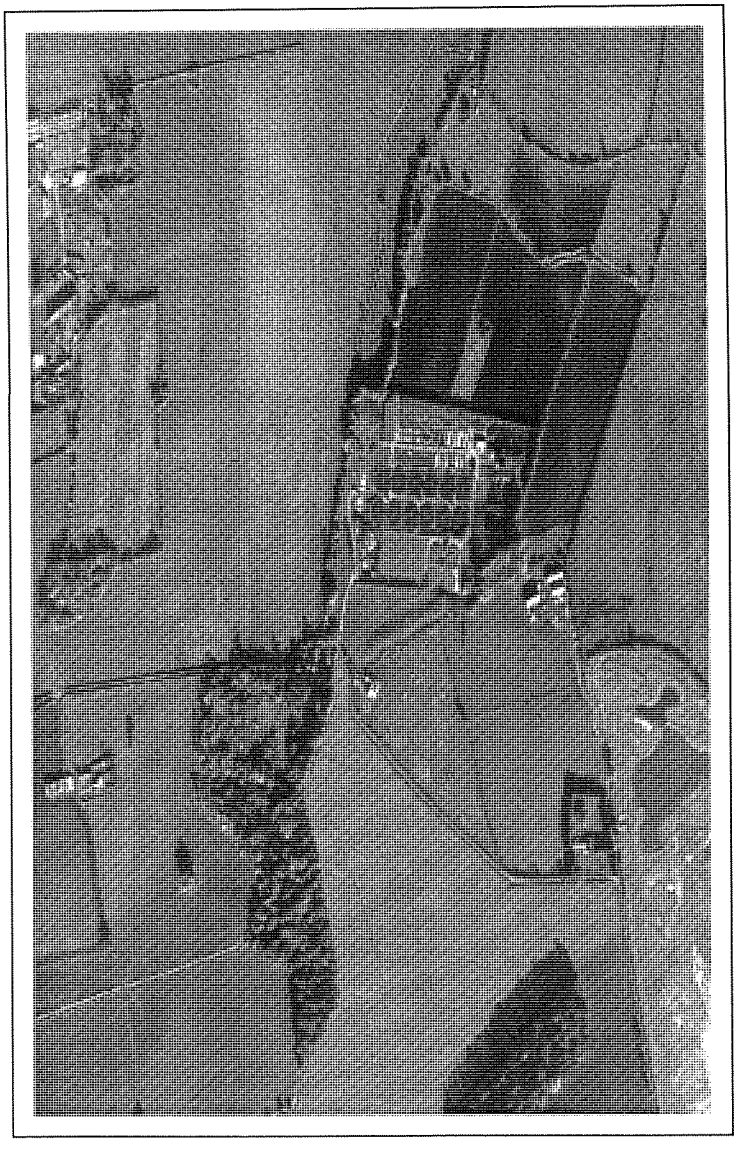

Figure 7.1 Test Scene 1 - ATM imagery (band 3) acquired over the Black Brook catchment.

Figure 7.2 is the uncorrected aerial photography (green band) acquired on the 23rd October 1996, over the region corresponding to the ATM imagery shown in Figure 7.1. It can be seen by comparing Figures 7.1 and 7.2 that the orientation of the imagery is significantly different, although they correspond largely to the same geographical area.

Figure 7.2 Test Scene 1 – Aerial photography (green band) acquired over the Black Brook catchment.

7.1.2 Test Scene 2

Figure 7.3 is the second scene extracted from the raw ATM image data acquired on the 8th November 1996. The region is centred on Little Hay Farm, which lies approximately 2 km South-East of Shenstone at grid co-ordinates E412200 N302500 (see Figure 3.1). The imagery predominantly consists of a number of farm buildings connected by rural roads, and is surrounded by relatively large open fields and woodland.

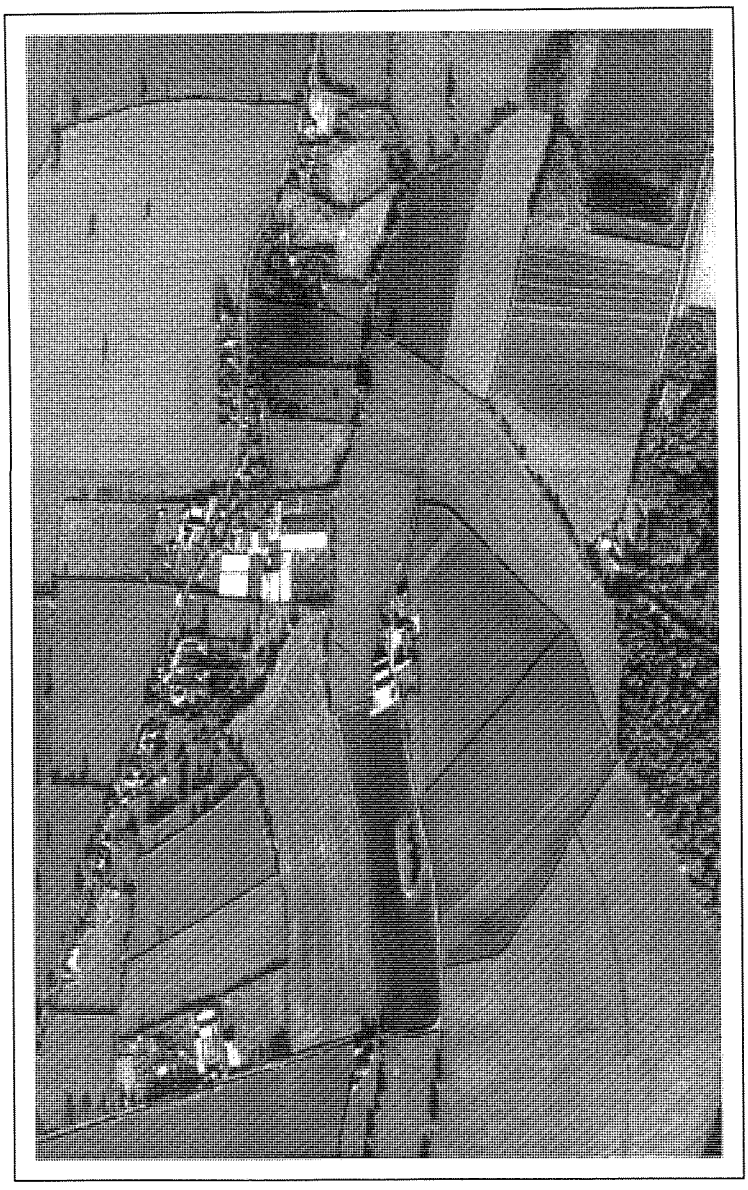

Figure 7.3 Test Scene 2 - ATM imagery (band 3) acquired over the Black Brook Catchment.

Figure 7.4 is the aerial photography (green band) corresponding to Figure 7.3 acquired on the 23rd October 1996. It can be seen that both orientation and geographical coverage of the two sets of imagery are relatively closely aligned. Within the imagery it is possible to identify evidence of the time difference between the two images. In the top-right corner of the aerial photography, a number of features can be identified which are not present in the ATM imagery. These features appear to be the result of earthworks, and although they represent only minor differences between the imagery, the potential difficulties in registering temporal image data using digital pattern matching techniques is clearly demonstrated.

Figure 7.4 Test Scene 2 – Aerial photography (green band) acquired over the Black Brook Catchment.

7.2 Application of Dumbbell Correlation Method and Results

7.2.1 Approximate Alignment of Image Geometry

The Dumbbell Correlation Method described in Chapter 6 was originally developed and applied to imagery taken from the Black Country data, and as such, the orientation and geographical coverage of the aerial photography and ATM imagery was very closely aligned. However, since the Black Brook test data was acquired on separate days, the orientation and coverage are noticeably different.

In order to apply the Dumbbell Correlation Method the geometry of the two sets of imagery need to be approximately aligned. The End Correlation Method used a first order polynomial correction to tie the image geometry to a common grid co-ordinate system. This approach was criticised for introducing double-resampling errors later in the correction procedure. However, by using a polynomial transformation to register the aerial photography to the raw ATM imagery, the ATM imagery is maintained in its raw state and the problems described previously are overcome. This then allowed the Dumbbell Correlation Method to be applied to the image data in an identical manner to that described in Chapter 6.

Figure 7.5 shows the aerial photography (Test Scene 1) following registration to the raw ATM imagery. The RMSE for the registration procedure was 18.7 pixels, which clearly demonstrates how the polynomial transformation fails to provide a satisfactory level of registration accuracy even for small-scale, multi-temporal studies. Figure 7.6 is a colour composite image constructed using the polynomial corrected aerial photography (red) and the raw ATM imagery (green and blue). It can be seen from Figure 7.6 that considerable disparities exist between large regions of the imagery, and in some cases the magnitude of these errors approach 25-30 pixels.

Figure 7.7 shows the aerial photography for Test Scene 2, registered to the raw ATM imagery. The RMSE for the registration procedure was 14.8 pixels, and Figure 7.8 shows the corresponding colour composite image. It can be seen from Figure 7.8 that disparities as great as 16-17 pixels exist between the imagery, which again is clearly unacceptable for small-scale multi-temporal studies.

Figure 7.5 Aerial photography registered with the raw ATM imagery (Test Scene 1) using polynomial transformation.

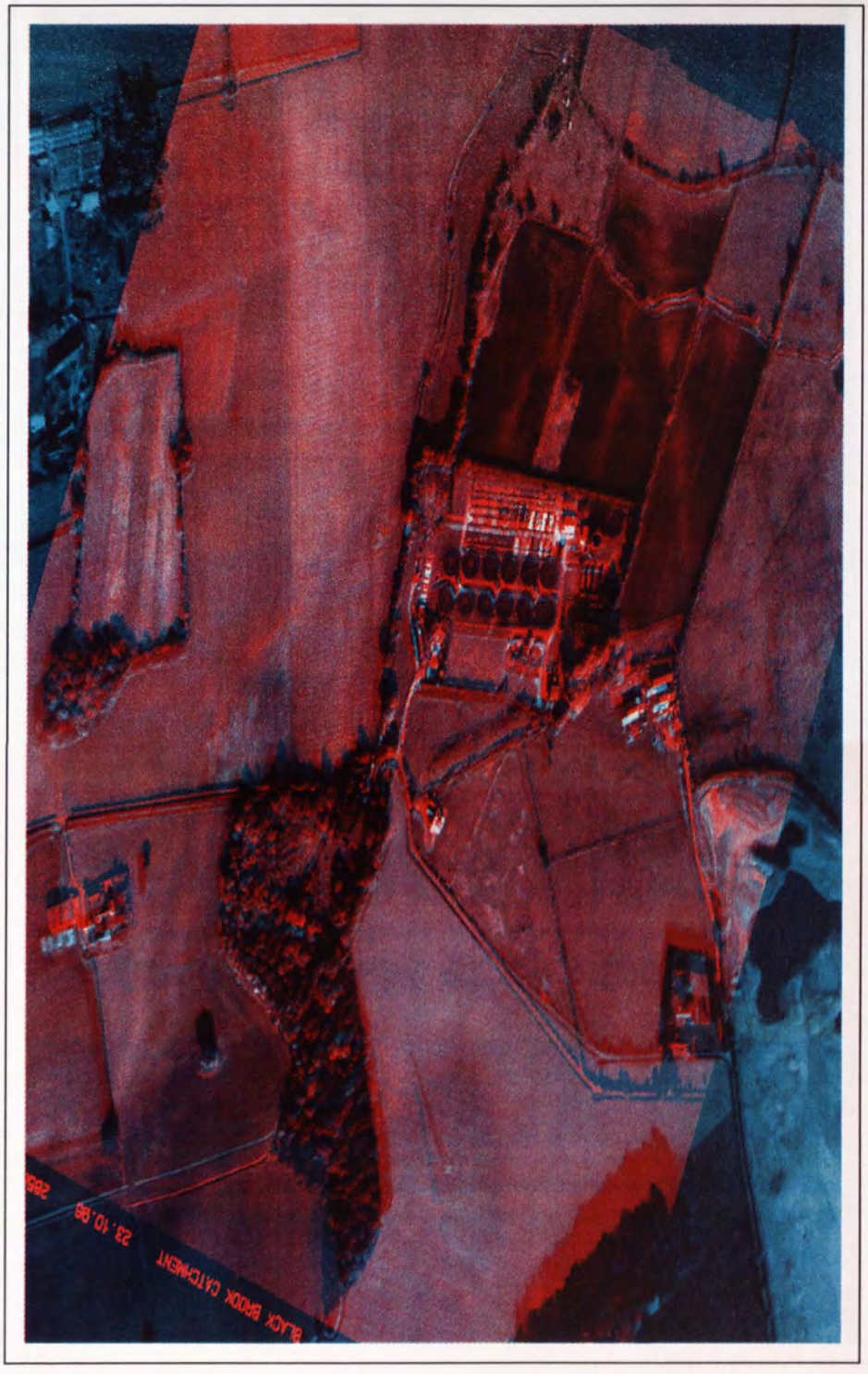

Figure 7.6 Colour composite image showing disparities between transformed aerial photography (red) and raw ATM imagery (green and blue) for Test Scene 1.

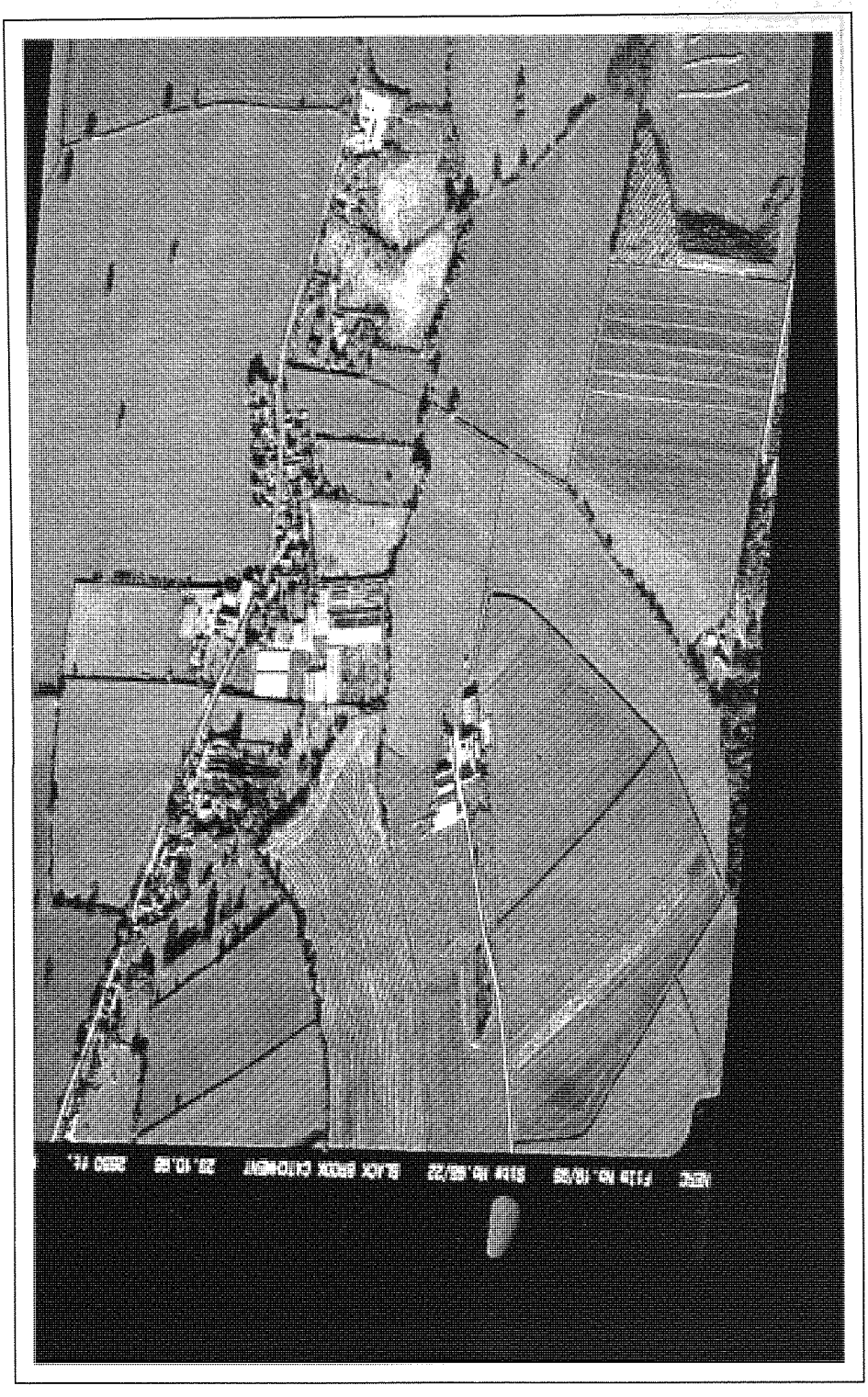

Figure 7.7 Aerial photography registered with the raw ATM imagery (Test Scene 2) using polynomial transformation.

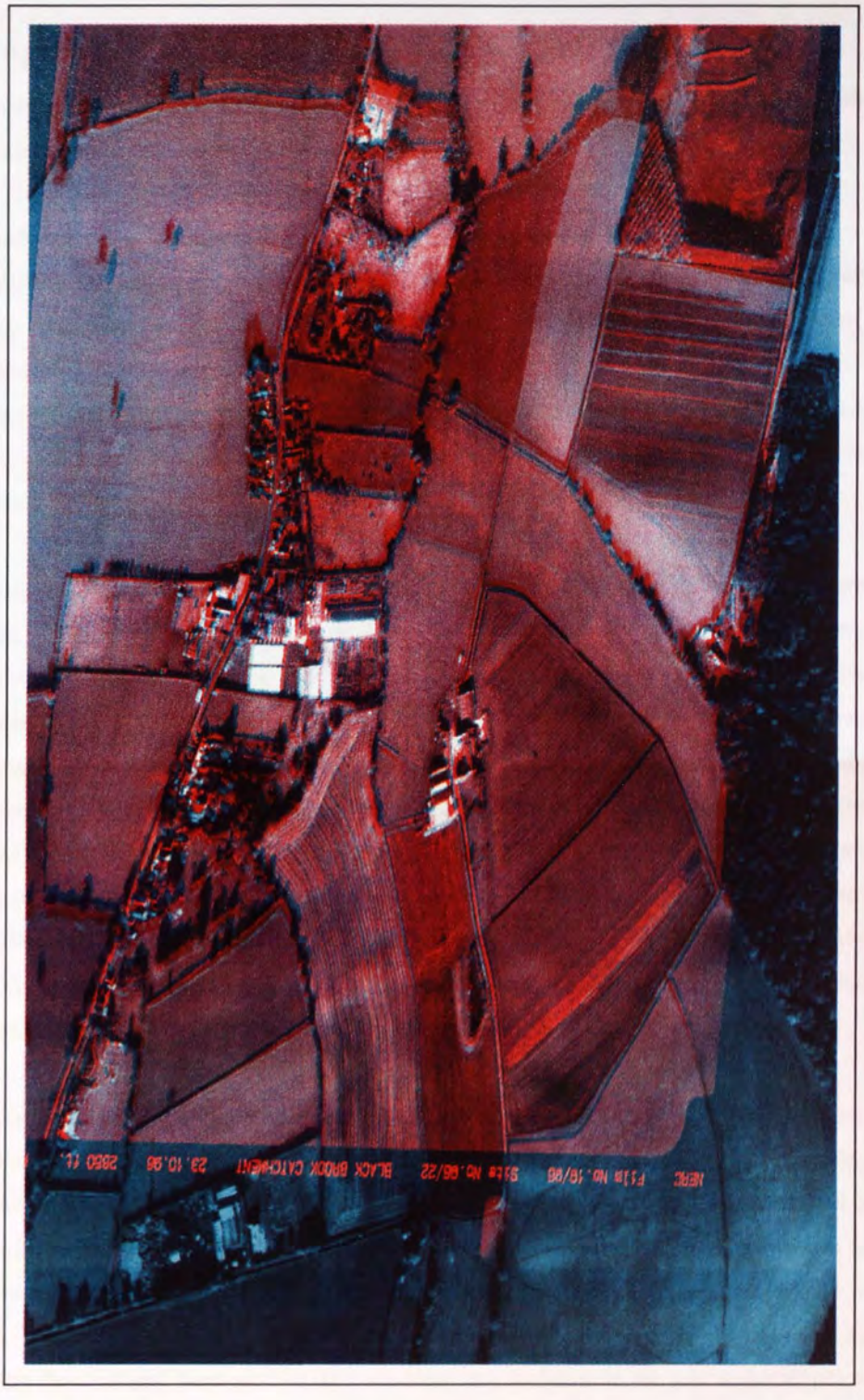

Figure 7.8 Colour composite image showing disparities between transformed aerial photography (red) and raw ATM imagery (green and blue) for Test Scene 2.

7.2.2 Application of Dumbbell Correlation Method

The Dumbbell Correlation Method was applied to the test image data by carrying out the following steps (see Section 6.4 for a full description of the method);

1. identify two pixels belonging to the same scan line in the raw ATM imagery;
2. identify the approximate co-ordinates of these pixels in the corresponding aerial photography;
3. supply this start-up data to the computer program (DUMBBELL.PAS), along with the search parameters (window size and extent of search area);
4. set the program running and observe results through scan line distribution (see Section 6.3.2);
5. modify the search parameters if the scan line distribution shows obvious errors, and repeat step 4;
6. define area for resampling and resample output image data.

In applying this method to the Black Brook test data a number of difficulties were encountered. Because the imagery consisted predominantly of large expansive fields of uniform cover, problems were experienced locating the ends of each scan line using pattern matching techniques. The Dumbbell Correlation Method was originally developed using imagery acquired over the Black Country, and this predominantly industrial region provided an abundance of well-defined features making the process of pattern matching far more reliable. However, one of the advantages of the Dumbbell Correlation Method is that the search parameters can be varied to reflect the nature of the imagery under investigation. For this reason, the size of the data windows corresponding to the ends of each scan line was increased to better reflect the size of the features within the imagery. Furthermore, the reliability of the correlation routine was further improved by ensuring the transects down which the pattern matching routine were run coincided with regions of high detail in the imagery.

Further problems were encountered whilst applying the correlation routine to the image data, and these were caused by the temporal differences between the two sets of imagery. By observing the colour composite images in Figures 7.6 and 7.8, significant differences between the magnitude and orientation of solar shadows can be identified. The aerial photography was clearly acquired at a different time of day to the line-scanned imagery, and the different solar angle has influenced the magnitude and orientation of shadows within the imagery. Since the Dumbbell Correlation Method determines disparities by calculating the similarity between two data windows, any variation in the size and orientation of shadows will have obvious implications on the accuracy with which disparities can be identified. In order to limit the introduction of errors to the disparity data, the correlation routine was therefore applied to areas of the imagery consisting of low level features, which have smaller, less well-defined shadows.

By constraining the search routine to regions satisfying the criteria described above, it was extremely difficult to locate suitable areas in the imagery on which to apply the Dumbbell Correlation Method. However, in overcoming these difficulties it was decided to apply the correction routine to small isolated regions, and use these individually registered sections of imagery to produce a mosaic representing the final output image. Areas of the raw imagery which could not be corrected with a satisfactory level of accuracy were therefore not incorporated into the final output imagery. This ensured that the final output imagery comprised only of regions which satisfied the desired level of accuracy. Furthermore, the correction process could be concentrated on specific areas of interest, and this allowed the dumbbell search parameters to be varied to reflect the nature of features within specific areas of the imagery.

7.2.3 Results from Dumbbell Correlation Method

Figure 7.9 shows the final output imagery for Test Scene 1. The image was constructed by combining three sub-regions, all produced using a dumbbell window size of 31×31 pixels moving in a search area of ±1 pixel. The final output imagery was constructed using raw disparity data (i.e. no smoothing applied), and it can be seen that the geometry is consistent across all the joins between adjacent sub-regions. Figure 7.10 combines the aerial photography (red band) and the final output imagery (green and blue bands) in a colour composite image, and it can be seen that the geometry of the two source images is virtually identical. The only red/blue 'shadows' observed in the composite image data are the result of radiometric differences between the aerial photography and ATM imagery.

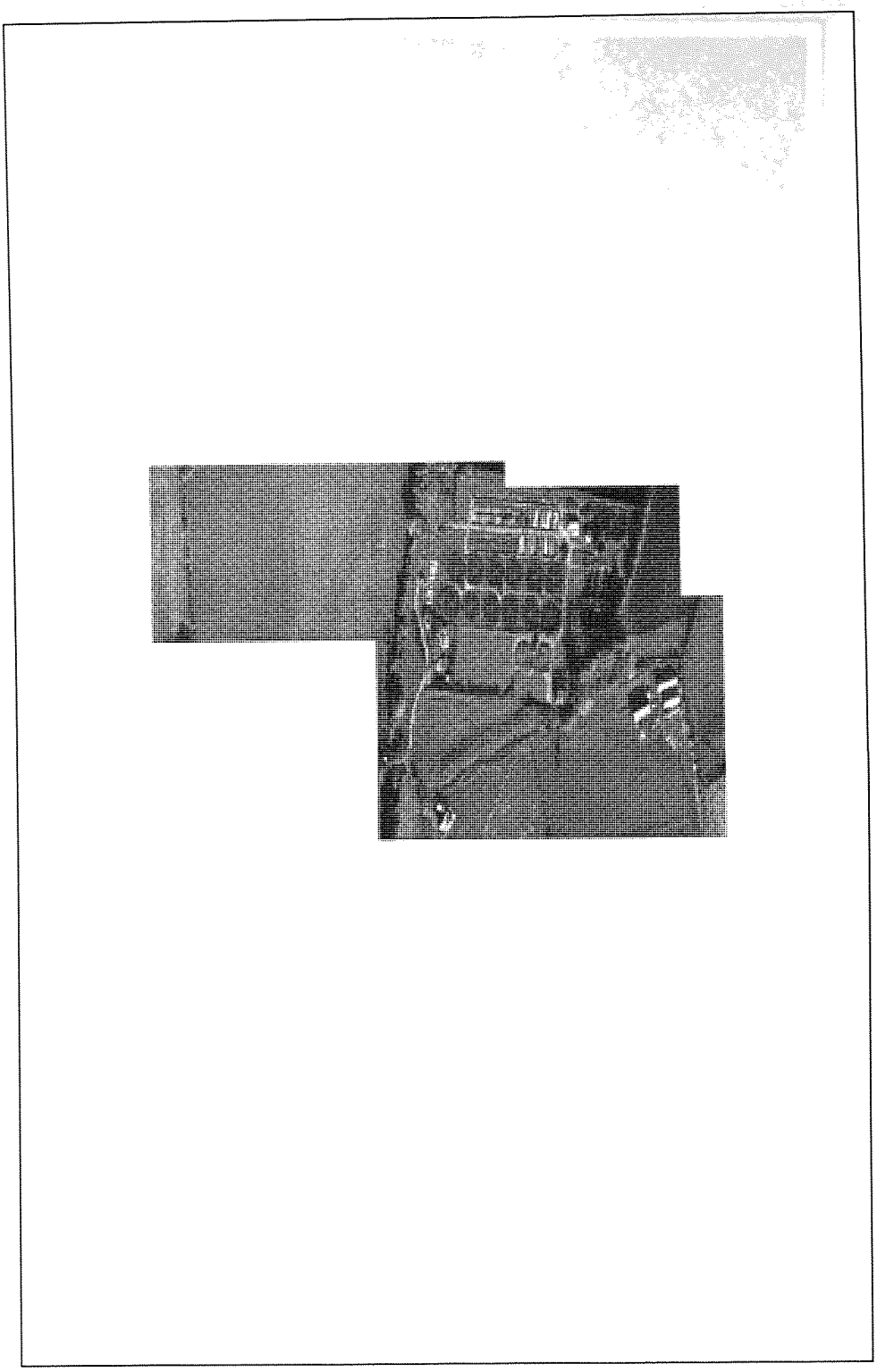

Figure 7.9 Final output image (mosaic) for Test Scene 1.

Figure 7.10 Colour composite image for Test Scene 1 – aerial photography (red) and final output imagery (green and blue).

Figure 7.11 shows the final output image for Test Scene 2. The image is constructed from 4 sub-regions – two of which overlap each other. The final output image is constructed using the raw disparity data which was acquired using a dumbbell window size of 31×31 pixels moving in a search area of ±1 pixel. Again, the geometry is consistent across the join between adjacent sub-regions, and although the imagery suffers from a small amount of noise, the overall geometry is very good. Figure 7.12 shows the colour composite image for Test Scene 2 which demonstrates the close correspondence between the resampled ATM imagery and the aerial photography.

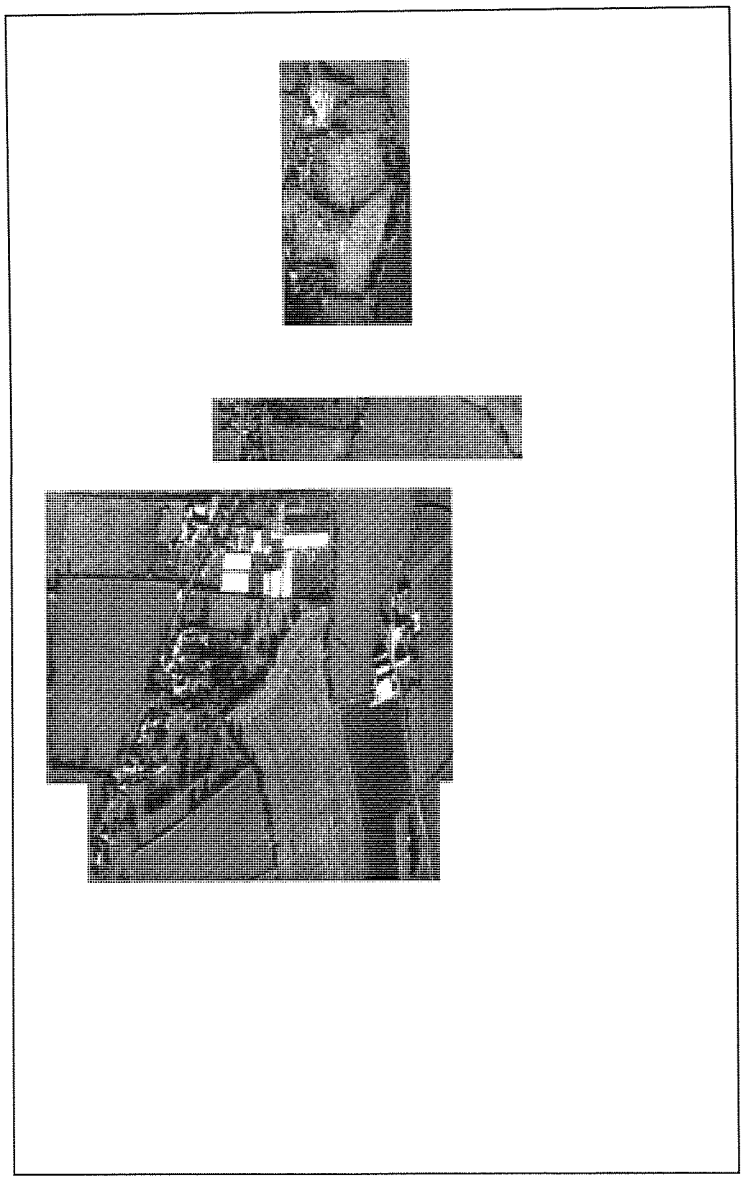

Figure 7.11 Final output image (mosaic) for Test Scene 2.

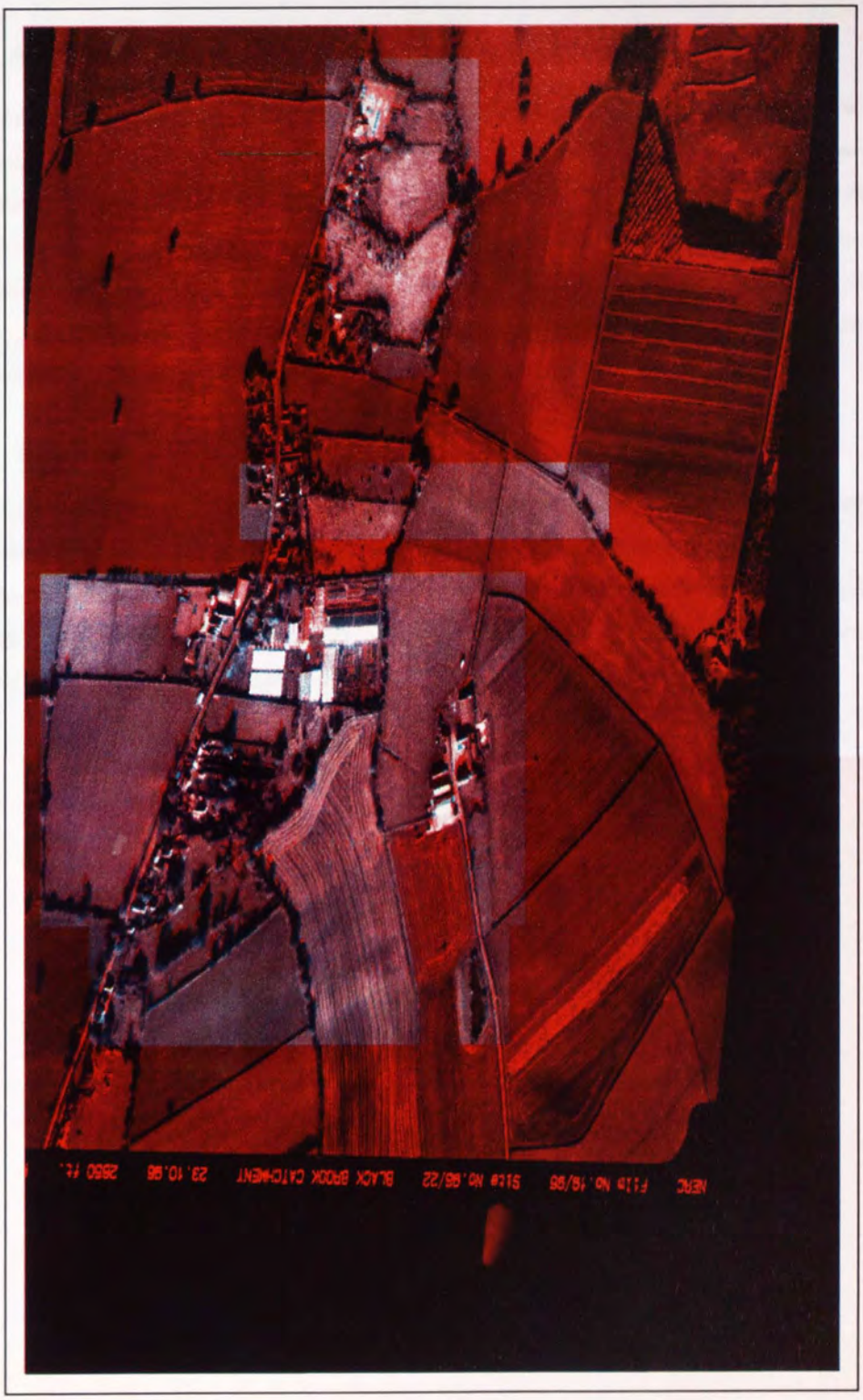

Figure 7.12 Colour composite image for Test Scene 2 – aerial photography (red) and final output imagery (green and blue).

7.3 Application of NERC Parametric Correction

In September 1999, NERC eventually delivered a number of flight lines from the Black Brook data set in a format capable of undergoing the parametric correction using supplied software. The following section briefly describes the application of this correction procedure, and discusses the accuracy of the resulting output imagery. Due to the late delivery of the image data, it was not possible to perform a comprehensive assessment of the geometric accuracy of the corrected image data. However, it was possible to rectify a single flight line, and the following section describes the application of the correction procedure and discusses the accuracy of the resulting output imagery.

7.3.1 Raw Image Data

Figure 7.13 shows the raw ATM data (band 3) for a complete flight line running for approximately 6km in an east-west direction, 2 km north of Shenstone. The imagery was acquired on the 23rd October 1996, and the flight line forms part of the detailed coverage over the Shenstone area (see Figure 3.1). Inspection of the image data reveals that the geometry appears consistent throughout the flight line, and there are relatively few obvious signs of distortions resulting from variations in platform attitude.

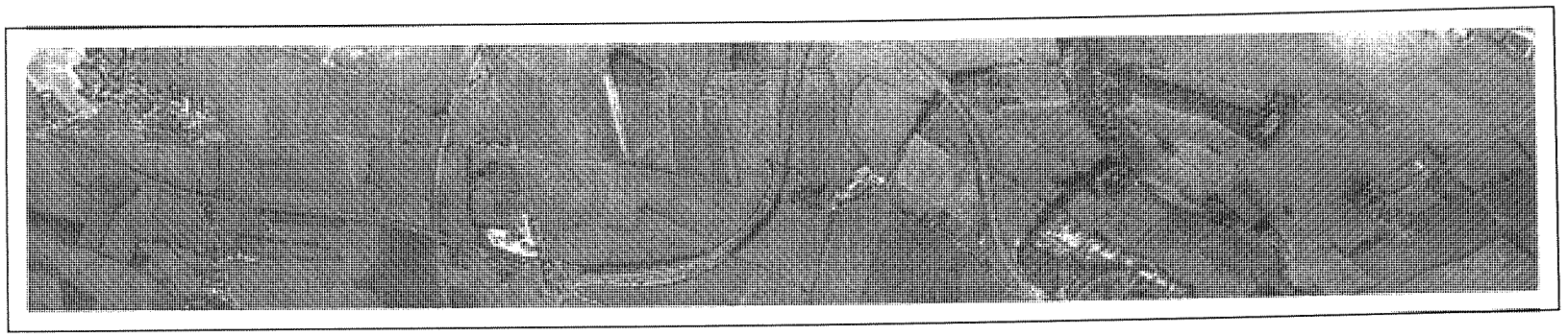

Figure 7.13 Raw ATM image data (band 3) for flight line over Shenstone area.

7.3.2 Application of the NERC Parametric Correction

The NERC parametric correction, called *GCORR*, reads the raw image data (as supplied by NERC) and combines this with post processed navigation data to interpolate the true ground position of each pixel comprising the imagery. Providing a digital elevation model (DEM) of the corresponding region is included in the correction process, the output image product is fully geo-referenced to the pertinent grid co-ordinate system.

Before applying *GCORR* to the flight line illustrated in Figure 7.13, it was necessary to create a DEM of the Shenstone area. This was done by simply measuring the terrain elevation from an Ordnance Survey Pathfinder map (1:25,000) at 1km intervals, and was supplied to the *GCORR* correction program as a flat text file. The output image data was resampled using the nearest neighbour approach with a pixel resolution of 2.5m.

7.3.3 Results from NERC Parametric Correction

Figure 7.14 shows the resulting flight line after application of the *GCORR* correction program. It can be seen that the output image has been padded with null data which highlights the effects of variations in platform orientation on the projected position of each progressive scan line throughout the flight line. Initial observations of Figure 7.14 suggest the overall geometry of the corrected image data is relatively consistent. However, comparison with a digitised map of the corresponding region (Figure 7.15) reveals a marked disparity. Illustrated in Figure 7.14 is a road running at an approximate angle of 10° west, which, when observed in Figure 7.15 runs in a precise north-south direction. This difference in orientation results in positional errors of up to 200-300m, which is obviously unacceptable for any quantitative studies.

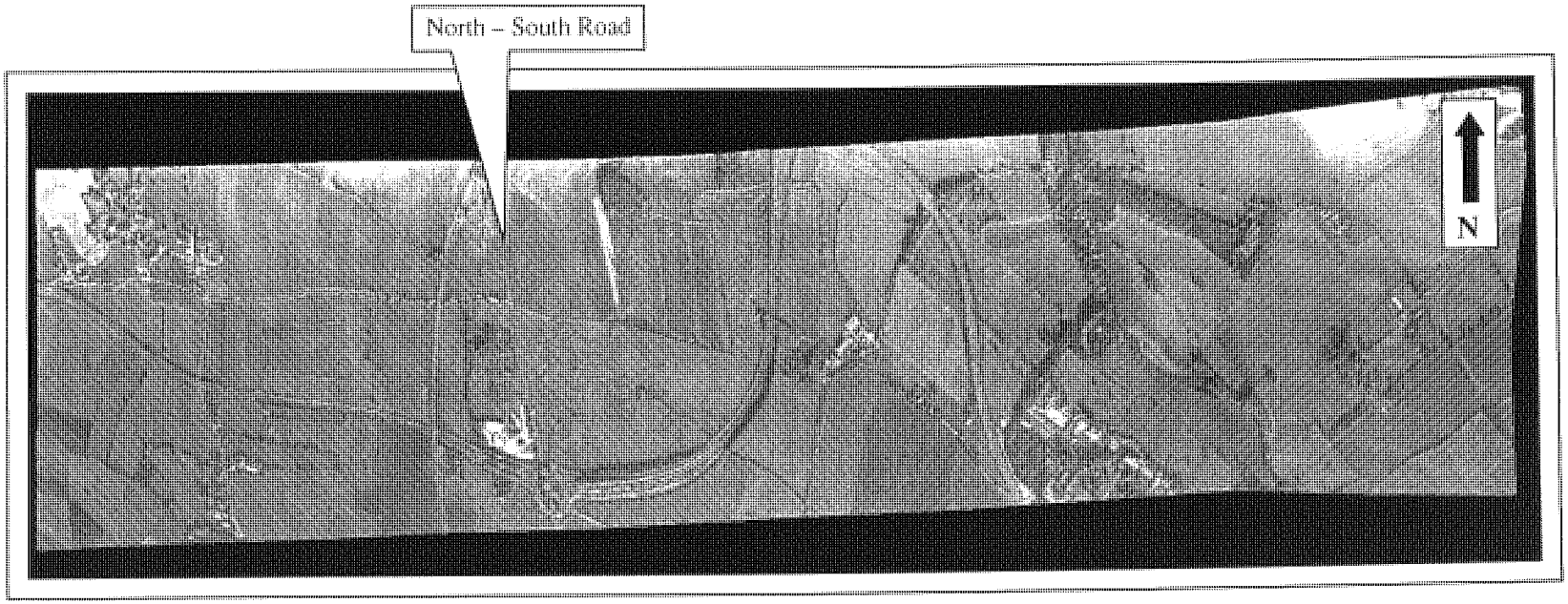

Figure 7.14 ATM image data (band 3) for flight line over Shenstone area, corrected using the NERC parametric correction.

Figure 7.15 Scanned Ordnance Survey map of region corresponding to Figure 7.14.

The errors observed in Figure 7.14 are the result of problems relating to the GPS navigation data. Since acquiring the raw image data, NERC have realised the inherent difficulties in using GPS navigation data alone to geo-rectify airborne line-scanner imagery. The literature reviewed in Chapter 4 reported the success of a number of systems which implemented GPS navigation systems combined with onboard inertial measuring devices. The level of accuracy achievable using this combined approach appears to surpass most other parametric techniques, and NERC have reviewed the configuration of their remote sensing facility and have updated it to include an inertial measuring device in their new Integrated Data System.

7.4 Summary of Results

In verifying the overall success of the Dumbbell Correlation Method a number of test images were extracted from the Black Brook data set. However, because of the delays in receiving the imagery from NERC (the ATM data was not delivered until the autumn of 1999), the only image data available for testing was the aerial photography acquired on the 23rd October, and the ATM imagery acquired on the 8th November 1996. Since the two sets of imagery were acquired on different days, the orientation and geographical coverage were not common. Furthermore, it is evident that the images were acquired at different times of the day as the orientation and magnitude of solar shadows are also disparate.

Despite these obvious complications, the main difficulties in applying the Dumbbell Correlation Method were due to the large fields which dominated the imagery. Even after increasing the size of the data windows, difficulties were encountered when applying the pattern matching routine. In overcoming these problems, the correction technique was only applied to areas in the imagery containing well defined features, and the final output imagery was composed of a mosaic of small sub-regions.

Using this approach, it was found that geometric disparities between the two images could be drastically reduced. Inspection of the colour composite images revealed that registration errors occurred only in a very few isolated areas, and the geometry of the two sets of imagery was generally inseparable.

Application of the NERC parametric correction to a flight line taken from the Black Brook data set indicated that the use of GPS navigation data alone to geo-rectify airborne line-scanned imagery is not sufficient, and this view is further endorsed by NERC's recent introduction of an inertial measuring device to accompany the GPS navigation system.

8. Quantitative Accuracy Assessment

By far the most widely used method of assessing the geometric accuracy of remotely sensed imagery is the root-mean-square error (RMSE), which provides a statistical measure of the correspondence between the position of GCPs common to both the imagery and another reference co-ordinate system. However, it has been shown that the RMSE can under-predict the actual error by up to 40% (see Chapter 4). Furthermore, whilst the RMSE provides a convenient one-value measure of geometric accuracy, it neither tells the observer where the errors are actually occurring, nor provides any information regarding the relative errors between two or more images.

To overcome these problems, a method was developed based on the correlation techniques described in Chapter 6 to determine the positional differences between a reference window in the ATM image and its corresponding location in the aerial photograph. By calculating the positional variations at regular grid nodes throughout the imagery, an overall picture of the magnitude *and* location of image disparities can be developed. Once acquired, this information can then be used to derive a number of different measures of geometric accuracy.

Section 8.1 describes the development and application of this approach to investigate the geometric accuracy of the imagery used in this study. In demonstrating the process, imagery from the Black Country data set was used and the relative accuracy of each alternative method of geometric correction is compared. Section 8.2 provides a quantitative analysis of the registration accuracy for the test imagery taken from the Black Brook data set (detailed in Chapter 7). Finally, the results are summarised in Section 8.3 and a number of conclusions are discussed.

8.1 Accuracy Assessment Using the Correlation Approach

8.1.1 Acquisition of Accuracy Assessment Data

A program called ACCASS.PAS was written in Turbo Pascal to apply the pattern matching routine to the test image data (see Appendix 2 for the complete source code). The theory behind the procedure was identical to that used in the End Correlation Method, except that the reference window was centred at regular grid nodes throughout the ATM imagery rather than at the ends of consecutive scan lines (see Chapter 6).

Before applying the correlation routine to the test image data, it was necessary to select the search parameters – namely the size of the data windows and the extent of the search area. As with the End Correlation Method, the size of the data windows were chosen to reflect the size of features within the imagery, and the search area chosen to reflect the maximum disparities between the imagery. The results from the pattern matching routine were expressed as the two-dimensional co-ordinates of the reference window, along with the Pythagorean distance between the location of the reference and search windows respectively.

8.1.2 Visualisation of Accuracy Assessment Data

Once the disparities between the reference image (ATM) and the search image (aerial photography) had been determined, the output data was analysed using a package called Surfer. Surfer is a surface mapping system which enables a wide range of analytical procedures to be carried out on three-dimensional data sets.

The process of importing the disparity data into Surfer was a straightforward procedure, and once completed, a wide range of surface plots could be generated to visualise the disparities between the test imagery. Figure 8.1 illustrates a simple contour plot of the disparities between the polynomial corrected ATM imagery and the aerial photography taken from the Black Country data set. The size of the data windows used in this procedure were 31×31 pixels, moving in a search area of ±30 pixels. Grid nodes were positioned at a spacing of 30 pixels within the frame illustrated in Figure 8.1.

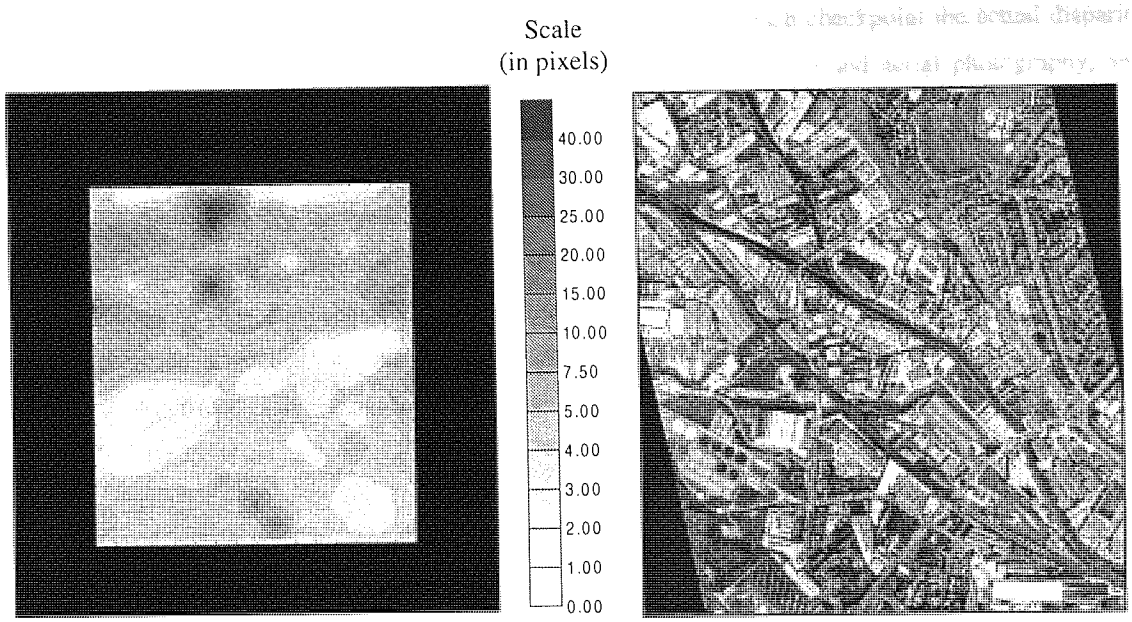

Figure 8.1 Contour plot (left) of image disparities between polynomial corrected ATM imagery (right) and aerial photography.

It can be seen from Figure 8.1 that with the exception of a small number of anomalies, the contours vary gradually throughout the plot. The magnitude of image disparities generally ranges between 2 and 7.5 pixels whilst in a small number of cases the magnitude is less than 2 pixels. The isolated peaks at both the top and bottom of the contour plot suggest image disparities of up to 30-40 pixels, but these are assumed to be the result of mis-correlation during the pattern matching routine rather than true disparity data. As with the End Correlation Method, noise can be identified as a rapid and 'uncharacteristic' deviation from the overall trend, and these peaks should clearly be ignored.

Figure 8.1 is pleasing in that it provides the observer with a quantitative description of both the location and magnitude of image disparities. From the contour plot it can be seen that the smallest disparities between the polynomial corrected ATM imagery and aerial photography are 2 pixels, which leads to the conclusion that the two sets of imagery cannot be overlaid and reliably used for quantitative temporal studies. This is an important conclusion since the standard measure of geometric accuracy, the RSME, provides no such information.

In order to verify the contour plot was a true reflection of the disparities between the imagery, a manual check was carried out. A number of checkpoints were randomly generated such that their co-ordinates fell

within the bounds of the contour plot illustrated in Figure 8.1. For each checkpoint the actual disparity was measured manually between the polynomial corrected ATM imagery and aerial photography, and compared with the disparity interpolated from the contour plot. Table 8.1 illustrates the findings where it can be seen that there is generally a very good correspondence between the manually measured disparities and those determined using the correlation approach. These findings are not surprising since the validity of the pattern matching routine was proven in the End Correlation Method (Section 6.2). The values which do not precisely correspond are believed to be caused by difficulties in manually measuring the image disparities rather than inaccuracies in the correlation routine, since the random checkpoints rarely fell over well-defined, easily recognisable features.

Polynomial Corrected ATM Image		Polynomial Corrected Aerial Photograph		Total Disparity $(\Delta x^2 + \Delta y^2)^{0.5}$	Disparity Interpolated from Contour Plot
Random Co-ordinates		Measured Co-ordinates			
x	y	x	y		
215	160	213	157	3.6	4.5
301	564	305	562	4.5	4.5
535	288	535	293	5.0	3.5
280	309	272	310	8.1	7.0
412	334	419	336	7.3	5.0
437	198	444	197	7.1	7.5
620	193	624	194	4.1	4.0
346	188	342	188	4.0	6.0
383	591	390	587	8.1	8.5
363	524	370	524	7.0	6.0
Average				**5.9**	**5.7**
RMS				**6.1**	**5.9**

Note:
Disparities given in number of pixels.
Co-ordinates refer to *image* system whereby the origin is positioned in the top-left corner - x refers to the row number and y to the column number.

Table 8.1 Verification of accuracy assessment data.

8.1.3 Interpretation of Accuracy Assessment Data

Whilst the contour plot illustrated in Figure 8.1 provides a detailed description of the magnitude and location of image disparities, it does not provide a useful one-value measure of registration accuracy. Conversely, the RMSE offers a convenient measure of the similarity between a remotely sensed image and some other reference co-ordinate system, but it is often criticised for failing to represent the true level of geometric accuracy. One of the main reasons for this is that the RMSE is calculated from relatively very few ground control points located within the imagery. Often, the best points are used in the correction procedure, so identifying reliable independent checkpoints is not always possible.

One of the main advantages of the accuracy assessment procedure based on the pattern matching theory, is that a multitude of checkpoints are used in assessing the geometric similarity between two images. Furthermore, by fitting a surface to these closely spaced checkpoints, the positional disparities for every pixel comprising the imagery (within the bounds of the contour plot) can be estimated. Using this information, it is possible to derive a number of one-value measurements for geometric similarity with far greater reliability than that achievable using a small number of manually identified checkpoints.

Figure 8.2 provides an alternative illustration of the accuracy assessment data shown in Figure 8.1. The peaks caused by mis-correlation have been identified manually and removed from the analysis, and a smooth surface has been plotted to the remaining disparity data.

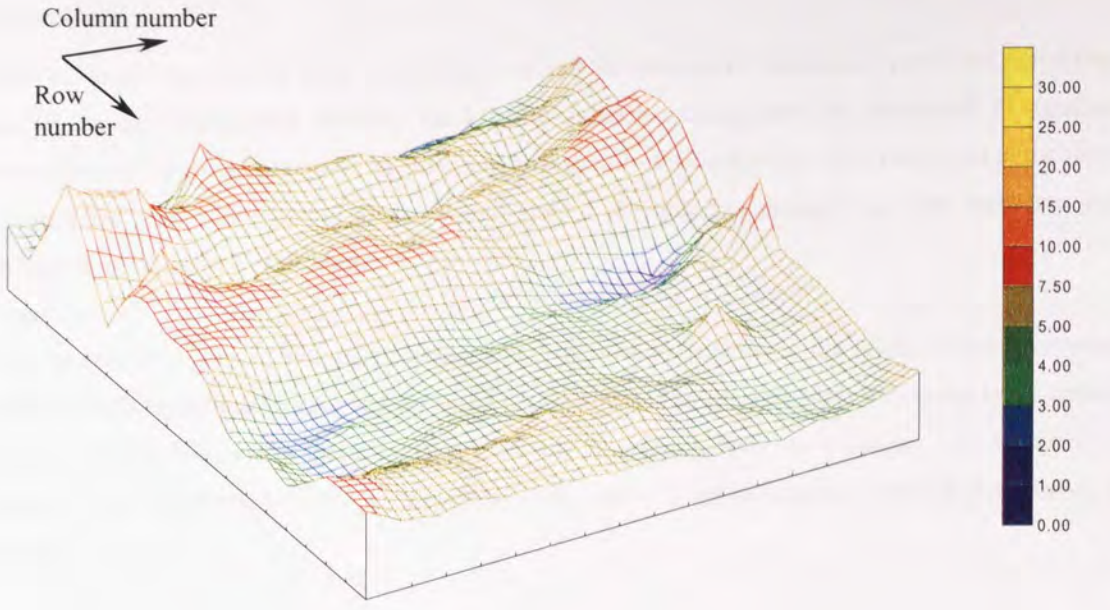

Figure 8.2 Three-dimensional surface plot of image disparities (pixels).

It is easy to visualise from Figure 8.2 that the volume beneath the plotted surface (relative to a zero datum) can be used to represent a total measure of registration accuracy. If the test imagery was precisely registered the volume beneath the surface plot would be zero, and with increasing registration errors this volume increases accordingly. Using this volume measurement it is also possible to determine the average disparity of pixels within the bounds of the surface plot, and this provides a useful indication of the expected level of disparities within the imagery. Since every pixel comprising the surface plot contributes towards the average disparity calculation, the resulting value is far more reliable than that achievable using a small number of manually identified checkpoints.

For the accuracy assessment data shown in Figure 8.2, the total volume beneath the fitted surface was calculated using Surfer, and for the illustrated area (consisting of 560 rows by 480 columns) the total volume was found to be 1,426,590 cubic pixels. The average disparity was found by dividing this total by the product of the number of rows and columns comprising the surface plot, and this gave an average disparity of 5.3 pixels (at an approximate resolution of 1.5m, this represents approximately 8m on the ground). These results provide further confirmation that the test imagery (corrected using the polynomial correction) cannot be overlaid and reliably used for quantitative temporal studies.

8.1.4 Comparison of Registration Errors for Alternative Methods of Geometric Correction

Figure 8.3 shows the contour plots obtained for each of the alternative methods of geometric correction (namely the End Correlation Method, the Line Correlation Method, and the Dumbbell Correlation Method) which were used to register the imagery from the Black Country data set. The extent of the plots are illustrated within the context of the overall size of the reference imagery, as each plot does not correspond to exactly the same region.

It can be seen from Figure 8.3a that considerable disparities exist between the ATM imagery corrected using the End Correlation Method and the aerial photography. The greatest disparities occur in the central region of Figure 8.3a, whilst the imagery is relatively closely registered at the edges. As described in Chapter 6, the distribution of image disparities is the result of approximations made in the correction process.

Figure 8.3b shows the disparities for imagery corrected using the Line Correlation Method, and a completely different distribution of errors can be seen. The central region of the contour plot displays the closest registration, where the magnitude of disparities is generally one pixel or less. Towards the edges of the plot the disparities are seen to increase up to a maximum of 10 pixels. This distribution of disparities was again explained in Chapter 6, and is considered to be caused by difficulties in positioning the ends of each scan line. These errors are averaged out with distance along the scan line from the ends, and effectively cancel each other out towards the centre of the scan line.

Figure 8.3c shows the disparities for imagery corrected using the Dumbbell Correlation Method, and this is the most accurate method of registering the imagery. Large regions of the contour plot are registered with an accuracy of less than one pixel, and with the exception of the peaks caused by mis-correlation, the disparities rarely exceed 1-2 pixels.

Table 8.2 provides a comparison of the one-value measures of registration accuracy for the polynomial correction method, along with each of the alternative methods of image registration. The average pixel disparities clearly show that the Dumbbell Correlation Method is the most accurate method of image registration, giving an average disparity of 1.5 pixels. These results also demonstrate how the registration accuracy has improved with the evolution of each alternative method of image correction.

Black Country Data Set	Total volume beneath fitted surface (cubic pixels)	Coverage of surface plot (rows×columns)	Average disparity (pixels)
Polynomial Correction	1,426,590	540×480	5.3
End Correlation Method	1,994,030	540×480	7.7
Line Correlation Method	600,283	420×510	2.8
Dumbbell Correlation Method	223,410	510×300	1.5

Table 8.2 Comparison of registration accuracy for different methods of geometric correction.

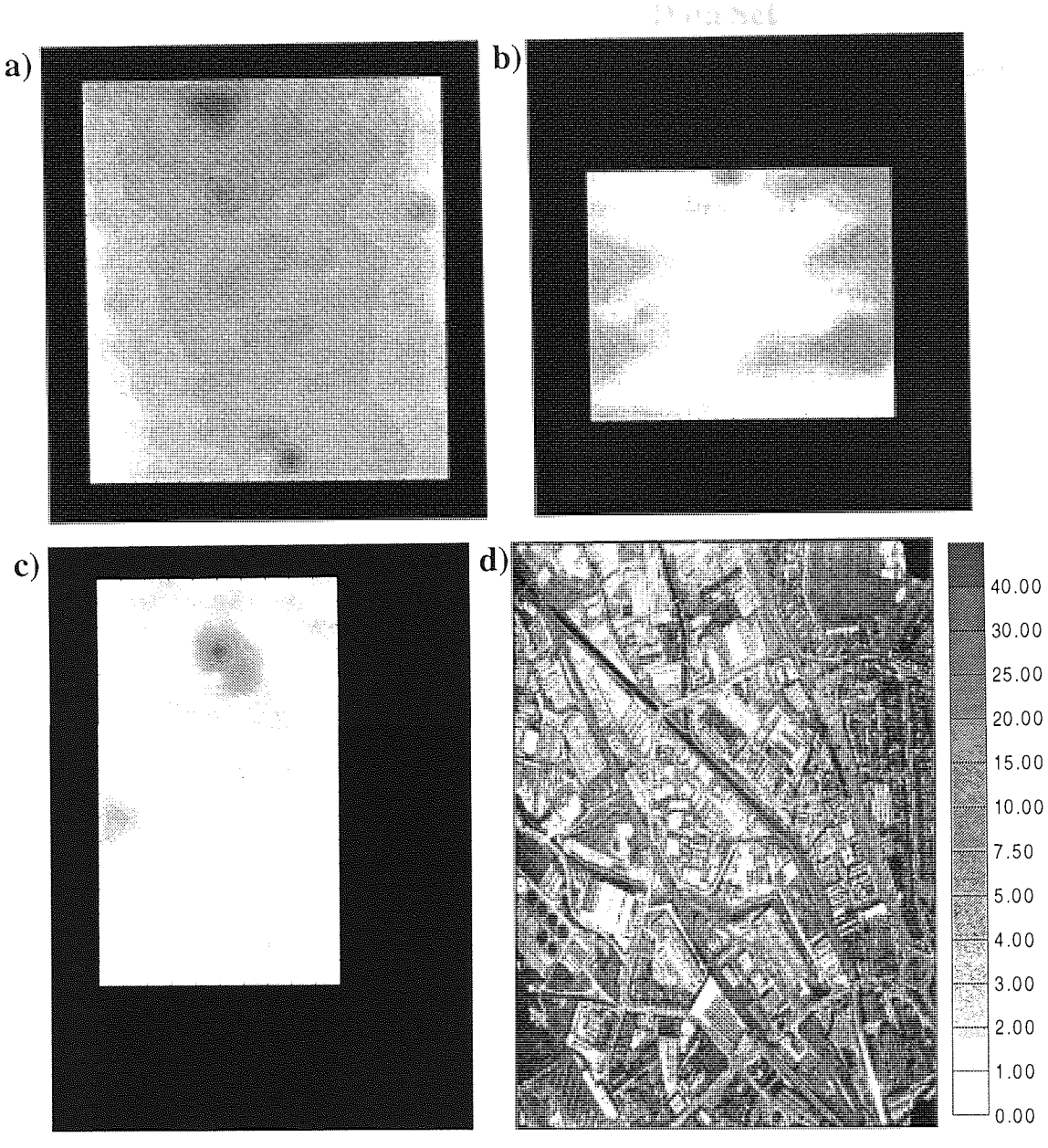

Figure 8.3 Contour plots of disparities (in pixels) identified using **a)** End Correlation Method, **b)** Line Correlation Method, and **c)** Dumbbell Correlation Method. Frame **d)** is the re-scaled aerial photograph which was used as the reference image for the Dumbbell Correlation Method.

8.2 Accuracy Assessment of Black Brook Data Set

Figure 8.4 shows the section of ATM imagery (Test Scene 1) corrected using the Dumbbell Correlation Method, along with the contour plot illustrating the disparities between the ATM imagery and aerial photography. Since the output image was produced as a mosaic of 3 sub-regions, it was necessary to execute two separate passes of the accuracy assessment routine in order to provide complete coverage.

It can be seen from Figure 8.4 that the disparities for the vast majority of the contour plot are less than one pixel. However, there is a notable region in the centre of Area 1 where the disparities are as great as 7.5 pixels. It can be seen from the Figure 8.4a that this region corresponds to a large homogeneous field which has almost no textural or structural detail. However, towards the left of this anomalous area runs a line of hedgerow which provides a well-defined feature on which to determine the registration accuracy. It can be seen from the contour plot that the disparities here are negligible, as are they at the opposite side of Area 1. Since the resampling procedure (during the correction method) interpolates pixel transformations for the centre of a scan line from those defined at the ends, the accuracy assessment data appears inconsistent since the errors in the centre of a scan line should always be less than those at the ends. It can therefore be deduced that the pattern matching routine has encountered difficulties in determining positional disparities over sparse regions (see Section 7.2.2). This anomalous data should therefore be ignored when determining quantitative measures of registration accuracy.

Figure 8.5 shows the contour plot for Test Image 2, which consists of four separate passes of the pattern matching procedure. Again, large regions exist where the disparities between the ATM imagery and aerial photography are less than one pixel. However, the contour plots are scattered with a number of peaks where the magnitude of disparity reaches up to 25-30 pixels. Comparison of Figures 8.5a and 8.5b reveals that these anomalous values again correspond to sparse regions of information in the imagery, and should therefore also be ignored.

Tables 8.3 and 8.4 provide additional one-value measurements of registration accuracy derived from the contour plots. In order to avoid distortion of the volume calculations, the anomalous peaks caused by mis-correlation have been removed from the analysis (Section 8.1.3). The average disparities for test images 1 and 2 are 0.52 and 0.63 pixels respectively, which clearly demonstrates the high level of registration accuracy achievable using the Dumbbell Correlation Method.

In order to provide further verification of the registration accuracy between the test imagery, a number of checkpoints were identified and the co-ordinates measured manually. The positional disparities for the checkpoints were recorded between the raw ATM imagery and the aerial photography, registered using the standard polynomial correction, as well as the ATM imagery corrected using the Dumbbell Correlation Method. Tables 8.5 and 8.6 show the results obtained for Test Image 1 and 2 respectively.

It can be seen that the polynomial correction is capable of registering the test imagery with an average pixel disparity of 9.2 and 8.0 pixels. The average pixel disparity for the checkpoints in the test imagery corrected using the Dumbbell Correlation Method is 0.5 pixels (for both images). These results clearly demonstrate the superiority of the Dumbbell Correlation Method in registering airborne line-scanned imagery to the corresponding aerial photography.

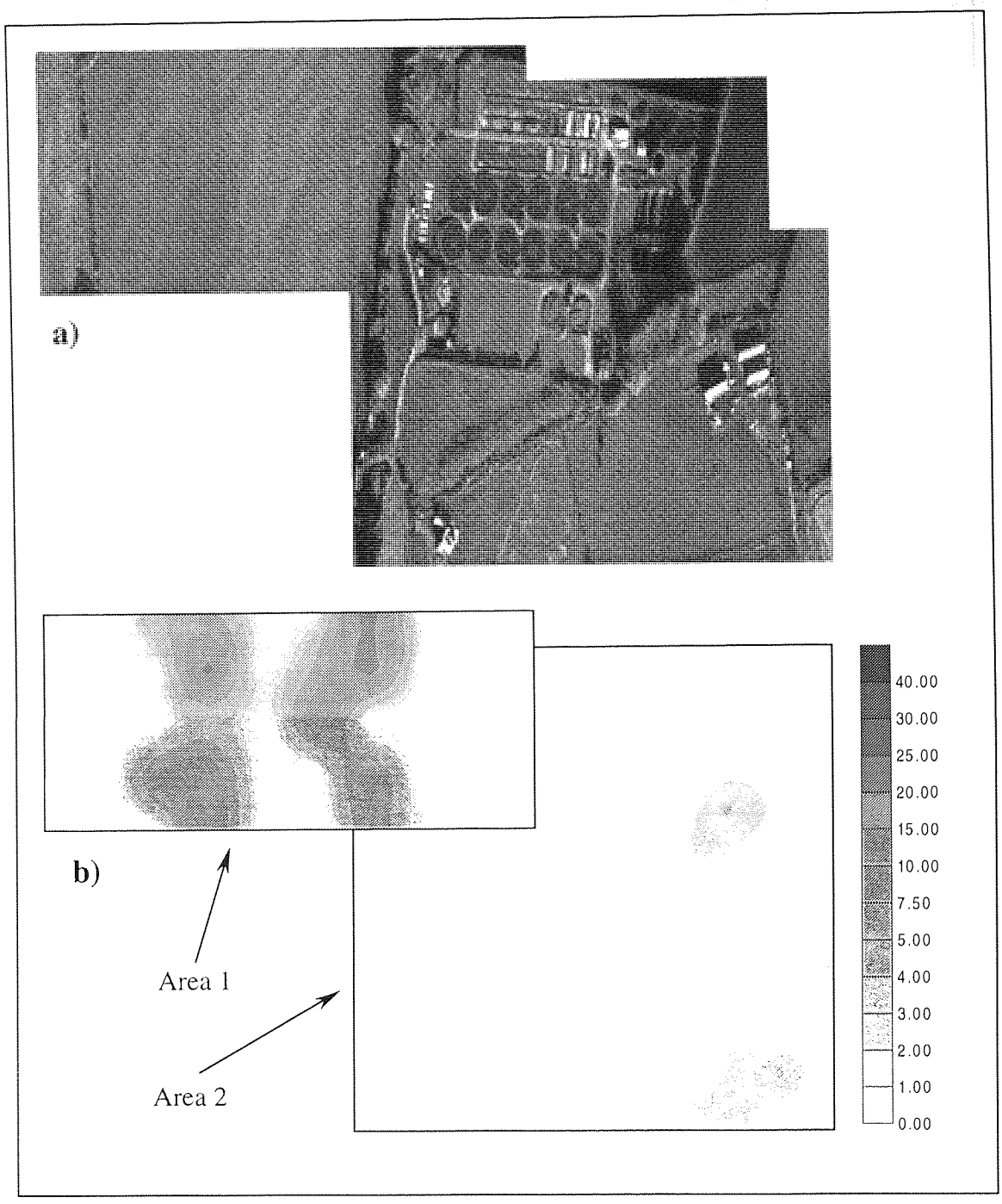

Figure 8.4 **a**) Section of Test Image 1 corrected using Dumbbell Correlation Method and **b**) the corresponding contour plot of disparities (pixels)between ATM imagery and aerial photography.

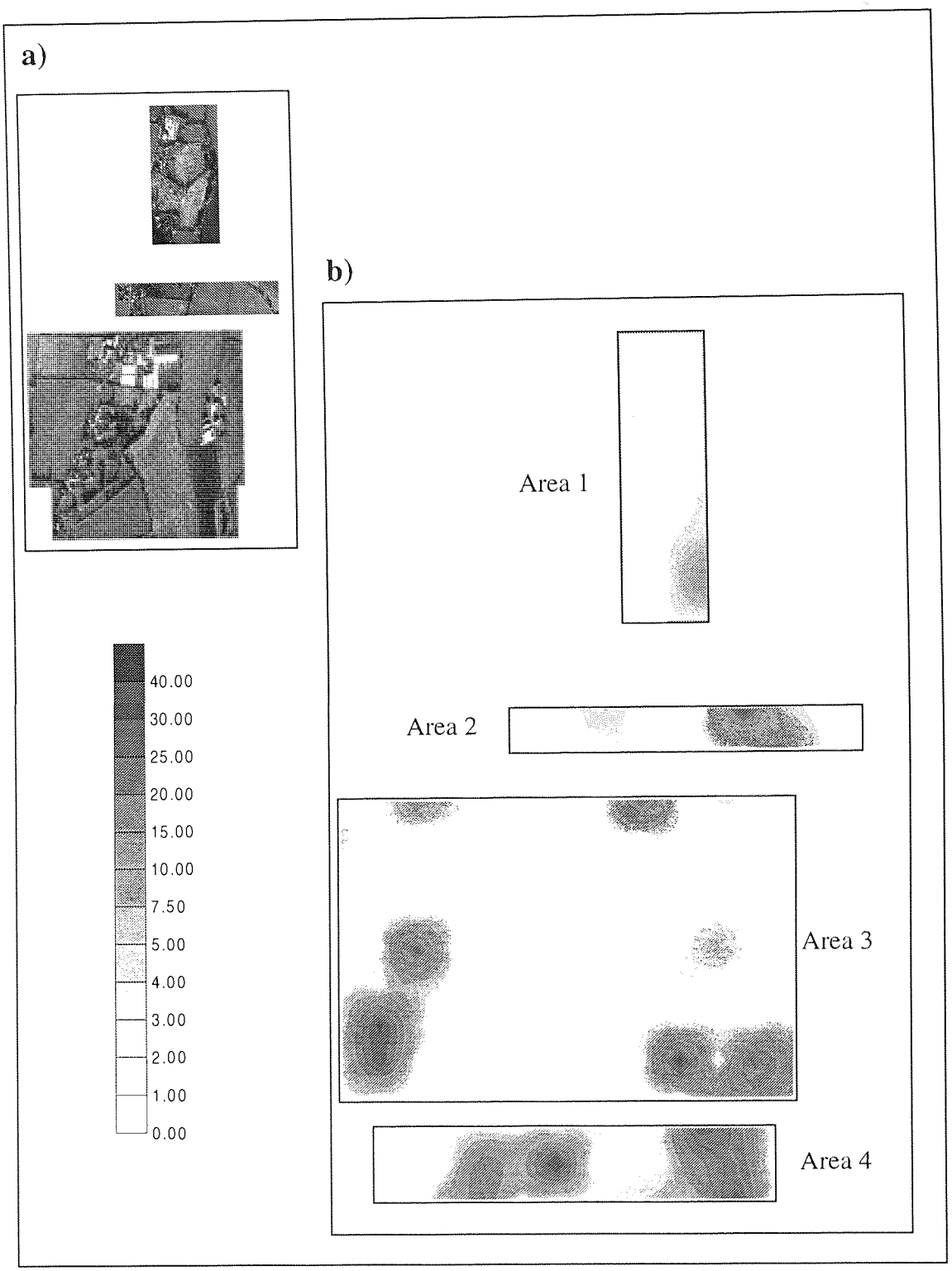

Figure 8.5 a) Test Image 2 corrected using Dumbbell Correlation Method and **b)** the corresponding contour plot of disparities (pixels) between ATM imagery and aerial photography.

Test Image 1	Coverage (rows×columns)	Total Volume (cubic pixels)	Average Disparity (pixels)
Area 1	120×270	27077	0.8
Area 2	270×270	28187	0.4
Total		55264	**0.5**
Note: Disparities given in number of pixels.			

Table 8.3 Registration accuracy for Test Scene 1.

Test Image 2	Coverage (rows×columns)	Total Volume (cubic pixels)	Average Disparity (pixels)
Area 1	210×60	10954	0.9
Area 2	30×270	5102	0.6
Area 3	240×360	42083	0.5
Area 4	60×320	21281	1.1
Total		79420	**0.6**
Note: Disparities given in number of pixels.			

Table 8.4 Registration accuracy for Test Scene 2.

Aerial Photograph		Raw ATM Imagery		Total Disparity $(\Delta x^2 + \Delta y^2)^{0.5}$	Dumbbell Corrected ATM Imagery		Total Disparity $(\Delta x^2 + \Delta y^2)^{0.5}$
Checkpoint Co-ordinates		Checkpoint Co-ordinates			Checkpoint Co-ordinates		
x	y	x	y		x	y	
471	373	479	372	8.1	471	373	0
432	482	440	481	8.1	433	482	1.0
602	527	610	524	8.5	601	527	1.0
689	369	697	369	8	689	369	0
569	362	581	360	12.2	569	363	1.0
538	444	548	441	10.4	538	444	0
Average				**9.2**	**Average**		**0.5**
RMS				**9.3**	**RMS**		**0.7**

Note:
Disparities given in number of pixels.
Co-ordinates refer to *image* system whereby the origin is positioned in the top-left corner - x refers to the row number and y to the column number.

Table 8.5 Image disparities for Test Scene 1

Aerial Photograph		Raw ATM Imagery		Total Disparity $(\Delta x^2 + \Delta y^2)^{0.5}$	Dumbbell Corrected ATM Imagery		Total Disparity $(\Delta x^2 + \Delta y^2)^{0.5}$
Checkpoint Co-ordinates		Checkpoint Co-ordinates			Checkpoint Co-ordinates		
x	y	x	y		x	y	
252	274	236	273	16.0	253	274	1.0
83	297	95	297	12.0	83	297	0
420	222	414	221	6.1	421	222	1.0
411	242	404	240	7.3	411	242	0
548	202	547	199	3.2	548	202	0
563	385	564	383	2.2	564	385	1.0
774	95	786	95	12.0	774	95	0
847	394	852	393	5.1	846	394	1.0
Average				**8.0**	**Average**		**0.5**
RMS				**9.2**	**RMS**		**0.7**

Note:
Disparities given in number of pixels.
Co-ordinates refer to *image* system whereby the origin is positioned in the top-left corner - x refers to the row number and y to the column number.

Table 8.6 Image disparities for Test Scene 2

8.3 Summary of Quantitative Accuracy Assessment

The alternative methods of geometric accuracy assessment developed in this chapter enable registration errors between two or more images to be visualised and understood far more clearly than that achievable using the standard measure or RMSE. The contour plots indicate both the location *and* magnitude of image disparities, and these can be developed using a fully automated process. Furthermore, the use of pattern matching techniques to identify image disparities enables a far greater number of checkpoints to be used in the assessment of registration accuracy. Measures of geometric accuracy using this approach are therefore more reliable than those determined using a very small number of checkpoints located in the imagery.

By fitting a surface to the accuracy assessment data, it is also possible to estimate the disparities associated with every pixel comprising the surface plot. This information can then be used to generate a number of one-value measures of geometric accuracy – total volume measures beneath the fitted surface to indicate the relative accuracy between two or more registered images, and the average disparity indicating the expected level of disparity within overlaid images.

Using these measures of accuracy assessment it has been shown that the Dumbbell Correlation Method can register line-scanned imagery to corresponding aerial photography with a far greater level of precision than that achievable using standard polynomial approaches. Furthermore, the Dumbbell Correlation Method can be applied without the need for platform attitude information and is almost fully automated.

9. Application of Correction Model to Dawn Imagery

The original aim of this research project (described in Chapter 1) was to use the NERC GPS-corrected line-scanned imagery to obtain a detailed understanding of the information carried within the thermal wave band. However, the problems encountered by NERC in pre-processing the image data resulted in considerable delays in receiving the imagery. As a direct result of these delays the main thrust of the research project was redirected, towards the end of 1997, to investigate alternative methods of rectifying and co-registering airborne line-scanned imagery.

In respect of the original aim of the research project, one of the main reasons for developing such rectification procedures was to enable daytime and dawn thermal image pairs to be accurately co-registered, allowing thermal inertia images of the study area to be created. Whilst it has been shown in the previous chapters that daytime ATM imagery can be successfully registered with corresponding aerial photography, the spectral characteristics of the dawn image data are significantly different to those of the daytime imagery, and the methods of image correction based on pattern matching do not lend themselves directly to the dawn image data.

The main problems are caused by the absence of image data in the visible spectral wave bands, and as there are no other common wavebands between the aerial photography and dawn ATM imagery, geometric disparities can not be reliably determined using simple correlation techniques. Whilst the ATM thermal band does contain exploitable data for both daytime and dawn imagery, the thermal signatures are vastly different during the pre-dawn and midday periods and therefore a direct correlation may not yield satisfactory results. The current chapter therefore provides a discussion of a number of techniques which were implemented in an attempt to overcome these difficulties.

9.1 Standard Pattern Matching

The use of pattern matching routines to identify image disparities was described in Chapter 6. In applying the correlation function it was necessary to split the aerial photography into its component wavebands (red, green and blue), and correlate the green band of the aerial photography with that of the ATM imagery (band 3). However, since the only available waveband in the dawn ATM imagery is thermal, it is not possible to register the ATM imagery directly to the aerial photography using pattern matching techniques. Nevertheless, assuming that the midday ATM imagery (all spectral wavebands) has been successfully registered to the aerial photography using the methods described previously, the daytime image data may then be used as the reference data set on which to correlate the dawn imagery, and it is therefore theoretically possible to apply the pattern matching routine to the common thermal wavebands.

However, daytime and dawn thermal imagery often have widely varying thermal responses due to both the effects of differential heating at the earth's surface and the varying thermal capacity of surface features – indeed, this is the very phenomenon under investigation. Figure 9.1 illustrates the difference between a section of raw ATM imagery acquired at midday and dawn. Whilst the structure of the features held within the corresponding daytime and dawn thermal imagery are common, the thermal response is markedly different for each image.

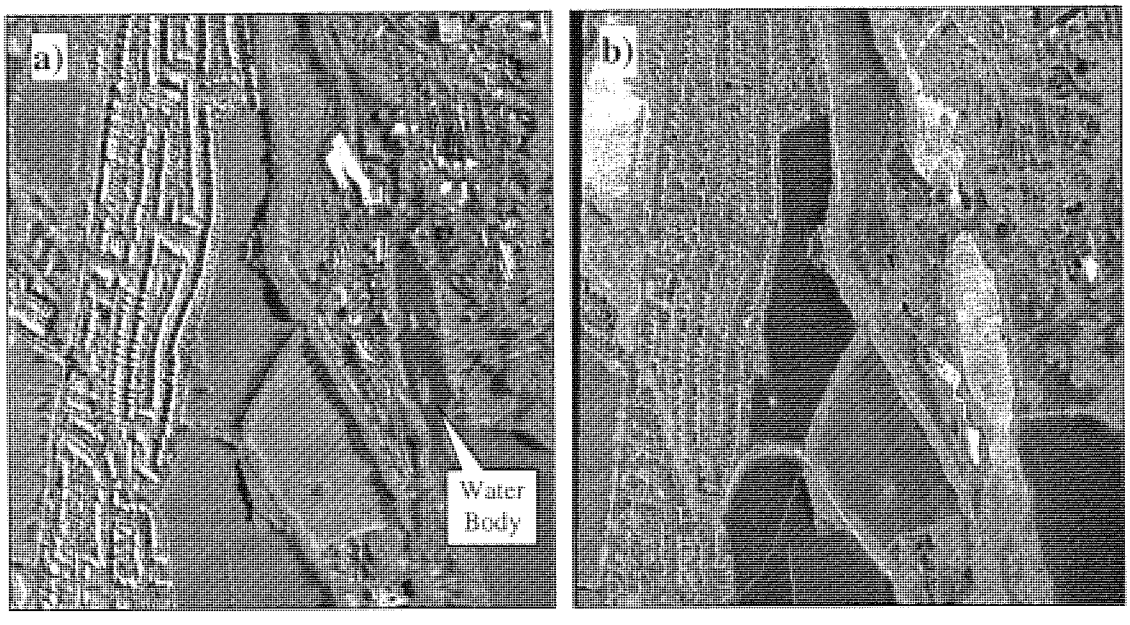

Figure 9.1 Thermal image data over Black Brook catchment acquired at a) midday and b) dawn.

The thermal properties of water were examined in Chapter 2, where it was found that the unusually high values of heat capacity led to high thermal inertia (i.e. its resistance to changes in temperature). The temperature of water therefore remains relatively static throughout a diurnal cycle, whilst that of surrounding materials has a far greater variation. This phenomenon can be seen in Figure 9.1, where the water body (illustrated) is seen to display a relatively low thermal response in the daytime imagery (dark colour) whilst in the dawn imagery, the water body is relatively warm (bright). Accordingly, the presence of water in other surface materials (such as soil) influences the temperature in a similar way, therefore creating contrasting thermal responses during the daytime and dawn periods.

The numeric value of the correlation coefficient used in the pattern matching routine varies from +1.0, indicating a perfect match, to –1.0, indicating one pattern is the negative of the other. Since the dawn thermal response for water is effectively a negative image of the daytime thermal response, it was felt that the standard correlation function could be used whereby a successful match is defined by the greatest *magnitude* of correlation coefficient. A high negative correlation would therefore define an equally successful match of data windows as a high positive correlation, overcoming the diurnal contrast in surface temperature between daytime and dawn thermal imagery.

The program code for the Dumbbell Correlation Method was therefore modified to reflect these changes, and the technique applied to the daytime – dawn thermal image pairs. However, after experimenting with a range of search parameters it was concluded that the modified pattern matching routine was not able to accurately determine the true nature of disparities between the thermal image pairs. Although the observed thermal response over water does display considerable variation at midday and dawn (relative to surrounding features in an equalised thermal image), many areas of the imagery do not show such a wide contrast, and the correlation coefficient over these regions was consequently low. This approach was therefore not developed further.

9.2 Co-Registration Using Classified Image Data

In an attempt to overcome the spectral variations between midday and dawn thermal imagery, it was decided to perform a classification of the image data prior to executing the pattern matching routine. Since the structure of the image data was consistent between the two images (subject to platform attitude errors), it was felt that the pattern matching routine needed to take advantage of this structural similarity. By classifying the daytime and dawn thermal image data prior to correction, it was hoped to give common

surface features the same classification, therefore eliminating the tonal differences associated with contrasting diurnal thermal signatures.

A number of classification techniques were applied to the thermal image data and the pattern matching routine carried out using the resulting classified ATM imagery. However, problems were immediately encountered using this approach. Firstly, classification errors meant that corresponding features in the thermal image pairs were not always allocated to the same class. This had obvious implications on the reliability of the pattern matching routine which was not able to identify a successful match between the same features. Gradual spatial boundaries within the imagery were also not identified consistently in both thermal images, and this resulted in similar pattern matching problems. Furthermore, the classification procedure actually removed a vast amount of detail from the imagery, and very often the data windows used in the pattern matching routine fell within large homogeneous regions where it was impossible to obtain sensible disparity data. This approach was therefore not considered further.

9.3 Co-Registration Using Edges

The only feature which is unequivocally common to both the daytime and dawn thermal imagery is the structure of the objects within the imagery (subject to platform attitude errors). It was therefore felt that to successfully identify the geometric disparities between the image data, the pattern matching routine must exploit this similarity. In order to extract the structural information from the imagery it was decided to apply an edge detection algorithm prior to executing the pattern matching routine. The Canny edge detector, a standard approach used widely in the field of remote sensing (Canny, 1986), was applied to the test imagery acquired over the Black Country.

For the purpose of demonstrating this approach, the edge detection algorithm was applied to the green spectral wave bands of the ATM imagery (band 3) and corresponding aerial photography – see Figures 6.1 and 6.2 for an illustration of the raw image data. Figure 9.2 shows the edge detected imagery, from which it can be seen that the tonal content of the imagery has been completely removed, leaving purely structural information.

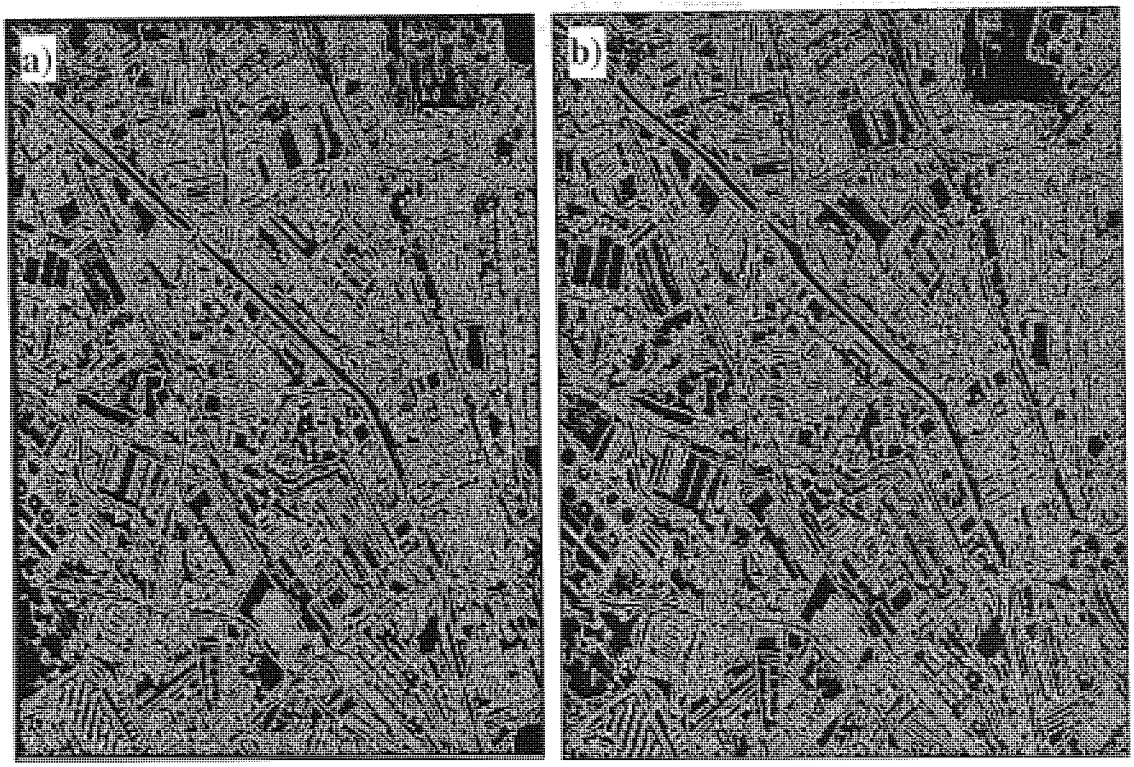

Figure 9.2 Edge detected imagery from Black Country data set; a) aerial photography and b) raw ATM imagery.

The Dumbbell Correlation Method was applied to the images shown in Figure 9.2 with a range of different window sizes. After resampling the output imagery it was found that, regardless of the size of the data windows, the correlation routine was not able to identify the true nature of image disparities. Figure 9.3 illustrates the resulting ATM imagery after applying the Dumbbell Correlation Method. It can be seen that the image geometry remains considerably distorted; for example, the correction procedure has failed to remove the geometric errors associated with the canal junction in the centre of Figure 9.2. Further inspection of the output imagery revealed substantial registration errors when compared with the aerial photography. It was therefore concluded that using this edge detection approach, the reliability of the Dumbbell Correlation Method was not improved when compared to standard approaches, and without significant additional work the dawn thermal imagery could not be registered to the aerial photography with a satisfactory level of accuracy.

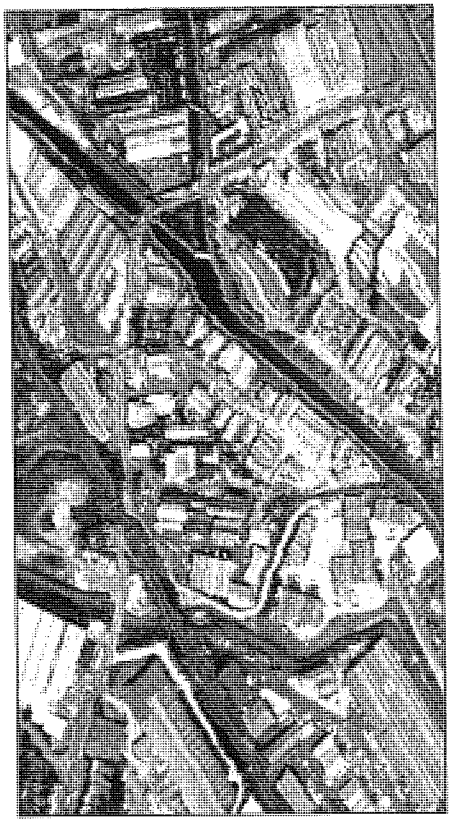

Figure 9.3 Section of ATM imagery corrected using the Dumbbell Correlation Method on edge detected source imagery.

9.4 Summary

Due to the absence of any usable data in the visible spectral wave band, it is not possible to identify image disparities by comparing the geometry of the line-scanned imagery to aerial photography using a simple pattern matching approach. A number of alternative techniques were therefore developed in an attempt to improve the pattern matching routine – these involved both pre-processing the image data as well as altering the way in which the correlation coefficient was calculated. Despite these modifications, none of the methods described in this chapter were capable of correcting and registering the dawn thermal imagery to a satisfactory degree of accuracy. Due to the time constraints it was not possible to investigate further methods for rectifying dawn thermal imagery with corresponding aerial photography.

10. Discussions

Chapter 5 described the main theoretical considerations in developing an alternative approach for rectifying airborne line-scanned imagery. It was proposed that by directly comparing the geometry of line-scanned imagery with simultaneously acquired aerial photography, the effects of variations in platform attitude could be isolated and rectified. By making the assumption that scan lines are straight, and platform attitude errors occur purely on a line-by-line basis, the number of GCPs required to describe image distortions was significantly reduced. The following chapter provides a discussion of the main issues which have arisen during the course of this research project. The strengths and weaknesses of each method of geometric correction are evaluated, and a number of recommendations for future study are made.

10.1 Identification of Image Disparities

The key stage for any method of rectifying remotely sensed imagery is the identification of the position and magnitude of geometric errors since it is impossible to reconstruct the geometry to a satisfactory level of accuracy without fully understanding the true nature of image distortions. The End Correlation Method is described in Section 6.2, and after applying the pattern matching routine to the image data, geometric distortions were visualised by plotting the magnitude of row and column disparities against row number (Section 6.2.2.3). Ignoring the presence of noise, image disparities varied smoothly throughout the imagery, and these were considered consistent with distortions expected from a line-scanning sensor mounted on an aircraft platform. However, before the disparity data could be used to rectify the line-scanned imagery, it was necessary to remove the presence of noise and a number of techniques were investigated. Section 6.2.3 describes the development of a semi-automated procedure enabling a cubic spline to be fitted to a series of 'correct' points selected from the disparity data.

The End Correlation Method is reviewed in Section 6.2.6, where it was concluded that although the pattern matching routine was able to accurately identify image disparities, the process of removing noise was somewhat cumbersome. Firstly, the technique was not fully automated (or had the potential to be fully automated) and therefore required human intervention which is generally time-consuming when compared to the speed with which automated procedures can be executed. Furthermore, after comparing the original and smoothed disparity data it was found that there were a number of instances where the fitted curve deviated, albeit by a small amount, from the original data. The presence of errors in the

disparity data directly influences the accuracy of the final output imagery, so it is important to minimise these errors prior to reconstructing the line-scanned imagery.

The second approach of geometric correction, the Line Correlation Method, was more simplistic than the End Correlation Method, and using pattern matching techniques positioned raw ATM scan lines directly onto a reference image provided by a rectified aerial photograph (Section 6.3). A key aspect of this approach is that scan lines are effectively one-dimensional elements so there was no need to align the scale and orientation of the imagery prior to applying the correlation routine. Furthermore, after manually positioning the first scan line on the aerial photography, the position of the next is, by definition, very close to the previous, and the search area for the pattern matching routine can be constrained to one or two pixels. However, whilst the efficiency of the correction procedure was improved significantly there was an increased risk that once a scan line was positioned incorrectly (due to mis-correlation), the true position of the next scan line lay outside the boundaries of the search area. If this situation occurred, subsequent scan lines were placed based on the best 'mis-correlation', reducing the accuracy and reliability of the disparity data.

Results for the Line Correlation Method are described in Section 6.3.2. It was found that although the Line Correlation Method overcame differences in scale and orientation between the imagery, the disparity data suffered from the high occurrence of noise caused by mis-correlation. However, the characteristics of noise were significantly different to those for the End Correlation Method, which was attributable to the constraints imposed on the search area during the pattern matching routine. The effects of noise were removed using a number of automated procedures, and these were described in Section 6.3.3.

The Line correlation Method is reviewed in Section 6.3.4 where it was concluded that the positioning of the ends of each scan line was a critical aspect of the correction procedure, since geometric transformations for all pixels belonging to a scan line are interpolated from those defined at the ends. It was felt that to improve the quality of the output imagery it was necessary to add greater emphasis to the ends of scan lines during the pattern matching routine.

Section 6.4 describes the final approach, the Dumbbell Correlation Method, which, by representing scan lines using a dumbbell shape provided greater weighting to the end positions during the calculation of the correlation coefficient. The inclusion of these additional data windows meant that scan lines were no longer one-dimensional elements and it was again necessary to align the scale and orientation of the photography and ATM imagery to enable pattern matching procedures to be used. However, in order to preserve the scan line – pixel row correspondence in the ATM image data, the aerial photography was

registered to the raw ATM imagery using a first order polynomial correction. Individual scan lines (represented by a dumbbell shape) were then drawn from the raw ATM imagery and positioned on the aerial photography in an identical manner to that in the Line Correlation Method.

Results are illustrated in Section 6.4.2, where it was clearly observed that the use of a dumbbell shape during the pattern matching routine had a marked effect on the reduction of noise. The occurrence of gaps and bunches between scan lines were almost completely removed, and the 'stability' of the scan line plot was far more consistent than that observed for the Line Correlation Method.

10.2 Reconstruction of the Line-Scanned Imagery

The process of compensating for geometric disparities and resampling to the output grid was examined in Chapter 6, and is virtually identical for each of the methods of geometric correction described in this thesis. It was concluded in Chapter 4 that the most preferred resampling technique is the backward nearest neighbour approach due to the computational efficiency and preservation of raw pixel values. A routine was therefore written in Turbo Pascal to reconstruct the geometry of the ATM image data using this method, and the main theoretical considerations were illustrated and described in Section 6.2.4.

One of the main difficulties encountered whilst developing the resampling procedure was minimising the amount of processing time required to produce the final output imagery. The assumption that scan lines are straight allowed the resampling process to be broken down into two stages, and this greatly increased the speed of the resampling procedure. The first stage determined which source scan line projected the closest to the target pixel (after applying positional transformations to compensate for image disparities), and the use of equations of a straight line to represent scan lines enabled this to be determined extremely rapidly. The second stage of the resampling procedure was to determine the co-ordinates of the source pixel which projected the closest to the target pixel, and as stated previously, this was interpolated from the end positions of the scan line.

In order to qualitatively assess the geometric accuracy of each correction procedure, colour composite images were created by observing the reconstructed ATM imagery and the aerial photography through different coloured guns of the VDU display. The internal structure of each source image was visible in the resulting composite image, and this provided a clear indication of the nature of geometric disparities between the two images.

Figures 6.11, 6.16 and 6.23 show the colour composite for each method of geometric correction, and comparison demonstrates the Dumbbell Correlation Method was the most successful at registering the ATM imagery with the aerial photography. The visual quality of the output imagery was effected, to some degree, by the presence of noise (Figure 6.22) in the disparity data. However, the output imagery was resampled using unmodified disparity data, so it is expected that the quality could be improved significantly by using the methods of noise reduction described in Section 6.3.3.

10.3 Quantitative Accuracy Assessment of the Output Imagery

A method for quantitatively assessing the registration accuracy between the reconstructed ATM imagery and the corresponding aerial photography was developed using the pattern matching theory developed for the End Correlation Method (Chapter 8). This approach provides a unique indication of the location *and* magnitude of registration errors, enabling the reliability of the imagery for quantitative temporal studies to be assessed. Although this technique is almost completely automated, there are a number of limitations with its use. Since the approach exploits the pattern matching theory developed for the End Correlation Method, it is therefore also subject to similar problems, particularly those of mis-correlation over sparse regions. Furthermore, this technique can only be applied to image data which has a corresponding reference image against which to compare the geometry. The procedure simply provides an indication of the registration accuracy between two or more images, and, assuming that the reference image represents a digital map, registration errors then correspond to actual geometric errors.

Section 8.1.4 describes the registration accuracy for each of the alternative methods of geometric correction. From the two-dimensional surface plots (Figure 8.3) it was obvious that the Dumbbell Correlation Method was able to register the Black Country imagery with the highest level of accuracy, whilst the End Correlation Method was the least successful technique, being out-performed even by the polynomial correction. The two-dimensional surface plots also illustrate the distribution of registration errors, and these provided a clear indication as to which areas of the imagery could be overlaid and used for temporal studies. This is a key feature since conventional methods of accuracy assessment provide no such information. Finally, the average registration accuracy was determined for each method of geometric correction (Table 8.2), and these again confirmed that the Dumbbell Correlation Method was able to register the test imagery with the highest level of accuracy.

10.4 Rectification of Black Brook Imagery

Due to the problems suffered by NERC in pre-processing the Black Brook image data, the development work for each method of geometric correction was initially carried out on imagery acquired previously within the department, namely the Black Country data set. It was shown in Section 6.2 that the pattern matching routine performed extremely well over the densely packed industrial and residential buildings of the Black Country. However, when the method was extended to the Black Brook data set (Chapter 7), difficulties were encountered over regions of the imagery where the frequency of spectral variations was low. Whilst the Black Country data set consisted primarily of buildings which have a relatively rough texture, the Black Brook data set was composed largely of open fields, the interior of which have a relatively smooth texture. When the pattern matching routine was applied to these regions, the value of the correlation coefficient was influenced by spectral variations associated with subtle features such as vegetation cover and soil moisture. These features are not well defined and since the aerial photography and ATM imagery do not share identical spectral wave bands, they are not consistent to both sets of imagery. The positional disparities identified using the pattern matching technique over sparse regions did not therefore accurately represent the true nature of geometric errors between the two sets of imagery. This is an problem inherent to the pattern matching routine, and clearly, any method of geometric correction which relies on the use of pattern matching procedures to identify GCPs is subject to problems of this nature.

Further difficulties were encountered due to the temporal nature of the Black Brook data set. Since the aerial photography and ATM image data were acquired at different times of the day (and on separate days), the orientation of solar shadows was not consistent between the imagery. Since shadows tend to produce well-defined, high frequency features they therefore have a considerable influence on the value of the correlation coefficient. The geometric disparities identified using the pattern matching procedure were therefore more representative of differences in orientation of solar shadows rather than true geometric errors.

Similar problems were encountered when attempting to register the daytime and dawn thermal imagery. Due to the effects of differential heating at the earth's surface, the spectral signatures for corresponding features may be markedly different in the daytime and dawn thermal imagery. Since the pattern matching routine determines positional errors based on these spectral signatures, any inconsistencies between the imagery will adversely influence the reliability of the disparity data. Chapter 9 described a number of techniques which were aimed at suppressing these spectral variations between the imagery. However, little success was achieved in rectifying the dawn thermal imagery and considerable doubts exist as to the

viability of using pattern matching techniques when the spectral characteristics of the imagery vary so widely.

Despite the problems with the Black Brook data set, it was possible to register sub-regions of the imagery with a high level of success. By constraining the pattern matching procedure to favourable areas of the imagery (i.e. those with high frequency spectral variations), the problems described previously were overcome and the final output imagery constructed as a mosaic of sub-regions. Section 7.2.3 illustrates the final output imagery, and it was found that the geometry of the reconstructed imagery was almost indistinguishable from that of the aerial photography. Furthermore, the boundaries between adjacent sub-regions in the rectified imagery were virtually seamless, which further confirmed the Dumbbell Correlation Method was able to reconstruct the line-scanned imagery with a high level of accuracy.

Quantitative accuracy assessment of the reconstructed ATM image data was performed and results are described in Chapter 8. The average registration accuracy for the test imagery was found to be 0.5 pixels for both images using the Dumbbell Correlation Method, compared to an average of over 8 pixels for the standard polynomial correction (Tables 8.5 and 8.6). Despite the temporal differences between the Black Brook image data, and the difficulties caused by the sparse nature of study region, the Dumbbell Correlation Method was still able to register the line-scanned imagery with an average registration accuracy of better than one pixel.

Towards the latter stages of the research project, NERC delivered a number of flight lines from the Black Brook data set, in a format capable of being geometrically rectified using the NERC parametric correction. Due to the late arrival of this image data it was not possible to perform an in-depth investigation into the correction procedure. However, Section 7.3.2 describes the application of the NERC parametric correction to a single flight line, and the geometric accuracy was qualitatively assessed by comparing the output imagery with a map of the corresponding region (Section 7.3.3). It was evident from the image data that positional errors of up to 200-300m existed, demonstrating the NERC parametric correction was not suitable for rectifying imagery for quantitative temporal studies.

10.5 Recommendations for Future Work

Throughout the course of this thesis, the process of geometric correction of airborne line-scanned imagery has evolved in response to experiences gained from each method of image registration. This evolution was apparent even in the last approach, whereby the Dumbbell Correlation Method was modified in order to overcome the problems caused by the sparse nature of the test image data. Due to time constraints

imposed on this study by the late delivery from NERC of the Black Brook data set, it was not possible to explore the full potential of each alternative approach of geometric correction. However, in light of the studies carried out so far, it is possible to recommend a number of key areas which, given more time, would have benefited from further investigation.

The use of pattern matching procedures to identify image disparities has been shown to perform extremely well when the image characteristics are favourable. The Black Country data set was composed predominantly of highly textured features such as buildings and roads, and since the aerial photography and ATM imagery were synchronously acquired, spectral variations between the imagery were minimal. However, the pattern matching procedure was less successful at rectifying the Black Brook image data, where the frequency of spectral variations was much lower. In the absence of highly textured image data, the pattern matching routine relies on subtle spectral features to identify geometric disparities, and these are not represented consistently in the aerial photography and ATM imagery. In order to exploit these subtle spectral variations more fully, the use of mutlispectral image data may increase the textural content of the image data. Although the only spectral wave bands available to the aerial photography are in the visible spectrum, the use of colour composite images or other image derivatives, such as principal component analysis, may improve the reliability of the pattern matching routine.

In overcoming the problems of sparse image data, Section 6.4.2 describes how the Dumbbell Correlation Method was applied only to favourable regions of the imagery. Extending this theory further, rather than applying the pattern matching routine down two pre-defined transects, it may be possible to identify a number of positions on each scan line where the frequency of spectral variations is sufficiently high to enable pattern matching procedures to be reliably used. Since a number of algorithms already exist which provide a measure of texture (Reed and du Buf, 1993), this technique also has the potential to be fully automated. Whilst the resampling procedure has so far only been used to interpolate pixel transformations within the bounds of the transects, it is theoretically possible to extrapolate the position of pixels beyond this boundary. By constraining the pattern matching routine to favourable regions of the imagery, and extending the resampling procedure, it may be possible to resample the entire imagery based on the transformations determined from any two favourable points on each scan line.

The problems of solar shadows in temporal image data are potentially more worrying that those of sparse imagery since there appears to be no satisfactory approach for suppressing the spectral variations associated with shadows in imagery acquired at different times of the day. Indeed, any temporal variations between the imagery, whether caused by the presence of shadows or by changes in land cover, will reduce the reliability of the pattern matching procedure. In these circumstances, pattern matching

procedures may not represent the best solution for identifying positional disparities between the imagery. However, assuming that the ATM imagery is acquired simultaneously with the aerial photography, problems of this nature should not arise.

In addressing the problems associated with registering the dawn image data, Chapter 9 described a number of techniques aimed at suppressing the spectral variations associated with differential heating at the earth's surface, but these were not found successful. Considerable doubts exist as to the viability of using pattern matching procedure when the spectral characteristics of the image data vary so widely. However, it has been shown that once the disparities for each scan line have been successfully identified, image rectification is a relatively straightforward procedure. During the development of the End Correlation Method, noise associated with the pattern matching routine was removed by fitting a cubic spline to a series of data points selected from the disparity data (Section 6.2.3). It may therefore be possible to construct a curve representative of the true image distortions simply by fitting a cubic spline to a series of manually identified GCPs. If the spacing between these GCPs is kept within reasonable limits, the assumption that scan lines are straight enables the true nature of image distortions to be approximated without introducing significant errors. The accuracy achievable using this technique is dependent on the frequency and accuracy with which GCPs can be identified within the imagery, and clearly requires further investigation to examine its viability.

11. Conclusions

The aims and objectives of this research project are described in Chapter 1. In line with the original project aim, one of the main findings of the literature review described in Chapter 2 was that relatively little work has been carried out examining the effects of differential heating at the earth's surface using airborne thermal imagery. The use of daytime and dawn thermal image pairs has largely been limited by the lack of reliable methods to register the imagery to a satisfactory level of accuracy, which is an essential step when performing quantitative analyses of surface differential heating.

As a direct result of the delays in receiving from NERC the Black Brook data set, the main thrust of the research project was redirected to investigate alternative approaches for rectifying airborne line-scanner imagery, which can be applied without the need for synchronous platform attitude data. The first project objective was to examine existing correction techniques to identify sources of error, and investigate potential methods for overcoming them. In pursuit of this objective, it was necessary to perform a second literature review, where it was found that conventional non-parametric techniques are unable to remove the high levels of distortion associated with platform attitude errors in airborne line-scanned imagery. Non-parametric correction techniques rely on a relatively small number of GCPs selected from within the imagery to model the unpredictable and rapidly varying distortions associated with airborne line-scanned imagery. Parametric approaches differ from non-parametric methods by measuring the aircraft's exterior orientation during image acquisition, and these approaches have been shown to be capable of rectifying imagery with an accuracy approaching one pixel. However, this emerging technology is still not widely available, and does not address the issue of historic data which has no associated platform attitude information.

It was also found during the literature review that very little work has been carried out investigating methods of geometric accuracy assessment for remotely sensed imagery. Since the geometric accuracy is such a vital indication of the reliability with which remotely sensed image data can be used for quantitative studies, it seems surprising that so little work has been carried out in this field. The most common approach, the RMSE, has been shown to significantly under-predict the actual error and provides no indication of the location of geometric error. In overcoming these problems, Chapter 4 highlights the advantages of using map overlays to illustrate the location and magnitude of geometric errors.

The second objective was to develop an alternative method of geometric correction, and in light of the literature review described in Chapter 4, it was possible to identify a number of improvements on existing

correction procedures. The key difference between current non-parametric techniques and the approach described in Chapter 5 is that geometric errors are identified by comparing the geometry of the line-scanned imagery with that of corresponding aerial photography. Furthermore, by assuming scan lines are straight, it is possible to determine geometric disparities simply by identifying the two-dimensional positional differences for two points along each scan line. This allows the imagery to be rectified on a purely line-by-line basis, therefore better reflecting the true nature of the geometric errors.

Chapter 6 describes three different methods for rectifying airborne line-scanned imagery which all exploit the underlying principles developed in Chapter 5. A key feature of each of the methods is that geometric disparities between the line-scanned imagery and aerial photography are identified using pattern matching techniques allowing the speed of the correction procedure to be greatly increased. The accuracy and reliability of the disparity data acquired using automated pattern matching was assessed through manual verification and by examining the distribution of the shifted scan lines. However, the ultimate indication of the accuracy was through the examination of the final output imagery, and through the application of a number of geometric accuracy assessment techniques.

It was found that the pattern matching procedure performed differently over different types of land cover. All three methods of geometric correction were originally developed using imagery from the Black Country data set which consists of highly textured land cover providing ample spectral variation on which to obtain well-defined peaks in the correlation surface. However, the Black Brook data set consists predominantly of open fields where the frequency of spectral variation for sizeable areas of the imagery is small. In these circumstances, the pattern matching routine often failed to identify image disparities with any reliability. Furthermore, temporal differences between the photography and line-scanned imagery resulted in solar shadows with different orientations, and since shadows tend to produce well defined features they had a significant adverse effect on the reliability of the pattern matching routine.

In spite of the difficulties using the pattern matching routine, it was shown to perform extremely well when the conditions were favourable. The correction procedure was most successful when applied to imagery which was acquired during the same flight, and therefore shared similar characteristics such as illumination, orientation and ground cover. Furthermore, the pattern matching routine was most successful when the image data consisted of well-defined, highly textured features such as roads and buildings. The Black Country data set, which comprises predominantly industrial and residential buildings, was therefore rectified with a relatively high level of geometric accuracy using an almost fully automated correction procedure. Although difficulties were encountered in applying the correction procedure to the Black Brook data set owing to the sparse nature of the imagery, the reliability of the

procedure was improved by constraining the pattern matching procedure to areas of the imagery which displayed sufficient spectral variation. Despite the differences in illumination and orientation, the geometry of the rectified Black Brook imagery was almost indistinguishable from that of the corresponding aerial photography.

The third project objective was to assess the accuracy of the correction procedure, and a number of existing techniques were investigated. The most commonly used measure of geometric accuracy, the RMSE, neither tells the observer where the errors exist, nor provides any information regarding the relative errors between two or more images. Both these measures are important when overlaying multiple images for temporal quantitative studies. In addressing the limitations of existing approaches, colour composite images were created by displaying different images through different coloured guns on the VDU display. This technique was useful in assessing the registration accuracy – colour composite images were produced extremely rapidly and provided an immediate indication of the nature of registration errors between the imagery.

In order to provide a quantitative measure of geometric accuracy, an approach was developed based on the pattern matching theory described for the End Correlation Method. After rectifying the line-scanned imagery, the pattern matching routine was re-applied to the image data in a dense net in order to assess the positional disparities between the aerial photography and rectified line-scanned imagery. A smooth surface was then fitted to this accuracy assessment data enabling both the magnitude and location of geometric errors to be visualized. Using the surface plot it was possible to derive a number of single-value measures of geometric accuracy. Firstly, the total volume under the surface was used to indicate the overall magnitude of registration errors between the aerial photography and line-scanned imagery. This measure was useful when assessing the registration accuracy of multiple scenes of the same area. Secondly, the average disparity for pixels within the imagery was determined by dividing the total volume under the surface by the number of pixels. The advantage of deriving these measures from the surface plot was that every pixel in the image contributed to the final value, and were therefore more representative of the imagery. Using these alternative methods of accuracy assessment, the Dumbbell Correlation Method was shown to rectify regions of the imagery with an average registration error of 0.5 pixels.

Chapter 9 describes the difficulties encountered in using automated pattern matching routines to identify image disparities between daytime and dawn imagery. Because there is no visible wave band available in the dawn imagery, it was not possible to apply the pattern matching routine to a waveband common to both the dawn line-scanned imagery and aerial photography. Furthermore, the thermal band, which is

common to the daytime and dawn line-scanned imagery, displays markedly different spectral distributions owing to differential heating throughout a diurnal cycle (i.e. the very phenomenon under investigation). Despite examining a number of variations of the pattern matching routine, little success was achieved and considerable doubts exist as to the viability of using pattern matching procedures to rectify dawn thermal imagery.

Due to the late arrival of the Black Brook data set, it was not possible to carry out a detailed investigation of the fourth objective, which was to apply the NERC parametric correction to the line-scanned imagery and compare the results to those obtained using the alternative approach. However, it was possible to perform a preliminary examination of the NERC parametric correction facility, and after rectifying a flight line and comparing the geometry to that of a map of the corresponding region, errors in the order of 1-2 hundred metres were found. Problems with the remote sensing facility stemmed from jumps in the navigation data, which were caused by the failure of the GPS receivers to provide uninterrupted positional information throughout a flight line. In response to these problems, NERC have now updated their remote sensing facility to include an inertial measuring device to resolve the aircraft platform attitude. It has been shown through studies for similar remote sensing systems that this combined approach has the potential to rectify image data with an average accuracy approaching one pixel.

The final project objective was based largely around the initial project aim, and due to the late delivery by NERC of the Black Brook data set, very little work was carried out towards this objective. The NERC parametric correction was shown unsuccessful at rectifying airborne line-scanned imagery, and a number of problems were encountered whilst using the alternative methods of geometric correction to register daytime and dawn thermal imagery. Due to time constraints it was not possible to investigate further correction techniques and since the daytime and dawn thermal imagery could not be registered to a satisfactory level of accuracy, the widespread effects of differential heating at the earth's surface were not examined.

In conclusion, the investigations carried out during this research project have demonstrated that by treating airborne line-scanned imagery on a line-by-line basis, it is possible to greatly improve the accuracy of the rectification procedure. Despite being severely affected by the delays in receiving the Black Brook data set from NERC, it is felt that considerable developments have been made in the rectification of airborne line-scanned imagery. Using the approaches developed during this research project, daytime airborne line-scanned imagery has been registered to corresponding aerial photography with an average accuracy of better than one pixel. A number of recommendations for further study have also been suggested, and through further investigation it is envisaged that the methodologies described in

this thesis have the potential to register daytime and dawn thermal imagery to a satisfactory level of accuracy.

References

Abdel-Hady, M. (1971). Depth to groundwater table by remote sensing, *Journal of Irrigation, Proc. American Society of Civil Engineering*, **97**(IR3), 355-367.

American Society of Photogrammetry (1960). *Manual of Photogrammetry*, 2nd Edition.

Avery, T.E. & Berlin, L.B. (1992). *Fundamentals of Remote Sensing and Airphoto Interpretation*, 5th Edition, Macmillan Publishing Company, New York.

Baker, J.R., Marks, G.W. & Mikhail, E.M. (1975). Analysis of digital multispectral scanner (MSS) data, *Bildmessung und Luftbildwesen*, **43**, 22-27.

Becker, F. & Li, Z.L. (1993). Surface temperature and emissivity at various scales: definition, measurement and related problems, *Proc. Workshop on Thermal Remote Sensing*, La Londe les Maures, France, September 20-24th, 1993. Int. report by CEMAGREF, France and Penn State University, USA. 35-60.

Bell, K.R., Blanchard, B.J., Schmugge, T.J. & Witczak, M.W. (1980). Analysis of surface moisture variations within large-field sites, *Water Resources Research*, **16**(4), 796-810.

Benny, A.H. (1981). Automatic relocation of ground control points in Landsat imagery, *Proceedings of the International Conference of Matching Remote Sensing Technologies and their Applications*, Remote Sensing Society, University of Nottingham, 307-315.

Bowen, I.S. (1926). The ratio of heat losses by conduction and evaporation from any water surface, *Phys. Rev.*, **27**, 779-789.

Brunt, D. (1932). Notes on radiation in the atmosphere, *Quart. J. Royal Met. Soc.*, 58, 389-418.
BS1377, (1975). *Methods of Test for Soils for Civil Engineering Purposes*, British Standards Institute.

Burrough, P.A. (1983). Multiscale sources of spatial variation in soil, I, The application of fractal concepts to nested levels of soil variation, *J. Soil Sci.*, **34**(3), 577-597.

Canny, J. (1986). A computational approach to edge detection, *IEEE Transactions on Pattern Matching and Machine Intelligence, **PAMI-8**, 6, 679-698.*

Capehart, W.J. & Carlson, T.N. (1997). Decoupling of surface and near-surface soil water content: A remote sensing perspective. *Water Resources Research*, **33**, 6, 1383-1395.

Carlson, T.N. & Boland, F.E. (1978), Analyses of urban-rural canopy using a surface heat flux / temperature model, *Journal of Applied Meteorology*, **17**, 998-1013.

Carlson, T.N. & Gillies, R.R. (1993). A physical approach for inverting vegetation index with surface radiometric temperature to estimate surface soil water content, *Proc. Workshop on Thermal Remote Sensing*, La Londe les Maures, France, September 20-24, 1993. Int. report by CEMAGREF, France and Penn State University, USA, 297-302.

Carlson, T.N. (1986). Regional-scale estimates of surface moisture availability and thermal inertia using remote thermal measurements, *Remote Sensing Rev.*, **1**, 197-247.

Carlson, T.N., (1999), "http://www.essc.psu.edu/~tnc/". Internet reference obtained January, 1999.

Carlson, T.N., Dodd, J.K., Benjamin, S.G. & Cooper, J.N. (1981). Remote estimation of surface energy balance, moisture availability and thermal inertia. *Journal of Applied Meteorology*, **20**, 67-87.

Carlson, T.N., Gillies, R.R. & Schmugge, T.J. (1995). An interpretation of methodologies for indirect measurement of soil water content, *Agricultural and Forest Meteorology*, **77**, 191-205.

Carlson, T.N., Taconet, O., Vidal, A., Gillies, R.R., Olioso, A. & Humes, K. (1993). An overview of the workshop on thermal remote sensing held at La Londes les Maures, France, September 20-24, 1993. *Agricultural and Forest Meteorology*, **77**, 141-151.

Carslaw, H.S. & Jaeger, J.C. (1959). *Conduction of heat in solids*, Oxford, London.

Chen, L.C. & Rau, J.Y. (1993). Geometric correction of airborne scanner imagery using orthophotos and triangulated feature point matching, *International Journal of Remote Sensing*, **14**(16), 3041-3059.

Clapp, R.B. & Hornberger, G.M. (1978). Empirical equations for some soil hydraulic properties, *Water Resources Research*, **14** (4), 601-604.

Colwell, R.N. (1983). *Manual of Remote Sensing*, Vols 1 and 2, American Society of Photogrammetry.

Cosby, B.J., Hornberger, G.M., Clapp, R.B. & Ginn, T.R. (1984). A statistical explanation of the relationship of soil moiture characteristics in the physical properties of soils, *Water Resources Research*, **20**, 682-690.

Crabtree, D.L. & Brown, M. (1989). A stabilization system for a large aperture reconnaissance camera, *SPIE Airborne Reconnaissance XIII*, **1156**, 266-271.

Craig, M.D. & Green, A.A. (1987). One-dimensional resampling of digital imagery to sparse output grids, *Photogrammetric Engineering and Remote Sensing*, **53**(5), 501-506.

Curran, P.J. (1985). *Principles of Remote Sensing*, Longman, London.

Deardorff, J.W. (1978). Efficient prediction of ground surface temperature and moisture with inclusion of a layer of vegetation, *J. Geophysical Research*, **83**, 1889-1903.

Devereux, B.J., Fuller, M., Carter, L. & Parsell, R.J. (1990). Geometric correction of airborne scanner imagery by matching Delaunay triangles, *International Journal of Remote Sensing*, **11**(12), 2237-2251.

Diak, G.R., Rabin, R.M., Gallo, K.P. & Neale, C.M. (1995). Regional-scale comparisons of NDVI, soil moisture indices from surface and microwave data and surface energy budgets evaluated from satellite and in-situ data, *Rem. Sens. Rev.*, submitted for publication.

Dickinson, R.E. (1984). Modelling evapotranspiration for three-dimensional global climate models, *Climate Processes and Climate Sensitivity*, American Geophys. Union, Geophys. Monogr., 58-72.

Dickinson, R.E. (1983). Land surface processes and climate-surface albedos and energy balance, *Advances in Geophysics*, 25, 305-353.

Eastman, R.J., (1995), *Idrisi for Windows. User's Guide Version 1.0.* Clark Labs for Cartographic Technology and Geographic Analysis, Clark University, Worcester, Massachusetts, USA.

Ehlers, M. (1994). Geometric correction of airborne scanner data using multiquadric interpolation techniques, *Proceedings of the First International Airborne Remote Sensing Conference and Exhibition*, Strasbourg, France, 11-15 September 1994, **2**, 494-502.

Ehlers, M. (1997). Rectification and Registration. In *Integration of Geographical Information Systems and Remote Sensing*, J. Star, J. Estes and K McGwire, eds., Cambridge University Press.

Ehlers, W.L. & Van Bavel, C.H.M. (1967). Sorghum foliar responses to changes in soil water content, *Agron. J.*, **59**, 243-246.

Ek, M. & Cuenca, R.H. (1994). Variation in soil parameters: Implications for modeling surface fluxes and atmospheric boundary-layer development, *Boundary Layer Meteorology*, **70**, 369-383.

Elachi, C. (1987). *Introduction to the Physics and Techniques of Remote Sensing*, John Wiley & Sons.

Ellis, R.J. (1997). *Evaluation of Remote Sensing for Monitoring Landfill Gas and Leachate within an Urban Environment*, Ph.D. Thesis, Aston University, UK.

Ford, G.E. & Zanelli, C.I. (1985). Analysis and quantification of errors in the geometric correction of satellite images, *Photogrammetric Engineering and Remote Sensing*, **51**, 11, 1725-1734.

Fukuhara, M., Hayashi, S., Yasuda, Y., Asanuma, I., Emori, Y. & Iisaka, J. (1978). Extraction of soil information from vegetated areas, *Proc. 12th Int. Symp. Rem. Sens. Env.*, **3**, 1707-1711.

Gates, D.M. (1966). Transpiration and energy exchanges, *Quart. Rev. Biol.*, **41**, 353-364.

Gates, W.L. (1975). The January global climate simulated by a two-level general circulation model: A comparison with observation, *J. Atmos. Sci.*, **32**, 449-477.

Gee, H.R. (1988). A new model for the geometric correction of multispectral scanner data, *Multispectral Image Processing and Enhancement*, **SPIE 933**, 70-76.

Ghosh, S.K. (1988). *Analytical Photogrammetry,* 2nd Ed., Pergamon Press.

Gibson, J., Park, W., Hollinger, A., Dunlop, J. & O'Neill, N. (1987). Geometric correction of airborne line scanner data, *Proceedings of the 11th Canadian Symposium on Remote Sensing*, Waterloo, 671-673.

Gillies, R.R. & Carlson, T.N. (1995). Thermal remote sensing of surface soil water content with partial vegetation cover for incorporation into climate models, *Journal of Applied Meteorology*, **34**, 745-756.

Gopfert, W. (1982). Methodology for thematic image processing using thematic and topographic data bases and base-integrated multi-sensor imagery, *Proceedings ISPRS Commission VII Symposium*, Toulouse, France, **1**, 13-19.

Goshtaby, A. (1988). Registration of images with geometric distortions, *IEEE Transactions on Geoscience and Remote Sensing*, **26**(1), 60-64.

Goshtaby, A., Stockman, G.C. & Page, C.V. (1986). A region-based approach to digital image registration with sub-pixel accuracy, *IEEE Transactions on Geoscience and Remote Sensing*, **GE-24**(3), 390-399.

Greulach, V.A. (1973). *Plant Function and Structure,* The Macmillan Company, New York.

Hains, B.A. & Horton, A. (1987). *British Regional Geology of Central England*, 3rd Edition, British Geological Survey.

Hallert, B. (1960). *Photogrammetry*, McGraw-Hill Book Company.

Hardy, R.L. (1971). Multiquadric equations of topology and other irregular surfaces, *Journal of Geophysical Research*, **76**(8), 1905-15.

Harold, L.L. & Dreibelbis, F.R. (1958). Evaluation of agricultural hydrology by monolith lysimeters, *USDA Tech. Bul. 1179.*

Hiler, E.A., & Clark, R.N. (1971). Stress day index to characterise effects of water stress on crop yields, *Trans. Amer. Soc. Agr. Eng.*, **14**, 757-761.

Hillel, D. (1971). *Soil and Water: Physical Principles and Processes*, Academic Press, London.

Hilton, K. (1986). *Process and Pattern in Physical Geography*, Bell and Hyman.

Hollis, J.M. (1985). *Soils in Staffordshire IV: Sheet SK00/10 (Lichfield)*, Soil Survey Record No. 89, Lawes Agricultural Trust (Soil Survey of England and Wales), Harpenden.

Idso, S.B., Aase, J.K. & Jackson, R.D. (1975d). Net rediation-soil heat flux relations as influenced by soil water variations, *Boundary Layer Meteorology*, **9**, 113-122.

Idso, S.B., Jackson, R.D. & Reginato, R.J. (1975b). Estimating evaporation: A technique adaptable to remote sensing, *Science*, **189**, 991-992.

Idso, S.B., Jackson, R.D. & Reginato, R.J. (1977). Remote sensing of crop yields, *Science*, **196**, 19-25.

Idso, S.B., Reginato, R.J. & Jackson, R.D. (1975c). Assessing bare soil evaporation via surface temperature measurements, *Proceedings of the 1975 meeting on Hydrology and Water Resources in Arizona and the Southwest*, Arizona Academy of Science, Tempe, AZ, **5**, 199-205.

Idso, S.B., Reginato, R.J., Jackson, R.D., Kimball, B.A. & Nakajama, F.S. (1974). The three stages of drying of a field soil, *Soil Science Society of America Proceedings*, **38**, 831-837.

Idso, S.B., Schmugge, T.J., Jackson, R.D. & Reginato, R.J. (1975a). The utility of surface temperature measurements for remote sensing of soil water studies, *J. Geophys. Res.*, **80**, 3044-3049.

Jackson, R.D., Reginato, R.J. & Idso, S.B. (1977). Wheat canopy temperature: a practical tool for evaluating water requirements, *Water Resources Research*, **13**, 651-656.

Jaeger, J.C. (1953). Conduction of heat in a solid with periodic boundary conditions, with an application to the surface temperature of the moon, *Cambridge Phil. Soc. Proc.*, **49**(2), 355-359.

Kasahara, A. & Washington, W.M. (1971). General circulation experiments with a six-layer NCAR model including orography, cloudiness and surface temperature circulation, *J. Atmos. Sci.*, **28**, 657-701.

Khale, A.B., Gillespie, A.R., & Goetz, A.F.H. (1976). Thermal inertia mapping: A new geologic mapping tool, *Geophys. Res. Lett.*, **3**(1), 26-28.

Khale, A.B., Gillespie, A.R., & Goetz, A.F.H., & Addington, J.D. (1975). Thermal inertia mapping, *Proc. 10th Int. Symp. Rem. Sens. Env.*, Ann Arbor, Michigan, USA, October, 1975, **2**, 985-994.

Kondo, J., Saigusa, N. & Sato, T. (1990). A parameterisation of evaporation from bare soil surfaces, *Journal of Applied Meteorology*, **29**, 385-389.

Konecny, G. (1976). Mathematical models and procedures for the geometrical restitution of remote sensing imagery, *International Archives of Photogrammetry and Remote Sensing*, **21**(3), 1-33.

Levitt, J. (1974). *Introduction to Plant Physiology*, 2nd Edition, The C.V. Mosby Company.

Lillesand, T.M. & Kiefer, R.W. (1994). *Remote Sensing and Image Interpretation,* John Wiley & Sons.

Luvall, J.C. (1997). The use of remotely sensed surface temperatures from an aircraft-based thermal infrared multispectral scanner (TIMS) to estimate the spatial and temporal variability of latent heat fluxes and thermal response numbers from White Pine plantation. In *Scale in Remote Sensing and GIS,* edited by D.A. Quattrochi and M.F. Goodchild, 1997, Macmillan.

Luvall, J.C. and Holbo, H.R. (1989). Measurement of short-term thermal responses of coniferous forest canopies using thermal scanner data, *Remote Sensing of the Environment*, **27**, 1-10.

Mahfouf, J.F. & Noilhan, J. (1991). Comparative study of various formulations of evaporation from bare soil using in-situ data, *Journal of Applied Meteorology*, **30**, 1354-1363.

Mahrer, Y. & Pielke, R. (1977). A numerical study of the air flow over irregular terrain, *Beit. Phys. Atmos.*, **50**, 98-113.

Mahrt, L. & Pan, H. (1984). A two-layer model of soil hydrology, *Journal of Applied Meteorology*, **29**, 1-20.

Manabe, S., Hahn, D.G. & Holloway Jr, J.L. (1974). The seasonal variation of the tropical circulation as simulated by a global model of the atmosphere, *J. Atmos. Sci.*, **31**, 43-83.

Markarian, H., Bernstein, R., Ferneyhough, D.G., Gregg, L.E. & Sharp, F.S. (1973). Digital correction for high-resolution images, *Photogrammetric Engineering*, **39**, 1311-1320.

Mather, P.M. (1999). *Computer Processing of Remotely Sensed Images,* 2nd Ed., John Wiley & Sons.

McCuen, R.H., Rawls, W.J. & Brakensiek, D.L. (1981). Statistical analysis of the Brooks-Corey and the Green-Ampt parameters across soil textures, *Water Resources Research*, **17**, 1005-1013.

McCullagh, M. & Ross, C. (1980). Delaunay triangulation of a random data set for isarithmic mapping, *Cartographic Journal,* **17**, 93-99.

McCumber, J.W. & Pielke, R.A. (1981). Simulation of the effects of surface fluxes of heat and moisture in a mesoscale numerical model, Part 1: Soil layer, *J. Geophys. Res.*, **86**, 9929-9938.

McGwire, K.C. (1996). Cross-validated assessment of geometric accuracy, *Photogrammetric Engineering and Remote Sensing*, **62**(10), 1179-1187.

McGwire, K.C.(1998). Mosaicking airborne scanner data with the multiquadric rectification technique, *Photogrammetric Engineering and Remote Sensing*, **64**(6), 601-606.

Medioni, G. & Nevatia, R. (1984). Matching images using linear features, *IEEE Transactions on Pattern Matching and Machine Intelligence*, **PAMI-6** (6), 675-685.

Meyer, B.S., Anderson, D.B., Bohning, R.H., and Fratianne, D.G. (1973). *Introduction to Plant Physiology*, 2nd Edition, Van Nostrand Company, New York.

Miller, S.H. & Watson, K. (1977). Evaluation of algorithms for geological thermal inertia mapping, *Proc. 11th Int. Symp. Rem. Sens. Env.*, 1147-1160.

Monteith, J.L. (1963). Gas exchange in plant communities. In *Environmental Control of Plant growth*, edited by L.T. Evans, Academic Press, New York, 95-112.

Monteith, J.L. (1965). Evaporation and environment. In *The State and Movement of Water in Living Organisms*, edited by G.E. Fogg, Academic Press, New York, 205-234.

Monteith, J.L. (1973). *Principles of Environmental Physics*, Edward Arnold, London.

Monteith, J.L. (1981). Evaporation and surface temperature, *Quart. J. Royal. Meteor. Soc.*, **107**, 1-27.

Moran, M.S., Clarke, T.R., Inoue, Y. & Vidal, A. (1994). Estimating crop water deficit using the relation between surface-air temperature and spectral vegetation index, *Remote Sensing of Environment*, **49**(3), 246-263.

Noilhan, J. & Planton, S. (1989). A simple parameterisation of land surface processes for meteorological models, *Mon. Wea. Rev.*, **117**, 536-549.

Penman, H.L. (1948). Natural evaporation from open water, bare soil and grass, *Proc. Roy. Soc. London*, A193: 120-146.

Pratt, D.A. & Ellyett, C.D. (1978). Image registration for thermal inertia mapping, and its potential use for mapping of soil moisture and geology in Australia, *Proc. 12th Int. Symp. Rem. Sens. Env.*, Manila, Philippines, April 20-26, 1978, **3**, 1207-1217.

Pratt, D.A. & Ellyett, C.D. (1979). The thermal inertia approach to mapping soil moisture and geology, *Remote sensing of Environment*, **8**, 151-168.

Pratt, D.A. (1980). Two-dimensional model variability in thermal inertia surveys, *Remote Sensing of Environment*, **9**, 325-338.

Pratt, D.A., Foster, S.J. & Ellyett, C.D. (1980). A calibration procedure for Fourier series thermal inertia surveys, *Photogrammetric Engineering and Remote Sensing*, **46**, 529-538.

Prevot, L., Bernard, R., Taconet, O. & Vidal-Madjar, D. (1984). Evaporation from bare soil evaluated from a soil water transfer model using remotely sensed surface soil moisture data, *Water Resources Research*, **20**, 311-316.

Price, J.C. (1977). Thermal inertia mapping: A new view of the Earth, *J. Geophys. Res.*, **82**(18), 2582-2590.

Price, J.C. (1980). The potential of remotely sensed thermal infrared data to infer surface soil moisture and evaporation, *Water Resources Research*, **16**, 787-795.

Price, J.C. (1990). Using spatial context in satellite data to infer regional scale evapotranspiration, *IEEE Transactions on Geoscience and Remote Sensing*, **28**(5), 940-948.

Pruitt, W.O. & Angus, D.E. (1960). Large weighing lysimeters for measuring evapotranspiration, *Trans. Amer. Soc. Civ. Eng.*, **3**, 13-18.

Richards, J.A. (1986). *Remote Sensing Digital Image Analysis*, Springer-Verlag.

Ritchie, J.T. (1972). Model for predicting evaporation from a row crop with incomplete cover, *Water Resources Research*, **8**(5), 1204-1213.

Rosema, A. & Bijleveld, J.H. (1978). 'TELL-US' A combined surface temperature, soil moisture and evaporation mapping approach, *Proc. 12th Int. Symp. Rem. Sens. Env.*, Manila, Philippines, 20-26 April, 1978, **3**, 2267-2277.

Reed, T.R. & du Buf, J.M.H. (1993). A review of recent texture segmetation and feature extraction techniques, *CVGIP: Image Understanding*, 57(**3**), 359-372.

Roy, D.P., Devereux, B., Grainger, B. & White, S.J. (1997). Parametric geometric correction of airborne thematic mapper imagery, *International Journal of Remote Sensing*, **18**(9), 1865-1887.

Sabins, F.F. (1984). Geologic mapping of Death Valley from thematic mapper, thermal infrared, and RADAR images, *Proc. International Symposium on Remote Sensing of Environment*, April 16-19, 1984, Colorado, USA, 1, 139-145.

Sabins, F.F. (1986). *Remote Sensing, Principles and Interpretation*, Longman, London.

Saltzman, B. & Pollack, J.A. (1977). Sensitivity of the diurnal surface temperature range to changes in physical paramters, *Journal of Applied Meteorology*, **16**, 614-619.

Schmer, F.A. & Werner, H.D. (1974). Remote sensing techniques for evaluation of soil water conditions, *Trans. Amer. Soc. Agri. Eng.*, **17**(2), 310-314.

Schmugge, T. (1995). TIMS observation of surface emissivity in Hapex-Sahel, *Proc. of the 1995 International Geoscience and Remote Sensing Symposium*, IEEE; URSI, Firenze, Italy, **3**, 2224-2226.

Schmugge, T., Blanchard, B., Anderson, A. & Wang, J. (1978). Soil moisture sensing with aircraft observations of the diurnal range of surface temperature, *Water Resources Bulletin*, **14**, 169-172.

Schmugge, T.J., Jackson, T.J. & McKim, H.L. (1980). Survey of methods for soil moisture determination, *Water Resources Research*, **16**, 961-979.

Seguin, B. & Couralt, D. (1993). Crop water stress detection using thermal remote sensing: from local to regional scales, *Proc. Workshop on Thermal Remote Sensing*, La Londe les Maures, France, September 20-24, 1993. Int. report by CEMAGREF, France and Penn State University, USA, 133-136.

Seguin, B. & Itier, B. (1983). Using midday surface temperature to estimate daily evaporation from satellite thermal data, *Int. J. Remote Sensing*, **4**, 371-383.

Seguin, B., Baelz, S., Monget, J.M. & Petit, V. (1982). Utilisation de la thermographie IR pour l'estimation de l'evaporation regionale II. Resultats obtenus a partir des donnees de satellite. *Agronomie*, **2**, 113-118.

Sellers, P.J., Mintz, Y., Sud, Y.C. & Dalcher, A. (1986). A simple biosphere model (SiB) for use with general circulation models, *J. Atmos. Sci.*, **43**, 505-531.

Sellers, W.D. (1965). *Physical Climatology*, University of Chicago Press, Chicago.

Serpell, D. (1979). *Report of the Ordnance Survey Review Committee*, London, Her Majesty's Stationary Office.

Shapiro, M., (1993), *Geographic Resource Analysis Support System Manual*, US Army Corps of Engineers, Construction Engineering Research Laboratories.

Shaw, E. (1993). *Hydrology in Practice*, 2nd Edition, Chapman and Hall, London, UK.

Shuttleworth, W.J. & Wallace, J.C. (1985). Evaporation from sparse crops - an energy combination theory, *Quart. J. Roy. Meteorol. Soc.*, **11,** 839-855.

Singhroy, V.H. & Barnett, P.J. (1984). Locating subsurface mineral aggregate deposits from airborne infrared imagery (reflected and thermal): A case study in Southern Ontario. *Proc. International Symposium on Remote Sensing of Environment*, April 16-19, 1984, Colorado, USA, **2**, 523-539.

Soares, J.V., Bernard, R., Taconet, O., Vidal-Madjar, D. & Weill, A. (1988). Estimation of bare soil evapotranspiration from microwave measurements, *J. Hydrol.*, **99**, 281-296.

Sunar, F. & Kaya, S. (1996). Assessment of the geometric accuracy of remotely sensed images, *International Journal of Remote Sensing*, **18**(14), 3069-3074.

Tanner, C.B. & Fuchs, M. (1968). Evaporation from unsaturated surfaces: A generalised combination method, *J. Geophys. Res.*, **73**(4), 1299-1304.

Thompson, G.R. and Turk, J. (1991). *Modern Physical Geology*, Saunders College Publishing.

Tobler, W. (1988). Resolution resampling and all that. In *Building Databases for Global Science*, Taylor and Francis, London.

Ton, J. & Jain, A. (1989). Registering Landsat images by point matching, *IEEE Transactions on Geoscience and Remote Sensing*, **27**(5), 642-651.

Van Bavel, C.H. & Reginato, R.J. (1965). Precision lysimetry for direct measurement of evaporative flux, *Proc. Symp. Methodology of Plant Eco-Physiology*, Montpelier, France, April 1962, UNESCO, 129-135.

Vincent, R.D. (1984). Integration of airborne thematic mapper and thermal infrared multispectral scanner data for lithographic and hydrothermal alteration mapping, *Proc. International Symposium on Remote Sensing of Environment*, April 16-19, 1984, Colorado, USA, **2**, 523-539.

Vlcek, J. & King, D. (1983). Detection of subsurface soil moisture by thermal sensing. Results of laboratory close range and aerial studies. *Photogrammetric Engineering and Remote Sensing*, **49**, 1593-1597.

Wadsworth, A., Looyen, W.J., Reuter, R. & Petit, M. (1992). Aircraft experiments with visible and infrared sensors, *International Journal of Remote Sensing*, **13**(6), 1175-1199.

Watson, K. (1973). Periodic heating of a semi-infinite solid, *J. Geophys. Res.*, **78**(26), 5904-5910.

Watson, K. (1975). Geologic applications of thermal infrared images, *Proc. IEEE*, **63**(1), 128-137.

Watson, K., Rowan, L.C. & Offield, T.W. (1971). Application of thermal modelling in the geologic interpretation of IR images, *Proc. 7th Int. Symp. Rem. Sens. Env.*, ERIM, Ann Arbor, 2014-2041.

Wetzel, P.J. & Chang, J.T. (1987). Concerning the relationship between evapotranspiration and soil moisture, *J. Climate Appl. Meteor.*, **26**, 18-27.

Wewel, F., Scholten, F. & Gwinner, K. (1999). High resolution stereo camera (HRSC) – multispectral 3D data acquisition and photogrammetric data processing, *Proceedings of the Fourth International Airborne Remote Sensing Conference and Exhibition*, Ottawa, Canada, 21-24 June, 1999, **1**, 263-272.

White, S.J., Devereux, B.J. & Fuller, R.M. (1990). NERC airborne remote sensing and the geometric correction of airborne imagery, *10th EARSEL Symposium*, Toulouse, France, 189-199.

Wiegand, C.L. & Namken, L.N. (1966). Influence of plant moisture stress, solar radiation, and air temperature on cotton leaf temperature, *Agron. J.*, **58**, 582-586.

Wiesner, C.J. (1970). *Climate, Irrigation and Agriculture,* Angus and Robertson Ltd., UK.

Wilson, A.K. (1994). The NERC integrated ATM/CASI/GPS system, *Proceedings of the First International Airborne Remote Sensing Conference and Exhibition*, Strasbourg, France, 11-15 September, 1994, **2**, 249-259.

Wilson, A.K. (1999). First results from the NERC's airborne integrated system, *Proceedings of the Fourth International Airborne Remote Sensing Conference and Exhibition*, Ottawa, Canada, 21-24 June, 1999, **2**, 493-500.

Zhang, W., Albertz, J. and Li, Z. (1994). Rectification of airborne line-scanner imagery utilising flight parameters, *Proceedings of the First International Airborne Remote Sensing Conference and Exhibition*, Strasbourg, France, 11-15 September, 1994, **2**, 447-456.

APPENDIX 1

Ground Truth Data

Temperature Measurements at Farm Study Sites

Sample Reference	Temperature Data for Noon Flight (23rd October 1996)			Temperature Data for Dawn Flight (24th October 1996)		
	Air Temp (°C)	Surf Temp (°C)	Soil Temp (°C)	Air Temp (°C)	Surf Temp (°C)	Soil Temp (°C)
S1	18.0	17.8	13.4	9.8	8.9	9.7
S1a	18.3	19.5	12.2			
S2	17.4	18.6	12.0	9.8	8.6	10.0
S2a	17.3	17.1	11.6			
S3	17.2	19.7	12.6	9.5	9.0	9.7
S3a	17.1	17.7	12.4			
S4	17.6	19.6	11.9	9.7	8.8	9.7
S4a	17.1	17.3	12.4			
S5	17.0	15.4	12.4	9.7	9.1	9.9
S5a	17.3	17.2	11.6			
S6	16.4	15.6	12.6	9.7	8.8	9.7
S6a	17.3	15.2	11.8			
A1	16.5	16.0	14.9	11.2	10.7	9.4
A1a	16.1	16.2	13.8	11.0	10.9	9.4
A2	16.5	16.5	14.6	10.9	10.7	9.3
A2a	16.6	16.6	14.3	11.0	10.7	9.4
A3	16.8	16.5	14.1	10.8	10.7	9.3
A3a	17.0	16.7	14.5	10.8	10.5	9.2
A4	16.7	16.7	14.8	10.3	10.0	9.2
A4a	16.9	16.8	14.8	10.5	10.2	9.2
A5	16.8	16.9	15.7	10.1	9.8	9.3
A5a	17.0	16.9	14.2	10.5	10.3	9.2
A6	17.0	17.1	15.2	10.2	9.7	8.7

Notes

Sample references refer to Saxton Farm site (S1 – S6a) and Abel Farm site (A1 – A6); see Figure 3.3.

Blanks in Saxton Farm temperature readings during dawn flight indicate absence of data (these sites were skipped due to time constraints at time of sampling).

Temperature Measurements at Grid Study Site

Sample Reference	Temperature Data for Noon Flight (23rd October 1996)			Temperature Data for Dawn Flight (24th October 1996)		
	Air Temp (°C)	Surf Temp (°C)	Soil Temp (°C)	Air Temp (°C)	Surf Temp (°C)	Soil Temp (°C)
1A	19.6	19.2	15.4	10.2	9.5	9.5
1B	19.0	19.1	15.5	10.4	9.3	9.5
1C	18.8	18.9	15.9	10.6	9.2	9.8
1D	18.9	18.8	15.3	10.4	9.0	9.7
1E	18.5	18.2	15.4	10.3	9.4	9.8
1F	16.6	16.8	15.9	10.4	9.6	9.9
2A	15.5	15.9	15.9	10.1	9.4	10.0
2B	16.3	16.5	16.0	11.3	9.6	9.9
2C	16.5	16.7	15.9	11.1	9.1	10.0
2D	17.9	18.0	16.3	10.4	9.4	10.3
2E	16.8	17.3	15.9	10.1	9.6	10.2
2F	18.0	18.0	16.1	10.4	9.9	9.7
3A	18.7	18.8	16.0	9.7	9.0	9.9
3B	18.6	18.7	17.7	10.7	9.3	10.1
3C	18.8	18.6	15.5	10.2	9.0	9.9
3D	18.8	18.7	14.5	9.8	9.2	9.6
3E	18.1	18.0	14.0	10.3	9.6	9.8
3F	17.9	18.0	15.0	10.3	9.9	9.9
4A	17.5	17.3	13.9	10.0	9.6	9.6
4B	18.7	16.2	13.8	10.7	9.3	10.1
4C	18.7	15.6	12.5	9.9	9.2	9.8
4D	18.3	18.0	14.5	10.3	9.4	10.1
4E	18.5	19.5	14.3	10.4	9.9	9.8
4F	18.9	21.6	14.1	10.2	9.6	10.1
5A	17.3	22.0	12.8	10.4	9.3	9.6
5B	18.7	27.1	14.2	10.7	9.1	9.6
5C	18.9	21.7	14.0	10.1	8.8	9.7
5D	18.8	20.0	13.3	10.3	8.8	9.2
5E	18.8	24.8	13.5	10.5	10.1	9.6
5F	18.9	22.0	12.9	10.3	9.6	10.5

Notes
Sample references refer to grid study site; see Figure 3.4.

Neutron Probe Measurements at Farm Study Sites

Tube Ref: S1	Average Count for Neutron Probe (16s interval)				
Depth Below Surface (cm)*	20th Oct 1996	22nd Oct 1996	23rd Oct 1996	24th Oct 1996	5th Nov 1996
-20	964	647	646	656	661
-10	464	459	429	370	428
0	26	22	74	22	25
10	134	110	317	125	133
20	323	310	438	309	355
30	308	323	463	318	356
40	309	323	445	323	380
50		265	295	261	323
60		413	211	462	465
80	858	847	235	853	862
100		587	243	567	576
109	309	322	276	333	340

Notes

* Negative depth indicates distance above ground level (this situation occurs due to access tube protruding out of the ground).

Average count calculated as the average of the upward and downward passes of the neutron probe.

Blank entries indicate absence of data.

Tube Ref: S2	Average Count for Neutron Probe (16s interval)				
Depth Below Surface (cm)*	20th Oct 1996	22nd Oct 1996	23rd Oct 1996	24th Oct 1996	5th Nov 1996
-20		649	646	654	681
-10		428	450	443	397
0		23	24	24	25
10		154	144	126	188
20		459	461	448	531
30		457	464	459	544
40		389	375	392	531
50		175	172	176	223
60		113	111	110	141
72		110	108	110	141

Notes

* Negative depth indicates distance above ground level (this situation occurs due to access tube protruding out of the ground).

Average count calculated as the average of the upward and downward passes of the neutron probe.

Blank entries indicate absence of data.

Tube Ref: S3	Average Count for Neutron Probe (16s interval)				
Depth Below Surface (cm)*	20th Oct 1996	22nd Oct 1996	23rd Oct 1996	24th Oct 1996	5th Nov 1996
-12		652	646	664	737
-2		436	429	463	458
8		70	74	67	73
18		309	317	309	386
28		441	438	444	500
38		463	463	463	518
48		452	445	449	469
58		309	295	294	342
68		209	211	209	231
88		237	235	239	239
108		248	243	244	246
128		264	276	268	269

Notes

* Negative depth indicates distance above ground level (this situation occurs due to access tube protruding out of the ground).

Average count calculated as the average of the upward and downward passes of the neutron probe.

Blank entries indicate absence of data.

Tube Ref: S4	Average Count for Neutron Probe (16s interval)				
Depth Below Surface (cm)*	20th Oct 1996	22nd Oct 1996	23rd Oct 1996	24th Oct 1996	5th Nov 1996
-9		652	651	655	721
-1		496	488	497	482
11		104	101	92	135
21		203	202	205	272
31		220	222	219	276
41		221	225	222	260
51		229	230	240	270
61		230	232	228	255
71		220	225	216	236
83		156	149	152	158

Notes

* Negative depth indicates distance above ground level (this situation occurs due to access tube protruding out of the ground).

Average count calculated as the average of the upward and downward passes of the neutron probe.

Blank entries indicate absence of data.

Tube Ref: S5	Average Count for Neutron Probe (16s interval)				
Depth Below Surface (cm)*	20th Oct 1996	22nd Oct 1996	23rd Oct 1996	24th Oct 1996	5th Nov 1996
-12		655	644	652	719
-2		492	442	493	453
8		67	68	61	83
18		207	204	204	261
28		246	246	241	306
38		260	264	262	312
48		282	282	278	315
58		272	264	263	289
68		257	263	263	282
88		244	248	250	253
108		229	219	219	221
128		221	226	231	232

Notes

* Negative depth indicates distance above ground level (this situation occurs due to access tube protruding out of the ground).

Average count calculated as the average of the upward and downward passes of the neutron probe.

Blank entries indicate absence of data.

Tube Ref: S6	Average Count for Neutron Probe (16s interval)				
Depth Below Surface (cm)*	20th Oct 1996	22nd Oct 1996	23rd Oct 1996	24th Oct 1996	5th Nov 1996
-9	726	651	653	657	671
-1	427	509	509	494	549
11	170	126	119	111	146
21	244	246	231	224	300
31	248	261	261	260	338
41	267	284	279	280	357
51	287	279	285	283	366
61		277	273	274	321
71	237	238	240	240	275
83	234	237	236	239	254

Notes

* Negative depth indicates distance above ground level (this situation occurs due to access tube protruding out of the ground).

Average count calculated as the average of the upward and downward passes of the neutron probe.

Blank entries indicate absence of data.

Tube Ref: A1	Average Count for Neutron Probe (16s interval)				
Depth Below Surface (cm)*	20th Oct 1996	22nd Oct 1996	23rd Oct 1996	24th Oct 1996	5th Nov 1996
-9	675	655	650	689	657
-1	406	498	473	499	489
11	278	216	216	210	259
21	317	326	322	320	369
31	222	234	231	240	297
41	170	175	173	176	253
51	156	159	158	161	232
61	166	168	162	164	232
71	183	183	185	179	239
83	182	189	189	188	222

Notes

* Negative depth indicates distance above ground level (this situation occurs due to access tube protruding out of the ground).

Average count calculated as the average of the upward and downward passes of the neutron probe.

Blank entries indicate absence of data.

Tube Ref: A2	Average Count for Neutron Probe (16s interval)				
Depth Below Surface (cm)*	20th Oct 1996	22nd Oct 1996	23rd Oct 1996	24th Oct 1996	5th Nov 1996
-6		649	669	687	655
-4		574	590	607	610
14		231	236	220	274
24		291	286	286	343
34		269	238	284	341
44		217	225	227	268
54		199	198	198	235
64		212	206	207	247
74		231	231	236	278
86		241	243	239	279

Notes

* Negative depth indicates distance above ground level (this situation occurs due to access tube protruding out of the ground).

Average count calculated as the average of the upward and downward passes of the neutron probe.

Blank entries indicate absence of data.

Tube Ref: A3	Average Count for Neutron Probe (16s interval)				
Depth Below Surface (cm)*	20th Oct 1996	22nd Oct 1996	23rd Oct 1996	24th Oct 1996	5th Nov 1996
-8		656	675	657	660
2		505	495	537	520
12		167	162	159	218
22		277	273	272	352
32		297	297	295	369
42		263	254	260	305
52		223	226	226	248
62		233	237	239	259
72		247	243	245	270
84		236	231	232	254

Notes

* Negative depth indicates distance above ground level (this situation occurs due to access tube protruding out of the ground).

Average count calculated as the average of the upward and downward passes of the neutron probe.

Blank entries indicate absence of data.

Tube Ref: A4	Average Count for Neutron Probe (16s interval)				
Depth Below Surface (cm)*	20th Oct 1996	22nd Oct 1996	23rd Oct 1996	24th Oct 1996	5th Nov 1996
-8		652	687	657	669
-2		497	462	495	475
12		179	176	149	225
22		330	337	320	424
32		398	393	398	473
42		418	420	421	459
52		431	428	429	449
62		400	395	413	406
72		257	258	270	266
84		189	189	188	207

Notes

* Negative depth indicates distance above ground level (this situation occurs due to access tube protruding out of the ground).

Average count calculated as the average of the upward and downward passes of the neutron probe.

Blank entries indicate absence of data.

Tube Ref: A5	Average Count for Neutron Probe (16s interval)				
Depth Below Surface (cm)*	20th Oct 1996	22nd Oct 1996	23rd Oct 1996	24th Oct 1996	5th Nov 1996
-8		658	677	682	674
2		526	513	503	520
12		166	160	159	219
22		292	284	285	397
32		325	324	334	406
42		347	351	346	392
52		307	304	301	363
62		431	426	428	452
72		638	641	627	639
84		658	666	671	669

Notes

* Negative depth indicates distance above ground level (this situation occurs due to access tube protruding out of the ground).

Average count calculated as the average of the upward and downward passes of the neutron probe.

Blank entries indicate absence of data.

Tube Ref: A6	Average Count for Neutron Probe (16s interval)				
Depth Below Surface (cm)*	20th Oct 1996	22nd Oct 1996	23rd Oct 1996	24th Oct 1996	5th Nov 1996
-9	717	654	657	652	655
-1	449	549	523	540	538
11	446	381	407	394	430
21	631	615	618	621	654
31	743	716	726	726	751
41	886	859	871	868	865
51	838	868	845	851	862
61	494	528	532	528	531
71	399	403	393	394	402
81	398		390	387	
89	391	387	379	391	387

Notes

* Negative depth indicates distance above ground level (this situation occurs due to access tube protruding out of the ground).

Average count calculated as the mean of the upward and downward passes of the neutron probe.

Blank entries indicate absence of data.

Gravimetric Soil Moisture Content for Farm Study Sites

Sample Reference	Noon Flight (23rd October 1996)		Dawn Flight (24th October 1996)		Tube Retrieval (15th November 1996)	
	MC (%) 0-50mm	MC (%) 50-100mm	MC (%) 0-50mm	MC (%) 50-100mm	MC (%) 0-50mm	MC (%) 50-100mm
S1	12.52	13.58	13.78	13.63	17.21	15.84
S1a	21.77	20.21				
S2	25.72	26.44	26.12	24.08	28.13	27.10
S2a	20.63	21.73				
S3	16.27	16.12	13.06	15.75	16.91	18.16
S3a	10.15	12.27				
S4	9.38	10.92	9.76	11.00	12.52	13.18
S4a	8.50	11.69				
S5	9.83	10.80	8.72	10.08	11.50	13.00
S5a	9.68	10.63				
S6	11.14	10.64	8.51	10.90	10.92	13.53
S6a	10.59	11.59				
A1	10.96	11.51	11.20	11.56	12.53	13.66
A1a	11.14	11.57	10.39	11.27		
A2	11.12	11.85	10.32	11.72	11.88	12.67
A2a	11.47	12.24	10.42	11.71		
A3	12.47	12.96	11.19	11.14	13.83	15.95
A3a	13.15	13.21	12.81	13.03		
A4	16.11	16.35	16.40	17.17	19.63	18.32
A4a	14.99	15.41	13.78	14.23		
A5	14.70	15.66	14.45	14.74	16.54	17.60
A5a	18.17	17.33	17.43	17.72		
A6	28.07	29.20	27.89	29.73	31.37	29.10

Notes

Sample references refer to Saxton Farm site (S1 – S6a) and Abel Farm site (A1 – A6); see Figure 3.3.

Blanks indicate absence of data (these sites were skipped due to time constraints at time of sampling).

Soil Samples taken from two depth zones; 0-50mm and 50-100mm.

Gravimetric Soil Moisture Content for Grid Study Site

Sample Reference	Noon Flight (23rd October 1996)		Dawn Flight (24th October 1996)	
	MC (%) 0-50mm	MC (%) 50-100mm	MC (%) 0-50mm	MC (%) 50-100mm
1A	13.89	13.94	14.85	13.36
1B	17.56	17.46	14.73	17.56
1C	21.39	23.12	22.11	21.23
1D	20.88	22.08	21.68	22.44
1E	22.57	23.71	25.49	23.20
1F	23.84	26.98	25.70	25.98
2A	19.82	16.98	15.46	17.42
2B	21.41	23.21	20.16	20.76
2C	25.94	24.20	23.66	25.52
2D	29.64	32.01	29.90	26.50
2E	13.39	16.68	13.27	16.18
2F	15.76	16.28	12.35	15.49
3A	8.92	9.62	8.98	11.07
3B	9.93	8.26	8.94	8.45
3C	17.82	17.75	14.34	18.07
3D	18.62	18.84	17.78	18.41
3E	14.43	16.74	15.84	15.47
3F	16.03	15.63	16.29	17.01
4A	14.80	16.94	16.94	15.98
4B	16.18	18.12	18.04	18.07
4C	19.91	19.42	16.01	19.92
4D	15.13	16.27	15.61	15.78
4E	15.38	15.69	15.66	16.56
4F	20.28	20.89	16.98	18.12
5A	12.82	15.99	16.37	16.76
5B	17.01	17.73	16.66	16.38
5C	16.98	18.33	17.69	18.32
5D	13.77	14.30	16.11	16.06
5E	19.24	19.22	17.11	18.51
5F	17.17	18.73	16.22	17.85

Notes
Sample references refer to Saxton Farm site (S1 – S6a) and Abel Farm site (A1 – A6); see Figure 3.3.
Blanks indicate absence of data (these sites were skipped due to time constraints at time of sampling).
Soil Samples taken from two depth zones; 0-50mm and 50-100mm.

Particle Size Distribution for Farm Study Sites

Sample Reference	Particle Size Distribution (percentage of total soil mass)							
	Gravel	Coarse Sand	Medium Sand	Fine Sand	Coarse Silt	Medium Silt	Fine Silt	Clay
S1	7.33	4.64	28.90	24.84	15.50	5.29	2.15	11.35
S1a	11.75	5.03	17.52	17.47	19.40	8.44	6.15	14.23
S2	12.45	4.49	14.18	13.11	20.02	11.25	5.99	18.51
S2a	2.01	3.18	37.15	24.15	11.33	3.82	4.97	13.38
S3	3.89	2.30	29.50	30.73	10.14	5.34	3.48	14.63
S3a	2.30	2.12	41.29	28.68	12.07	4.99	2.49	6.05
S4	4.96	1.50	27.53	38.62	10.05	4.19	3.81	9.34
S4a	3.77	2.63	39.81	29.16	11.74	4.54	1.90	6.45
S5	3.23	1.67	33.78	35.05	9.90	4.24	2.92	9.21
S5a	0.67	2.49	46.83	27.58	10.05	3.73	2.37	6.27
S6	0.47	2.69	46.01	26.72	7.46	5.05	1.85	9.76
S6a	3.39	1.72	19.80	43.15	15.14	7.35	3.15	6.30
A1	0.04	1.43	57.68	20.02	12.60	2.75	2.40	3.09
A1a	0.42	1.51	55.05	22.91	8.55	2.85	2.51	6.20
A2	0.58	1.70	54.26	22.65	14.79	3.23	2.37	0.43
A2a	1.75	1.19	22.51	38.49	16.90	5.97	5.00	8.19
A3	2.38	2.06	37.42	29.50	17.36	5.96	3.40	1.92
A3a	3.45	2.74	25.76	25.18	18.96	9.17	5.38	9.37
A4	4.00	3.18	38.08	23.54	12.28	5.05	4.42	9.46
A4a	2.42	3.76	34.90	23.62	15.49	7.26	3.34	9.22
A5	6.47	3.89	32.59	22.05	12.67	5.47	5.31	11.56
A5a	3.78	2.74	24.16	21.43	23.24	5.96	5.17	13.51
A6	2.54	1.74	17.24	20.57	23.05	8.87	6.34	19.64

Notes
Particle size distribution calculated for soil samples taken from depth zone 0 – 50mm.

Particle Size Distribution for Grid Study Sites

Sample Reference	Particle Size Distribution (percentage of total soil mass)							
	Gravel	Coarse Sand	Medium Sand	Fine Sand	Coarse Silt	Medium Silt	Fine Silt	Clay
1A	2.22	2.96	42.53	27.70	16.09	3.53	2.57	2.41
1B	9.85	4.86	18.02	21.69	27.18	6.84	6.31	5.26
1C	9.91	6.25	24.21	20.44	19.82	7.85	6.01	5.51
1D	5.09	3.52	21.64	27.89	25.74	10.39	3.31	2.43
1E	2.81	4.49	33.10	26.31	20.80	6.43	3.39	2.68
1F	5.39	4.38	28.40	26.03	22.72	6.33	5.06	1.69
2A	8.50	4.44	17.14	19.92	28.08	10.40	6.13	5.39
2B	5.39	5.50	26.47	21.64	21.42	7.91	6.46	5.21
2C	4.67	5.11	27.76	21.10	24.12	7.68	4.68	4.87
2D	2.27	3.85	36.17	24.29	19.24	6.48	4.46	3.24
2E	11.82	4.92	9.47	11.06	33.66	14.90	8.65	5.52
2F	8.96	4.18	10.32	14.49	31.09	11.88	9.15	9.93
3A	7.26	4.77	14.17	18.16	31.74	12.58	5.87	5.45
3B	2.79	5.90	36.12	19.93	18.06	7.23	3.32	6.65
3C	2.92	3.71	31.41	24.43	23.05	8.10	3.92	2.45
3D	4.12	4.64	16.38	23.86	28.87	10.39	6.78	4.97
3E	1.62	4.68	27.85	16.20	23.54	8.44	7.91	9.76
3F	4.93	5.83	17.86	20.91	29.55	10.34	5.53	5.05
4A	12.49	3.60	5.15	9.16	36.70	19.66	6.43	6.80
4B	2.16	5.86	35.21	19.14	20.19	6.86	5.09	5.49
4C	1.12	1.84	19.48	30.46	24.27	9.36	5.93	7.53
4D	18.55	8.56	18.92	6.64	26.72	9.07	7.75	3.78
4E	6.89	6.79	20.95	18.95	27.25	10.21	5.84	3.13
4F	5.93	4.48	19.36	25.68	24.10	11.22	4.52	4.70
5A	3.43	3.84	26.40	24.46	22.64	7.51	5.13	6.59
5B	6.73	2.66	4.73	0.60	27.95	26.11	14.79	16.43
5C	11.95	6.72	4.54	0.29	22.03	28.79	16.31	9.37
5D	6.36	6.28	17.24	4.16	29.66	19.62	9.47	7.22
5E	2.82	8.16	27.46	18.43	23.05	8.43	4.62	7.03
5F	3.83	4.92	15.68	17.97	28.51	16.41	7.27	5.40

Notes
Particle size distribution calculated for soil samples taken from depth zone 0 – 50mm.

Rainfall Data

Date	Time	Rainfall (mm)
26th October 1996	17:30	6.70
27th October 1996	17:00	5.10
29th October 1996	10:00	6.20
2nd November 1996	16:30	10.95
5th November 1996	15:45	8.25

Wind Speed Data

Wind Speed for Noon Flights (23rd October 1996)			
Time	Estimated Mean Wind Speed (m/s)	Gusting Wind Speed (m/s)	Approximate Direction
11:30	3.5	5.0	SE
11:35	2.5	3.5	SE
11:40	4.0	5.0	SE
11:45	5.0	5.5	SE
11:50	2.5	3.0	SE
11:55	2.5	3.0	SE
12:00	4.0	5.5	SE
12:05	1.0	2.0	SE
12:10			
12:15	2.5	3.0	SE
12:20			
12:25	0.5	1.5	SE
12:30	0.5	1.5	SE
12:35	0.5	1.0	SE
12:40	1.0	2.0	SE
12:45	4.0	5.0	SE
Notes Wind speed measured using a handheld anenometer, positioned approximately 2m from the ground surface. Blanks indicate absence of data.			

Wind Speed for Dawn Flights (24th October 1996)			
Time	Estimated Mean Wind Speed (m/s)	Gusting Wind Speed (m/s)	Approximate Direction
07:00	1.0	2.0	SE
07:05	0.5	0.5	SE
07:10	0.5	1.5	SE
07:15	1.0	2.0	SE
07:20	0.5	1.5	SE
07:25	2.5	3.0	SE
07:30	1.5	2.5	SE
07:35	0.5	1.0	SE
07:40	1.0	2.0	SE
07:45	1.0	2.0	SE
07:50	1.0	2.0	SE
Notes Wind speed measured using a handheld anenometer, positioned approximately 2m from the ground surface.			

APPENDIX 2

Computer Programs Developed During Research Project

ENDCORR.PAS

```
PROGRAM ENDCORR;

{*********************************************************************
*  CALCULATES THE DISPARITIES BETWEEN TWO APPROXIMATELY CO-REGISTERED
*  IMAGES OF THE SAME REGION, AND WRITES THE OUTPUT FILE AS
*  [ORIGX, ORIGY, NEWX, NEWY, CORRELATION]
*  PROCEDURE CORRELATES ATM(REFERENCE) TO PHOTO(SEARCH)
*********************************************************************}

USES CRT, DOS;

CONST
   TAB=#9;

TYPE
   MATRIX=ARRAY[1..100,1..100] OF BYTE;

VAR
FILE1, FILE2            :FILE OF BYTE;
GPHOTO, BAND3           :MATRIX;
FILENAME_OUT            :STRING;
OUTPUT_FILE                     :TEXT;

STARTROW, STARTCOL       :INTEGER;
ROW, COL                 :INTEGER;
W                               :INTEGER;
C                               :INTEGER;
G,H                             :INTEGER;
N                               :INTEGER;
CENTRE                  :INTEGER;
GRADIENT, INTERCEPT      :REAL;
MAXROW, MAXCOL          :LONGINT;
ENDROW                  :INTEGER;
CORRELATION              :REAL;
CAST, BESTCORR           :REAL;

PROCEDURE SAVE_NAME;
BEGIN
   WRITE('ENTER THE FILE NAME FOR THE OUTPUT DATA:- ');
   READLN(FILENAME_OUT);
   IF FILENAME_OUT='' THEN FILENAME_OUT:='DEFAULT';
   FILENAME_OUT:=('D:\RES\') + FILENAME_OUT + ('.TXT');
   WRITELN('');

   ASSIGN(OUTPUT_FILE, FILENAME_OUT);
   REWRITE(OUTPUT_FILE);
   WRITE(OUTPUT_FILE, 'ORIG X', TAB, 'ORIG Y', TAB);
   WRITELN(OUTPUT_FILE, 'NEW X', TAB, 'NEW Y', TAB, 'CORRELATION');
END;



PROCEDURE READ_GPHOTO_TXT;
VAR
   X,Y          :INTEGER;
   TEXTFILE             :TEXT;
   VAL          :BYTE;

BEGIN
   ASSIGN(TEXTFILE, 'D:\RES\PHOTO.TXT');
   RESET(TEXTFILE);
   ASSIGN(FILE1, 'D:\RES\PHOTO');
   REWRITE(FILE1);

   FOR X:=1 TO MAXROW DO
   BEGIN
    FOR Y:=1 TO MAXCOL DO
```

```
    BEGIN
     READ(TEXTFILE, VAL);
     WRITE(FILE1, VAL);
    END;
   END;
END;


PROCEDURE READ_BAND3_TXT;
VAR
   X,Y          :INTEGER;
   TEXTFILE             :TEXT;
   VAL          :BYTE;

BEGIN
   ASSIGN(TEXTFILE, 'D:\RES\BAND3.TXT');
   RESET(TEXTFILE);
   ASSIGN(FILE2, 'D:\RES\ATM');
   REWRITE(FILE2);

   FOR X:=1 TO MAXROW DO
   BEGIN
    FOR Y:=1 TO MAXCOL DO
    BEGIN
     READ(TEXTFILE, VAL);
     WRITE(FILE2, VAL);
    END;
   END;
END;


PROCEDURE INITIAL_SETUP;
VAR
   WAIT_FOR_KEY : CHAR;

BEGIN
   WRITELN;
   WRITELN('DO DATA FILES ALREADY EXIST IN BYTE FORMAT? (Y/N) ');
   REPEAT
    WAIT_FOR_KEY:=READKEY;
    WAIT_FOR_KEY:=UPCASE(WAIT_FOR_KEY);
   UNTIL (WAIT_FOR_KEY='Y') OR (WAIT_FOR_KEY='N');

   IF WAIT_FOR_KEY='Y' THEN
   BEGIN
    WRITELN;
    WRITE('HOW MANY ROWS DO DATA SETS HAVE? '); READLN(MAXROW);
    WRITE('HOW MANY COLUMNS DO DATA SETS HAVE? '); READLN(MAXCOL);
    ASSIGN(FILE1, 'D:\RES\PHOTO');
    ASSIGN(FILE2, 'D:\RES\ATM');
   END;

   IF WAIT_FOR_KEY='N' THEN
   BEGIN
    WRITELN;
    WRITE('HOW MANY ROWS DO DATA SETS HAVE? '); READLN(MAXROW);
    WRITE('HOW MANY COLUMNS DO DATA SETS HAVE? '); READLN(MAXCOL);
    WRITELN('READING DATA NOW...COULD TAKE A WHILE!');
    READ_GPHOTO_TXT;
    READ_BAND3_TXT;
   END;
   WRITELN;
END;

PROCEDURE WRITE_WINDOWS_TO_MEMORY(A,B:INTEGER);
VAR X,Y : INTEGER;

BEGIN
  RESET(FILE2);
    FOR X:=(A-W) TO (A+W) DO
    BEGIN
      FOR Y:=(B-W) TO (B+W) DO
```

```
      BEGIN
        SEEK(FILE2, MAXCOL*(X-1)+(Y-1));
        READ(FILE2,BAND3[X-(A-W-C-1),Y-(B-W-C-1)]);
      END;
    END;

  RESET(FILE1);
  FOR X:=(A-W-C) TO (A+W+C) DO
    BEGIN
      FOR Y:=(B-W-C) TO (B+W+C) DO
      BEGIN
        SEEK(FILE1, MAXCOL*(X-1)+(Y-1));
        READ(FILE1,GPHOTO[X-(A-W-C-1),Y-(B-W-C-1)]);
      END;
    END;
END;

PROCEDURE CALCULATE_KERNAL_CORRELATION(VAR P,Q:INTEGER; VAR TEMPCOR:REAL);
VAR
  X,Y : INTEGER;
  SIGMAXY, SIGMAX, SIGMAY, SIGMAX2, SIGMAY2 : REAL;
  CAST1, CAST2 : LONGINT;

BEGIN
  SIGMAXY:=0; SIGMAX:=0; SIGMAY:=0; SIGMAX2:=0; SIGMAY2:=0;

  FOR X:=(G-W) TO (G+W) DO
  BEGIN
    FOR Y:=(H-W) TO (H+W) DO
    BEGIN
      CAST1:=BAND3[CENTRE+X-G, CENTRE+Y-H]; CAST2:=GPHOTO[X,Y];
      SIGMAXY:=SIGMAXY+CAST1*CAST2;
      SIGMAX:=SIGMAX+CAST1;
      SIGMAY:=SIGMAY+CAST2;
      SIGMAX2:=SIGMAX2+SQR(CAST1);
      SIGMAY2:=SIGMAY2+SQR(CAST2);
    END;
  END;

  IF SIGMAX2=0 THEN SIGMAX2:=1; IF SIGMAY2=0 THEN SIGMAY2:=1;

  CORRELATION:=((N*SIGMAXY)-(SIGMAX*SIGMAY))/(SQRT((N*SIGMAX2)-
SQR(SIGMAX))*SQRT((N*SIGMAY2)-SQR(SIGMAY)));
  TEMPCOR:=CORRELATION;

  IF BESTCORR < CORRELATION THEN BESTCORR:=CORRELATION;
  IF BESTCORR = CORRELATION THEN P:=G;
  IF BESTCORR = CORRELATION THEN Q:=H;
END;


PROCEDURE CALCULATE_LOCAL_WINDOW_CORRELATION(A,B:INTEGER);
VAR
  P,Q     :INTEGER;
  TEMPCOR :REAL;

BEGIN
  P:=CENTRE; Q:=CENTRE; BESTCORR:=-1;
  FOR G:=(CENTRE-C) TO (CENTRE+C) DO
  BEGIN
    FOR H:=(CENTRE-C) TO (CENTRE+C) DO
    BEGIN
      CALCULATE_KERNAL_CORRELATION(P,Q,TEMPCOR);
    END;
  END;
  WRITE('BEST CORRELATION FOR ',A,' ',B,' IS ');
  WRITELN(BESTCORR:2:3,' AT ',(P+(A-W-C-1)),' ',(Q+(B-W-C-1)),' ',
        (-P+W+C+1),'',(-Q+W+C+1));
  WRITELN(OUTPUT_FILE,A,TAB,B,TAB,(P+(A-W-C-1)),TAB,(Q+(B-W-C-1)),
        TAB,BESTCORR:2:3);
END;
```

```
{MAIN PROGRAM}
BEGIN
  CLRSCR;
  INITIAL_SETUP;
  SAVE_NAME;

  ASSIGN(CONTOUR_OUT, 'D:\RES\CONTOUR.DAT');
  REWRITE(CONTOUR_OUT);

  WRITE('ENTER COORDINATES FOR CENTRE OF STARTING WINDOW ');
  READLN(STARTROW,STARTCOL);
  WRITE('ENTER ROW NUMBER ON WHICH TO STOP CALCULATING CORRELATION ');
  READLN(ENDROW);
  WRITE('ENTER GRADIENT OF SIDE OF IMAGE '); READLN(GRADIENT);

  WRITELN;
  WRITE('INPUT WIDTH OF KERNAL TO BE USED '); READLN(W);
  WRITE('INPUT NUMBER OF PIXELS WINDOW CAN MOVE '); READLN(C);
  WRITELN; WRITELN;
  CENTRE:=C+W+1; N:=SQR(2*W+1);

  INTERCEPT:=(STARTROW-0.5)+GRADIENT*(STARTCOL-0.5);

  FOR ROW:=1 TO MAXROW DO
  BEGIN
    CAST:=(INTERCEPT-(ROW-0.5))/GRADIENT;
    COL:=ROUND(CAST+0.5);

    IF (ROW>=STARTROW) AND (ROW<=ENDROW) THEN
    BEGIN
      WRITE_WINDOWS_TO_MEMORY(ROW,COL);
      CALCULATE_LOCAL_WINDOW_CORRELATION(ROW,COL);
    END
    ELSE WRITELN(OUTPUT_FILE,ROW,TAB,COL,TAB,ROW,TAB,COL,TAB,'0');
  END;
  CLOSE(OUTPUT_FILE);
END.
```

RESAMPLE.PAS

```
PROGRAM RESAMPLE;

USES CRT, DOS;                          {PROGRAM TO RESAMPLE IMAGE BASED ON}
                                        {LINE DISPARITIES FOR EACH SCANLINE}
CONST
TAB=#9;

VAR
DISP                    :ARRAY[1..1000,1..8] OF INTEGER;
EQUATIONS               :ARRAY[1..1000,1..2] OF REAL;
SOURCE,TARGET           :FILE OF BYTE;
FILENAME_OUT           :STRING;
OUTPUT_FILE                    :TEXT;
MAXROW, MAXCOL          :LONGINT;
PAD                     :INTEGER;


PROCEDURE INITIALISE_DATA_FILES;
                                        {CREATES SERIAL FILE FOR RESAMPLED}
VAR                                     {IMAGE, AND WRITES VALUES AS WHITE}
  X,Y    :INTEGER;
  WHITE :BYTE;

BEGIN
  ASSIGN(TARGET,'D:\RES\TARGET');
  REWRITE(TARGET);
  WHITE:=255;
  WRITE('INITIALISING DATA FILES...');
  FOR X:=1 TO (MAXROW) DO
  BEGIN
    FOR Y:=1 TO (MAXCOL) DO
    WRITE(TARGET,WHITE);
  END;
  WRITELN('DONE.');
  CLOSE(TARGET);
END;


PROCEDURE READ_SOURCE_IMAGE;
                                        {WRITES SOURCE IMAGE TEXT FILE}
VAR                                     {TO SERIAL FILE WITH PADDING  }
   X,Y          :INTEGER;                  {EQUAL TO MAXIMUM DISPARITY    }
   TEXTFILE     :TEXT;
   VAL       :BYTE;

BEGIN
   ASSIGN(TEXTFILE, 'D:\RES\BAND3.TXT');
   RESET(TEXTFILE);
   ASSIGN(SOURCE, 'D:\RES\SOURCE');
   REWRITE(SOURCE);

   WRITE('READING SOURCE IMAGE...');
   FOR X:=1 TO (MAXROW) DO BEGIN
     FOR Y:=1 TO (MAXCOL) DO BEGIN
       READ(TEXTFILE, VAL);
       WRITE(SOURCE, VAL);
     END;
   END;
   CLOSE(TEXTFILE); CLOSE(SOURCE);
   WRITELN('DONE.');
END;


PROCEDURE SAVE_NAME;                    {PROCEDURE TO CREATE FILE FOR}
                                        {RESAMPLED IMAGE             }
BEGIN
   WRITE('ENTER THE FILE NAME FOR THE OUTPUT IMAGE:- ');
   READLN(FILENAME_OUT);
```

```
   IF FILENAME_OUT='' THEN FILENAME_OUT:='DEFAULT';
   FILENAME_OUT:=('D:\RES\') + FILENAME_OUT + ('.PGM');
   WRITELN('');
END;

PROCEDURE INITIAL_SETUP;                {PROCEDURE ALLOWS THE CREATION}
                                        {OF SERIAL FILE FOR SOURCE     }
VAR                                     {IMAGE TO BE SKIPPED IF IT     }
   WAIT_FOR_KEY : CHAR;                 {ALREADY EXISTS                }

BEGIN
   WRITELN;
   WRITELN('DOES SOURCE DATA ALREADY EXIST IN BYTE FORMAT? (Y/N) ');
   REPEAT
    WAIT_FOR_KEY:=READKEY;
    WAIT_FOR_KEY:=UPCASE(WAIT_FOR_KEY);
   UNTIL (WAIT_FOR_KEY='Y') OR (WAIT_FOR_KEY='N');

   IF WAIT_FOR_KEY='Y' THEN
   BEGIN
    WRITELN;
    ASSIGN(SOURCE, 'D:\RES\SOURCE');
   END;

   IF WAIT_FOR_KEY='N' THEN
     READ_SOURCE_IMAGE;
END;


PROCEDURE READ_DISPARITIES;
                                        {READS IMAGE DISPARITIES FROM      }
VAR                                     {TEXT FILE XL,YL,NEWXL,NEWYL...ETC}
  X,Y       :INTEGER;                   {AND WRITES THEM TO AN ARRAY:      }
  TEXTFILE  :TEXT;                      {SAME FORMAT                       }

BEGIN
  WRITE('READING DISPARITIES...');
  ASSIGN(TEXTFILE, 'D:\RES\DISP02.TXT');
  RESET(TEXTFILE);

  FOR X:=1 TO MAXROW DO
  BEGIN
    FOR Y:=1 TO 8 DO
    READ(TEXTFILE, DISP[X,Y]);
  END;
  CLOSE(TEXTFILE);
  WRITELN('DONE');
END;


PROCEDURE CALCULATE_EQUATIONS;
                                        {CALCULATES THE EQUATIONS OF A }
VAR X,Y      :INTEGER;                  {STRAIGHT LINE REPRESENTING THE}
                                        {SHIFTED SCANLINES AND WRITES  }
BEGIN                                   {THEM TO AN ARRAY : GRAD, INT. }
  WRITE('CALCULATING EQUATIONS...');
  FOR X:=1 TO MAXROW DO
  BEGIN
{GRAD} EQUATIONS[X,1]:=(DISP[X,3]-DISP[X,7]) / (DISP[X,8]-DISP[X,4]);
{INT } EQUATIONS[X,2]:=(DISP[X,3]-0.5)+(DISP[X,4]-0.5)*EQUATIONS[X,1];
  END;
  WRITELN('DONE');
END;


PROCEDURE WRITE_PIXEL_VALUE(A,B,XOLD:INTEGER;YNEAR:REAL);
VAR                                     {FUNCTION WRITES THE SOURCE IMAGE}
  YOLD    :INTEGER;                     {PIXEL VALUE TO TARGET ONCE THE  }
  CAST1   :REAL;                        {NEAREST PIXEL HAS BEEN FOUND    }
  VAL     :BYTE;
```

```
BEGIN
  YOLD:=ROUND(DISP[XOLD,2]+ (YNEAR-DISP[XOLD,4])*(DISP[XOLD,6]-
    DISP[XOLD,2])/(DISP[XOLD,8]-DISP[XOLD,4]));

  SEEK(SOURCE, MAXCOL*(XOLD-1)+YOLD-1);  READ(SOURCE, VAL);
  SEEK(TARGET, MAXCOL*(A-1)+B-1); WRITE(TARGET, VAL);
END;


PROCEDURE FIND_NEAREST_POINT(A,B:INTEGER);
                                          {FUNCTION FINDS NEAREST PIXEL}
                                    {TO INPUT COORDS (A,B)        }
                                    {NOTE:EQUATION IN FORM X+MY=C}
VAR X, LINE :INTEGER;
    PERP_GRAD, PERP_INTERCEPT, P, Q, XNEAR, YNEAR, DIST :REAL;

BEGIN                                {P & Q ARE NEAREST POINTS}
  DIST:=PAD;                         {FOR EACH ITERATION      }
  FOR X:=(A-PAD) TO (A+PAD) DO
  BEGIN
    IF (X>0) AND (X<MAXROW) THEN
    BEGIN
      IF EQUATIONS[X,1] <> 0 THEN
      PERP_GRAD:= (-1/EQUATIONS[X,1])
      ELSE
      PERP_GRAD:= 100000;     {INFINITY}
      PERP_INTERCEPT:= (A-0.5)+PERP_GRAD*(B-0.5);

      Q:=(EQUATIONS[X,2]-PERP_INTERCEPT) / (EQUATIONS[X,1]-PERP_GRAD);
      P:=EQUATIONS[X,2]-(EQUATIONS[X,1]*Q);

      IF SQRT(SQR(P-A+0.5)+SQR(Q-B+0.5)) < DIST THEN
      BEGIN
        XNEAR:=P; YNEAR:=Q; LINE:=X;
        DIST:=SQRT(SQR(XNEAR-A+0.5)+SQR(YNEAR-B+0.5));
      END;
    END;
  END;
  WRITE_PIXEL_VALUE(A,B,LINE,YNEAR);
END;


PROCEDURE WRITE_IMAGE_TO_FILE;
                                    {FUNCTION WRITES FINAL TARGET}
VAR                                 {IMAGE TO OUTPUT TEXT FILE   }
  X,Y   :INTEGER;
  VAL   :BYTE;

BEGIN
  SAVE_NAME;
  ASSIGN(OUTPUT_FILE, FILENAME_OUT);
  REWRITE(OUTPUT_FILE);
  RESET(TARGET);

  WRITELN(OUTPUT_FILE,'P2');
  WRITELN(OUTPUT_FILE,'#');
  WRITELN(OUTPUT_FILE,MAXCOL,' ',MAXROW);
  WRITELN(OUTPUT_FILE, '255');

  FOR X:=1 TO (MAXROW) DO
  BEGIN
    FOR Y:=1 TO (MAXCOL) DO
    BEGIN
      READ(TARGET, VAL);
      WRITE(OUTPUT_FILE, VAL, ' ');
    END;
    WRITELN(OUTPUT_FILE,'');
  END;
  CLOSE(OUTPUT_FILE); CLOSE(TARGET);
END;
```

```
PROCEDURE READ_COORDS;
                                    {FUNCTION SEARCHES TARGET AND }
VAR A,B             :LONGINT;       {PERFORMS RESAMPLING INSIDE   }
    VAL, BLACK      :BYTE;          {FRAME DRAW PREVIOUSLY        }
    AA,BB,CC,DD     :INTEGER;

BEGIN
  AA:=50; BB:=50; CC:=830; DD:=760;  {LIMITS OF AREA TO RESAMPLE}

  RESET(SOURCE); RESET(TARGET);
  FOR A:=1 TO (MAXROW) DO BEGIN
    FOR B:=1 TO (MAXCOL) DO BEGIN
      IF (A>=AA) AND (A<=CC) AND (B>=BB) AND (B<=DD)
       THEN FIND_NEAREST_POINT(A,B);
    END;
  WRITELN(A);
  END;
  CLOSE(SOURCE); CLOSE(TARGET);
END;

      {MAIN PROGRAM}
BEGIN
MAXCOL:=811; MAXROW:=886; PAD:=20;
INITIAL_SETUP;
INITIALISE_DATA_FILES;
READ_DISPARITIES;
CALCULATE_EQUATIONS;
READ_COORDS;
WRITE_IMAGE_TO_FILE;
END.
```

LINECORR.PAS

```
PROGRAM LINECORR;

{$M 32768,0,655360}              {CHANGE STACK SIZE TO 32K}

USES DOS, CRT;

CONST
       {RAW ATM IMAGE}
       INFILE1 = 'D:\RES\BAND3RAW.PGM';
       ROWS    = 1168;
       COLUMNS = 714;

       {CORRECTED OR RESCALED PHOTOGRAPH}
       INFILE2 = 'D:\RES\GPHOTO.PGM';
       MAXROW  = 886;
       MAXCOL  = 811;

       {SEARCH OPTIONS}
       INITIAL_SEARCH = 2;
       RUNNING_SEARCH = 2;

       AA = 250;       {RESAMPLED AREA}
       BB = 90;
                CC = 690;
                DD = 660;

       TAB     = #9;

TYPE
  COLPTR    = ^COLARRAY;
  COLARRAY  = ARRAY[1..MAXCOL] OF BYTE;
  COLNODE   = RECORD
                COL : COLPTR
              END;
  ROWPTR    = ^ROWARRAY;
  ROWARRAY  = ARRAY[1..MAXROW] OF COLNODE;

  LINEPTR   = ^LINEARRAY;
  LINEARRAY = ARRAY[1..COLUMNS] OF BYTE;

  NODEPOINT = ^NODETYPE;
  NODETYPE  = RECORD
                NEXT :NODEPOINT;
                DATA :INTEGER;
              END;

VAR
  PHOTODATA                       :ROWPTR;
  BAR                             :LINEPTR;
  FIRSTNODEPTR, CURRENTNODEPTR    :NODEPOINT;
  TEMPNODEPTR, PREVIOUSNODE       :NODEPOINT;
  EQUATIONS                       :ARRAY[1..ROWS,1..4] OF REAL;
  STRETCHED_SCANLINE              :ARRAY[1..MAXCOL] OF BYTE;
  CORRECTED_SCANLINE              :ARRAY[1..MAXCOL] OF BYTE;
  RANK1, RANK2                    :ARRAY[1..MAXCOL] OF REAL;

  PHOTO, RAWATM, TEMP             :FILE OF BYTE;

  CORRELATION, BESTCORR           :REAL;
  YL, YR                          :LONGINT;


PROCEDURE GET_ANSWER(QUESTION:STRING; VAR WAIT_FOR_KEY:CHAR);

BEGIN
  WRITELN(QUESTION);
  REPEAT
    WAIT_FOR_KEY:=READKEY;
```

```
    WAIT_FOR_KEY:=UPCASE(WAIT_FOR_KEY);
  UNTIL (WAIT_FOR_KEY='Y') OR (WAIT_FOR_KEY='N');
END;


PROCEDURE SAVE_NAME(VAR FILENAME_OUT,QUESTION:STRING);

BEGIN
   WRITE(QUESTION);
   READLN(FILENAME_OUT);
   IF FILENAME_OUT='' THEN FILENAME_OUT:='DEFAULT';
   FILENAME_OUT:=('D:\RES\') + FILENAME_OUT;
END;


PROCEDURE READ_SOURCE_IMAGES;

VAR
   X,Y          :LONGINT;
   TEXTFILE     :TEXT;
   VAL                  :BYTE;
   JUNK          :STRING;

BEGIN
   ASSIGN(TEXTFILE, INFILE1);
   RESET(TEXTFILE);
   ASSIGN(RAWATM, 'D:\RES\RAWATM');
   REWRITE(RAWATM);
   FOR X:=1 TO 4 DO            {MOVE PAST HEADER INFORMATION}
     READLN(TEXTFILE,JUNK);

   FOR X:=1 TO ROWS DO
   BEGIN
     FOR Y:=1 TO COLUMNS DO
     BEGIN
       READ(TEXTFILE, VAL);
       WRITE(RAWATM, VAL);
     END;
   END;
   CLOSE(TEXTFILE); CLOSE(RAWATM);

   ASSIGN(TEXTFILE, INFILE2);
   RESET(TEXTFILE);
   ASSIGN(PHOTO, 'D:\RES\PHOTO');
   REWRITE(PHOTO);
   FOR X:=1 TO 4 DO            {MOVE PAST HEADER INFORMATION}
     READLN(TEXTFILE, JUNK);

   FOR X:=1 TO MAXROW DO
   BEGIN
     FOR Y:=1 TO MAXCOL DO
     BEGIN
       READ(TEXTFILE, VAL);
       WRITE(PHOTO, VAL);
     END;
   END;
   CLOSE(TEXTFILE); CLOSE(PHOTO);
END;


PROCEDURE INITIAL_SETUP;

VAR QUESTION :STRING;
    ANSWER   :CHAR;
    TEXTFILE :TEXT;
    X,Y      :INTEGER;

BEGIN
  WRITELN;
  QUESTION:='DO SOURCE IMAGES ALREADY EXIST IN BYTE FORMAT? (Y/N) ';
  GET_ANSWER(QUESTION, ANSWER);
```

```
 IF ANSWER='Y' THEN BEGIN
   ASSIGN(RAWATM, 'D:\RES\RAWATM');
   ASSIGN(PHOTO, 'D:\RES\PHOTO');
 END;

 IF ANSWER='N' THEN BEGIN
   WRITE('READING SOURCE DATA NOW...');
   READ_SOURCE_IMAGES;
   WRITELN('DONE.');
 END;

 {EMPTY EQUATIONS ARRAY}
 FOR X:=1 TO ROWS DO BEGIN
   FOR Y:=1 TO 4 DO
     EQUATIONS[X,Y]:=0;
 END;
END;


PROCEDURE CALCULATE_EQUATIONS(LINE, XLEFT, YLEFT, XRIGHT, YRIGHT:INTEGER);

BEGIN
  IF (YRIGHT-YLEFT)<>0 THEN EQUATIONS[LINE,1]:=(XLEFT-XRIGHT)/(YRIGHT-YLEFT)
   ELSE EQUATIONS[LINE,1]:=1000000;     {GRADIENT}
  EQUATIONS[LINE,2]:=(XLEFT-0.5)+((YLEFT-0.5)*EQUATIONS[LINE,1]);  {INTERCEPT}
  EQUATIONS[LINE,3]:=YLEFT;
  EQUATIONS[LINE,4]:=YRIGHT;
END;


PROCEDURE READ_EQUATIONS;

VAR TEXTFILE                  :TEXT;
    STARTL, ENDL              :INTEGER;
    LINE, LOOP                :INTEGER;
    INPUT_STR                 :STRING;
    TEMP                      :ARRAY[1..8] OF INTEGER;

BEGIN
  WRITE('ENTER FILE NAME CONTAINING CORRELATION DATA :- ');
  READLN(INPUT_STR);
  INPUT_STR:='D:\RES\' + INPUT_STR + '.TXT';
  ASSIGN(TEXTFILE, INPUT_STR);
  RESET(TEXTFILE);

  READLN(TEXTFILE);          {MOVE PAST HEADER INFORMATION}
  READ(TEXTFILE,STARTL);
  READLN(TEXTFILE,ENDL);
  READLN(TEXTFILE);
  READ(TEXTFILE,YL);
  READLN(TEXTFILE,YR);

  FOR LOOP:=1 TO 4 DO
    READLN(TEXTFILE);

  FOR LINE:=STARTL TO ENDL DO BEGIN
    FOR LOOP:=1 TO 8 DO
      READ(TEXTFILE, TEMP[LOOP]);

      IF (TEMP[8]-TEMP[6])<>0 THEN
        EQUATIONS[LINE,1]:=(TEMP[5]-TEMP[7]) / (TEMP[8]-TEMP[6])  {GRADIENT}
      ELSE EQUATIONS[LINE,1]:=1000000; {INFINITY}
      EQUATIONS[LINE,2]:=(TEMP[5]-0.5)+((TEMP[6]-0.5)*EQUATIONS[LINE,1]);  {INTERCEPT}
      EQUATIONS[LINE,3]:=TEMP[6];
      EQUATIONS[LINE,4]:=TEMP[8];
   END;
   CLOSE(TEXTFILE);
 END;


 PROCEDURE READ_PHOTO_DATA_TO_MEMORY(FIRSTLINE, ENDLINE:LONGINT);
```

```
VAR
  X,Y        :LONGINT;
  VAL        :BYTE;

BEGIN
  WRITELN;
  WRITE('READING DATA TO MEMORY...');
  RESET(PHOTO);

  GETMEM(PHOTODATA, SIZEOF(ROWARRAY));
  FOR X:=FIRSTLINE TO ENDLINE DO
    GETMEM(PHOTODATA^[X].COL, SIZEOF(COLARRAY));

  FOR X:=FIRSTLINE TO ENDLINE DO BEGIN
    FOR Y:=1 TO MAXCOL DO BEGIN
      SEEK(PHOTO, MAXCOL*(X-1)+Y-1);
      READ(PHOTO, VAL);
      PHOTODATA^[X].COL^[Y] := VAL;
    END
  END;
  CLOSE(PHOTO);
  WRITELN('DONE.');
END;


PROCEDURE READ_REFERENCE_DATA(X:LONGINT);

VAR
  Y      :INTEGER;
  VAL    :BYTE;

BEGIN
  RESET(RAWATM);
  GETMEM(BAR, SIZEOF(LINEARRAY));
  FOR Y:=YL TO YR DO BEGIN
    SEEK(RAWATM, COLUMNS*(X-1)+Y-1);
    READ(RAWATM, VAL);
    BAR^[Y]:=VAL;
  END;
END;


PROCEDURE GENERATE_STRETCHED_SCANLINE(SF:REAL;YLEFT,YRIGHT:INTEGER);

VAR  Y, YGRAB   :INTEGER;

BEGIN
  FOR Y:=YLEFT TO YRIGHT DO BEGIN
    YGRAB:=ROUND(YL + (Y-YLEFT)*SF);
    STRETCHED_SCANLINE[Y]:=BAR^[YGRAB];    {I.E. BACKWARD RESAMPLING}
  END;
END;


PROCEDURE GRAB_CORRECTED_SCANLINE(XLEFT,YLEFT,XRIGHT,YRIGHT:INTEGER);

VAR  GRAD_OF_X   :REAL;
     XGRAB,Y     :INTEGER;

BEGIN
  GRAD_OF_X:=(XLEFT-XRIGHT)/(YRIGHT-YLEFT);
  FOR Y:=YLEFT TO YRIGHT DO BEGIN
    XGRAB:= ROUND(XLEFT - GRAD_OF_X*(Y-YLEFT));
    CORRECTED_SCANLINE[Y]:=PHOTODATA^[XGRAB].COL^[Y];
  END;
END;


PROCEDURE RANK_DATA_SETS(A:ARRAY OF BYTE; VAR B:ARRAY OF
                                    REAL;YLEFT,YRIGHT:INTEGER);

VAR X,Y,RANK,LASTRANK,VALUE,COUNTER   :INTEGER;
```

```
    AVERAGERANK                          :REAL;

BEGIN
  LASTRANK:=1;
  NEW(FIRSTNODEPTR);
  FIRSTNODEPTR^.NEXT:=NIL;
  CURRENTNODEPTR:=FIRSTNODEPTR;   {INITIALISED LIST}
  TEMPNODEPTR:=FIRSTNODEPTR;

  FOR VALUE:=0 TO 255 DO BEGIN
    COUNTER:=0;
    AVERAGERANK:=0;
    FOR Y:=YLEFT TO YRIGHT DO BEGIN
      IF A[Y] = VALUE THEN
      BEGIN
        INC(COUNTER);
        IF COUNTER=1 THEN TEMPNODEPTR:=CURRENTNODEPTR;
        NEW(CURRENTNODEPTR^.NEXT);
        CURRENTNODEPTR:=CURRENTNODEPTR^.NEXT;
        CURRENTNODEPTR^.NEXT:=NIL;
        CURRENTNODEPTR^.DATA:=Y;
      END;
    END;
    FOR X:=LASTRANK TO (LASTRANK+COUNTER-1) DO
      AVERAGERANK:=AVERAGERANK+X;

    IF COUNTER>1 THEN AVERAGERANK:=AVERAGERANK/COUNTER;
    LASTRANK:=LASTRANK+COUNTER;

    CURRENTNODEPTR:=TEMPNODEPTR;
    WHILE CURRENTNODEPTR^.NEXT <> NIL DO BEGIN
      CURRENTNODEPTR:=CURRENTNODEPTR^.NEXT;
      B[CURRENTNODEPTR^.DATA]:=AVERAGERANK;
    END;
    TEMPNODEPTR:=CURRENTNODEPTR;
  END;

  {DISPOSE OF LIST}
  PREVIOUSNODE:=FIRSTNODEPTR;
  WHILE CURRENTNODEPTR <> NIL DO BEGIN
    CURRENTNODEPTR:=PREVIOUSNODE^.NEXT;
    DISPOSE(PREVIOUSNODE);
    PREVIOUSNODE:=CURRENTNODEPTR;
  END;
END;


PROCEDURE PERFORM_RANK_CORRELATION(A,B:ARRAY OF REAL;
                                   VAR CORRELATION:REAL; YLEFT,YRIGHT:INTEGER);
VAR
  N,Y    :INTEGER;
  SIGMAXY, SIGMAX2,SIGMAY2   :REAL;
  XBAR, YBAR                 :REAL;

BEGIN
  N:=0; SIGMAXY:=0; SIGMAX2:=0; SIGMAY2:=0;
  XBAR:=0; YBAR:=0;

  FOR Y:=YLEFT TO YRIGHT DO BEGIN
    XBAR:=XBAR+A[Y];
    YBAR:=YBAR+B[Y];
    INC(N);
  END;

  XBAR:=XBAR/N;
  YBAR:=YBAR/N;

  FOR Y:=YLEFT TO YRIGHT DO BEGIN
    SIGMAXY:=SIGMAXY+(A[Y]-XBAR)*(B[Y]-YBAR);
    SIGMAX2:=SIGMAX2+SQR(A[Y]-XBAR);
    SIGMAY2:=SIGMAY2+SQR(B[Y]-YBAR);
  END;
```

```
  CORRELATION:=SIGMAXY / SQRT(SIGMAX2*SIGMAY2);
END;


PROCEDURE PERFORM_STANDARD_CORRELATION(A,B:ARRAY OF BYTE;
                                       VAR CORRELATION:REAL; YLEFT,YRIGHT:INTEGER);
VAR
  N,Y    :INTEGER;
  SIGMAXY, SIGMAX2,SIGMAY2   :REAL;
  XBAR, YBAR                 :REAL;

BEGIN
  N:=0; SIGMAXY:=0; SIGMAX2:=0; SIGMAY2:=0;
  XBAR:=0; YBAR:=0;

  FOR Y:=YLEFT TO YRIGHT DO BEGIN
    XBAR:=XBAR+A[Y];
    YBAR:=YBAR+B[Y];
    INC(N);
  END;

  XBAR:=XBAR/N;
  YBAR:=YBAR/N;

  FOR Y:=YLEFT TO YRIGHT DO BEGIN
    SIGMAXY:=SIGMAXY+(A[Y]-XBAR)*(B[Y]-YBAR);
    SIGMAX2:=SIGMAX2+SQR(A[Y]-XBAR);
    SIGMAY2:=SIGMAY2+SQR(B[Y]-YBAR);
  END;
  CORRELATION:=SIGMAXY / SQRT(SIGMAX2*SIGMAY2);
END;


PROCEDURE CORRELATE_BY_LINE(STARTL,ENDL:INTEGER; VAR OUTPUT_FILE:TEXT;
                            GUESS_XL, GUESS_YL, GUESS_XR, GUESS_YR:INTEGER;
                            RANK:BOOLEAN);

VAR LINE,X,Y,SEARCH                        :INTEGER;
    FIRSTLINE, ENDLINE                     :LONGINT;
    XLEFT,YLEFT,XRIGHT,YRIGHT              :INTEGER;
    BESTXL, BESTYL, BESTXR, BESTYR         :INTEGER;
    SCANLINES                              :TEXT;
    XBAR,YBAR,SF                           :REAL;
    CORRELATION, BESTCORR                  :REAL;
    QUESTION                               :STRING;
    PARAMETERS                             :ARRAY[1..ROWS,1..4] OF INTEGER;

BEGIN
  SEARCH:=INITIAL_SEARCH;

  {EMPTY PARAMETERS ARRAY}
  FOR X:=1 TO ROWS DO BEGIN
    FOR Y:=1 TO 4 DO
      PARAMETERS[X,Y]:=0;
  END;

  {READ PHOTO DATA TO MEMORY}
  IF GUESS_XR>GUESS_XL THEN FIRSTLINE:=GUESS_XL
  ELSE FIRSTLINE:=GUESS_XR;
  IF GUESS_XL>GUESS_XR THEN ENDLINE:=GUESS_XL ELSE ENDLINE:=GUESS_XR;
  IF (FIRSTLINE-10)<1 THEN FIRSTLINE:=1 ELSE FIRSTLINE:=(FIRSTLINE-
   10);
  IF (ENDLINE+100)>MAXROW THEN ENDLINE:=MAXROW
  ELSE ENDLINE:=(ENDLINE+100);
  READ_PHOTO_DATA_TO_MEMORY(FIRSTLINE, ENDLINE);

  {DEFINE STARTING POSITION}
  PARAMETERS[STARTL,1]:=GUESS_XL;  PARAMETERS[STARTL,2]:=GUESS_YL;
  PARAMETERS[STARTL,3]:=GUESS_XR;  PARAMETERS[STARTL,4]:=GUESS_YR;

  FOR LINE:=STARTL TO ENDL DO
  BEGIN
```

```
IF KEYPRESSED THEN BEGIN              {BREAK FUNCTION}
  WRITELN;
  WRITELN('      ***PROGRAM TERMINATED***');
  WRITELN;
  EXIT;
END;

{READ REFERENCE SCANLINE TO MEMORY}
READ_REFERENCE_DATA(LINE);

{TEST LIMITS AND READ RELEVANT SECTION OF SEARCH IMAGE TO MEMORY}
IF ((PARAMETERS[LINE,1]+SEARCH+5)>ENDLINE)
OR ((PARAMETERS[LINE,3]+SEARCH+5)>ENDLINE) THEN
BEGIN
  {DISPOSE OF EXISTING DATA IN MEMORY}
  FOR X:=FIRSTLINE TO ENDLINE DO
    DISPOSE(PHOTODATA^[X].COL);
  DISPOSE(PHOTODATA);

  {DEFINE NEW FIRSTLINE AND ENDLINE}
  IF PARAMETERS[LINE,1] <= PARAMETERS[LINE,3]
    THEN FIRSTLINE:=PARAMETERS[LINE,1]-SEARCH-5
    ELSE FIRSTLINE:=PARAMETERS[LINE,3]-SEARCH-5;
  IF PARAMETERS[LINE,1] <= PARAMETERS[LINE,3]
    THEN ENDLINE:=PARAMETERS[LINE,3]+SEARCH+100
    ELSE ENDLINE:=PARAMETERS[LINE,1]+SEARCH+100;
  IF ENDLINE>MAXROW THEN ENDLINE:=MAXROW;

  READ_PHOTO_DATA_TO_MEMORY(FIRSTLINE, ENDLINE);
END;

{RESET CORRELATION COEFFICIENTS}
BESTCORR:=-1;

{BEGIN SEARCH LOOP}
FOR XLEFT:=(PARAMETERS[LINE,1]-SEARCH) TO
                        (PARAMETERS[LINE,1]+SEARCH) DO BEGIN
  FOR YLEFT:=(PARAMETERS[LINE,2]-SEARCH) TO
                        (PARAMETERS[LINE,2]+SEARCH) DO BEGIN
    FOR XRIGHT:=(PARAMETERS[LINE,3]-SEARCH) TO
                        (PARAMETERS[LINE,3]+SEARCH) DO BEGIN
      FOR YRIGHT:=(PARAMETERS[LINE,4]-SEARCH) TO
                        (PARAMETERS[LINE,4]+SEARCH) DO BEGIN

        {CALCULATE SCALING FACTOR}
        SF:= (YR-YL){REF} / (YRIGHT-YLEFT){SEARCH};

        GENERATE_STRETCHED_SCANLINE(SF,YLEFT,YRIGHT);
        GRAB_CORRECTED_SCANLINE(XLEFT,YLEFT,XRIGHT,YRIGHT);

        IF RANK=TRUE THEN BEGIN
          RANK_DATA_SETS(STRETCHED_SCANLINE,RANK1,YLEFT,YRIGHT);
          RANK_DATA_SETS(CORRECTED_SCANLINE,RANK2,YLEFT,YRIGHT);
             PERFORM_RANK_CORRELATION(RANK1,RANK2,CORRELATION,YLEFT,
              YRIGHT);
        END
        ELSE
           PERFORM_STANDARD_CORRELATION(STRETCHED_SCANLINE,
            CORRECTED_SCANLINE,CORRELATION,YLEFT,YRIGHT);

        {RANK AND STANDARD CORRELATION HAVE DIFFERENT PROCEDURES}
        {BY VIRTUE OF DIFFERENT DATA ARRAY TYPES (REAL AND BYTE)}

        IF BESTCORR < CORRELATION THEN BEGIN
          BESTCORR:=CORRELATION;
          BESTXL:=XLEFT; BESTYL:=YLEFT;
          BESTXR:=XRIGHT; BESTYR:=YRIGHT;
        END;
      END;
    END;
  END;
END;
```

```
  WRITE('(',LINE,',',YL,')X(',LINE,',',YR,') --> ');
  WRITELN('(',BESTXL,',',BESTYL,')X(',BESTXR,',',BESTYR,') -
   CORR=',BESTCORR:5:2);
  WRITELN(OUTPUT_FILE,LINE,TAB,YL,TAB,LINE,TAB,YR,TAB,BESTXL,TAB,
   BESTYL,TAB,BESTXR,TAB,BESTYR);
  CALCULATE_EQUATIONS(LINE,BESTXL,BESTYL,BESTXR,BESTYR);

  {DEFINE NEXT LINE'S STARTING POSITION}
  PARAMETERS[LINE+1,1]:=BESTXL+1; PARAMETERS[LINE+1,2]:=BESTYL;
  PARAMETERS[LINE+1,3]:=BESTXR+1; PARAMETERS[LINE+1,4]:=BESTYR;

  SEARCH:=RUNNING_SEARCH;

  {DISPOSE OF REFERENCE DATA}
  DISPOSE(BAR);

  END; {(OF LINE LOOP)}
END;


PROCEDURE PROMPT_FOR_CORRELATION;

VAR QUESTION, OUTPUT_STR    :STRING;
    ANSWER                  :CHAR;
    STARTL, ENDL            :INTEGER;
    OUTPUT_FILE             :TEXT;
    X,Y                     :INTEGER;
    WIDTH                   :INTEGER;
    WAIT_FOR_KEY            :CHAR;
    RANK                    :BOOLEAN;
    GUESS_XL,GUESS_YL,GUESS_XR,GUESS_YR   :INTEGER;

BEGIN
  QUESTION:='DO YOU WANT TO RUN CORRELATION PROGRAM NOW? (Y/N) ';
  GET_ANSWER(QUESTION, ANSWER);

  IF ANSWER='Y' THEN
  BEGIN
    {PROMPT FOR RANK OR STANDARD CORRELATION}
    QUESTION:='RANK OR STANDARD CORRELATION? (R/S) ';
    WRITELN(QUESTION);
    REPEAT
      WAIT_FOR_KEY:=READKEY;
      WAIT_FOR_KEY:=UPCASE(WAIT_FOR_KEY);
    UNTIL (WAIT_FOR_KEY='R') OR (WAIT_FOR_KEY='S');
    IF WAIT_FOR_KEY='R' THEN RANK:=TRUE ELSE RANK:=FALSE;

    QUESTION:=('ENTER FILE NAME FOR CORRELATION DATA :- ');
    SAVE_NAME(OUTPUT_STR, QUESTION);
    OUTPUT_STR:= OUTPUT_STR + ('.TXT');
    ASSIGN(OUTPUT_FILE, OUTPUT_STR);
    REWRITE(OUTPUT_FILE);

    WRITE('ENTER START AND END ROWS '); READLN(STARTL,ENDL);
    WRITE('ENTER LEFT AND RIGHT HAND COLUMN NUMBERS '); READLN(YL,YR);

    {READ INITIAL POSITION OF SCAN LINE ON CORRECTED PHOTO}
    WRITE('ENTER PHOTO COORDS FOR LEFTHAND SIDE  ');
    READLN(GUESS_XL,GUESS_YL);
    WRITE('ENTER PHOTO COORDS FOR RIGHTHAND SIDE ');
    READLN(GUESS_XR,GUESS_YR);

    {WRITE HEADER TO OUTPUT FILE}
    IF RANK=TRUE THEN WRITELN(OUTPUT_FILE, 'RANK CORRELATION ',
      INFILE1,'(REF) TO ',INFILE2,'(SEARCH) BETWEEN ROWS ')
    ELSE WRITELN(OUTPUT_FILE, 'STANDARD CORRELATION ',INFILE1,
      '(REF) TO ',INFILE2,'(SEARCH) BETWEEN ROWS ');
    WRITELN(OUTPUT_FILE,STARTL,TAB,ENDL);
    WRITELN(OUTPUT_FILE, 'AND COLUMNS');
    WRITELN(OUTPUT_FILE,YL,TAB,YR);
    WRITE(OUTPUT_FILE,'SEARCH =',INITIAL_SEARCH,'(',RUNNING_SEARCH,'),
```

```
      INITIAL GUESS AT (');
    WRITELN(OUTPUT_FILE,GUESS_XL,',',GUESS_YL,') -> (',GUESS_XR,',
      ',GUESS_YR,')');
    WRITELN(OUTPUT_FILE);
    WRITELN(OUTPUT_FILE,'ATM',TAB,TAB,TAB,TAB,'PHOTO');
    WRITELN(OUTPUT_FILE,'XL',TAB,'YL',TAB,'XR',TAB,'YR',TAB,'XL',TAB,
      'YL',TAB,'XR',TAB,'YR');

    CORRELATE_BY_LINE(STARTL,ENDL,OUTPUT_FILE,GUESS_XL,GUESS_YL,
      GUESS_XR,GUESS_YR,RANK);
    CLOSE(OUTPUT_FILE);
  END;

  IF ANSWER='N' THEN
  BEGIN
    READ_EQUATIONS;
  END;
END;


PROCEDURE WRITE_IMAGE_TO_FILE(OUTPUT_STR:STRING; X,Y:INTEGER);

VAR
  ROW,COL              :INTEGER;
  VAL                  :BYTE;
  OUTPUT_FILE          :TEXT;

BEGIN
  WRITE('WRITING IMAGE TO FILE...');
  ASSIGN(OUTPUT_FILE, OUTPUT_STR);
  REWRITE(OUTPUT_FILE);
  RESET(TEMP);

  WRITELN(OUTPUT_FILE,'P2');
  WRITELN(OUTPUT_FILE,'#');
  WRITELN(OUTPUT_FILE,Y,' ',X);
  WRITELN(OUTPUT_FILE, '255');

  FOR ROW:=1 TO X DO BEGIN
    FOR COL:=1 TO Y DO BEGIN
      READ(TEMP, VAL);
      WRITE(OUTPUT_FILE, VAL, ' ');
    END;
    WRITELN(OUTPUT_FILE);
  END;
  CLOSE(OUTPUT_FILE); CLOSE(TEMP);
  WRITELN('DONE.'); WRITELN;
END;


PROCEDURE PREPARE_OUTPUT_FILE(OUTPUT_STR:STRING);
                              {CREATES SERIAL FILE FOR RESAMPLED}
                              {IMAGE, AND WRITES VALUES AS WHITE}
VAR
  X,Y   :LONGINT;
  WHITE :BYTE;

BEGIN
  ASSIGN(TEMP,'OUTPUT_STR');
  REWRITE(TEMP);
  WHITE:=255;
  WRITE('PREPARING OUTPUT IMAGE...');
  FOR X:=1 TO MAXROW DO
  BEGIN
    FOR Y:=1 TO MAXCOL DO
      WRITE(TEMP,WHITE);
  END;
  WRITELN('DONE.');
  CLOSE(TEMP);
END;
```

```
PROCEDURE PLOT_SCANLINES;

VAR
  QUESTION, OUTPUT_STR      :STRING;
  ANSWER                    :CHAR;
  LEFT, RIGHT               :INTEGER;
  XPUT, YPUT                :LONGINT;
  CAST                      :REAL;
  LINE                      :INTEGER;
  BLACK                     :BYTE;

BEGIN
  BLACK:=0;
  QUESTION:='DO YOU WANT TO CREATE A PLOT OF SCANLINES? (Y/N)';
  GET_ANSWER(QUESTION, ANSWER);

  IF ANSWER='Y' THEN
  BEGIN
    PREPARE_OUTPUT_FILE('C:\RES\TEMP');
    RESET(TEMP);
    WRITE('PLOTTING SCANLINES NOW...');
    FOR LINE:=1 TO ROWS DO
    BEGIN
      WRITELN(LINE);
      IF EQUATIONS[LINE,2]<>0 THEN
            {I.E. INTERCEPT <> 0 HENCE DATA EXISTS}
      BEGIN
        LEFT:=ROUND(EQUATIONS[LINE,3]);
         RIGHT:=ROUND(EQUATIONS[LINE,4]);
        FOR YPUT:=LEFT TO RIGHT DO
        BEGIN
          CAST:=EQUATIONS[LINE,2]-(YPUT+0.5)*EQUATIONS[LINE,1];
          XPUT:=ROUND(CAST+0.5);
          SEEK(TEMP, MAXCOL*(XPUT-1)+(YPUT-1));
          WRITE(TEMP, BLACK);
        END;
      END;
    END;
  WRITELN('DONE');
  QUESTION:='ENTER FILE NAME FOR LINE PLOT :- ';
  SAVE_NAME(OUTPUT_STR, QUESTION);
  OUTPUT_STR:= OUTPUT_STR + ('.PGM');
  WRITE_IMAGE_TO_FILE(OUTPUT_STR,MAXROW,MAXCOL);
  END;
END;


PROCEDURE WRITE_PIXEL_VALUE(X,Y,LINE:LONGINT;YNEAR:REAL);

VAR                                {FUNCTION WRITES THE SOURCE IMAGE}
  YGRAB   :LONGINT;                {PIXEL VALUE TO TEMP ONCE THE     }
  VAL     :BYTE;                   {NEAREST PIXEL HAS BEEN FOUND     }
  SF      :REAL;

BEGIN
  {NEED TRANSFORMATION TO GET ACTUAL PIXEL VALUE}
  SF:=(YR-YL)/(EQUATIONS[LINE,4]-EQUATIONS[LINE,3]);
  YGRAB:=ROUND(YL + SF*(YNEAR-EQUATIONS[LINE,3]+0.5));

  SEEK(RAWATM, COLUMNS*(LINE-1)+YGRAB-1); READ(RAWATM, VAL);
  SEEK(TEMP, MAXCOL*(X-1)+Y-1); WRITE(TEMP, VAL);
END;


PROCEDURE FIND_NEAREST_POINT(A,B,LINE:INTEGER;VAR TEMP_X,TEMP_Y:REAL);

VAR
  PERP_GRAD, PERP_INTERCEPT  :REAL;

BEGIN
  IF EQUATIONS[LINE,1] <> 0 THEN       {NEED TO OBTAIN COORDS}
  PERP_GRAD:= (-1/EQUATIONS[LINE,1])   {OF SOURCE OF NEAREST POINT}
```

```
  ELSE PERP_GRAD:= 1000000;     {INFINITY}
  PERP_INTERCEPT:= (A-0.5)+PERP_GRAD*(B-0.5);

  {PIXEL CENTRES}
  TEMP_Y:=(EQUATIONS[LINE,2]-PERP_INTERCEPT) / (EQUATIONS[LINE,1]-
    PERP_GRAD);
  TEMP_X:=EQUATIONS[LINE,2]-(EQUATIONS[LINE,1]*TEMP_Y);
END;


PROCEDURE WRITE_OUTPUT;

VAR QUESTION, OUTPUT_STR  :STRING;

BEGIN
  QUESTION:='ENTER THE FILE NAME FOR THE OUTPUT IMAGE :-  ';
  SAVE_NAME(OUTPUT_STR, QUESTION);
  OUTPUT_STR:= OUTPUT_STR + ('.PGM');
  WRITE_IMAGE_TO_FILE(OUTPUT_STR,MAXROW,MAXCOL);
END;


PROCEDURE RESAMPLE_IMAGE;
                                    {FUNCTION SEARCHES TEMP AND          }
VAR X,Y   :LONGINT;                 {PERFORMS RESAMPLING INSIDE          }
    VAL,BLACK,WHITE,PREVIOUS_VAL:BYTE;    {FRAME DRAW PREVIOUSLY       }
    TEMP_X,TEMP_Y,DIST          :REAL;
    STOP                        :BOOLEAN;
    COUNT,SEARCH_LINE,BEST_LINE :INTEGER;
    XCLOSEST,YCLOSEST           :REAL;
    QUESTION                    :STRING;
    ANSWER                      :CHAR;

BEGIN
  QUESTION:='DO YOU WANT TO RESAMPLE IMAGE NOW? (Y/N) ';
  GET_ANSWER(QUESTION, ANSWER);
  IF ANSWER='Y' THEN BEGIN
    PREPARE_OUTPUT_FILE('C:\RES\TEMP');
    WRITE('RESAMPLING IMAGE...');
    RESET(TEMP);
    RESET(RAWATM);

    FOR Y:=BB TO DD DO BEGIN    {RESAMPLE VERTICALLY                  }
      FOR X:=AA TO CC DO BEGIN  {TO IMPROVE EFFICIENCY OF RESAMPLING}
        DIST:=1000; STOP:=FALSE;
        IF X=AA{IE FIRST LINE} THEN BEGIN
          {SWEEP THROUGH EQUATIONS[] TO FIND NEAREST LINE}
          SEARCH_LINE:=1; COUNT:=0;
          WHILE STOP=FALSE DO BEGIN
            IF EQUATIONS[SEARCH_LINE,2]<>0{IE DATA EXISTS} THEN BEGIN
              FIND_NEAREST_POINT(X,Y,SEARCH_LINE,TEMP_X,TEMP_Y);
              IF SQRT(SQR(TEMP_X-X+0.5)+SQR(TEMP_Y-Y+0.5)) < DIST
                 THEN BEGIN
                XCLOSEST:=TEMP_X; YCLOSEST:=TEMP_Y;
                DIST:=SQRT(SQR(TEMP_X-X+0.5)+SQR(TEMP_Y-Y+0.5));
                COUNT:=0;
                BEST_LINE:=SEARCH_LINE;
              END {IF}
              ELSE INC(COUNT);
              IF COUNT>=10 THEN STOP:=TRUE;
            END; {IF}
            INC(SEARCH_LINE);
          END; {WHILE}
        WRITE_PIXEL_VALUE(X,Y,BEST_LINE,YCLOSEST);
        END  {IF}

        ELSE BEGIN
          {PASS CLOSEST SEARCH LINE TO RESAMPLING PROCEDURE}
          SEARCH_LINE:=BEST_LINE-5;
          COUNT:=0;
          WHILE STOP=FALSE DO BEGIN
            IF EQUATIONS[SEARCH_LINE,2]<>0{IE DATA EXISTS} THEN BEGIN
```

```
            FIND_NEAREST_POINT(X,Y,SEARCH_LINE,TEMP_X,TEMP_Y);
            IF SQRT(SQR(TEMP_X-X+0.5)+SQR(TEMP_Y-Y+0.5)) < DIST
               THEN BEGIN
              XCLOSEST:=TEMP_X; YCLOSEST:=TEMP_Y;
              DIST:=SQRT(SQR(TEMP_X-X+0.5)+SQR(TEMP_Y-Y+0.5));
              COUNT:=0;
              BEST_LINE:=SEARCH_LINE;
            END {IF}
            ELSE INC(COUNT);
          END {IF}
          ELSE INC(COUNT);
          IF COUNT>=10 THEN STOP:=TRUE;
          INC(SEARCH_LINE);
        END; {WHILE}
        WRITE_PIXEL_VALUE(X,Y,BEST_LINE,YCLOSEST);
      END; {ELSE}

    END; {ROW LOOP}
  IF FRAC(Y/25)=0 THEN WRITE('.');
  END;  {COLUMN LOOP}
 WRITELN('DONE.');
 CLOSE(TEMP); CLOSE(RAWATM);
 WRITE_OUTPUT;
 END; {IF ANSWER='Y'}
END;


BEGIN

INITIAL_SETUP;
PROMPT_FOR_CORRELATION;
PLOT_SCANLINES;
RESAMPLE_IMAGE;
END.
```

RESCALE.PAS

```
PROGRAM DUMBEL3;                        {PROGRAM TO RE-SCALE THE UN-CORRECTED   }
                                        {AERIAL PHOTOGRAPH TO THE RAW ATM IMAGE}
USES DOS, CRT;

CONST  MAXROW = 886;
       MAXCOL = 811;
       TAB = #9;

VAR
  PHOTO, RAWATM, TARGET                 :FILE OF BYTE;      {SERIAL FILES}
  HORIZONTAL_SCALE, VERTICAL_SCALE      :REAL;


PROCEDURE GET_ANSWER(QUESTION:STRING; VAR WAIT_FOR_KEY:CHAR);

BEGIN
  WRITELN(QUESTION);
  REPEAT
    WAIT_FOR_KEY:=READKEY;
    WAIT_FOR_KEY:=UPCASE(WAIT_FOR_KEY);
  UNTIL (WAIT_FOR_KEY='Y') OR (WAIT_FOR_KEY='N');
END;


PROCEDURE READ_SOURCE_IMAGES;

VAR
  X,Y        :LONGINT;
  TEXTFILE   :TEXT;
  VAL        :BYTE;

BEGIN
  ASSIGN(TEXTFILE, 'C:\RES\GPHOTRAW.PGM');
  RESET(TEXTFILE);
  ASSIGN(PHOTO, 'C:\RES\PHOTO');
  REWRITE(PHOTO);

  FOR X:=1 TO 4 DO                      {MOVE POINTER PAST HEADER INFORMATION}
    READLN(TEXTFILE);

  FOR X:=1 TO MAXROW DO BEGIN
    FOR Y:=1 TO MAXCOL DO BEGIN
      READ(TEXTFILE, VAL);
      WRITE(PHOTO, VAL);
    END;
  END;
  CLOSE(TEXTFILE); CLOSE(PHOTO);
END;


PROCEDURE INITIAL_SETUP;

VAR QUESTION :STRING;
    ANSWER   :CHAR;

BEGIN
   WRITELN;
   QUESTION:='DOES SOURCE IMAGE ALREADY EXIST IN BYTE FORMAT? (Y/N) ';
   GET_ANSWER(QUESTION, ANSWER);

   IF ANSWER='Y' THEN
   BEGIN
    ASSIGN(PHOTO, 'C:\RES\PHOTO');
   END;

   IF ANSWER='N' THEN
```

```
   BEGIN
     WRITE('READING SOURCE DATA NOW...');
     READ_SOURCE_IMAGES;
     WRITELN('DONE.')
   END;
END;


PROCEDURE WRITE_IMAGE_TO_FILE(OUTPUT_STR:STRING;MAX_X,MAX_Y:LONGINT);

VAR
  X,Y                    :INTEGER;
  VAL                    :BYTE;
  OUTPUT_FILE            :TEXT;

BEGIN
  WRITE('WRITING IMAGE TO FILE....');
  ASSIGN(OUTPUT_FILE, OUTPUT_STR);
  REWRITE(OUTPUT_FILE);
  RESET(TARGET);

  WRITELN(OUTPUT_FILE,'P2');
  WRITELN(OUTPUT_FILE,'#');
  WRITELN(OUTPUT_FILE,MAX_Y,' ',MAX_X);
  WRITELN(OUTPUT_FILE, '255');

  FOR X:=1 TO MAX_X DO BEGIN
    FOR Y:=1 TO MAX_Y DO BEGIN
      READ(TARGET, VAL);
      WRITE(OUTPUT_FILE, VAL, ' ');
    END;
    WRITELN(OUTPUT_FILE,'');
  IF FRAC(X/100)=0 THEN WRITE('.');
  END;
  CLOSE(OUTPUT_FILE); CLOSE(TARGET);
  WRITELN('DONE.'); WRITELN;
END;


PROCEDURE PREPARE_OUTPUT_FILE(MAX_X,MAX_Y:LONGINT);
                              {CREATES SERIAL FILE FOR RESAMPLED}
                              {IMAGE, AND WRITES VALUES AS WHITE}
VAR
  X,Y    :LONGINT;
  WHITE  :BYTE;

BEGIN
  ASSIGN(TARGET,'C:\RES\TARGET');
  RESET(TARGET);
  WHITE:=255;
  WRITE('PREPARING OUTPUT IMAGE...');
  FOR X:=1 TO MAX_X DO BEGIN
    FOR Y:=1 TO MAX_Y DO
      WRITE(TARGET,WHITE);
  IF FRAC(X/100)=0 THEN WRITE('.');
  END;
  WRITELN('DONE.');
  CLOSE(TARGET);
END;


PROCEDURE SAVE_NAME(VAR FILENAME_OUT,QUESTION:STRING);

BEGIN
   WRITE(QUESTION);
   READLN(FILENAME_OUT);
   IF FILENAME_OUT='' THEN FILENAME_OUT:='DEFAULT';
   FILENAME_OUT:=('C:\RES\') + FILENAME_OUT;
END;


PROCEDURE RESAMPLE_IMAGE;
```

```
VAR
  X,Y,XGRAB,YGRAB        :LONGINT;
  MAX_X, MAX_Y           :LONGINT;
  QUESTION, OUTPUT_STR   :STRING;
  ANSWER                 :CHAR;
  VAL                    :BYTE;

BEGIN
  QUESTION:=('DO YOU WANT TO RESAMPLE IMAGE NOW? (Y/N) ');
  GET_ANSWER(QUESTION,ANSWER);

  IF ANSWER='Y' THEN BEGIN
    MAX_X:=ROUND(MAXROW*VERTICAL_SCALE);
    MAX_Y:=ROUND(MAXCOL*HORIZONTAL_SCALE);

    {PREPARE TARGET SERIAL FILE}
    PREPARE_OUTPUT_FILE(MAX_X,MAX_Y);

    {RESAMPLE IMAGE}
    WRITE('RESAMPLING IMAGE NOW.....');
    RESET(PHOTO);
    RESET(TARGET);
    FOR X:=1 TO MAX_X DO BEGIN
      FOR Y:=1 TO MAX_Y DO BEGIN
        XGRAB:=ROUND(0.5+(X-0.5)/VERTICAL_SCALE);
        YGRAB:=ROUND(0.5+(Y-0.5)/HORIZONTAL_SCALE);
        SEEK(PHOTO, MAXCOL*(XGRAB-1)+(YGRAB-1));
        READ(PHOTO, VAL);
        WRITE(TARGET, VAL);
      END;
    IF FRAC(X/100)=0 THEN WRITE('.');
    END;
    WRITELN('DONE');

    {WRITE RESAMPLED IMAGE TO FILE}
    QUESTION:='ENTER THE FILE NAME FOR THE OUTPUT IMAGE :-  ';
    SAVE_NAME(OUTPUT_STR, QUESTION);
    OUTPUT_STR:= OUTPUT_STR + ('.PGM');
    WRITE_IMAGE_TO_FILE(OUTPUT_STR,MAX_X,MAX_Y);

  END;  {IF STATEMENT}

END;


BEGIN {MAIN PROGRAM}

VERTICAL_SCALE:=1;
HORIZONTAL_SCALE:=0.774;

INITIAL_SETUP;
RESAMPLE_IMAGE;

END.
```

DUMBBELL.PAS

```
PROGRAM DUMBBELL;

USES DOS, CRT;

CONST
       {REFERENCE IMAGE - ATM}
       INFILE1 = 'D:\RES\BAND3RAW.PGM';
       ROWS    = 1168;
       COLUMNS = 714;

       {SEARCH IMAGE - PHOTOGRAPH}
       INFILE2 = 'D:\RES\RES-PHO1.PGM';
       SCALED_X  = 886;
       SCALED_Y  = 628;

       {INITIAL SEARCH OPTIONS}
       INITIAL_WIDTH  = 20;    {WIDTH OF SEARCH BLOB}
       INITIAL_SEARCH = 20;    {SEARCH AREA FOR BLOB}

       {DUMBELL OPTIONS}
       PAD   = 2;              {SEARCH AREA FOR DUMBELL}
       WIDTH = 7;              {WIDTH OF DUMBELL BLOB}

       {RESAMPLING AREA}
       AA = 60;  {ROW}        {AREA FOR RESAMPLING}
       BB = 90;  {COL}        {TOP-LEFT TO BOTTOM-RIGHT}
                CC = 640;  {ROW}
                DD = 455;  {COL}

       DEPTH = 300;
       TAB = #9;

TYPE
  COLPTR    = ^COLARRAY;
  COLARRAY  = ARRAY[1..COLUMNS] OF BYTE;
  COLNODE   = RECORD
              COL :COLPTR
              END;
  ROWPTR    = ^ROWARRAY;
  ROWARRAY  = ARRAY[1..ROWS] OF COLNODE;

  LINEPTR   = ^LINEARRAY;
  LINEARRAY = ARRAY[1..COLUMNS] OF BYTE;

VAR
  PHOTODATA                      :ROWPTR;
  BLOB1, BLOB2                   :ROWPTR;  {LEFT AND RIGHT HAND 'BLOBS'}
  BAR                            :LINEPTR;

  PARAMETERS                     :ARRAY[1..ROWS,1..4] OF INTEGER;
  EQUATIONS                      :ARRAY[1..ROWS,1..4] OF REAL;

  RAWATM, SCALED_PHOTO, TARGET :FILE OF BYTE;     {SERIAL FILES}
  YL, YR                         :INTEGER; {LEFT AND RIGHT COLUMNS}
  WAIT_FOR_KEY                   :CHAR;


PROCEDURE READ_SOURCE_IMAGES;    {SOURCE IMAGES IN PGM TEXT FORMAT}

VAR
  X,Y       :LONGINT;
  TEXTFILE  :TEXT;
  VAL       :BYTE;
  JUNK      :STRING;

BEGIN
  ASSIGN(TEXTFILE, INFILE1);
  RESET(TEXTFILE);
```

```
 ASSIGN(RAWATM, 'D:\RES\RAWATM');
 REWRITE(RAWATM);
 RESET(TEXTFILE);
 FOR X:=1 TO 4 DO                {MOVE POINTER PAST HEADER INFORMATION}
   READLN(TEXTFILE,JUNK);

 FOR X:=1 TO ROWS DO BEGIN
   FOR Y:=1 TO COLUMNS DO BEGIN
     READ(TEXTFILE, VAL);
     WRITE(RAWATM, VAL);
   END;
 END;
 CLOSE(TEXTFILE); CLOSE(RAWATM);

 ASSIGN(TEXTFILE, INFILE2);
 RESET(TEXTFILE);
 ASSIGN(SCALED_PHOTO, 'D:\RES\PHOTO');
 REWRITE(SCALED_PHOTO);

 FOR X:=1 TO 4 DO                {MOVE POINTER PAST HEADER INFORMATION}
   READLN(TEXTFILE,JUNK);

 FOR X:=1 TO SCALED_X DO BEGIN
   FOR Y:=1 TO SCALED_Y DO BEGIN
     READ(TEXTFILE, VAL);
     WRITE(SCALED_PHOTO, VAL);
   END;
 END;
 CLOSE(TEXTFILE); CLOSE(SCALED_PHOTO);
END;


PROCEDURE PREPARE_OUTPUT_FILE(OUTPUT_STR:STRING;X,Y:INTEGER);
                              {CREATES SERIAL FILE FOR RESAMPLED}
VAR                           {IMAGE, AND WRITES VALUES AS WHITE}
  WHITE    :BYTE;
  ROW,COL  :LONGINT;

BEGIN
  ASSIGN(TARGET,'OUTPUT_STR');
  REWRITE(TARGET);
  WHITE:=255;
  WRITE('PREPARING OUTPUT IMAGE...');
  FOR ROW:=1 TO X DO
  BEGIN
    FOR COL:=1 TO Y DO
      WRITE(TARGET,WHITE);
  END;
  WRITELN('DONE.');
  CLOSE(TARGET);
END;


PROCEDURE WRITE_IMAGE_TO_FILE(OUTPUT_STR:STRING; X,Y:INTEGER);

VAR
  VAL                    :BYTE;
  CAST_ROW, CAST_COL     :LONGINT;
  OUTPUT_FILE            :TEXT;

BEGIN
  WRITE('WRITING IMAGE TO FILE...');
  ASSIGN(OUTPUT_FILE, OUTPUT_STR);
  REWRITE(OUTPUT_FILE);
  RESET(TARGET);

  WRITELN(OUTPUT_FILE,'P2');
  WRITELN(OUTPUT_FILE,'#');
  WRITELN(OUTPUT_FILE,Y,' ',X);
  WRITELN(OUTPUT_FILE, '255');

  CAST_ROW:=X; CAST_COL:=Y;
```

```
 FOR X:=1 TO CAST_ROW DO
 BEGIN
   FOR Y:=1 TO CAST_COL DO
   BEGIN
     READ(TARGET, VAL);
     WRITE(OUTPUT_FILE, VAL, ' ');
   END;
   WRITELN(OUTPUT_FILE);
 END;
 CLOSE(OUTPUT_FILE); CLOSE(TARGET);
 WRITELN('DONE.'); WRITELN;
END;


PROCEDURE SAVE_NAME(VAR FILENAME_OUT,QUESTION:STRING);

BEGIN
   WRITE(QUESTION);
   READLN(FILENAME_OUT);
   IF FILENAME_OUT='' THEN FILENAME_OUT:='DEFAULT';
   FILENAME_OUT:=('D:\RES\') + FILENAME_OUT;
END;


PROCEDURE GET_ANSWER(QUESTION:STRING; VAR WAIT_FOR_KEY:CHAR);

BEGIN
  WRITELN(QUESTION);
  REPEAT
    WAIT_FOR_KEY:=READKEY;
    WAIT_FOR_KEY:=UPCASE(WAIT_FOR_KEY);
  UNTIL (WAIT_FOR_KEY='Y') OR (WAIT_FOR_KEY='N');
END;


PROCEDURE INITIAL_SETUP;

VAR QUESTION :STRING;
    ANSWER   :CHAR;
    X,Y      :INTEGER;

BEGIN
   WRITELN;
   QUESTION:='DO SOURCE IMAGES ALREADY EXIST IN BYTE FORMAT? (Y/N) ';
   GET_ANSWER(QUESTION, ANSWER);

   IF ANSWER='Y' THEN
   BEGIN
    ASSIGN(RAWATM, 'D:\RES\RAWATM');
    ASSIGN(SCALED_PHOTO, 'D:\RES\PHOTO');
   END;

   IF ANSWER='N' THEN
   BEGIN
     WRITE('READING SOURCE DATA NOW...');
     READ_SOURCE_IMAGES;
     WRITELN('DONE.')
   END;

   {EMPTY PARAMETER ARRAY}
   FOR X:=1 TO ROWS DO BEGIN
     FOR Y:=1 TO 4 DO
     PARAMETERS[X,Y]:=0;
   END;
END;


PROCEDURE READ_EQUATIONS;

VAR TEXTFILE                 :TEXT;
    LINE, STARTL, ENDL,LOOP  :INTEGER;
    INPUT_STR                :STRING;
```

```
    TEMP                        :ARRAY[1..8] OF INTEGER;

BEGIN
  WRITE('ENTER FILE NAME CONTAINING CORRELATION DATA :- ');
  READLN(INPUT_STR);
  INPUT_STR:='D:\RES\' + INPUT_STR + '.TXT';
  ASSIGN(TEXTFILE, INPUT_STR);
  RESET(TEXTFILE);

  READLN(TEXTFILE);          {MOVE PAST HEADER INFORMATION}
  READ(TEXTFILE,STARTL);
  READLN(TEXTFILE,ENDL);
  READLN(TEXTFILE);
  READ(TEXTFILE,YL);
  READLN(TEXTFILE,YR);

  FOR LOOP:=1 TO 4 DO
    READLN(TEXTFILE);

  FOR LINE:=STARTL TO ENDL DO BEGIN
    FOR LOOP:=1 TO 8 DO
      READ(TEXTFILE, TEMP[LOOP]);
    READLN(TEXTFILE);

      IF (TEMP[8]-TEMP[6])<>0 THEN
        EQUATIONS[LINE,1]:=(TEMP[5]-TEMP[7]) / (TEMP[8]-TEMP[6])
        {GRADIENT}
      ELSE EQUATIONS[LINE,1]:=1000000; {INFINITY}
      EQUATIONS[LINE,2]:=(TEMP[5]-0.5)+((TEMP[6]-
          0.5)*EQUATIONS[LINE,1]);  {INTERCEPT}
      EQUATIONS[LINE,3]:=TEMP[6];
      EQUATIONS[LINE,4]:=TEMP[8];
    END;
    CLOSE(TEXTFILE);
  END;


  PROCEDURE READ_PHOTO_DATA_TO_MEMORY(FIRSTLINE, ENDLINE:LONGINT);

  VAR
    X,Y         :LONGINT;
    VAL         :BYTE;

  BEGIN
    WRITELN;
    WRITE('READING DATA TO MEMORY...');
    RESET(SCALED_PHOTO);

    GETMEM(PHOTODATA, SIZEOF(ROWARRAY));
    FOR X:=FIRSTLINE TO ENDLINE DO
      GETMEM(PHOTODATA^[X].COL, SIZEOF(COLARRAY));

    FOR X:=FIRSTLINE TO ENDLINE DO BEGIN
      FOR Y:=1 TO SCALED_Y DO BEGIN
        SEEK(SCALED_PHOTO, SCALED_Y*(X-1)+Y-1);
        READ(SCALED_PHOTO, VAL);
        PHOTODATA^[X].COL^[Y] := VAL;
      END
    END;
    CLOSE(SCALED_PHOTO);
    WRITELN('DONE.');
  END;


  PROCEDURE CALCULATE_INITIAL_PARAMETERS(STARTL,YCOORD:INTEGER;
                                         GUESS_X,GUESS_Y:INTEGER;
                                         VAR BESTX,BESTY:INTEGER);

  VAR
    BLOB                    :ROWPTR;
    X,Y                     :LONGINT;
    XGRAB, YGRAB            :LONGINT;
```

```
  VAL                          :BYTE;
  TOTAL                        :LONGINT;
  XBAR,YBAR                    :REAL;
  CORRELATION, BESTCORR        :REAL;
  SIGMAXY,SIGMAX2,SIGMAY2      :REAL;

BEGIN
  {READ BLOB TO MEMORY}
  RESET(RAWATM);
  TOTAL:=0;
  GETMEM(BLOB, SIZEOF(ROWARRAY));
  FOR X:=(STARTL-INITIAL_WIDTH) TO (STARTL+INITIAL_WIDTH) DO
    GETMEM(BLOB^[X].COL, SIZEOF(COLARRAY));

  FOR X:=(STARTL-INITIAL_WIDTH) TO (STARTL+INITIAL_WIDTH) DO BEGIN
    FOR Y:=(YCOORD-INITIAL_WIDTH) TO (YCOORD+INITIAL_WIDTH) DO BEGIN
      SEEK(RAWATM, COLUMNS*(X-1)+(Y-1));
      READ(RAWATM, VAL);
      BLOB^[X].COL^[Y] := VAL;
      TOTAL:=TOTAL+VAL;  {FOR XBAR CALCULATION}
    END;
  END;
  XBAR:=TOTAL/SQR(2*INITIAL_WIDTH+1);

  {BEGIN CORRELATION ON BLOB}
  BESTCORR:=-1;
  FOR X:=(GUESS_X-INITIAL_SEARCH) TO (GUESS_X+INITIAL_SEARCH) DO BEGIN
    {SEARCH LOOP}
    FOR Y:=(GUESS_Y-INITIAL_SEARCH) TO (GUESS_Y+INITIAL_SEARCH)
    DO BEGIN
      TOTAL:=0;   {FOR YBAR CALCUATION}
      FOR XGRAB:=(X-INITIAL_WIDTH) TO (X+INITIAL_WIDTH) DO BEGIN
        {KERNEL LOOP}
        FOR YGRAB:=(Y-INITIAL_WIDTH) TO (Y+INITIAL_WIDTH) DO
          TOTAL:=TOTAL+PHOTODATA^[XGRAB].COL^[YGRAB];
      END;
      YBAR:=TOTAL/SQR(2*INITIAL_WIDTH+1);

      {CALCULATE CORRELATION COEFFICIENT}
      SIGMAXY:=0; SIGMAX2:=0; SIGMAY2:=0; CORRELATION:=0;
      FOR XGRAB:=(X-INITIAL_WIDTH) TO (X+INITIAL_WIDTH) DO BEGIN
       {KERNEL LOOP}
        FOR YGRAB:=(Y-INITIAL_WIDTH) TO (Y+INITIAL_WIDTH) DO BEGIN
          SIGMAXY:=SIGMAXY+(BLOB^[XGRAB+STARTL-X].COL^[YGRAB+YCOORD-Y]
            -XBAR)*(PHOTODATA^[XGRAB].COL^[YGRAB]-YBAR);
          SIGMAX2:=SIGMAX2+SQR(BLOB^[XGRAB+STARTL-X].COL^[YGRAB
            +YCOORD-Y]-XBAR);
          SIGMAY2:=SIGMAY2+SQR(PHOTODATA^[XGRAB].COL^[YGRAB]-YBAR);
        END;
      END;
      CORRELATION:=SIGMAXY / SQRT(SIGMAX2*SIGMAY2);
      IF CORRELATION>BESTCORR THEN BEGIN
        BESTCORR:=CORRELATION;
        BESTX:=X;  BESTY:=Y;
      END;
    END;
  END; {SEARCH LOOP}
  WRITELN('BEST CORRELATION FOR ',STARTL,',',YCOORD,' IS ',
    BESTCORR:4:2,' AT ',BESTX,',',BESTY);

  {DISPOSE OF REFERENCE DATA IN MEMORY (BLOBS)}
  FOR X:=(STARTL-INITIAL_WIDTH) TO (STARTL+INITIAL_WIDTH) DO
    DISPOSE(BLOB^[X].COL);
  DISPOSE(BLOB);
END;


PROCEDURE READ_BELL(VAR BLOB:ROWPTR; ROW,COL:INTEGER; VAR TOTAL:REAL);

VAR
  X,Y    :LONGINT;
  VAL    :BYTE;
```

```
BEGIN
  GETMEM(BLOB, SIZEOF(ROWARRAY));
  FOR X:=(ROW-WIDTH) TO (ROW+WIDTH) DO
    GETMEM(BLOB^[X].COL, SIZEOF(COLARRAY));

  FOR X:=(ROW-WIDTH) TO (ROW+WIDTH) DO BEGIN
    FOR Y:=(COL-WIDTH) TO (COL+WIDTH) DO BEGIN
      SEEK(RAWATM, COLUMNS*(X-1)+(Y-1));
      READ(RAWATM, VAL);
      BLOB^[X].COL^[Y] := VAL;
      TOTAL:=TOTAL+VAL;  {FOR XBAR CALCULATION}
    END;
  END;
END;


PROCEDURE READ_BAR(VAR BAR:LINEPTR; X,YL,YR:LONGINT;VAR TOTAL:REAL);

VAR
  Y      :INTEGER;
  VAL    :BYTE;

BEGIN
  GETMEM(BAR, SIZEOF(LINEARRAY));
  FOR Y:=YL TO YR DO BEGIN
    SEEK(RAWATM, COLUMNS*(X-1)+Y-1);
    READ(RAWATM, VAL);
    TOTAL:=TOTAL+VAL;
    BAR^[Y]:=VAL;
  END;
END;


PROCEDURE DISPOSE_OF_BELL(VAR BLOB:ROWPTR; ROW:INTEGER);

VAR
  X    :INTEGER;

BEGIN
  FOR X:=(ROW-WIDTH) TO (ROW+WIDTH) DO
    DISPOSE(BLOB^[X].COL);
  DISPOSE(BLOB);
END;



PROCEDURE READ_REFERENCE_DATA(X,YL,YR:LONGINT;VAR XBAR:REAL);

VAR
  TOTAL    :REAL;

BEGIN
  TOTAL:=0;  {FOR XBAR CALCULATION}
  READ_BELL(BLOB1,X,YL,TOTAL);
  READ_BELL(BLOB2,X,YR,TOTAL);
  READ_BAR(BAR,X,YL,YR,TOTAL);
  XBAR:=TOTAL/( 2*SQR(2*WIDTH+1) + (YR-YL+1) );
  {XBAR CALCULATION WILL BE WRONG WHEN SCANLINE IS SHORTENED
   (OR LENGTHENED) DUE TO SEARCH - HOWEVER, THIS DISCREPENCY
   WILL BE VERY SMALL COMPARED TO TOTAL SUMMATION SINCE IF PAD=2,
   TOTAL WILL CONTAIN A MAXIMUM OF 4 VALUES TOO MANY (OR LESS).}
END;


PROCEDURE FIND_YBAR(XL,YL,XR,YR:INTEGER; VAR YBAR:REAL);

VAR
  X,Y,XGRAB          :INTEGER;
  TOTAL              :LONGINT;
  BAR_GRAD,BAR_INT   :REAL;
```

```
BEGIN
  TOTAL:=0;
  {LEFT HAND BLOB}
  FOR X:=(XL-WIDTH) TO (XL+WIDTH) DO BEGIN
    FOR Y:=(YL-WIDTH) TO (YL+WIDTH) DO
      TOTAL:=TOTAL+PHOTODATA^[X].COL^[Y];
  END;

  {RIGHT HAND BLOB}
  FOR X:=(XR-WIDTH) TO (XR+WIDTH) DO BEGIN
    FOR Y:=(YR-WIDTH) TO (YR+WIDTH) DO
      TOTAL:=TOTAL+PHOTODATA^[X].COL^[Y];
  END;

  {BAR}
  IF (YR-YL)<>0 THEN BAR_GRAD:=(XL-XR)/(YR-YL)
  ELSE BAR_GRAD:=10000000; {INFINITY}
  BAR_INT:=(XL-0.5)+BAR_GRAD*(YL-0.5);    {DEALS WITH PIXEL CENTRES}
  FOR Y:=YL TO YR DO BEGIN
    XGRAB:=ROUND(BAR_INT + 0.5 - BAR_GRAD*(Y-0.5));
    TOTAL:=TOTAL+PHOTODATA^[XGRAB].COL^[Y];
  END;

  YBAR:=TOTAL / (2*SQR(2*WIDTH+1) + (YR-YL+1));
END;


PROCEDURE CORRELATE_BLOB(BLOB                                  :ROWPTR;
                         VAR SIGMAXY,SIGMAX2,SIGMAY2           :REAL;
                         XBAR,YBAR                             :REAL;
                         X_SEARCH,Y_SEARCH,X_REF,Y_REF         :INTEGER);
VAR
  X,Y   :INTEGER;

BEGIN
  FOR X:=(-WIDTH) TO (WIDTH) DO BEGIN
    FOR Y:=(-WIDTH) TO (WIDTH) DO BEGIN
      SIGMAXY:=SIGMAXY+(BLOB^[X_REF+X].COL^[Y_REF+Y]-
          XBAR)*(PHOTODATA^[X_SEARCH+X].COL^[Y_SEARCH+Y]-YBAR);
      SIGMAX2:=SIGMAX2+SQR(BLOB^[X_REF+X].COL^[Y_REF+Y]-XBAR);
      SIGMAY2:=SIGMAY2+SQR(PHOTODATA^[X_SEARCH+X].COL^[Y_SEARCH+Y]-
          YBAR);
    END;
  END;
END;


PROCEDURE CORRELATE_BAR(SF,XBAR,YBAR:REAL;
   VAR SIGMAXY,SIGMAX2,SIGMAY2:REAL;
       XL_SEARCH,YL_SEARCH,XR_SEARCH,YR_SEARCH,YL_REF,YR_REF:INTEGER);
VAR
  BAR_GRAD, BAR_INT    :REAL;
  XGRAB,Y,SCALED_Y     :INTEGER;

BEGIN
  IF (YR_SEARCH-YL_SEARCH)<>0 THEN
    BAR_GRAD:=(XL_SEARCH - XR_SEARCH) / (YR_SEARCH - YL_SEARCH)
  ELSE BAR_GRAD:=10000000; {INFINITY}
  BAR_INT:=(XL_SEARCH-0.5)+BAR_GRAD*(YL_SEARCH-0.5);
  {DEALS WITH PIXEL CENTRES}

  FOR Y:=YL_SEARCH TO YR_SEARCH DO BEGIN
    XGRAB:=ROUND(0.5+BAR_INT - BAR_GRAD*(Y-0.5));
    {X COORD FOR THE SEARCH BAR}
    SCALED_Y:=ROUND(YL_REF+SF*(Y-YL_SEARCH));
    {Y COORD FOR THE REF BAR}

    SIGMAXY:=SIGMAXY+(BAR^[SCALED_Y]-XBAR)*
     (PHOTODATA^[XGRAB].COL^[Y]-YBAR);
    SIGMAX2:=SIGMAX2+SQR(BAR^[SCALED_Y]-XBAR);
    SIGMAY2:=SIGMAY2+SQR(PHOTODATA^[XGRAB].COL^[Y]-YBAR);
  END;
```

```
END;

PROCEDURE CALCULATE_CC(LINE,YL,YR,XLEFT,YLEFT,XRIGHT,YRIGHT:INTEGER;
                       XBAR,YBAR,SF:REAL;
                       VAR CORRELATION:REAL);

VAR
  SIGMAXY,SIGMAX2,SIGMAY2 :REAL;

BEGIN
  SIGMAXY:=0; SIGMAX2:=0; SIGMAY2:=0;
  CORRELATE_BLOB(BLOB1,SIGMAXY,SIGMAX2,SIGMAY2,
   XBAR,YBAR,XLEFT,YLEFT,LINE,YL);
  CORRELATE_BLOB(BLOB2, SIGMAXY,SIGMAX2,SIGMAY2,XBAR,YBAR,XRIGHT,
   YRIGHT,LINE,YR);
  CORRELATE_BAR(SF,XBAR,YBAR,SIGMAXY,SIGMAX2,SIGMAY2,XLEFT,
   YLEFT,XRIGHT,YRIGHT,YL,YR);
  CORRELATION:=SIGMAXY / SQRT(SIGMAX2*SIGMAY2);
END;


PROCEDURE CALCULATE_EQUATIONS(LINE, XLEFT, YLEFT, XRIGHT,
                              YRIGHT:INTEGER);

BEGIN
  IF (YRIGHT-YLEFT)<>0 THEN EQUATIONS[LINE,1]:=(XLEFT-XRIGHT)/
    (YRIGHT-YLEFT)
  ELSE EQUATIONS[LINE,1]:=1000000;     {GRADIENT}
  EQUATIONS[LINE,2]:=(XLEFT-0.5)+((YLEFT-0.5)*EQUATIONS[LINE,1]);
  {INTERCEPT}
  EQUATIONS[LINE,3]:=YLEFT;
  EQUATIONS[LINE,4]:=YRIGHT;
END;


PROCEDURE CORRELATE_BY_LINE(STARTL,ENDL,YL,YR:INTEGER;
                        VAR OUTPUT_FILE:TEXT;
                        GUESS_XL,GUESS_YL,GUESS_XR,GUESS_YR:INTEGER);

VAR LINE,X                                  :INTEGER;
    FIRSTLINE, ENDLINE                       :LONGINT;
    XLEFT,YLEFT,XRIGHT,YRIGHT              :INTEGER;
    BESTXL, BESTYL, BESTXR, BESTYR          :INTEGER;
    SCANLINES                               :TEXT;
    XBAR,YBAR,SF                            :REAL;
    CORRELATION, BESTCORR                   :REAL;

BEGIN
  IF (GUESS_XL-100)<1 THEN FIRSTLINE:=1
  ELSE FIRSTLINE:=(GUESS_XL-100);
  IF (GUESS_XL+100)>SCALED_X THEN ENDLINE:=SCALED_X
  ELSE ENDLINE:=(GUESS_XL+100);
  READ_PHOTO_DATA_TO_MEMORY(FIRSTLINE, ENDLINE);


  CALCULATE_INITIAL_PARAMETERS(STARTL,YL,GUESS_XL,GUESS_YL,
    BESTXL,BESTYL);
  CALCULATE_INITIAL_PARAMETERS(STARTL,YR,GUESS_XR,GUESS_YR,
    BESTXR,BESTYR);

  {DEFINE STARTING POSITION}
  PARAMETERS[STARTL,1]:=BESTXL;  PARAMETERS[STARTL,2]:=BESTYL;
  PARAMETERS[STARTL,3]:=BESTXR;  PARAMETERS[STARTL,4]:=BESTYR;

  FOR LINE:=STARTL TO ENDL DO BEGIN

    IF KEYPRESSED THEN BEGIN          {BREAK FUNCTION}
      WRITELN;
      WRITELN('     ***PROGRAM TERMINATED***');
      WRITELN;
      EXIT;
```

```
END;

{READ REFERENCE DUMBELL TO MEMORY}
READ_REFERENCE_DATA(LINE,YL,YR,XBAR);

{TEST LIMITS AND READ RELEVANT SECTION OF SEARCH IMAGE TO MEMORY}
IF ((PARAMETERS[LINE,1]+WIDTH+PAD+5)>ENDLINE)
OR ((PARAMETERS[LINE,3]+WIDTH+PAD+5)>ENDLINE) THEN
BEGIN
  {DISPOSE OF EXISTING DATA IN MEMORY}
  FOR X:=FIRSTLINE TO ENDLINE DO
    DISPOSE(PHOTODATA^[X].COL);
  DISPOSE(PHOTODATA);

  IF PARAMETERS[LINE,1] <= PARAMETERS[LINE,3]
    THEN FIRSTLINE:=PARAMETERS[LINE,1]-WIDTH-PAD-10
    ELSE FIRSTLINE:=PARAMETERS[LINE,3]-WIDTH-PAD-10;
  IF (FIRSTLINE+DEPTH)<ROWS
    THEN ENDLINE:=FIRSTLINE+DEPTH
    ELSE ENDLINE:=ROWS;
  READ_PHOTO_DATA_TO_MEMORY(FIRSTLINE, ENDLINE);
END;

{RESET CORRELATION COEFFICIENTS}
BESTCORR:=-1;

{BEGIN SEARCH LOOP}
FOR XLEFT:=(PARAMETERS[LINE,1]-PAD) TO (PARAMETERS[LINE,1]+PAD)
DO BEGIN
  FOR YLEFT:=(PARAMETERS[LINE,2]-PAD) TO (PARAMETERS[LINE,2]+PAD)
  DO BEGIN
    FOR XRIGHT:=(PARAMETERS[LINE,3]-PAD) TO
    (PARAMETERS[LINE,3]+PAD) DO BEGIN
      FOR YRIGHT:=(PARAMETERS[LINE,4]-PAD) TO
      (PARAMETERS[LINE,4]+PAD) DO BEGIN

        {CALCULATE SCALING FACTOR}
        SF:= (YR-YL){REF} / (YRIGHT-YLEFT){SEARCH};

        {PERFORM CORRELATION}
        FIND_YBAR(XLEFT, YLEFT, XRIGHT, YRIGHT, YBAR);
        CALCULATE_CC(LINE,YL,YR,XLEFT,YLEFT,XRIGHT,YRIGHT,
          XBAR,YBAR,SF,CORRELATION);

        IF BESTCORR < CORRELATION THEN BEGIN
          BESTCORR:=CORRELATION;
          BESTXL:=XLEFT; BESTYL:=YLEFT;
          BESTXR:=XRIGHT; BESTYR:=YRIGHT;
        END;

      END;
    END;
  END;
END;

WRITE('(',LINE,',',YL,')X(',LINE,',',YR,') -> ');
WRITELN('(',BESTXL,',',BESTYL,')X(',BESTXR,',',BESTYR,') - CC=',
    BESTCORR:5:2);
WRITELN(OUTPUT_FILE,LINE,TAB,YL,TAB,LINE,TAB,YR,TAB,BESTXL,
  TAB,BESTYL,TAB,BESTXR,TAB,BESTYR);
CALCULATE_EQUATIONS(LINE,BESTXL,BESTYL,BESTXR,BESTYR);

{DEFINE NEXT LINE'S STARTING POSITION}
PARAMETERS[LINE+1,1]:=BESTXL+1; PARAMETERS[LINE+1,2]:=BESTYL;
PARAMETERS[LINE+1,3]:=BESTXR+1; PARAMETERS[LINE+1,4]:=BESTYR;

{DISPOSE OF REFERENCE DUMBELL}
DISPOSE_OF_BELL(BLOB1,LINE);
DISPOSE_OF_BELL(BLOB2,LINE);
DISPOSE(BAR);

END; {(OF LINE LOOP)}
```

```
END;


PROCEDURE PROMPT_FOR_CORRELATION;

VAR QUESTION, OUTPUT_STR    :STRING;
    ANSWER                  :CHAR;
    STARTL, ENDL            :INTEGER;
    OUTPUT_FILE             :TEXT;
    X,Y                     :INTEGER;
    GUESS_XL,GUESS_YL,GUESS_XR,GUESS_YR   :INTEGER;

BEGIN
  {EMPTY EQUATIONS ARRAY}
  FOR X:=1 TO ROWS DO BEGIN
    FOR Y:=1 TO 4 DO
    EQUATIONS[X,Y]:=0;
  END;

  QUESTION:='DO YOU WANT TO RUN CORRELATION PROGRAM NOW? (Y/N) ';
  GET_ANSWER(QUESTION, ANSWER);

  IF ANSWER='Y' THEN
  BEGIN
    QUESTION:=('ENTER FILE NAME FOR CORRELATION DATA :- ');
    SAVE_NAME(OUTPUT_STR, QUESTION);
    OUTPUT_STR:= OUTPUT_STR + ('.TXT');
    ASSIGN(OUTPUT_FILE, OUTPUT_STR);
    REWRITE(OUTPUT_FILE);

    WRITE('ENTER START AND END ROWS '); READLN(STARTL,ENDL);
    WRITE('ENTER LEFT AND RIGHT HAND COLUMN NUMBERS '); READLN(YL,YR);

 {CALCULATE THE POSITION OF THE INITIAL WINDOWS TO GIVE BESTX..BESTY}
    WRITE('ENTER INITIAL GUESS FOR LEFT COORD  ');
    READLN(GUESS_XL,GUESS_YL);
    WRITE('ENTER INITIAL GUESS FOR RIGHT COORD ');
    READLN(GUESS_XR,GUESS_YR);

    WRITELN(OUTPUT_FILE, 'DUMBELL CORRELATION ',INFILE1,'(REF) TO ',
      INFILE2,'(SEARCH) BETWEEN ROWS ');
    WRITELN(OUTPUT_FILE,STARTL,TAB,ENDL);
    WRITELN(OUTPUT_FILE, 'AND COLUMNS');
    WRITELN(OUTPUT_FILE,YL,TAB,YR);
    WRITE(OUTPUT_FILE,'WIDTH=',WIDTH,', PAD=',PAD,', INITIAL GUESS
      AT (');
    WRITELN(OUTPUT_FILE,GUESS_XL,',',GUESS_YL,') ->
      (',GUESS_XR,',',GUESS_YR,')');
    WRITELN(OUTPUT_FILE);
    WRITELN(OUTPUT_FILE,'ATM',TAB,TAB,TAB,TAB,'PHOTO');
    WRITELN(OUTPUT_FILE,'XL',TAB,'YL',TAB,'XR',TAB,'YR',TAB,'XL',
      TAB,'YL',TAB,'XR',TAB,'YR');

    CORRELATE_BY_LINE(STARTL,ENDL,YL,YR,OUTPUT_FILE,GUESS_XL,
      GUESS_YL,GUESS_XR,GUESS_YR);
    CLOSE(OUTPUT_FILE);
  END;

  IF ANSWER='N' THEN
  BEGIN
    READ_EQUATIONS;
  END;
END;


PROCEDURE FIND_NEAREST_POINT(A,B,LINE:INTEGER;VAR TEMP_X,TEMP_Y:REAL);

VAR
  PERP_GRAD, PERP_INTERCEPT       :REAL;

BEGIN
  IF EQUATIONS[LINE,1] <> 0 THEN            {NEED TO OBTAIN COORDS}
```

```
  PERP_GRAD:= (-1/EQUATIONS[LINE,1])          {OF SOURCE OF NEAREST POINT}
  ELSE PERP_GRAD:= 1000000;     {INFINITY}
  PERP_INTERCEPT:= (A-0.5)+PERP_GRAD*(B-0.5);

  {PIXEL CENTRES}
  TEMP_Y:=(EQUATIONS[LINE,2]-PERP_INTERCEPT) / (EQUATIONS[LINE,1]-
    PERP_GRAD);
  TEMP_X:=EQUATIONS[LINE,2]-(EQUATIONS[LINE,1]*TEMP_Y);
END;


PROCEDURE WRITE_PIXEL_VALUE(X,Y,LINE:LONGINT;YNEAR:REAL);

VAR                                  {FUNCTION WRITES THE SOURCE IMAGE}
  YGRAB          :LONGINT;           {PIXEL VALUE TO TARGET ONCE THE   }
  VAL            :BYTE;              {NEAREST PIXEL HAS BEEN FOUND     }
  SF             :REAL;

BEGIN
  {NEED TRANSFORMATION TO GET ACTUAL PIXEL VALUE}
  SF:=(YR-YL)/(EQUATIONS[LINE,4]-EQUATIONS[LINE,3]);
  YGRAB:=ROUND(YL + SF*(YNEAR-EQUATIONS[LINE,3]+0.5));
  SEEK(RAWATM, COLUMNS*(LINE-1)+YGRAB-1); READ(RAWATM, VAL);
  SEEK(TARGET, SCALED_Y*(X-1)+Y-1); WRITE(TARGET, VAL);
END;


PROCEDURE WRITE_OUTPUT;

VAR QUESTION, OUTPUT_STR  :STRING;

BEGIN
  QUESTION:='ENTER THE FILE NAME FOR THE OUTPUT IMAGE :-  ';
  SAVE_NAME(OUTPUT_STR, QUESTION);
  OUTPUT_STR:= OUTPUT_STR + ('.PGM');
  WRITE_IMAGE_TO_FILE(OUTPUT_STR,SCALED_X,SCALED_Y);
END;


PROCEDURE READ_COORDS;

VAR X,Y                                 :LONGINT;
    VAL,BLACK,WHITE,PREVIOUS_VAL        :BYTE;
    TEMP_X,TEMP_Y,DIST                  :REAL;
    STOP                                :BOOLEAN;
    COUNT,SEARCH_LINE,BEST_LINE         :INTEGER;
    XCLOSEST,YCLOSEST                   :REAL;
    QUESTION,FILENAME,JUNK              :STRING;
    ANSWER,ANSWER2                      :CHAR;
    TEXTFILE                            :TEXT;

BEGIN
  QUESTION:='DO YOU WANT TO RESAMPLE IMAGE NOW? (Y/N) ';
  GET_ANSWER(QUESTION, ANSWER);
  IF ANSWER='Y' THEN BEGIN
    QUESTION:='DO YOU WANT TO ADD TO AN EXISTING IMAGE FILE? (Y/N) ';
    GET_ANSWER(QUESTION, ANSWER2);
    IF ANSWER2='Y' THEN BEGIN
      {READ EXISTING IMAGE FILE}
      WRITE('ENTER FILE NAME :- '); READLN(FILENAME);
      FILENAME:='D:\RES\' + FILENAME + '.PGM';
      ASSIGN(TEXTFILE, FILENAME);
      RESET(TEXTFILE);
      ASSIGN(TARGET, 'D:\RES\TARGET');
      REWRITE(TARGET);

      WRITE('READING IMAGE FILE...');
      FOR X:=1 TO 4 DO          {MOVE POINTER PAST HEADER INFORMATION}
        READLN(TEXTFILE,JUNK);
      FOR X:=1 TO SCALED_X DO BEGIN
        FOR Y:=1 TO SCALED_Y DO BEGIN
          READ(TEXTFILE, VAL);
```

```
        WRITE(TARGET, VAL);
      END;
    END;
    WRITELN('DONE.');
    CLOSE(TEXTFILE); CLOSE(TARGET);
  END
  ELSE PREPARE_OUTPUT_FILE('D:\RES\TARGET',SCALED_X,SCALED_Y);

  WRITE('RESAMPLING IMAGE...');
  RESET(TARGET);
  RESET(RAWATM);

  FOR Y:=BB TO DD DO BEGIN      {RESAMPLE VERTICALLY}
    FOR X:=AA TO CC DO BEGIN
      DIST:=1000; STOP:=FALSE;
      IF X=AA{IE FIRST LINE} THEN BEGIN
        {SWEEP THROUGH EQUATIONS[] TO FIND NEAREST LINE}
        SEARCH_LINE:=1; COUNT:=0;
        WHILE STOP=FALSE DO BEGIN
          IF EQUATIONS[SEARCH_LINE,2]<>0{IE DATA EXISTS} THEN BEGIN
            FIND_NEAREST_POINT(X,Y,SEARCH_LINE,TEMP_X,TEMP_Y);
            IF SQRT(SQR(TEMP_X-X+0.5)+SQR(TEMP_Y-Y+0.5)) < DIST
            THEN BEGIN
              XCLOSEST:=TEMP_X; YCLOSEST:=TEMP_Y;
              DIST:=SQRT(SQR(TEMP_X-X+0.5)+SQR(TEMP_Y-Y+0.5));
              COUNT:=0;
              BEST_LINE:=SEARCH_LINE;
            END {IF}
            ELSE INC(COUNT);
            IF COUNT>=30 THEN STOP:=TRUE;
          END; {IF}
          INC(SEARCH_LINE);
        END; {WHILE}
      WRITE_PIXEL_VALUE(X,Y,BEST_LINE,YCLOSEST);
      END  {IF}

      ELSE BEGIN
        {PASS CLOSEST SEARCH LINE TO RESAMPLING PROCEDURE}
        SEARCH_LINE:=BEST_LINE-15;
        COUNT:=0;
        WHILE STOP=FALSE DO BEGIN
          IF EQUATIONS[SEARCH_LINE,2]<>0{IE DATA EXISTS} THEN BEGIN
            FIND_NEAREST_POINT(X,Y,SEARCH_LINE,TEMP_X,TEMP_Y);
            IF SQRT(SQR(TEMP_X-X+0.5)+SQR(TEMP_Y-Y+0.5)) < DIST
            THEN BEGIN
              XCLOSEST:=TEMP_X; YCLOSEST:=TEMP_Y;
              DIST:=SQRT(SQR(TEMP_X-X+0.5)+SQR(TEMP_Y-Y+0.5));
              COUNT:=0;
              BEST_LINE:=SEARCH_LINE;
            END {IF}
            ELSE INC(COUNT);
          END {IF}
          ELSE INC(COUNT);
          IF COUNT>=30 THEN STOP:=TRUE;
          INC(SEARCH_LINE);
        END; {WHILE}
        WRITE_PIXEL_VALUE(X,Y,BEST_LINE,YCLOSEST);
      END; {ELSE}

    END; {ROW LOOP}
    IF FRAC(Y/25)=0 THEN WRITE('.');
    END;  {COLUMN LOOP}
  WRITELN('DONE.');
  CLOSE(TARGET); CLOSE(RAWATM);
  WRITE_OUTPUT;
  END; {IF ANSWER='Y'}
END;


PROCEDURE PLOT_SCANLINES;

VAR
```

```
  QUESTION, OUTPUT_STR      :STRING;
  ANSWER                    :CHAR;
  LEFT, RIGHT               :INTEGER;
  XPUT, YPUT                :LONGINT;
  CAST                      :REAL;
  LINE                      :INTEGER;
  BLACK,GREY                :BYTE;

BEGIN
  BLACK:=0;
  QUESTION:='DO YOU WANT TO CREATE A PLOT OF SCANLINES? (Y/N)';
  GET_ANSWER(QUESTION, ANSWER);

  IF ANSWER='Y' THEN
  BEGIN
    PREPARE_OUTPUT_FILE('D:\RES\TARGET',SCALED_X,SCALED_Y);
    RESET(TARGET);
    WRITE('PLOTTING SCANLINES NOW...');
    FOR LINE:=1 TO ROWS DO
    BEGIN
      IF EQUATIONS[LINE,2]<>0 THEN
      {I.E. INTERCEPT <> 0 HENCE DATA EXISTS}
      BEGIN
        IF FRAC(LINE/2)=0 THEN GREY:=0 ELSE GREY:=100;
        LEFT:=ROUND(EQUATIONS[LINE,3]);
        RIGHT:=ROUND(EQUATIONS[LINE,4]);
        FOR YPUT:=LEFT TO RIGHT DO
        BEGIN
          CAST:=EQUATIONS[LINE,2]-(YPUT+0.5)*EQUATIONS[LINE,1];
          XPUT:=ROUND(CAST+0.5);
          SEEK(TARGET, SCALED_Y*(XPUT-1)+(YPUT-1));
          WRITE(TARGET, GREY);
        END;
      END;
    END;
  WRITELN('DONE.');
  QUESTION:='ENTER FILE NAME FOR LINE PLOT :- ';
  SAVE_NAME(OUTPUT_STR, QUESTION);
  OUTPUT_STR:= OUTPUT_STR + ('.PGM');
  WRITE_IMAGE_TO_FILE(OUTPUT_STR,SCALED_X,SCALED_Y);
  END;
END;


BEGIN {MAIN PROGRAM}

{INITIAL SETUP - READ IMAGE FILES}
INITIAL_SETUP;

{PROMPT FOR CORRELTATION}
PROMPT_FOR_CORRELATION;

{PLOT SCANLINES}
PLOT_SCANLINES;

{BEGIN RESAMPLING IMAGE}
READ_COORDS;

END.
```

ACCASS.PAS

```
PROGRAM IMAGE_CORRELATION;

{*************************************************************************
*  CALCULATES THE DISPARITIES BETWEEN TWO APPROXIMATELY CO-REGISTERED
*  IMAGES OF THE SAME REGION, AND WRITES THE OUTPUT FILE AS
*  [ORIGX, ORIGY, NEWX, NEWY, CORRELATION]
*  PROCEDURE CORRELATES REFERENCE TO SEARCH
*************************************************************************}


USES CRT, DOS;

CONST
   TAB=#9;

   {REFERENCE IMAGE ATM}
   INFILE1='D:\RES\02LINCOR\LCO2BRE1.PGM';

   {SEARCH IMAGE}
   INFILE2 = 'D:\RES\GPHOTO.PGM';

   {NO. ROWS}     MAXROW = 886;
   {NO. COLS}     MAXCOL = 811;

   {SEARCH AREA}       C = 15;
   {WIDTH}             W = 15;

   {AREA FOR ACCURACY ASSESSMENT}
   {COORDS FOR TOP-LEFT CORNER}       TOPX=246;
                                      TOPY=116;
   {COORDS FOR BOTTOME-RIGHT CORNER}  BOTX=684;
                                      BOTY=634;


TYPE
   MATRIX=ARRAY[1..100,1..100] OF BYTE;

VAR
FILE1, FILE2           :FILE OF BYTE;
REFN, SRCH                    :MATRIX;
FILENAME_OUT           :STRING;
OUTPUT_FILE              :TEXT;

ROW, COL:              INTEGER;
G,H,P,Q                :INTEGER;
N                      :INTEGER;
CENTRE                 :INTEGER;
GRADIENT, INTERCEPT    :REAL;
ENDROW                 :INTEGER;
CORRELATION            :REAL;
CAST, BESTCORR         :REAL;
SPACES                 :INTEGER;

PROCEDURE SAVE_NAME;

BEGIN
   WRITE('ENTER THE FILE NAME FOR THE OUTPUT DATA:- ');
   READLN(FILENAME_OUT);
   IF FILENAME_OUT='' THEN FILENAME_OUT:='DEFAULT';
   FILENAME_OUT:=('D:\') + FILENAME_OUT + ('.TXT');
   WRITELN('');
   ASSIGN(OUTPUT_FILE, FILENAME_OUT);
   REWRITE(OUTPUT_FILE);
   WRITE(OUTPUT_FILE, 'ORIG X', TAB, 'ORIG Y', TAB);
   WRITELN(OUTPUT_FILE, 'NEW X', TAB, 'NEW Y', TAB, 'CORRELATION');
END;
```

```
PROCEDURE READ_REFERENCE_IMAGE;

VAR
   X,Y          :INTEGER;
   TEXTFILE     :TEXT;
   VAL          :BYTE;
   TEMP          :STRING;

BEGIN
   ASSIGN(TEXTFILE,INFILE1);
   RESET(TEXTFILE);
   ASSIGN(FILE1, 'D:\RES\PHOTO');
   REWRITE(FILE1);

   FOR X:=1 TO 4 DO          {MOVE PAST HEADER}
     READLN(TEXTFILE,TEMP);

   FOR X:=1 TO MAXROW DO
   BEGIN
    FOR Y:=1 TO MAXCOL DO
    BEGIN
     READ(TEXTFILE, VAL);
     WRITE(FILE1, VAL);
    END;
   END;
END;


PROCEDURE READ_SEARCH_IMAGE;

VAR
   X,Y          :INTEGER;
   TEXTFILE     :TEXT;
   VAL          :BYTE;
   TEMP          :STRING;

BEGIN
   ASSIGN(TEXTFILE,INFILE2);
   RESET(TEXTFILE);
   ASSIGN(FILE2, 'D:\RES\ATM');
   REWRITE(FILE2);

   FOR X:=1 TO 4 DO          {MOVE PAST HEADER}
     READLN(TEXTFILE,TEMP);

   FOR X:=1 TO MAXROW DO
   BEGIN
    FOR Y:=1 TO MAXCOL DO
    BEGIN
     READ(TEXTFILE, VAL);
     WRITE(FILE2, VAL);
    END;
   END;
END;


PROCEDURE INITIAL_SETUP;

VAR
   WAIT_FOR_KEY : CHAR;

BEGIN
   WRITELN;
   WRITELN('DO DATA FILES ALREADY EXIST IN BYTE FORMAT? (Y/N) ');
   REPEAT
    WAIT_FOR_KEY:=READKEY;
    WAIT_FOR_KEY:=UPCASE(WAIT_FOR_KEY);
   UNTIL (WAIT_FOR_KEY='Y') OR (WAIT_FOR_KEY='N');

   IF WAIT_FOR_KEY='Y' THEN
   BEGIN
    WRITELN;
```

```
    ASSIGN(FILE1, 'D:\RES\PHOTO');
    ASSIGN(FILE2, 'D:\RES\ATM');
   END;

   IF WAIT_FOR_KEY='N' THEN
   BEGIN
    WRITELN;
    WRITELN('READING DATA NOW...COULD TAKE A WHILE!');
    READ_REFERENCE_IMAGE;
    READ_SEARCH_IMAGE;
   END;
   WRITELN;
END;

PROCEDURE WRITE_WINDOWS_TO_MEMORY(A,B:INTEGER);

VAR X,Y    :LONGINT;
    CAST1 :LONGINT;

BEGIN
  RESET(FILE1);
    FOR X:=(A-W) TO (A+W) DO
    BEGIN
      FOR Y:=(B-W) TO (B+W) DO
      BEGIN
        CAST:=MAXCOL*(X-1)+(Y-1);
        SEEK(FILE1, MAXCOL*(X-1)+(Y-1));
        READ(FILE1,REFN[X-(A-W-C-1),Y-(B-W-C-1)]);
      END;
    END;

   RESET(FILE2);
   FOR X:=(A-W-C) TO (A+W+C) DO
     BEGIN
       FOR Y:=(B-W-C) TO (B+W+C) DO
       BEGIN
         SEEK(FILE2, MAXCOL*(X-1)+(Y-1));
         READ(FILE2,SRCH[X-(A-W-C-1),Y-(B-W-C-1)]);
       END;
     END;
END;

PROCEDURE CALCULATE_KERNAL_CORRELATION;

VAR
  X,Y : INTEGER;
  SIGMAXY, SIGMAX, SIGMAY, SIGMAX2, SIGMAY2 : REAL;
  CAST1, CAST2 : LONGINT;

BEGIN
  SIGMAXY:=0; SIGMAX:=0; SIGMAY:=0; SIGMAX2:=0; SIGMAY2:=0;

  FOR X:=-W TO W DO
  BEGIN
    FOR Y:=-W TO W DO
    BEGIN
      CAST1:=REFN[CENTRE+X, CENTRE+Y]; CAST2:=SRCH[G+X,H+Y];
      SIGMAXY:=SIGMAXY+CAST1*CAST2;
      SIGMAX:=SIGMAX+CAST1;
      SIGMAY:=SIGMAY+CAST2;
      SIGMAX2:=SIGMAX2+SQR(CAST1);
      SIGMAY2:=SIGMAY2+SQR(CAST2);
    END;
  END;

  IF ((N*SIGMAXY)-(SIGMAX*SIGMAY))=0 THEN CORRELATION:=0
  ELSE CORRELATION:=((N*SIGMAXY)-(SIGMAX*SIGMAY))/(SQRT((N*SIGMAX2)-
       SQR(SIGMAX))*SQRT((N*SIGMAY2)-SQR(SIGMAY)));

  IF BESTCORR < CORRELATION THEN BESTCORR:=CORRELATION;
  IF BESTCORR = CORRELATION THEN P:=G;
  IF BESTCORR = CORRELATION THEN Q:=H;
```

```
END;

PROCEDURE CALCULATE_LOCAL_WINDOW_CORRELATION(A,B:INTEGER);

BEGIN
  {P AND Q ARE THE COORDS OF THE BEST CORR - INITIALLY SET TO CENTRE}
  P:=CENTRE; Q:=CENTRE; BESTCORR:=-1;

  {G AND H ARE CENTRAL COORDS OF SEARCH WINDOW (IN MEMORY)}
  FOR G:=(CENTRE-C) TO (CENTRE+C) DO
  BEGIN
    FOR H:=(CENTRE-C) TO (CENTRE+C) DO
    BEGIN
      CALCULATE_KERNAL_CORRELATION;
    END;
  END;
  WRITE('BEST CORRELATION FOR ',A,' ',B,' IS ');
  WRITELN(BESTCORR:2:3,' AT ',(P+(A-W-C-1)),' ',(Q+(B-W-C-1)),' ',
          (-P+W+C+1),' ',(-Q+W+C+1));
  WRITELN(OUTPUT_FILE,A,TAB,B,TAB,(P+(A-W-C-1)),TAB,
          (Q+(B-W-C-1)),TAB,BESTCORR:2:3);
END;

BEGIN
  CLRSCR;
  INITIAL_SETUP;
  SAVE_NAME;

  SPACES:=2*W;
  CENTRE:=C+W+1; N:=SQR(2*W+1);

  ROW:=TOPX;
  WHILE ROW<=BOTX DO BEGIN
    COL:=TOPY;
    WHILE COL<=BOTY DO BEGIN

      WRITE_WINDOWS_TO_MEMORY(ROW,COL);
      CALCULATE_LOCAL_WINDOW_CORRELATION(ROW,COL);
      COL:=COL+SPACES;
    END;
    ROW:=ROW+SPACES;
  END;

  CLOSE(OUTPUT_FILE);
END.
```